

DISS. ETH NO. 26194

SEASONAL RESPONSE OF A SCREE SLOPE

A thesis submitted to attain the degree of
DOCTOR OF SCIENCES of ETH ZURICH
(Dr. sc. ETH Zurich)

presented by

Daisy Ruth Lucas Guzman

Master of Science in Civil Engineering, Rensselaer Polytechnic Institute

born on 03.06.1976

citizen of Chile

accepted on the recommendation of

Prof. Dr. Sarah M. Springman
Prof. Dr. Andrew Take
Prof. Dr. Lukas U. Arenson
Dr. Brian McArdell

2019

[This page is intentionally left blank]

Acknowledgments

I would like to express my great appreciation to Professor Sarah Springman for her support, time, mentoring and invaluable guidance during my doctoral studies. It has been a great honour to work with her. I would like to thank Professors Andy Take, Amin Askarinejad, Hansruedi Maurer, Peter Molnar and Dr. Brian McArdell for all their interest, valuable comments, time and collaboration in my research. I wish to acknowledge my co-examiner Dr. Lukas Arenson for his review and mentoring. I am very grateful to Markus Iten, Ernst Bleiker, Heinz Buschor, Andreas Kieper, Reto Grob, Nicole Oggier, Felix Wietlisbach, Anita Abt and in particular to Ralf Herzog and Kerstin Fankhauser for their crucial collaboration in my research project. My special thanks to Gabriela Laios, Sonja Zwahlen, Julia Boss and Marianne Mandrin for their support and administrative help. Also my thanks to Marco Huggenberger, Alexandru Marin, Yuko Yamamoto, Linda Seward, Ferney Morales and Thomas Büchli for their encouraging friendship. I express my gratitude to Professor Ioannis Anastasopoulos and IGT colleagues, Council authorities in Leuk and Agarn, and people in and outside of ETH who helped me in any way to develop my work thesis. Finally, I would like to thank my family and friends for all their support during these years, particularly to Filomena Guzman, Elizabeth Lucas, Alfredo Lucas, Daniel Aguilar, Pablo Lucas and Gian Andrea Colombo.

Table of Contents

Acknowledgments	I
Table of Contents	II
Abstract	VII
Zusammenfassung	IX
1 Introduction	1
1.1 Research motivation	1
1.1.1 Landslide definition and hazard	1
1.1.2 Landslides in Switzerland.....	1
1.1.3 Hydrological conditions in alpine environment	2
1.1.4 Rainfall-induced landslides	3
1.1.5 Scree slopes	4
1.1.6 Research in scree slopes	5
1.2 Site study: Scree slope at Meretschibach catchment	6
1.3 Previous studies at Meretschibach	10
1.4 Objectives of the research project.....	13
1.5 Method of research.....	14
1.5.1 Field in situ monitoring of landslide source areas	15
1.5.2 Laboratory	19
1.5.3 Numerical modelling	20
1.5.4 Physical modelling and physical (model) testing	21
1.6 Research Project Groups.....	23
1.7 Structure of the thesis	27
1.8 References.....	30
2 Study of the seasonal response of a scree slope and debris flow catchment in the Swiss Alps	43
2.1 Introduction.....	47
2.2 Site characterisation	47
2.2.1 Geology	48
2.2.2 Geotechnical characterisation.....	50
2.2.3 Geophysics.....	50
2.2.4 Monitoring.....	51
2.2.5 Modelling & analysis	55
2.3 Conclusions.....	55

2.4	Acknowledgements	56
2.5	References	56
3	Volumetric water content determination by TDR sensors and Decagons in gravelly soils	59
3.1	Introduction.....	62
3.2	Location and soil characteristics.....	62
3.2.1	Soil profile in IT1 and IT2.....	63
3.3	Methodology	64
3.4	Instrumentation.....	65
3.4.1	Sensors	65
3.4.2	Sensor Calibration.....	65
3.5	Instrumented trench construction	66
3.5.1	Instrumentation.....	66
3.5.2	Installation.....	66
3.6	Results	69
3.6.1	Instrumented trench IT1.....	69
3.6.2	Instrumented trench IT2.....	69
3.7	Conclusions	72
3.8	Acknowledgements	72
3.9	References	72
4	Study of the seasonal response of a scree slope and debris flow catchment in the Swiss Alps	75
4.1	Introduction.....	78
4.2	Soil ground characteristics	80
4.2.1	Soil classification	80
4.2.2	In situ unit weight.....	82
4.2.3	Slope inclination	82
4.2.4	Instrumented trenches	83
4.2.5	Electrical Resistivity Tomography (ERT).....	86
4.2.6	Archie's law	87
4.3	Results and discussion.....	88
4.3.1	VWC and temperature monitoring in instrumented trenches IT1-IT4.....	88
4.3.2	Seasonal response of the scree slope	88
4.3.3	Tensiometers.....	93
4.3.4	Temperature and VWC with depth	97
4.3.5	Sensor comparison: TDR vs. capacitance sensors.....	100

4.3.6	Electrical Resistivity Tomography (ERT).....	104
4.3.7	Slope characteristics	107
4.4	Conclusions.....	112
4.5	Acknowledgements.....	113
4.6	References.....	114
4.7	Appendix: Supplementary data on sensors and calibration.	118
4.7.1	Moisture content sensors description	118
4.7.2	Electrical resistivity tomography (ERT) and Archie’s law	118
4.7.3	Sensor operation difficulties.....	119
4.8	Appendix: Annual temperature curves and profile of VWC and temperature vs depth	121
4.8.1	Temperatures	121
4.8.2	VWC and Temperatures vs depth.....	122
5	Slope stability of a scree slope based on integrated	125
5.1	Introduction.....	130
5.2	The Meretschibach-Böchtur scree slope experiment	131
5.2.1	Location and description of the site	131
5.2.2	Preliminary hazard assessment.....	132
5.2.3	Soil characterisation	133
5.2.4	Seasonal monitoring	134
5.3	Methodology	135
5.3.1	Characterisation	135
5.3.2	Field monitoring.....	144
5.3.3	Preliminary numerical modelling	146
5.4	Results	147
5.4.1	Characterisation	147
5.4.2	Monitoring.....	155
5.4.3	Numerical modelling	166
5.5	Interpretation and discussion	168
5.5.1	Characterisation	168
5.5.2	Field monitoring.....	170
5.5.3	Numerical modelling	171
5.5.4	Hazard	171
5.6	Conclusion	172
5.7	Acknowledgments	174
5.8	References.....	174

5.9	Appendix. Supplementary Material	181
5.9.1	Characterisation	181
5.9.2	Monitoring.....	184
5.9.3	References.	192
6	Modelling of landslides in a scree slope induced by groundwater and rainfall.....	193
6.1	Introduction.....	197
6.2	Methodology	199
6.2.1	Test soil properties	201
6.2.2	Model geometry and hydraulic conditions	202
6.2.3	Hydraulic regime	203
6.2.4	Numerical model.....	205
6.2.5	Physical model	206
6.3	Results	210
6.3.1	Numerical modelling	210
6.3.2	Physical modelling.....	218
6.4	Discussion	224
6.4.1	Representation of field conditions	224
6.4.2	Numerical versus physical modelling results	224
6.4.3	Triggering of surficial landslides	225
6.4.4	Failure mechanisms	226
6.5	Summary and conclusions.....	230
6.6	Practical relevance and potential applications	232
6.7	Acknowledgements	232
6.8	References	233
6.9	Appendix. Supplementary material.....	238
6.9.1	Field and instrumentation location	238
6.9.2	Physical model	239
6.9.3	Results.....	259
7	Conclusions and outlook	263
7.1	Field monitoring	263
7.2	Soil characterisation.....	265
7.3	Numerical and physical modelling	266
7.4	Preliminary hazard assessment.....	268
7.5	Outlook	270

7.6	References.....	273
8	Appendix: Application of geotechnical and geophysical field measurements in an active alpine environment	277
8.1	Introduction.....	280
8.2	Soil and ground characteristics.....	282
8.2.1	Soil classification	282
8.3	Monitoring methodology	283
8.3.1	Instrumented trench.....	283
8.3.2	ERT.....	284
8.3.3	Archie's law	285
8.4	Results and discussion.....	286
8.4.1	Instrumented trench IT1.....	286
8.4.2	Instrumented trench IT3.....	288
8.4.3	Comparison between instrumented trenches.....	291
8.4.4	Comparison between ERT and TDR.....	293
8.5	Conclusions.....	293
8.6	Acknowledgments	296
8.7	References.....	297

Abstract

The mountains in the Swiss Alps are frequently subjected to extreme weather conditions, with periods of freezing temperatures, snow-melting, intense rainfall and daily temperature variations. Depending on the characteristics of the slope, geology and soil properties, several types of slope instabilities could increase the hazard to local communities. The most relevant, due to a combination of likelihood and potential mobilised volume of debris, would be during or following an intense or sustained period of rainfall that could lead to significant mass movements.

The objective of this research project, over several years, was to characterise and monitor the seasonal response of a scree slope located in the Swiss Alps (canton Valais) at an elevation of (1840-1910 m.a.s.l.). Not only are scree slopes rarely investigated in this way, they also present a number of challenges due to the deposition mechanisms in the slope and the poorly graded granular soil. The scree slope is also adjacent to an active channel that is known for having led to extensive debris flows reaching the valley below in the past. There was some concern about whether a slope failure in the scree could cause additional debris to lodge temporarily in the channel prior to release of another debris flow event.

The soil was characterised and then classified in the laboratory and stress-path dependent geotechnical strength parameters were determined. The soil response to natural meteorological events was monitored continuously during several winter and summer seasons. A schematic ground model was developed and modelled in physical and numerical simulations of surficial landslides induced by rainfall. Finally, the results are discussed in terms of the potential hazard for the community.

The project was particular by its location, which represented several challenges in terms of instrumentation and data collection techniques. The soil response was monitored through a long term field campaign, which provided information regarding soil volumetric water content (VWC) and soil temperature with depth (up to 1m) at specific locations, where trenches had been excavated and instruments had been installed. A geophysical campaign was performed simultaneously by another team member. She used Ground-based Penetrating Radar and Electrical Resistivity Tomography techniques to define bedrock depth. Additionally, the data were completed by precipitation recorded by two meteostations.

In situ and laboratory testing of the gravelly soil properties was performed, including in situ density tests and triaxial stress-path testing specific for rainfall infiltration. All these results were integrated in a ground model, which eventually served to design a prototype of the slope for investigation of the effects of groundwater and/or rainfall infiltration. Preliminary numerical modelling was then conducted using SEEP-SLOPE/W, followed by a programme of centrifuge tests in the IGT geotechnical drum centrifuge at ETH Zürich. The results showed that the soil layer is heterogeneous poorly graded gravel in terms of grain size, with some silt content. A critical state friction angle of 41° was obtained, with zero cohesion. The bedrock was located typically between 1.5-3 m depth, in a slope with inclination of $33\text{-}43^\circ$.

The soil behaviour, in terms of VWC and temperature, responded to the seasonal weather changes with a pattern: the VWC was mainly low in winter due to snow insulation and freezing temperatures, and higher and more variable in spring and summer due to the rise in temperatures with subsequent snow-melting and rainfall. The soil remained mainly in an unsaturated state because the gravel was well drained and the slope is steep. Assuming that the slope had an initial stress state ratio close to failure, the physical and numerical simulations confirmed that a shallow landslide could be triggered, depending on the combination of bedrock geometry, soil thickness, antecedent groundwater and rain intensity. Furthermore, it was found that the presence of a bedrock step outcrop that approached the ground surface is the worst scenario in terms of slope stability. A shallow landslide would be induced at lower groundwater flows than for bedrock parallel to the slope, because of the generation and rise of pore water pressure upslope of the step in the bedrock, where finally the slope failure would occur.

The study concludes from the hazard point of view that the scree slope studied in this thesis is unlikely to experience a significant slope failure, which would mobilise a considerable volume of debris that would endanger the village below; this due to the well drained conditions, shear strength of the gravel and the limited soil thickness (1-3 m). An estimate of the total debris volume overlying bedrock on this slope is 15000 m^3 . However a surficial landslide could be triggered in locations where the bedrock is shallow, or there is a step in the bedrock, which could force groundwater to rise following sustained rainfall and form a spring at some point. A combination of local erosion and soil saturation under a critical rainfall intensity would lead to a subsequent loss of effective stress of the gravelly soil.

Zusammenfassung

Die Berge in den Schweizer Alpen sind häufig extremen Wetterbedingungen ausgesetzt, mit Perioden mit Minustemperaturen, Schneeschmelze, starken Niederschlägen und täglichen Temperaturschwankungen. Abhängig von den Eigenschaften des Hanges, der Geologie und den Bodeneigenschaften können verschiedene Arten von Instabilitäten die lokalen Gemeinschaften bedrohen. Aufgrund der Wahrscheinlichkeit und des potenziellen Mobilisierungsvolumens von Ablagerungen ist eine intensive oder anhaltende Regenperiode, die zu erheblichen Massenbewegungen führen kann, am relevantesten.

Ziel dieses Forschungsprojekts war es, das saisonale Verhalten eines Geröllhangs in den Schweizer Alpen (Kanton Wallis) auf einer Höhe von (1840-1910 m.a.s.l.) über mehrere Jahre hinweg zu charakterisieren und zu überwachen. Geröllhalden werden auf diese Weise nicht nur selten untersucht, sondern sie stellen auch eine Reihe von Herausforderungen aufgrund der Ablagerungsmechanismen im Hang und des schlecht abgestuften körnigen Bodens. Die Geröllhalde grenzt auch an einen aktiven Kanal an, von dem bekannt ist, dass er in der Vergangenheit zu umfangreichen Murgängen geführt hat, die das darunter liegende Tal erreichten. Es gab Bedenken, ob ein Versagen im Geröllhang dazu führen könnte, dass sich vor dem Auslösen eines Murganges vorübergehend zusätzliche Ablagerungen im Kanal ansammeln.

Der Boden wurde charakterisiert und anschließend im Labor klassifiziert und spannungspfadabhängige geotechnische Scherfestigkeitsparameter wurden bestimmt. Die Reaktion des Bodens auf natürliche meteorologische Ereignisse wurde während mehrerer Winter- und Sommersaisons kontinuierlich überwacht. Ein Bodenmodell wurde entwickelt, mit welchem physikalische und numerische Simulationen bezüglich von durch Regen verursachten oberflächennahen Erdrutschen durchgeführt wurden. Abschließend wurden die Ergebnisse im Hinblick auf die potenzielle Gefahr für die Gemeinde diskutiert.

Das Projekt zeichnete sich insbesondere durch seinen Standort aus, der verschiedene Herausforderungen hinsichtlich Instrumentierung und Datenerfassungstechniken darstellte. Das Bodenverhalten wurde durch eine langfristige Feldkampagne überwacht. An bestimmten Stellen wurden Gräben ausgehoben und Instrumente installiert, welche

Informationen zum volumetrischen Wassergehalt des Bodens (VWC) und zur Bodentemperatur bis zu einer Tiefe von 1 m lieferten. Gleichzeitig wurde von einem anderen Teammitglied eine geophysikalische Kampagne durchgeführt, welche bodengestützte Penetrationsradar- und Widerstands-Tomographietechniken (GPR und ERT) verwendete, um die Tiefe des Grundgesteins zu bestimmen. Zusätzlich wurden die Daten durch Niederschlagsmessungen vervollständigt, welche von zwei Meteo Stationen aufgezeichnet wurden.

Die Eigenschaften des kiesigen Bodens wurden durch In-situ- und Laborversuche untersucht. In-situ-Dichtebestimmungen und triaxiale Spannungspfadversuche, die spezifisch für die Regeninfiltration waren, wurden durchgeführt. Alle diese Ergebnisse wurden in ein Bodenmodell integriert, das schließlich dazu diente, einen Prototyp des Hanges zur Untersuchung der Auswirkungen von Grundwasser- und / oder Niederschlagsinfiltration zu entwerfen. Anschließend wurde eine vorläufige numerische Modellierung mit SEEP-SLOPE / W durchgeführt, gefolgt von einer Serie von Zentrifugenversuchen in der geotechnischen Trommelzentrifuge des IGT an der ETH Zürich.

Die Ergebnisse zeigten, dass die untersuchte Bodenschicht als heterogener, schlecht abgestufter Kies mit variierendem Siltanteil klassifiziert werden kann. Es wurde ein kritischer Reibungswinkel von 41° mit einer Kohäsion von Null gemessen. Das Grundgestein befand sich typischerweise zwischen 1.5 und 3 m Tiefe mit einer Neigung von 33 bis 43° .

Das Bodenverhalten in Bezug auf VWC und Temperatur reagierte auf die jahreszeitlichen Wetteränderungen mit einem Muster: Der VWC war im Winter aufgrund der Schneeisolierung und der Gefriertemperaturen überwiegend niedrig und im Frühjahr und Sommer aufgrund des Temperaturanstiegs höher und variabler mit anschließender Schneeschmelze und Regenfällen. Der Boden blieb hauptsächlich in einem ungesättigten Zustand, da der Kies gut entwässert und steil abfallend war.

Unter der Annahme, dass die Neigung ein nahezu versagendes Anfangsspannungsverhältnis aufweist, bestätigten die physikalischen und numerischen Simulationen, dass ein flacher Erdrutsch ausgelöst werden kann, abhängig von der Kombination aus Grundgesteinsgeometrie, Bodendicke, vorhergehendem Grundwasser

und Regenintensität. Darüber hinaus wurde festgestellt, dass das Vorhandensein eines Felsvorsprungs, der sich der Bodenoberfläche näherte, das schlechteste Szenario in Bezug auf die Hangstabilität ist. Ein flacher Erdrutsch würde bei niedrigeren Grundwasserflüssen als bei hangparallelem Grundgestein ausgelöst, da Porenwasserdruckanstiege oberhalb des Felsvorsprungs entstehen, welche ein Versagen des Hanges bewirken.

Die Studie kommt unter dem Gesichtspunkt der Gefährdungsanalyse zu dem Schluss, dass es unwahrscheinlich ist, dass der in dieser Arbeit untersuchte Geröllhang einen signifikanten Erdrutsch erfährt, der eine beträchtliche Menge an Trümmern mobilisieren würde, die das darunter liegende Dorf gefährden würden. Dies ist auf die gute Drainage, die Scherfestigkeit des Kieses und die begrenzte Bodendicke (1-3 m) zurückzuführen. Eine Schätzung des Gesamtvolumens, das auf diesem Hang über dem Grundgestein liegt, beträgt 15000 m³. An Stellen, an denen der Untergrund flach ist, kann jedoch ein oberflächlicher Erdrutsch ausgelöst werden, oder es gibt einen Felsvorsprung, die dazu führen kann, dass das Grundwasser nach anhaltendem Regen steigt und sich irgendwann eine Quelle bildet. Eine Kombination von lokaler Erosion und Bodensättigung bei kritischer Niederschlagsintensität würde zu einem anschließenden Verlust der effektiven Spannungen im Kiesbodens führen.

[This page is intentionally left blank]

1 Introduction

1.1 Research motivation

1.1.1 Landslide definition and hazard

A landslide is defined as the movement of a mass of rock, debris or earth down a slope (Cruden, 1991), that can cause damage to elements such as population, building and engineering works, economic activities, public services and utilities, infrastructure, and environmental features in the area potentially affected by its occurrence (Lee & Jones, 2004). Their classification relates to the type of movement and material and may include events described as: falling, toppling, rotational sliding, transitional sliding, lateral spreading and flow; consisting of rock, debris or earth material respectively (Varnes, 1978; Cruden & Varnes, 1996; Hungr et al., 2014), and including the estimated depth of sliding (<2 m: shallow, 2-10 m: intermediate, >10 m: deep) and long term mean velocity (<2 cm/year: substabilised, 2-10 cm/year: slow, >10 cm/year: active) (Lateltin et al., 2005).

Landslides have been of great concern worldwide; according to the global dataset of non-seismic fatal landslides during 2004-2016, the number of fatal landslide events recorded worldwide was 4862, killing 55997 people (Froude & Petley, 2018). Furthermore, nearly 300 million people were estimated to live in areas of potential landslides (Dilley et al., 2005), which has enormous hidden costs in terms of human life, habitat, and infrastructure. Global cooperation has been promoted for landslide hazard reduction, with research e.g. in Japan, Italy, Canada, USA, China, Switzerland, India and UK amongst others (Sassa et al., 2009).

Specifically in Europe, a study over 27 countries during (1995-2014) showed a great concentration of events in mountainous areas with 476 landslides, resulting in 1370 deaths and 784 injuries, with an average economic loss of 4.7 billion Euros and 108 ±82 casualties per year (Haque et al., 2016). These were triggered mostly by natural extreme events as storms, earthquakes and floods.

1.1.2 Landslides in Switzerland

In the case of Switzerland, 6 % of the country is prone to slope instability most of which is located in the Alps (Lateltin et al., 2005), which are conditioned by geological and glacial history. Periods of landslide activity are often related to precipitation events (Raetzo et al., 2002) but can be triggered as well by human intervention or earthquakes.

Specific meteorological conditions, for example continuous precipitation associated with snow melting increases the occurrence of instabilities (Lateltin et al., 2005). The loss associated with this natural hazard is on average, the death of 1 person per year and financial damage of US \$20 million (over 30 years) (Schmid et al., 2004).

1.1.3 Hydrological conditions in alpine environment

In terms of climate, Switzerland reports on average near to 1500 mm/year of precipitation, with one third lost through evaporation, approximately two thirds contribution to surface run off, and a small amount storage in lakes, and recharge groundwater reserves (Beniston, 2012). The run off from the catchments in the Swiss Alps is a very important source of water for many rivers and a key element of the hydrological cycle (Liniger & Weingarten, 1998; Beniston et al., 1997; Weingartner & Pearson, 2001; Beniston, 2011; 2012). The hydrological cycle (Figure 1.1) shows the precipitation, in the form of rain or snow, falling over the Alps subjected to the ambient air temperature. The rainfall can runoff, and infiltrate into the soil (groundwater), the snow can melt (warmer temperatures) or remain where it has been deposited (snow pack). The water product of snowmelt, groundwater and runoff flow downhill is reduced by water uptake of any vegetation. Eventually it discharges in to river or lakes once it reaches the valley. During this cycle, the sun radiation produces evaporation in rivers/lakes and evapotranspiration in plants, resulting in water vapour ascending into the air. At higher altitude, the air pressure decreases and the temperature drops, condensing the water vapour to droplets (clouds). If there is any wind, it can transport the cloud again to the mountain (Chahine, 1992; Oki & Kanae, 2006; beniston et al., 2011).

This cycle repeats during the whole year and is strongly influenced by the seasonal and daily temperature variations in alpine environments. Ambient air temperature affects' the rate and timing of snow melting, the soil moisture and temperature in the soil. The hydraulic properties of the soil layers and the geology of the underlying bedrock are also important factors in the determination of groundwater recharge and water runoff rates (Beniston, 2003).

Additional studies on climate change in Switzerland, reveal that temperatures have risen up to 2 °C since year 1900 at high elevations e.g. Säntis at 2500 m.a.s.l. (Beniston & Stephenson, 2004), and the potential result of a warming condition will lead to reduced snow at lower levels where the precipitation is likely to fall in the form of rain

(Beniston, 2011, 2012). This reinforces the idea of studying rainfall as a triggering factor of landslides.

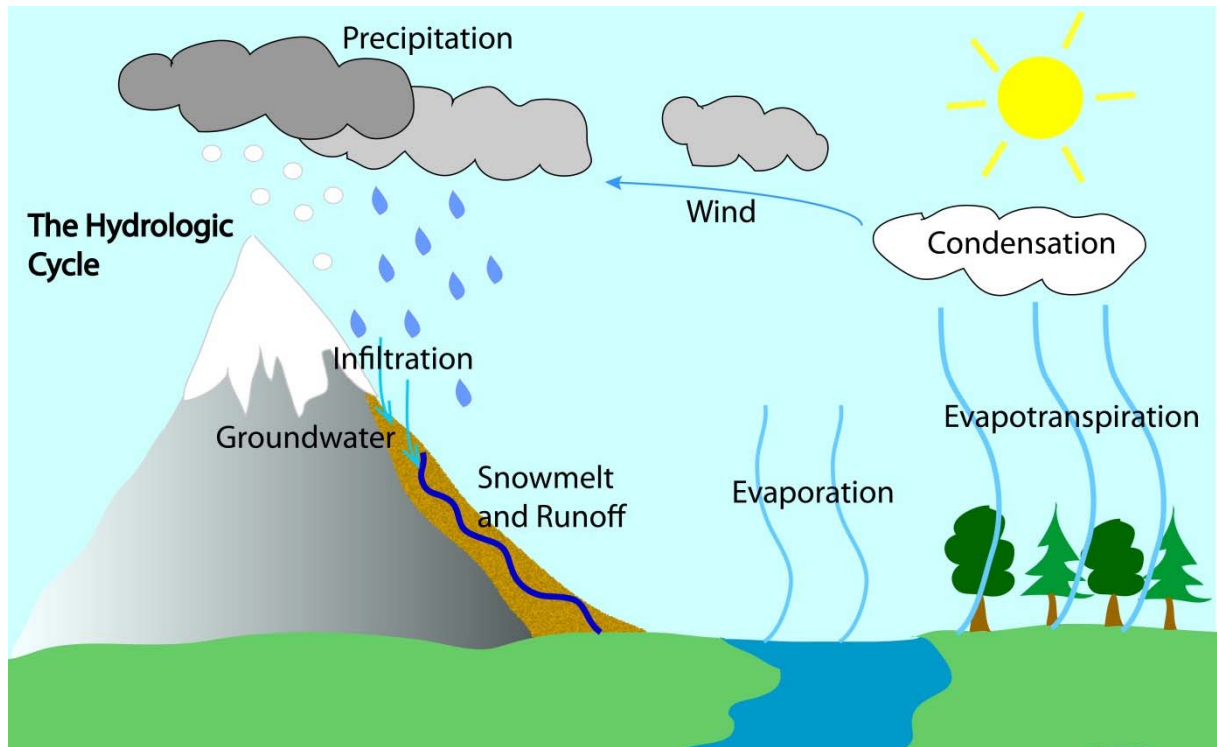


Figure 1.1. The hydrologic cycle at the Swiss Alps.

1.1.4 Rainfall-induced landslides

Heavy rainfall events can trigger instabilities in natural slopes due to the rise in pore water pressure in the ground, followed by loss in suction that occurs during infiltration and saturation; this reduces the effective stress and therefore the shear resistance in soils. This process can trigger shallow landslides and the remobilisation of soil in a slope. In some cases, this can also fuel a debris flow, which exhibits significant mobility and extended run out with the resulting hazard to the local communities living in valleys below.

The assessment of slope stability and the effect of meteorological perturbations on steep slopes can be studied by different methods: monitoring, GIS/Remote sensing, field investigation, laboratory experimental testing, and theoretical / analytical / numerical study, inventory (Sassa et al., 2009). The analysis can use single or a combination of methods to solve a determined instability case. Sassa et al.,(2009) suggested the use of several independent methods because it strengthen the reliability of studies because and enables deeper investigation from different viewpoints.

Due to the hazard associated with such superficial landslides and the potential losses, worldwide rainfall-induced instabilities have been widely studied (Fujii, 1969; Lumb, 1975; Caine, 1980; Keefer et al., 1987; Kimura et al., 1991; Larsen & Simon, 1993; De Vita et al., 1998; Dai & Lee, 2001; Cai & Ugai, 2004; Collins & Znidarcic, 2004; Cho & Lee, 2002; Chen et al., 2004; Mikoš et al., 2004; Lourenço et al., 2006; Guzzetti et al., 2007; Guzzetti et al., 2008; Baum & Godt, 2009; Petrovsek et al., 2011). In Switzerland, this type of instabilities have been investigated by several researchers e.g. Springman et al. (2003, 2011, 2012); Friedel et al. (2006), Askarinejad et al. (2012), Rickli & Graf (2009), Lateltin et al. (2005), Pedrozzi (2004), Seno & Thüring (2016), Mueller & Loew (2009), Leonarduzzi et al. (2017). Mechanisms of failure triggered by rainfall were studied, field and laboratory experiments were carried out, which have typically preceded any centrifuge and numerical modelling prior to identifying learnings about hazard process development.

1.1.5 Scree slopes

A special case of interest in the Alps in Switzerland is a scree slope, which is formed in mountain areas by rock debris, which loses potential energy in falling from weathered and fractured bedrock walls, following a downslope trajectory until it decelerates and stops i.e. until it reaches zero kinetic energy once again. Typical dynamic processes occurring in an active scree slope are toppling failures, rockfalls, landslides (small or large mass movements), and the fragmenting and sorting of materials (De Freitas et al., 1973; Statham, 1973; Gerber & Scheidegger, 1974; Evans & Hungr, 1993). These slopes are mostly found as a steep slope in a state of incipient failure.

Scree slopes typically consist of a surficial layer of loose rock debris underlain by a granular soil that can have a variable percentage of fines. There are sparsely vegetated and non-vegetated scree slopes. The slope angle can be close to the repose angle but also can be less steep. Both cases are possible in the same scree slope, and due to its mountain location the topography is strongly influenced by the hydrology and climate changes.

Instabilities in a scree slope can be triggered by intense rainfall, snow melting and earthquakes amongst others. The first two can trigger a shallow landslide caused by the increase of pore water pressure with the consequent decrease of suction, effective stress and soil shear strength. Depending on the rise of pore water pressure, the failure occurs under saturated or partially saturated conditions. Therefore, characterisation of the soil

and underlying bedrock is important in order to understand how the slope will saturate, drain, and potentially fail.

1.1.6 Research in scree slopes

Scree slopes have been investigated in the past by other researchers e.g. Statham (1973) studied the characteristics of slope form and material sorting, which develop when scree is subjected to the movement of individual blocks, immediately after falling on a non-vegetated surface. Borga et al. (2002) analysed a model for the simulation of shallow landsliding triggered by heavy rainstorms, which combines hydrologic concepts with infinite slope analysis. They compared the simulation with locations of observed landslides from the Eastern Italian Alps. Leach (1930) studied the effect of vegetation in some non-calcareous British scree slopes in viz. Wales and the Lake District at elevations below 762 m and stated the differences with alpine screes upon elevation, vegetation (very limited in Great Britain) and the absence of long-lasting supply or water product of snow melting. He stated that the variety, type and permanency of vegetation in a scree slope is highly affected by climate, and mostly by gravity. Pierson (1982) classified scree slope deposits in the Northern Craigieburn range in New Zealand and investigated the hydrological characteristics. He is one of the few researchers who has focussed on the characterisation of the soil under the surficial layer of rock debris in a scree slope. He describes three types of scree slope according to the form (sheet, cones, and gullies) and deposits (openwork gravel, stratified gravel and fines, buried truncated soil) and performed a mixture of in situ and laboratory tests to determine grain size distributions, moisture content, water retention tests, free drainage tests and permeability tests in situ.

Since investigations in this type of soil and slope are few (Pierson, 1982) and rather basic, and such slopes are prevalent in some areas in Switzerland, there is strong need to investigate, compile and document experience in monitoring, physical and numerical modelling for future research in scree slopes. The triggering factors and mechanism of failures are complex, as is the determination of modelling parameters. A comprehensive understanding of the process of remobilisation and failure mechanism of a scree slope under either intense or sustained rainfall will improve prediction of instability, and help to develop more efficient and cost effective measurements to mitigate the hazard.

1.2 Site study: Scree slope at Meretschibach catchment

The research study was carried out in the Bochtür area of the Meretschibach, above Agarn village in the Valais (Switzerland) (Figure 1.2 (a)) (Springman et al., 2015). The process of rock weathering created extensive scree slopes (sheet geometry) between elevations of 1500-2000 m, with an inclination angle of approximately 40°. Data of movements recorded by satellite InSAR are of 0.5 m/year at some places in the slope (unpublished data, Dr. Hugo Raetzo, 2012, Foen, pers. Comm.), which indicate that there is a form of instability, although the cause was unknown prior to the field campaign. The potential hazard of rockfalls, landslides, debris flow and avalanches is of great concern for Agarn Village. The events of mass movements in the Meretschibach reported in the area since the year 2000, are mostly debris flow type: 2 events in October 2000, 31 July 2002, 21 May 2003, 19 August 2003, 29 July 2008 (Szymczack et al., 2010), 20 July 2014, 28-29 July, 2014 (Frank et al., 2017).

The scree slope at Meretschibach (Figure 1.2 (b), (c)), is an erosional area covered by a surficial layer of cobbles, boulder sizes, underlain by heterogeneous gravel with sand and some fines up to 3 m thickness (Lucas et al., 2017). The underlying bedrock is mainly quartzite, heavily jointed, dipping southwards (10-30°) (Figures 1.3, 1.4), and is susceptible to extreme weathering, which favours the occurrence of rockfalls, slidings and saggings (GeotestAG/K. Zumhofen, 1990; Gabus et al., 2008a, 2008b; Oggier, 2011). A Geological profile and map of the catchment in Figures 1.3, 1.4, (further details in Oggier 2011).

The slope is partially vegetated due to the action of erosion processes, rockfall activity and snow avalanches in winter. The vegetation in the catchment includes Norway spruce (*Picea abies*) and broadleaves trees: Grey Alder, European Mountain ash, Pubescent birch and Great maple (Szymczack et al., 2010). Flora in the scree slope grows after the snow melting by late April -early May and wither again by the end of October (field observation). Erosional areas within the slope, with lack of vegetation, were reported to be more susceptible to landslides (ARGE Geotest AG. / K. Zumhofen, 1990; Askarinejad, 2013) and according to Oggier (2011) they are under dynamic changes, increasing from years 1945 -1999 and apparently recovering after this period (further details in Oggier 2011).

The climate in the scree slope is strongly marked by seasonal changes. Precipitation is in form of snow in winter, and there often a snow cover from November to late April with

the added hazard of avalanches when snow accumulates. Transition seasons are April/May and October/November with precipitation in the form of snow and/or rain, patches of snow, snow melting. Precipitation falls in the form of rain in summer showing greater variation in daily temperatures (further detail in Lucas et al., 2017). Rockfalls were observed more frequently in the transition and summer periods.

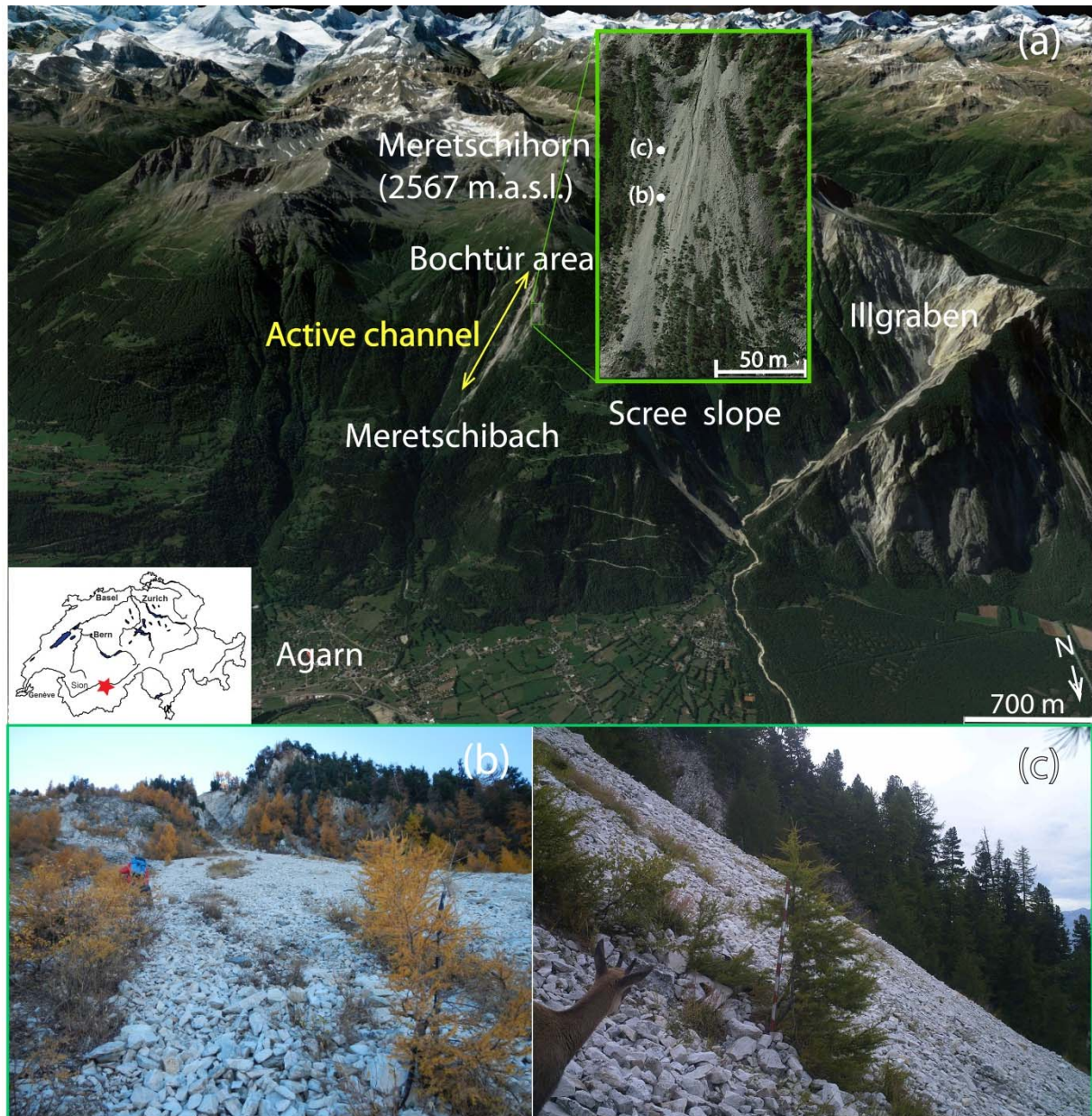


Figure 1.2. (a) Overview of the field area, located in canton Valais, Switzerland (star in small map). The image looking south shows the Meretschibach catchment, the most active area Böchtur, the active channel (debris flow path), and Agarn village located in the Rhone valley. The magnified image shows an enlargement of the scree slope (green rectangle) with a 50 m scale at the bottom (Image: Google Earth Pro). (b), (c) are close ups of the scree slope.

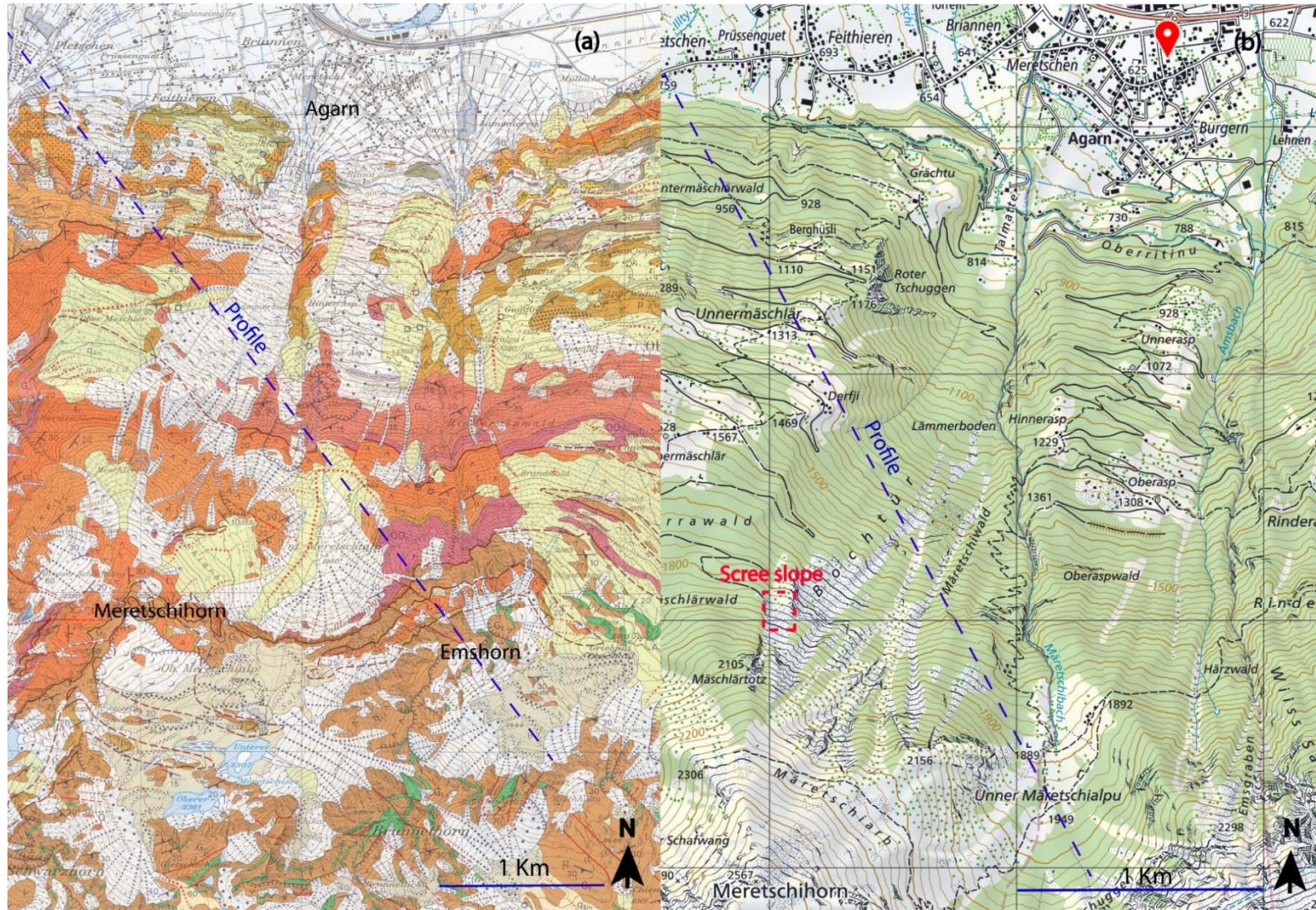


Figure 1.3. (a) Geology in the catchment area of Meretschibach (Source: Geological Atlas of Switzerland, map 1: 25'000, map leaf 1287 Sierre). Location of the cross section profile in Figure 1.4. shown as a dashed blue line (modified after N. Oggier 2011). (b) Map of the study site (Source: www.geo.admin.ch provided by the Federal Authorities of the Swiss Confederation).

6

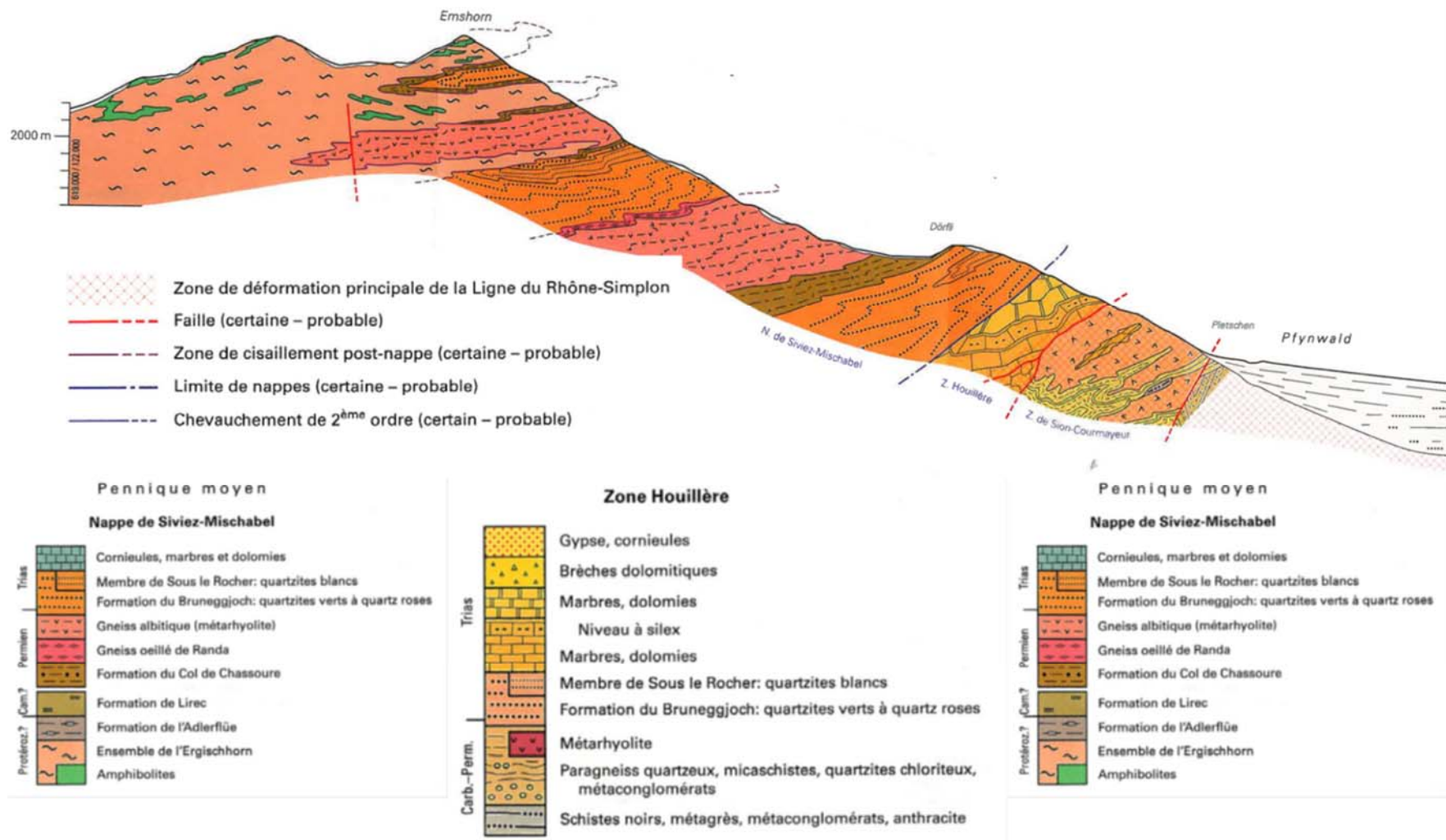


Figure 1.4. Geological profile in the catchment area of Meretschibach (source: Geological Atlas of Switzerland, map 1: 25: 000, map leaf 1287 Sierre). Modified after N. Oggier 2011.

1.3 Previous studies at Meretschibach

Before 2011, the reports and study mainly focused on the potential of debris flows occurring and on what protective measures could be installed in or adopted for in the Meretschibach catchment to reduce erosion in the subcatchment Böchtur (Table 1.1). The information corresponds to a compilation provided by Oggier (2011), with titles here translated from German (original language). After 2011, excluding the debris flow research, the studies correspond to the scree slope section and were performed by members of this project, during the course of this thesis.

Table 1.1. Previous studies at Meretschibach

Date	Title	Author
1973	Preliminary project for the construction and reforestation of the erosion area Bochtür, community Leuk and Agarn.	B. Teufen
November 21, 1989	Debris flow, rockfall and avalanche danger map for the settlement area of the municipality Agarn	Geotest AG.
1990	Erosion area Bochtür, renovation, general preliminary project	ARGE Geotest AG. / K. Zumhofen
August 13, 1992	Meretschibach, flood protection, structural measures, geological-geotechnical assessment, preliminary project with cost estimate	Geotest AG. Zumhofen & Glenz AG
October 1993	Correction of the Meretschibach	Zumhofen & Glenz AG.
May 1998	Detailed clarifications on the debris flow and flood hazard due to the Meretschibach, concept for action planning, hazard map	Geotest AG. T. & C. AG.
April 30, 2000	Evaluation of debris dam Meretschibach, summary report	Geo7 AG.
September 28, 2001	Evaluation of protective structures in the Meretschibach, spill retention basin vs. protective dams, short report	Geo7 AG.
June 06, 2002	Protection Concept Meretschibach, technical report	T. & C. AG.
revised July 2006	Meretschibach below Geschiebefang, summary report	T. & C. AG.
2009	Debris flow activity and snow avalanches in a steep watershed of the Valais alps (Switzerland): Dendrogeomorphic event reconstruction and identification of triggers.	S. Szymczak et al.
October 2010	Meretschibach, Technical Report on the executed building, and update of the hazard maps	T. & C. AG.
2010	Thesis Geomorphological mapping of sedimentary dynamics of mountain basins	D. Theler
2011	Emergency Planning Community Agarn	Geoplan
2011	Master Thesis. Simulation of debris flows with RAMMS. The example of Meretschibach	N. Oggier, ETH Zürich

2014	Master Thesis. Geophysical slope characterisation using GPR and ERT in an active debris flow catchment.	K. Fankhauser
2015	Master Thesis. Measurement of soil properties for gravels in a scree slope using large triaxial testing.	R. Grob
September 13, 2016	Radar interferometric measurements Meretschibach debris flow catchment, Canton Wallis.	Terrasense Switzerland AG
2017	Debris flow modelling at Meretschibach and Bondasca catchments, Switzerland: sensitivity testing of field-data-based entrainment model.	F. Frank et al.

The project/research reports before 2011 are briefly described as follow (after Oggier, 2011):

- Preliminary project for the construction and reforestation of the erosion area Bochtür, community Leuk and Agarn. Erosion of the Böchtur Area. (Teufen, 1973)
- Debris flow, rockfall and avalanche danger map for the settlement area of the municipality Agarn. Evaluation of the situation of debris flow, rockfall, and avalanche, hazard maps linked to these processes. (Geotest AG, 1989)
- Erosion area Bochtür, renovation, general preliminary project. Preliminary project for the rehabilitation of the erosion and rockfall area. (ARGE Geotest AG / K. Oven, 1990)
- Meretschibach, flood protection, structural measures, geological-geotechnical assessment, and preliminary project with cost estimate. Based in the previous report a preliminary project search to increase the protection of debris flow and flood in the catchment. (Geotest AG Zumhofen & Glenz AG, 1992)
- Correction of the Meretschibach. More detailed plans were added to the last report based on the solution selected, included stability on dam and rehabilitation of the creek bed with subsequent vegetation assessment. (Zumhofen & Glenz AG, 1993)
- Detailed clarifications on the debris flow and flood hazard due to the Meretschibach, concept for action planning, hazard map. The protective measures to reduce the hazard of debris flow and flooding were reviewed.(Geotest AG, T. & C. AG, 1998)
- Evaluation of debris dam Meretschibach, summary report. Review and optimisation of the protection (location, dimension, dam. Simulations of debris flow with dams. (Geo7 AG, 2000)
- Evaluation of protective structures in the Meretschibach, spill retention basin vs. protective dams, short report. This study was due to the debris flow in October 2000

and July 2001 and the potential danger in the protective structures; as a result, two variants were evaluated. (Geo7 AG, 2001)

- Protection Concept Meretschibach, technical report. After the storm in autumn 2000 an evaluation of the best solution was presented as a combination of a collector and a dam. (T. & C. AG, 2002)
- Meretschibach below Geschiebefang, summary report. Supplementary report. Issued to study the hydraulic problems of the channel and passages below collector which were small for the estimated 100 year flood event. (T. & C. AG, 2006)
- Meretschibach, technical report on the executed structures and update of hazard map after implemented protective measures executed between 2005-2007. These included a parallel protection dam, which protects Agarn, a deposit area, and two small dams to protect Briannen. (T. & C. AG, 2009)
- Geomorphological mapping of sedimentary dynamics of mountain basins. Hydro-morphological model of the slope of alpine areas and create a geomorphological legend and layers of GIS information. (Theler, 2010)
- Emergency Planning Community Agarn. Contingency planning and intervention measures at specific locations of Meretschibach. (Geoplan, 2011)
- Master Thesis. Simulation of debris flows with RAMMS, the example of Meretschibach. An updated collection of information related to the Meretschibach conditions, covering geology, past studies, erosion, debris flow potential and hazard maps. The thesis used the RAMMS program (rapid mass movement) to simulate debris flow in terms of run out prediction. The program was calibrated with past events and reproduced them with good results. The simulation with protective dams was challenging, requiring adjustments to the way in which the program could be used. (Oggier, 2011)
- Debris flow activity and snow avalanches in a steep watershed of the Valais alps (Switzerland): Dendrogeomorphic event reconstruction and identification of triggers. Analysis of growth disturbances versus time in samples from 93 trees from the debris flow transportation zone (760-860 m elevation), which allowed 20 debris flow and 3 avalanches to be reconstructed between 1930-2008. (Szymczak et al., 2009)
- Debris flow modelling at Meretschibach and Bondasca catchments, Switzerland: sensitivity testing of a field-data-based entrainment model. Computational debris flow modelling using RAMMS. The sensitivity of the initial landslide volume was explored and the results were compared to the resulting debris flow volume. (Frank et al., 2017)

The following research relates to the scree slope and as performed during the period encompassing this thesis project:

- Master Thesis. Geophysical slope characterisation using GPR and ERT in an active debris flow catchment. Determination of the depth of the bedrock using geophysical methods, and an alternative estimation of the Volumetric water content (VWC) using electrical resistivity tomography (ERT) and Archie's law. (Fankhauser, 2014)
- Master Thesis. Measurement of soil properties for gravels in a scree slope using large specimens in a triaxial stress path testing device. Determination of strength parameters of reconstituted gravel specimen from the scree slope using two triaxial testing devices with diameters 150 and 250 mm. The greater diameter allowed testing an average grain size distribution of the gravel at specific locations in the slope. (Grob, 2015)
- Radar interferometric measurements Meretschibach debris flow catchment, Canton Wallis. A significant component of remote sensing was originally planned, as an additional part of this project, to measure slope movements over a period of days and then months. However, the slope surface was so active that it was not found possible to continue this with any value, and so it was discontinued (Springman et al., 2015; Terrasense Switzerland AG, 2016).

The previous studies provide much information about the debris flow, and erosion hazards. However, there is still a gap in the characterisation of scree gravelly slopes in the Meretschibach catchment which is necessary to identify the hazard associated with mobilising a surficial landslide.

1.4 Objectives of the research project

The response of the scree slope to heavy rainfall events in the Bochtür area of Meretschibach was studied to improve prediction of soil behaviour in scree slopes and specifically, the response to saturation and desaturation events. The characterisation, including definition of strata and relevant geotechnical parameters was integrated into a realistic model. With simulation of the most critical scenarios, it would contribute to improving hazard identification for the local communities and development of a suitable early warning system to mitigate any threats.

To meet the goal, research questions and hypotheses were proposed and checked by means of a range of methodologies, which included, soil characterisation, monitoring, physical and numerical simulation.

It was hypothesised in this study that:

- the worst case hazard scenario in the scree slope would be a landslide triggered by rainfall; (analysed by field monitoring and soil characterisation)
- a combination of geophysical and geotechnical techniques can provide an adequate ground model and characterisation of the scree slope; (analysed by field monitoring and soil characterisation)
- the geometry of the bedrock and depth of the overlying scree soil influences the location, volume and type of any failure (analysed with numerical and physical models)
- the effect of an antecedent of groundwater flow combined with intense rainfall increases the occurrence of slope failure in a scree slope (physical models)
- the mechanism of failure is caused by loss of suction and saturation of the soil reducing effective strength (characterisation: triaxial testing).

1.5 Method of research

The project was mainly performed by one doctoral student from the Institute of Geotechnical engineering at ETH Zürich, with the support of an interdisciplinary team from several institutes and research groups: for Geotechnical Engineering, of Geophysics; and from the Swiss Federal Institute for Forest, Snow and Landscape Research (WSL). The activities required periodic site visits during the monitoring period, in parallel with laboratory and centrifuge testing at the facilities at ETH Zürich.

The research programme proposed (Figure 1.5) included the following phases: (i) field monitoring; ii) laboratory testing; (iii) numerical modelling and (iv) physical modelling in a geotechnical centrifuge. The internal structure of the soil and rock at the test site was investigated using state-of-the-art and novel geotechnical and geophysical methods. Eventually all of the information was combined to perform a preliminary hazard assessment of the scree slope.

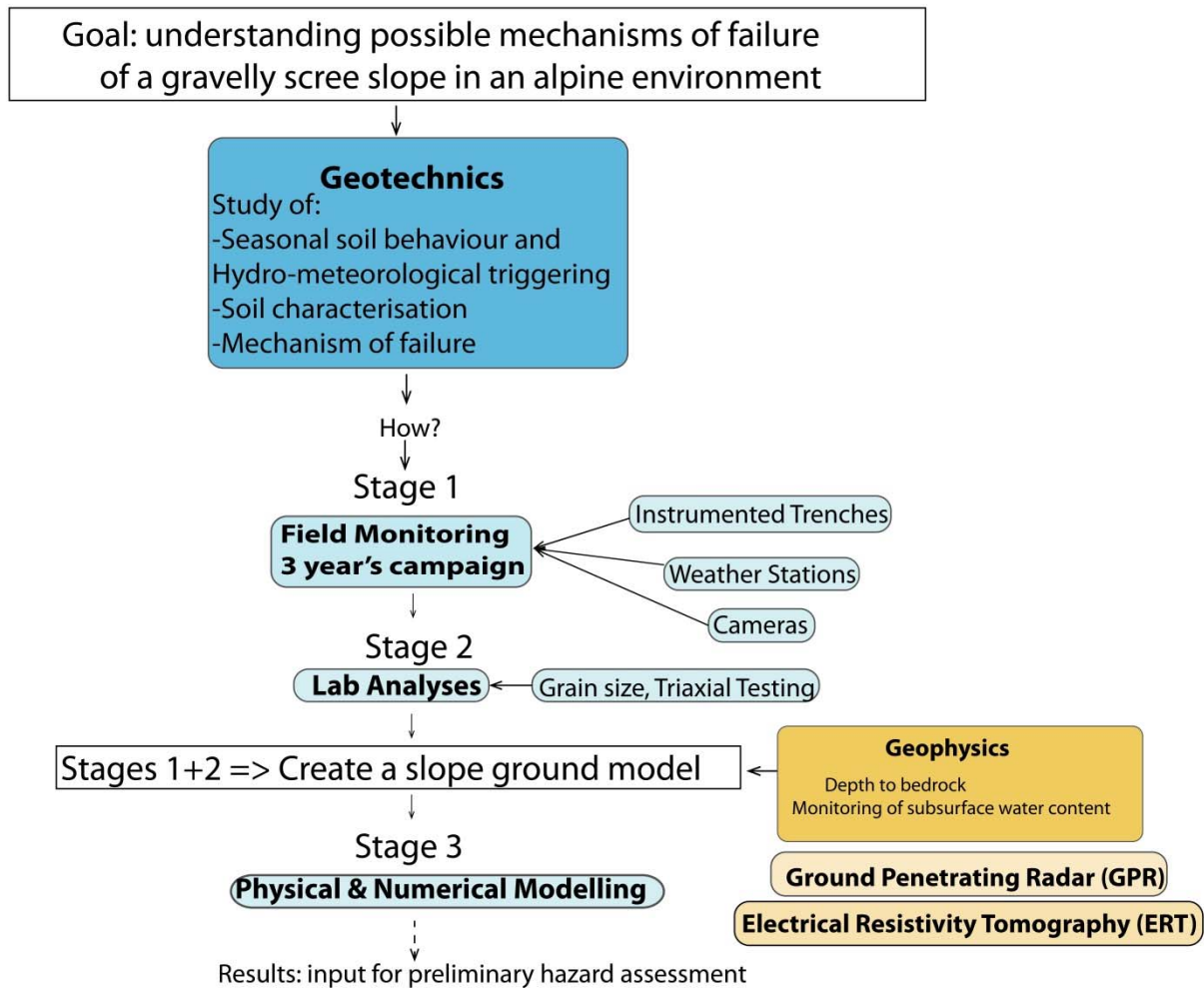


Figure 1.5. Purpose: understanding possible mechanisms of failure of a gravelly scree slope in an alpine environment to quantify the hazard for the Agarn community (flow chart by Lucas & Fankhauser, 2015).

1.5.1 Field in situ monitoring of landslide source areas

Integrated multidisciplinary methods have been adopted to evaluate slope response, in natural or artificial slopes. A few of the options available are here mentioned below.

Monitoring of displacements

Kane & Beck (2000) monitored potentially unstable slopes, reconstructed after landslides in 1998, and 1999, which were triggered by storms in Central and northern California. The sensors used were vibrating wire piezometer and time domain reflectometry (TDR) to monitor groundwater, electrolytic bubble inclinometer and tiltmeters, and TDR with cable tester to monitor ground movement. All sensors were connected to a data logger and a cell phone as radio transceiver. The advantage of remote monitoring is that the

data logger was able to trigger an alarm automatically if certain displacement time intervals were exceeded.

Intrieri et al. (2012) monitored the Torgiovannetto rockslide in Central Italy, consisting of 182000 m³ of potential volume hazard, next to a provincial road. The instrumentation included 13 wire extensometers, 1 thermometer, 1 rain gauge and three cameras. As a result, an early warning system was defined based on velocity thresholds of the extensometers.

The use of photogrammetry is reported by Ochiai et al. (2004, 2007) in a field site in Japan. The research involved artificial rainfall, which induced a landslide in a natural slope of weathered granite sand in Mountain Kaba-san, which was 30 m long, 5 m wide, with an inclination of 33°. The motion of the surface during failure was recorded by 5 stereo photogrammetry cameras, soil strain probes (up to 2 m depth) and tensiometers to detect changes in pore water pressure (PWP). The displacement was measured tracing 3-D targets using image analysis and allowed qualitative interpretation and timing definition of the shape and occurrence of landslide respectively. The landslide mass was 14 m long and 1.2 m deep with a travel distance up to 50 m in 17 s.

Monitoring of hydraulic conditions

Cascini et al. (2006) used 46 piezometers (in boreholes up to 70 m depth) to study the groundwater regime in a slope stability assessment in the southern Italy (Sila Massif). The site is an area of 20000 m² of a heterogeneous soil with colluvial, residual and saprolitic soil in slopes of 21-23° inclination under the threat of potential landslide reactivation. The result showed a marked seasonal water regime response, and was used to model the groundwater response using SEEP/W under assumptions of homogeneous and isotropic soil properties with good agreement in water levels monitored.

Schulz et al. (2009) measured displacements, pore-water pressure, and climatic conditions for 3 year at the Slumgullion landslide in Colorado, USA. The active landslide is 3.9 km long and has an average depth of 13 m. The soil was clayey gravel with sand with an average slope angle of 8°. The instrumentation consisted of 3 vibrating wire piezometers to measure the water table, sensors to measure air temperature, precipitation and snow depth, and a cable displacement transducer. The monitoring data showed characteristics of a seasonal behaviour, responsive increase of PWP due to rain and PWP reduction during drainage with an increase of acceleration during more extreme to soil displacements.

Chip et al. (1982) and Sweeney (1982), Low & Faisal (2000) and Yagi et al. (2000) reported monitoring of soil suction in unsaturated soil for slope instability prediction. The locations were Hong Kong, Kuala Lumpur in Malaysia, and Japan. The instruments were suction-meters, moisture sensors, tensiometers and rainfall gauge to study the suction behaviour versus time during rainfall and dry periods. The study predicts a relationship between rain intensity and failure initiation, and time of the failure with respect to the peak rain intensity.

Use of fiber optic sensors

Fiber optic acoustic emission sensors have been used in granular materials during the last half century, but their application has not yet been widely expanded due to issues related to signal attenuation in porous media, which requires a significant number of sensors (Michlmayr et al., 2012). Recent studies identify acoustic emission (AE) as a useful tool in early warning for landslides (Chichibu et al., 1989; Rouse et al., 1991; Dixon & Springs, 2007; Michlmayr et al., 2012; 2017), providing a suitable threshold that can be identified because the sensors installed in granular media respond to shearing, breakage and/or failure in the slope. Therefore they can be used to detect landslide occurrence, and can be used as a complementary system of monitoring (Michlmayr et al., 2017).

The use of fiber optic sensors in landslide assessment has been reported by several authors e.g. Huntley et al. (2014), in British Columbia, Canada. These sensors were complemented by GPS monitoring, piezometers, electrical resistivity tomography (ERT), electromagnetic (EM), ground penetrating radar (GPR), fiber Bragg grating (FBG) and Brillouin optical time domain reflectometry (BOTDR), subsurface inclinometers ShapeAccelArray (SAA), corner reflectors for satellite based (RADARSAT-2) interferometry and ground-based SAR and LiDAR. The authors used GPS and ERT data to complement the interpretation of data obtained from the fiber optic sensors.

Iten et al. (2008) used BOTDR technology in a road crossing St. Moritz landslide boundary. The data agreed with trends of geodetical data and field observations, and it was recommended to use BOTDR as a complementary technique for monitoring. Olivares et al. (2009), Zeni et al. (2015), and Michlmayr et al. (2017) used fiber optic sensors as well in the monitoring of landslides, and also under controlled laboratory conditions using a flume of a pre-determined inclination with sprinklers to simulate rainfall. The technique was complemented by use of tensiometers, TDR devices, rain

gauges, laser sensors, particle image velocimetry (PIV), pore pressure transducers (PPT) and video cameras. The soils tested were cohesionless pyroclastic soil, loose unsaturated granular soils, volcanic ashes from Cervinara Italy, and homogeneous material prone to landslide. The authors concluded that fiber optic sensors offer a suitable method to complement other monitoring techniques, providing distinguishable signs of acoustic emission under failure, and the advantage to measure in a spatial array and not only one point as other methods.

The assessment of slope stability and the effect of meteorological perturbations on steep slopes have been studied at 3 Swiss field sites by past members of the Institute: Gruben (1999-2001), Tössegg (2004-2006) and Rüdlingen (2008-2012). In all, the saturation regime of the slopes was a function of the inhomogeneity and permeability of the soil and any underlying rock layers, as well as possible drainage channels. Mechanisms of failure triggered by rainfall were studied; field and laboratory experiments were carried out, which have typically preceded the centrifuge and numerical modelling prior to identifying learnings about hazard process development.

The field monitoring was performed including geophysical techniques for characterisation (Friedel et al., 2006), novel sensor development (Askarinejad, 2009), instrumentation monitoring (Springman et al., 2003, 2012; Lehmann et al., 2012), photogrammetry (Akca et al., 2011), and bioengineering (Askarinejad et al., 2013). Instrumentation monitoring included weather stations, TDR (time domain reflectometry), decagons, tensiometers, inclinometers, piezometers, extensometers and temperature sensors, to measure in situ moisture content, suction, pore pressures and slope deformations.

Further details about these monitoring/triggering experiments and the resulting analyses have been published, which attempt to generalise the field and/or laboratory characterisation, monitoring, and modelling (Springman et al., 2003, 2009; Askarinejad, 2013; Casini et al., 2010 a&b; Thielen, 2007; Askarinejad et al., 2013) and summarise the findings to date (Springman, 2008; 2011).

In the research described in this dissertation, field measurements had to be designed for the site conditions and problem scale because of the challenging location (Figure 1.2). Desk studies were conducted, field visits were then carried out and the monitoring plan was developed following advice given by the multidisciplinary senior team. Samples were extracted from some exploratory test pits before the monitoring plan was implemented.

After preliminary tests, site monitoring of volumetric water content (VWC), temperature and suction measurements in the soil were implemented at specific points in the scree slope. The data was supported with geophysical measurements performed by the Institute of Geophysics at ETH to determine the depth of the bedrock, changes in soil layers and discontinuities. Additionally, in situ cameras captured aspects of the slope surface periodically (and up to 4 times per hour in summer), while two meteorostations recorded precipitation and air temperature.

Selected spots on the slopes (i.e. landslide source areas) were monitored in situ (up to 1 m depth) to measure water infiltration-suction characteristics in the ground, and the effect on the suction, and subsequent changes on the in situ effective stress. Four vertical monitoring profiles were installed, consisting of capacitance sensors (EC-5/10HS, Decagon devices), time domain reflectometry soil moisture (TDR) and temperature sensor sets of co-located tensiometers (IT1 and IT4). The instrumentation selected and installed was based on past field experience (Springman et al., 2003) and the requirements of the site (further details in Lucas et al. 2017).

The sensors were able to record data continuously through the years, after repeated periods of freeze/thaw conditions. The few cases of damage to instrumentation were due to rockfalls, debris flows or avalanches. Two weather stations were installed by WSL within the study area (rainfall, ambient air temperature, and humidity) and one of them removed after being hit by a rockfall. An additional precipitation gauge (OTT Pluvio2) was installed later (Nov. 2014) by IGT to measure solid-liquid and mixed precipitation, which remained functional till the end of the project.

The data collected served as input parameters for a programme of laboratory testing using reconstituted samples with triaxial stress-path testing that represents saturation due to rainfall infiltration. Subsequently, physical and numerical modelling was performed, simulating field conditions of the scree slope under intense rainfall events and the triggering of failure mechanisms induced by ground saturation.

1.5.2 Laboratory

In past studies, the soil characterisation and strength properties were obtained by testing programmes at the Institute for each site field experiment mentioned. The tests included strength mobilised due to stress paths that represent the increase in pore pressure, and are discussed in Casini et al. (2010b) and Askarinejad (2013). Some softening was observed as the stress path approached failure, but complete static

liquefaction (i.e. conversion to debris flow conditions) of the specimen in the triaxial apparatus was not observed (after Chu et al., 2003; Take et al., 2004).

A series of in situ unit weight measurements were conducted in the field, supported by a laboratory programme including grain size distribution of samples extracted from the instrumented trenches. Additionally, a programme of triaxial testing on large specimens (15 and 25 cm diameter) was performed to account the effects of grading and particle size using a stress path that simulated the rain infiltration processes in the soil.

1.5.3 Numerical modelling

Past numerical studies into slope stability included the work in from Leach & Herbert (1982), Ng et al. (2001), Cascini et al. (2009), and Elia et al. (2017) who used finite element analysis to study hydrological regimes in slopes. The study by Leach and Herbert focused on testing different scenarios and interpretations of the hydrogeological data collected in the field of 20 m layer of colluvium overlying decomposed granite in Hong Kong. Ng et al. (2001) performed simulations using a 3D numerical analysis (FEMWATER 3D finite element program) based on field monitoring data to study the groundwater response an unsaturated slope in Lai Ping Road in Hong Kong, subjected to rainfall with different patterns and duration. Cascini et al. (2009) modelled the failure and post failure run out of shallow landslides of a natural slope of a deposit of colluvial, weathered and pyroclastic origin under rainfall infiltration using SEEP/W and SIGMA/W from Geo-Studio. Elia et al. (2017) reviewed and commented on the limitations and benefits of the different numerical approaches in the study of natural and artificial slopes influenced by thermo-hydrmechanical conditions and by soil-vegetation-atmosphere interaction. Additionally, they provided general recommendations that should be to considered in numerical modelling and commented about the numerical simulation of real case studies.

Gilgen (2007) used a spatially distributed, conceptual hydrological model for his master's project and Thielen (2007) and Scheidegger (2007) conducted finite element analyses of the effects of natural rainfall infiltration and runoff at the Tössegg site. Thielen (2007) calibrated the hydraulic parameters on the basis of one year's data and then predicted outcomes from the meteorological data provided for the following year. Agreement was surprisingly good, also conducted 2D limit equilibrium analyses on a monthly basis to investigate the seasonal changes in factor of safety based on field data. Askarinejad (2013) extended this approach to unsaturated conditions and 3D spatial conditions,

respectively, for the Ruedlingen landslide, incorporating root reinforcement, bedrock drainage (after Bischof 2010) and exfiltration, carrying out uncoupled and coupled hydromechanical modelling using Geo-Studio (SEEP/W, Krahn, (2004a) and also plane strain limit equilibrium analysis using SLOPE/W, Krahn (2004b). Askarinejad (2013) also extended to a coupled unsaturated modelling and CODE Bright (Vaunat & Olivella 2002), and ran further 2D/3D numerical modelling of infiltration and exfiltration for Rüdlingen, to determine strain developments prior to triggering, this was validated by field data and centrifuge modelling of the same processes in the new environmental chamber. Sitarenios et al. (2019) advanced previous work by Askarinejad (2013) using coupled hydromechanical FEM analyses of soil cover to evaluate the response of the slope to rainfall and to explore the capability of reproducing the pre-failure behaviour of the silty sand Ruedlingen soil. The results were compared to field measurements with good agreement in terms of predicted time, area and displacements versus time at failure. Finally, their analysis was able to capture failure initiation with indication of significant straining and acceleration of the soil mass.

A preliminary numerical analysis was conducted for this project using a representative ground model of the field site, which integrated the information obtained from the soil monitoring and laboratory testing. The slope instabilities were simulated using the Program SEEP-SLOPE/W from Geostudio. The hydraulic conditions of groundwater and rainfall were applied with SEEP/W in a steady state analysis. Subsequently, these pore water pressures PWP obtained were applied to a model in SLOPE/W to calculate the factor of safety of the slope. The models considered different configurations of bedrock step geometry and soil thicknesses.

Steady state groundwater flow was applied on top of the slope to set up the hydrological conditions used in the analysis. The methodology consisted of calculating a groundwater flow intensity that would cause an instability, with a factor of safety equal to 1, for each of the analysed cases. The hazard then was identified in terms of magnitude of groundwater flow required to trigger the failure, the location of the slip surface in the slope and the volume of debris mobilised.

1.5.4 Physical modelling and physical (model) testing

According to Mayne et al. (2009) a geotechnical physical model (full or small scale) is a simplified physical representation (physical modelling) of a more complex boundary value problem (prototype) and leads to prediction; while physical (model) testing leads to

validation, while accepting certain conditions, including perturbations that may be imposed to investigate a hypothesis. Both are complementary, and require a clear problem definition, where relevant boundary conditions and perturbations to be applied contribute to the decision making of the type of model selection, instrumentation, equipment and timing. Mayne et al. (2009) emphasised that a key to modelling is the idealisation process to represent soil behaviour, geometry, loading, environmental and construction effects.

Centrifuge modelling has been used for geotechnical model testing for over four decades initially in the United States, the Soviet Union and Great Britain (Cheney et al., 1984; Craig, 2014). Today the technology is widely used to investigate a wide range of geotechnical problems, and it is frequently applied to the study of slope stability. The advantage of using centrifuge technology in slope stability analysis is the ability to test a scaled 3D model, at a specific N_g -level, under controlled hydrological conditions, while reproducing the soil behaviour, stresses, and failure mechanism of a process of interest. A scaled model is N times smaller than prototype (real scale), tested under N_g acceleration field (N times higher than earth gravity) to set up equivalent soil stresses at prototype and model scales (Schofield, 1980).

When testing landslides induced by groundwater/rainfall with centrifuge models, the model, soil, and hydrological regimes should match the relevant parameters of the real soil under study when at N_g . The N_g level is selected depending on the objective of the study, set up, scale of the prototype, boundary conditions of the problem, materials, sensors, and should consider the capacity of the centrifuge used for the testing. Scaling laws (Garnier et al., 2007; Dell'Avanzi & Zornberg, 2002; Askarinejad, 2014) are applied to convert the output data of the test back to prototype scale, allowing the comparison of these results with real problems.

Previous researchers have used centrifuge technology in many studies of slope stability, as is the case of Timpong & Toyosawa (2007); Milne et al. (2012); Ling et al. (2009a); Tamate et al. (2010); Lee & Bolton (2006); Take (2004, 2014); Askarinejad (2013); Take & Beddoe (2014); Take et al. (2015). The use of these techniques mostly required the application of rain to induce slope failure. This effect has been simulated by a climate chamber with calibrated nozzles (Craig et al., 1991; Ling et al., 2009b; Take et al., 2004, 2015; Tamate et al., 2010; Askarinejad, 2013). Some cases were studied by applying groundwater flow at the crest of the slope to create a phreatic surface in granular materials that could generate a landslide (Take et al., 2004; Take & Beddoe, 2014).

Take and Beddoe (2014), studied static liquefaction, in a granular slope (30°), applying a groundwater flux with a metering pump in a step-wise increase, under 30g. The results showed that the pore water pressure (measured by PPTs along the slope and at the toe) increased at the intersection of the inclined part of the slope to the bottom toe would be greater than in the well-drained and inclined part of the slope. This is because the water could pond in the bottom layer saturating the soil section above it, inducing a local failure. These results were used as a basis for the hypothesis of the effect of groundwater flow on the slope stability and were tested during the numerical and physical modelling.

A drum centrifuge (Cheney et al., 1984; Springman et al., 2001), has been used in research for slope stability analysis with good results (Cheney et al., 1984; Askarinejad, 2013). Past studies performed at the drum centrifuge at ETH Zürich (Figure 1.6), included centrifuge experiments for the Ruedlingen soil and slope were carried out using a climate chamber (Askarinejad, 2013) to study the triggering mechanism of landslides due to rainfall. Model infiltration and exfiltration events on unsaturated slope deposits were simulated in a 38° slope of silty sand material of 1 m thickness. Artificial rainfall was applied to a calibrated intensity during the test and the pore water pressure changes in the slope were recorded until failure occurred. Factors such as bedrock shape and drainage function (infiltration and exfiltration) and reinforcement by artificially grown vegetation already have been simulated successfully at model scale under enhanced gravity conditions in the centrifuge (Askarinejad, 2013). Other research projects looked at mobility and run out for debris flows (Bowman et al., 2006; 2007; 2010) and rock avalanches (Imre et al., 2010a & b).

A programme of centrifuge tests was conducted in the drum centrifuge at ETH, under 50-52g, with controlled conditions of groundwater flow and/or rainfall intensity-duration. The slopes was mantled with a sandy soil, which is scaled from the prototype gravel, to study the hydromechanical response of natural slopes. Different shapes and hydraulic properties of the bedrock, in terms of drainage, are provided for the model. Positive and negative pore pressures will be measured through miniature pore pressure transducers.

1.6 Research Project Groups

The goals of this project were achieved due to the collaboration of experts from different research disciplines. The project (Figure 1.5) was developed under the Institute for Geotechnical Engineering, led and supervised by Prof. Sarah Springman; the planning,

coordination, execution, analysis and lead on the research publications were under the responsibility of doctoral student Daisy Lucas.

The collaborators, and their interaction with the project, are shown in Figure 1.7 and can be grouped into four branches:

- Current employees from Dept. of Civil, Environmental and Geomatic Engineering (BAUG) working at the Institute for Geotechnical Engineering (IGT), ETH Zürich: including the laboratory manager and researcher Ralf Herzog, supported by a team of technicians of significant and varied experience: Ernst Bleiker in sensor technology, Marcus Iten in centrifuge testing, Heinz Buschor and Andreas Kieper in design and construction in the mechanical workshop for laboratory and field testing devices.
- Current employees from other institutes inside the Civil Engineering Department (BAUG) at ETH Zürich: Prof. Peter Molnar advised on rain data analysis, and Prof. Andreas Wieser and Daniel Willi from Institute for Environmental Engineering (IfU) and Institute of Geodesy and Photogrammetry (IGP), provided equipment for measure coordinates.
- Current and past employees of departments outside BAUG and within ETH: Department of Earth Sciences (D-ERDW) through the Institute of Geophysics, represented by Prof. Hansruedi Maurer and Kerstin Fankhauser, who performed extensive geophysical measurements and delivered data analysis included in this research.
- Finally external collaborators, included people outside ETH, who interacted in the project, providing relevant expert guidance, and collaborated with data measurements. In particular, the contribution of Dr. Brian McArdeall from WSL in hazard assessment, site geology context and provision of rainfall data is acknowledged; Dr Andrew Kos, for his remote sensing campaign; Prof. Andy Take for his expert advice and discussion about centrifuge modelling technology and development of equipment to apply groundwater flow to a slope; Prof. Amin Askarinejad, as a former doctoral student at IGT, for his mentoring and knowledge sharing in landslide simulation in the drum centrifuge at ETH, and his contribution to setting up the instrumentation and for further discussion on performance of the sensors.

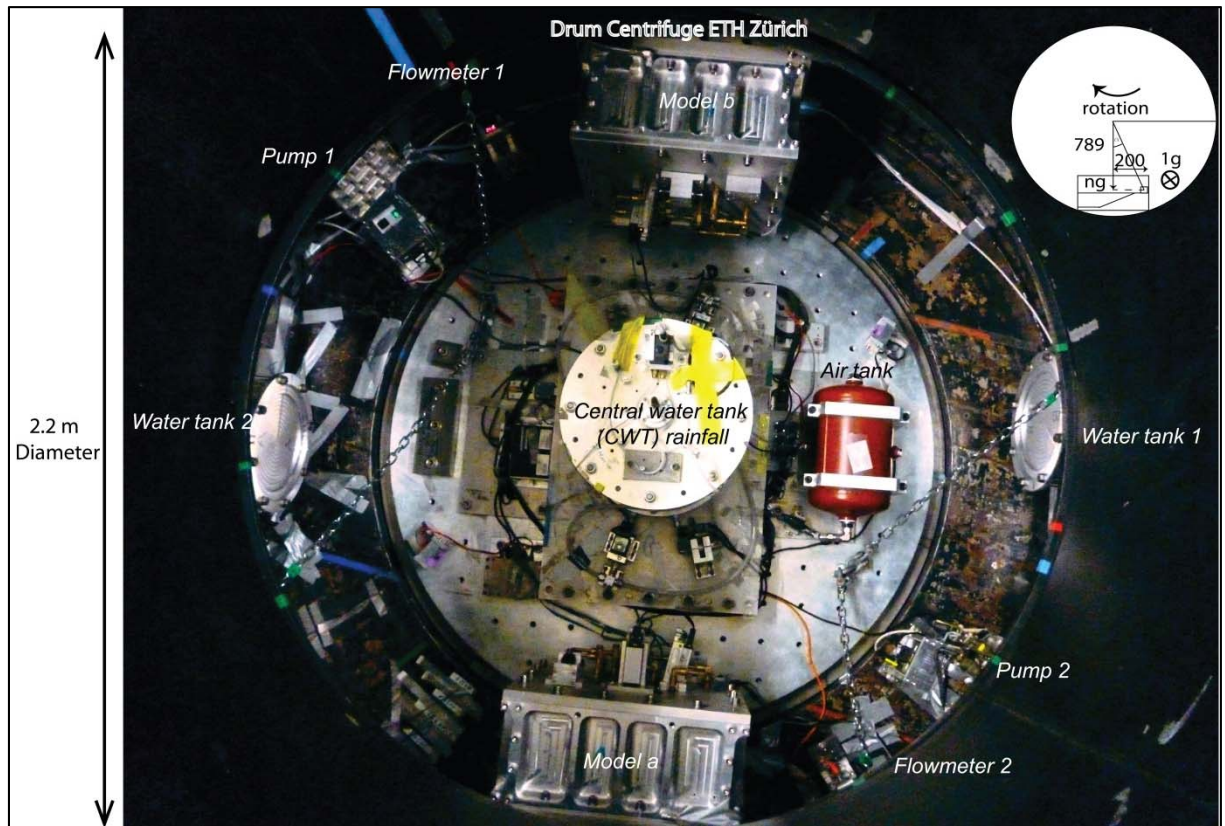


Figure 1.6. Drum centrifuge at Institute for Geotechnical engineering, ETH Zürich. The drum of 2.2 m diameter contains the set-up testing for slope stability under rainfall conditions with: two diametrically opposite models a, b; lateral and central water tanks for groundwater and rain supply respectively, an air tank, pumps and flowmeters to apply and measured the hydraulic conditions imposed in the testing. Units in the sketch of the model cross section, shown at the top right are in mm.

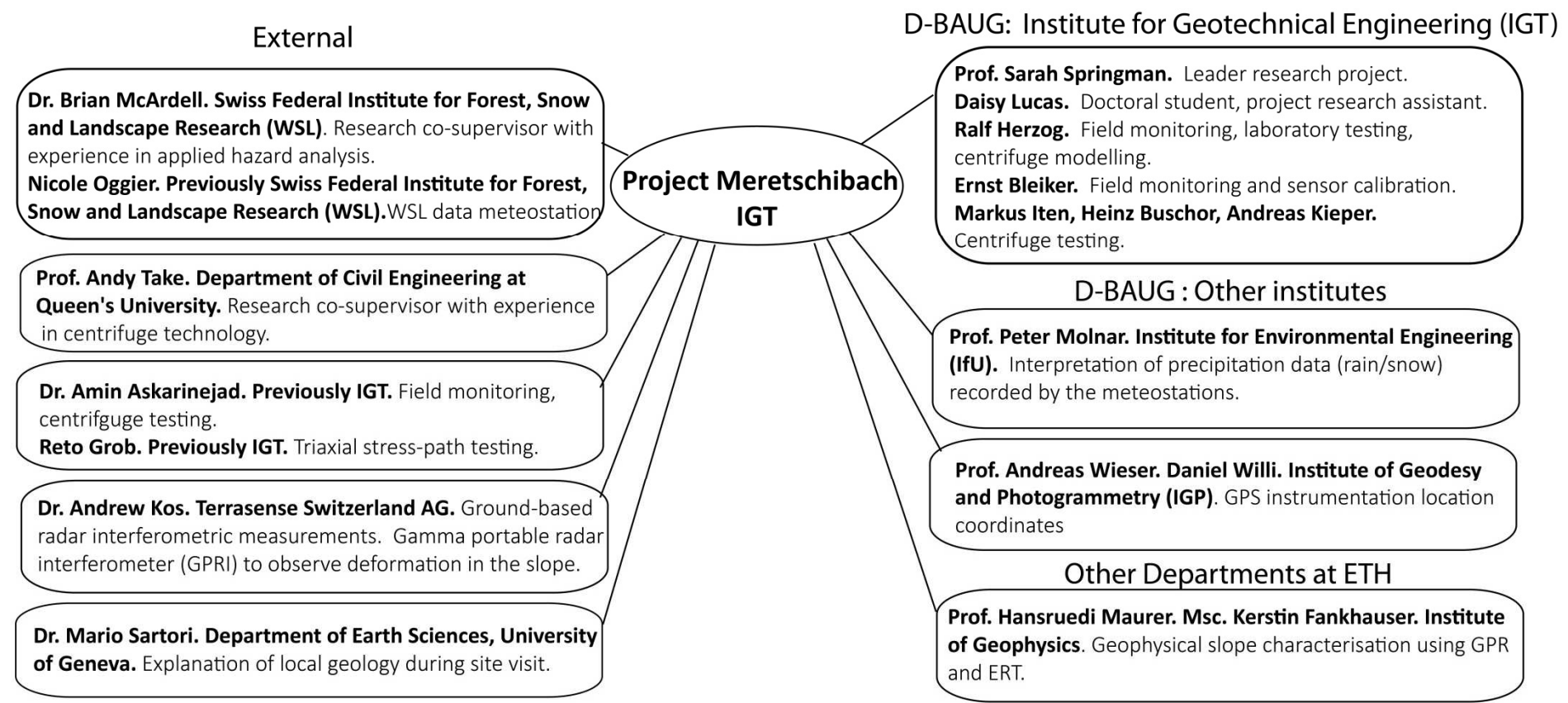


Figure 1.7. Participants and collaborations in the doctoral research project at Meretschibach.

1.7 Structure of the thesis

The research thesis is organised in eight chapters, each one of which corresponds mostly to the journal articles and conference papers written during the doctoral studies. More specifically:

Chapter 1. The first chapter is introductory, presents the research, objectives, methodology, a bibliographical review, parts involved in the research project and sections of the thesis.

Chapter 2. The second chapter presents an introductory and general overview of the research context and a description of some of the aspects in the field campaign and the monitoring. This includes one published conference paper with Daisy Lucas as a second author: “Study of the seasonal response of a scree slope and debris flow catchment in the Swiss Alps”, by Springman S.M., Lucas D., Oggier N.C., Kos A., Fankhauser K., and McArdell B.. The scope of the multidisciplinary project in the Swiss Alps, which involved the generation, mechanical production, storage and remobilisation of rock debris triggered by meteorological and hydrological processes in steep slopes, is introduced to identify the hazard. The site characteristics and field laboratory work, either in progress or planned, is described briefly.

Chapter 3. The third chapter provides an introduction to field instrumentation and data collection. It includes one conference paper that has been submitted and published. The paper was titled “Volumetric water content determination by TDR sensors and Decagons in gravelly soils”, by Lucas D., Askarinejad A., Herzog R., Bleiker E., and Springman S.M.. This paper article focuses on the preliminary geotechnical monitoring, which includes a description of the soil sensors, specifically those used for measuring temperature and capacitance EC-5/10HS, Time Domain Reflectometry (TDR) to measure VWC and tensiometers to obtain the suctions. Their calibration in the laboratory and installation in the gravelly soil in the field was also presented. The paper provided results and description of the measurements in instrumented trenches 1 and 2 (IT1, 2) for a period of 11 months.

Chapter 4. The fourth chapter addresses the analysis of measurements in the field, and comparison of these against measurements of geophysical properties that are converted to equivalent parameters for a period of up to 2 years. The validation is discussed, together with the extent of agreement between different sets of data. This chapter is a special issue article, which was published in the journal, engineering Geology. The

article's title is "Study of the seasonal response of a scree slope and debris flow catchment in the Swiss Alps" by Lucas D., Fankhauser K., and Springman S.M., which gives a thorough description of the geotechnical and geophysical monitoring campaigns, provides two years of recorded data of the geotechnical monitoring corresponding to VWC, temperature, rain, suction, and unit weight measurements and soil profile description. The paper include an analysis of the seasonal behaviour of the soil in terms of the measurements, as well as a comparison between sensor performance of those used to measured VWC, and the subsequent comparison to the VWC obtained from ERT measurements. The characterisation results were presented, including a map of slope angle in the scree slope, grain size distribution analysis, depth to the bedrock using electrical resistivity tomography (ERT) and a realistic ground model of the downslope section of the slope with strength parameters of the soil. The combination of techniques not only proved to be effective for the site characterisation of the field, they also complemented each other very well.

Chapter 5. The fifth chapter is dedicated to finishing the work related to soil monitoring and characterisation, and introduces the hazard assessment. This paper provided new findings and addressed the unsolved question posed in the paper presented in Chapter 4. The paper will be submitted to a special issue of the Journal Water imminently is entitled "Slope stability of a scree slope based on integrated characterisation and monitoring" by Lucas D., Fankhauser K., Maurer H., McArdell B., Grob R., Herzog R., Bleiker E., and Springman S.M.. The paper includes the final year of monitoring data, analyses variations found in soil behaviour in terms of VWC during the winter time, and delivers a new site-specific recalibration of VWC sensors, including the effect of variation of temperature over the range experienced in the field. A grain size distribution is performed for each instrumented trench at the end of the monitoring campaign to characterise the gravel, and a second campaign of in situ unit weight measurements is reported. Strength parameters of the soil are determined by a programme of triaxial stress-path testing for reconstituted samples of the gravel with specimen diameters either of 15 or 25 cm. Geophysical measurements using Ground-based Penetrating Radar led to development of a map contour of the bedrock depth below the entire scree slope. Finally, a preliminary numerical simulation was performed to simulate the influence of bedrock geometry and the consequences of all the findings on the hazard for the community downslope were discussed.

Chapter 6. This chapter examines the numerical and physical modelling of potential instabilities in the scree slope in terms of bedrock geometry, soil thickness under the action of groundwater flow (GW), and GW flow plus rain. The journal paper has been published by the International Journal of Physical Modelling in Geotechnics is titled “Modelling of Landslides in a scree slope induced by groundwater and rainfall” by Lucas D., Herzog R., Iten M., Buschor H., Kieper A., Askarinejad A. and Springman S.M.. This research addresses the influence of bedrock shape on the slope stability and used geological field observations to integrate the feature of a bedrock step into the analysis. Various bedrock step shapes and sizes are combined with a steep, coarse, granular slope. Additionally, different soil thicknesses (1-3 m) were tested. Triggering of shallow failures was investigated through two hydrological regimes: groundwater flow, and combined with additional intense rainfall in some cases. Results from physical and numerical modelling were compared to determine parameters that would lead to failure. It was found that for a given groundwater condition, slope stability decreases as the depth of soil decreases, and furthermore that the presence of a bedrock step would influence the location of where a surficial failure would be triggered.

Chapter 7. This chapter provides the conclusions and the outlook based on the research results, compared with the goals and objectives of the study. The validity of the hypotheses is reviewed, and new main findings are commented upon, providing the main conclusions for the relevant branches of the investigation. Unanswered questions from the research are commented on in the outlook, together with possible steps to address them. Observations are added about potential further research.

Chapter 8. Appendix. A conference paper is provided in this appendix, which is dedicated mostly to field monitoring and the combination with geophysics measurements. This paper was published in a conference series, and led to the invitation to write the journal paper presented in Chapter 4.

1.8 References

- Akca, D., Gruen, A., Askarinejad, A., & Springman, S.M. (2011). Photogrammetric monitoring of an artificially generated landslide. *Int Conf Geo-information Disaster Man (Gi4DM)*, Turkey CD-ROM.
- ARGE Geotest AG / K. Zumhofen (1990). Erosion area Bochtür, renovation, general preliminary project.
- Askarinejad, A. (2009). A method to locate the slip surface and measuring subsurface deformations in slopes. In *Proceedings of the Fourth International Young Geotechnical Engineers Conference: Alexandria 3rd-6th October 2009: 4th YGEC, Alexandria 2009*. pp. 171-174.
- Askarinejad, A., Casini, F., Bischof, P., Beck, A., & Springman, S. M. (2012). Rainfall induced instabilities: a field experiment on a silty sand slope in northern Switzerland. *Rivista italiana di geotecnica: RIG*, 2012(3), 50-71.
- Askarinejad, A. (2013). Failure Mechanisms in Unsaturated Silty Sand Slopes Triggered by Rainfall. Doctoral thesis, ETH Zurich, Zurich, Switzerland, <https://doi.org/10.3929/ethz-a-010002526>.
- Askarinejad, A., Beck, A., & Springman, S. M. (2014). Scaling law of static liquefaction mechanism in geocentrifuge and corresponding hydromechanical characterization of an unsaturated silty sand having a viscous pore fluid. *Canadian Geotechnical Journal*, 52(6), 708-720.
- Baum, R. L., & Godt, J. W. (2010). Early warning of rainfall-induced shallow landslides and debris flows in the USA. *Landslides*, 7(3), 259-272.
- Beniston, M., Diaz, H. F., & Bradley, R. S. (1997). Climatic change at high elevation sites: an overview. *Climatic Change*, 36(3-4), 233-251.
- Beniston, M., Stoffel, M., & Hill, M. (2011). Impacts of climatic change on water and natural hazards in the Alps: can current water governance cope with future challenges? Examples from the European “ACQWA” project. *Environmental Science & Policy*, 14(7), 734-743.
- Beniston, M. (2012). Impacts of climatic change on water and associated economic activities in the Swiss Alps. *Journal of Hydrology*, 412, 291-296.

- Beniston, M. (2003). Climatic change in mountain regions: a review of possible impacts. In *Climate variability and change in high elevation regions: Past, present & future* (pp. 5-31). Springer, Dordrecht.
- Beniston, M., & Stephenson, D. B. (2004). Extreme climatic events and their evolution under changing climatic conditions. *Global and planetary change*, 44(1-4), 1-9.
- Bischof, P. (2010). Modelling the interaction of the bedrock and slope in terms of drainage and exfiltration. IGT, ETH Zürich, Zürich, Switzerland.
- Borga, M., Dalla Fontana, G., Gregoretti, C., & Marchi, L. (2002). Assessment of shallow landsliding by using a physically based model of hillslope stability. *Hydrological Processes*, 16(14), 2833-2851.
- Cai, F., & Ugai, K. (2004). Numerical analysis of rainfall effects on slope stability. *International Journal of Geomechanics*, 4(2), 69-78.
- Caine, N. (1980). The rainfall intensity-duration control of shallow landslides and debris flows. *Geografiska annaler: series A, physical geography*, 62(1-2), 23-27.
- Cascini, L., Gullà, G., & Sorbino, G. (2006). Groundwater modelling of a weathered gneissic cover. *Canadian Geotechnical Journal*, 43(11), 1153-1166.
- Cascini, L., Cuomo, S., Pastor, M., & Sorbino, G. (2009). Modeling of rainfall-induced shallow landslides of the flow-type. *Journal of Geotechnical and Geoenvironmental Engineering*, 136(1), 85-98.
- Casini, F., Minder, P., & Springman, S. M. (2010). Shear strength of an unsaturated silty sand. In *Unsaturated Soils: Proceedings of the Fifth International Conference on Unsaturated Soils, Barcelona, Spain, 6-8 September 2010* (pp. 211-216). CRC Press/Balkema.
- Casini, F., Jommi, C., & Springman, S.M. (2010b) A laboratory investigation on an undisturbed silty sand from a slope prone to landsliding. *Granular Matter* 12(3) 303-316.
- Collins, B. D., & Znidarcic, D. (2004). Stability analyses of rainfall induced landslides. *Journal of Geotechnical and Geoenvironmental Engineering*, 130(4), 362-372.
- Craig, W. H. (2014). Pioneers of centrifuge modelling. In *ICPMG2014-Physical Modelling in Geotechnics: Proceedings of the 8th International Conference on Physical Modelling in*

Geotechnics 2014 (ICPMG2014), Perth, Australia, 14-17 January 2014 (p. 421). CRC Press.

Cruden, D. M. (1991). A simple definition of a landslide. *Bulletin of the International Association of Engineering Geology*, 43(1), 27-29.

Cruden, D.M. & Varnes D.J. (1996). Landslide types and processes. In: Turner AK, Schuster RL (eds) *Landslides investigation and mitigation*. Transportation research board, US National Research Council. Special Report 247, Washington, DC, Chapter 3, pp. 36–75.

Chahine, M. T. (1992). The hydrological cycle and its influence on climate. *Nature*, 359(6394), 373.

Chen, H., Lee, C. F., & Law, K. T. (2004). Causative mechanisms of rainfall-induced fill slope failures. *Journal of Geotechnical and Geoenvironmental Engineering*, 130(6), 593-602.

Cheney, J. A., Frigaszy, R. J., & Schofield, A. N. (1984). Drum centrifuge for geotechnical research. *Geotechnical Testing Journal*, 7(4), 188-194.

Chichibu, A., Jo, K., Nakamura, M., Goto, T. & Kamata, M. (1989). Acoustic emission characteristics of unstable slopes. *Journal of Acoustic Emission*, 8, 107–111.

Chipp, P. N., Henkel, D. J., Clare, D. G., & Pope, R. G. (1982). Field measurement of suction in colluvium covered slopes in Hong Kong. In *Proceedings of 7th Southeast Asian Geotechnical Conference* (Vol. 1, pp. 49-62).

Cho, S. E., & Lee, S. R. (2002). Evaluation of surficial stability for homogeneous slopes considering rainfall characteristics. *Journal of Geotechnical and Geoenvironmental Engineering*, 128(9), 756-763.

Chu, J., Leroueil, S., & Leong, W. K. (2003). Unstable behaviour of sand and its implication for slope instability. *Canadian Geotechnical Journal*, 40(5), 873-885.

Craig, W. H., Bujang, B. H., & Merrifield, C. M. (1991). Simulation of climatic conditions in centrifuge model tests. *Geotechnical Testing Journal*, 14(4), 406-412.

Dai, F. C., & Lee, C. F. (2001). Frequency–volume relation and prediction of rainfall-induced landslides. *Engineering Geology*, 59(3-4), 253-266.

- De Freitas, M. H. & Watters, R. J. (1973). Some field examples of toppling failure. *Géotechnique*, 23(4), 495-513.
- Dell'Avanzi, E., & Zornberg, J.G. (2002). "Scale Factors for Centrifuge Modeling of Unsaturated Flow." Proceedings of the Third International Conference on Unsaturated Soils, Recife, Brazil, March 10-13, Vol. 1, pp. 425-430.
- De Vita, P., Reichenbach, P., Bathurst, J. C., Borga, M., Crosta, G., Crozier, M., Glade, T., Guzzetti, F., Hansen, A., & Wasowski J. (1998). Rainfall-triggered landslides: a reference list. *Environmental Geology*, 35(2), 219-233.
- Dilley, M., Chen, R.S., Deichmann, U., Lerner-Lam, A.L., Arnold, M., Agwe, J., Buys, P., Kjekstad, O., Lyon, B. & Yetman, G. (2005). Natural disaster hotspots: a global risk analysis. The World Bank Hazard Management Unit, Washington.
- Dixon, N. & Spriggs, M. (2007). Quantification of slope displacement rates using acoustic emission monitoring. *Canadian Geotechnical Journal*, 44, 966–976.
- Elia, G., Cotecchia, F., Pedone, G., Vaunat, J., Vardon, P. J., Pereira, C., Springman, S., Rouainia, M., Van Esch, J., Koda, E., Josifovski, J., Nocilla, A., Askarinejad, A., Stirling, R., Helm, P., Lollino, P., & Osinski, P., (2017). Numerical modelling of slope–vegetation–atmosphere interaction: an overview. *Quarterly Journal of Engineering Geology and Hydrogeology*, 50(3), 249-270.
- Evans, S. G. & Hungr, O. (1993). The assessment of rockfall hazard at the base of talus slopes. *Can. Geotech. J.*, 30(4), 620-636.
- Fankhauser, K. (2014). Geophysical slope characterisation using GPR and ERT in an active debris flow catchment. (Master Thesis). ETH Zürich, Switzerland.
- Frank, F., McArdell, B. W., Oggier, N., Baer, P., Christen, M., & Vieli, A. (2017). Debris-flow modeling at Meretschibach and Bondasca catchments, Switzerland: sensitivity testing of field-data-based entrainment model. *Natural Hazards and Earth System Sciences*, 17(5), 801-815.
- Friedel, S., Thielen, A., & Springman, S. M. (2006). Investigation of a slope endangered by rainfall-induced landslides using 3D resistivity tomography and geotechnical testing. *Journal of Applied Geophysics*, 60(2) 100-114.

- Froude, M. J., & Petley, D. (2018). Global fatal landslide occurrence from 2004 to 2016. *Natural Hazards and Earth System Sciences*, 18, 2161-2181.
- Fujii, Y. (1969). Frequency distribution of landslides caused by heavy rainfall. *Journal Seismological Society Japan*, 22, 244-247.
- Gabus, J. H., Weidmann, M., Burri, M., & Sartori M. (2008a). Feuille 1287 Sierre, Atlas Géologique de la Suisse 1:25'000, Carte 111, swisstopo, Wabern.
- Gabus, J. H., Weidmann, M., Burri, M., & Sartori M. (2008b). Feuille 1287 Sierre, Atlas Géologique de la Suisse 1:25'000, Note explicative, swisstopo, Wabern.
- Garnier, J., Gaudin, C., Springman, S. M., Culligan, P. J., Goodings, D., König, D., Kutter, B., Randolph, M.F., & Thorel, L. (2007). Catalogue of scaling laws and similitude questions in geotechnical centrifuge modelling. *International Journal of Physical Modelling in Geotechnics*, 7(3), 1-23.
- Geotest AG. (1989). Debris flow, rockfall and avalanche danger map for the settlement area of the municipality Agarn.
- Geotest AG., Zumhofen & Glenz AG (1992). Meretschibach, flood protection, structural measures, geological-geotechnical assessment, preliminary project with cost estimate.
- Geotest AG. T. & C. AG (1998). Detailed clarifications on the debris flow and flood hazard due to the Meretschibach, concept for action planning, hazard map.
- Geo7 AG. (2000). Evaluation of debris dam Meretschibach, summary report.
- Geo7 AG. (2001). Evaluation of protective structures in the Meretschibach, spill retention basin vs. protective dams, short report.
- Gerber, E.; Scheidegger, A. E. (1974). On the dynamics of scree slopes. *Rock Mech. Rock Eng.*, 6(1), 25-38.
- Gilgen, M. (2007) Hydrological Simulations of a Hillslope Prone to Shallow Landslides. *IGT Diploma thesis*, ETH Zürich.
- Grob, R. (2015), Measurement of soil properties for gravels in a scree slope using large triaxial testing. (Master Thesis). ETH Zürich, Switzerland.

- Guzzetti, F., Peruccacci, S., Rossi, M., & Stark, C. P. (2007). Rainfall thresholds for the initiation of landslides in central and southern Europe. *Meteorology and Atmospheric Physics*, 98(3-4), 239-267.
- Guzzetti, F., Peruccacci, S., Rossi, M., & Stark, C. P. (2008). The rainfall intensity–duration control of shallow landslides and debris flows: an update. *Landslides*, 5(1), 3-17.
- Haque, U., Blum, P., Da Silva, P. F., Andersen, P., Pilz, J., Chalov, S. R., Malet, J.P., Auflic, M.J., Andres, N., Poyiadji, E., & Lamas, P.C. (2016). Fatal landslides in Europe. *Landslides*, 13(6), 1545-1554.
- Hungr, O., Leroueil, S., & Picarelli, L. (2014). The Varnes classification of landslide types, an update. *Landslides*, 11(2), 167-194.
- Imre, B., Laue, J., & Springman, S. M. (2010a). Fractal fragmentation of rocks within sturzstroms: insight derived from physical experiments within the ETH Geotechnical Drum Centrifuge. *Granular Matter*, 12(3), 267-285. DOI: 10.1007/s10035-009-0163-1
- Imre, B., Laue, J., & Springman, S. M. (2010b). A centrifuge experiment to derive insight on rock fragmentation within sturzstroms. 7th International Conference on Physical Modelling in Geotechnics ICPMG 2010, Zurich, Switzerland, 28.6.-1.7.2010, (2): 1253-1258. Taylor & Francis Group, London.
- Intrieri, E., Gigli, G., Mugnai, F., Fanti, R., & Casagli, N. (2012). Design and implementation of a landslide early warning system. *Engineering Geology*, 147, 124-136.
- Kane, W. F., & Beck, T. J. (2000). Instrumentation practice for slope monitoring. Engineering Geology Practice in Northern California. Sacramento and San Francisco Sections, Association of Engineering Geologists, Zanesville, OH, USA.
- Keefer, D. K., Wilson, R. C., Mark, R. K., Brabb, E. E., Brown, W. M., Ellen, S. D., Harp, E.L., Wieczorek, G.F., Alger, C.S. & Zatzkin, R.S., (1987). Real-time landslide warning during heavy rainfall. *Science*, 238(4829), 921-925.
- Kimura, T., Takemura, J., Suemasa, N. & Hiro-oka, A. (1991). Failure of fills due to rain fall. In *Centrifuge* (Vol. 91, pp. 509-516). Balkema.
- Krahn, J. (2004a). Seepage modelling with SEEP/W, an engineering methodology, Manual of Seep/W.
- Krahn, J. (2004b). Stability modelling with SLOPE/W: GEO-SLOPE/W International ltd.

- Larsen, M. C., & Simon, A. (1993). A rainfall intensity-duration threshold for landslides in a humid-tropical environment, Puerto Rico. *Geografiska Annaler: Series A, Physical Geography*, 75(1-2), 13-23.
- Lateltin, O., Haemmig, C., Raetzo, H., & Bonnard, C. (2005). Landslide risk management in Switzerland. *Landslides*, 2(4), 313-320.
- Leach, W. (1930). A preliminary account of the vegetation of some non-calcareous British screes (Gerolle). *Journal of Ecology*, 18(2), 321-332.
- Leach, B., & Herbert, R. (1982). The genesis of a numerical model for the study of the hydrogeology of a steep hillside in Hong Kong. *Quarterly Journal of Engineering Geology and Hydrogeology*, 15(3), 243-259.
- Lee, Y. S., & Bolton, M. D. (2006). Centrifugal modelling of the landslides triggering mechanism in layered fill slopes. In *Proceedings of the Sixth International Conference on Physical Modelling in Geotechnics, Hong Kong* (pp. 355-360).
- Lee, E. M., & Jones, D. K. (2004). Landslide risk assessment. Thomas Telford. London, UK.
- Lehmann, P., & Or, D. (2012). Hydromechanical triggering of landslides: From progressive local failures to mass release. *Water Resources Research*, 48(3).
- Leonarduzzi, E., Molnar, P., & McArdell, B. W. (2017). Predictive performance of rainfall thresholds for shallow landslides in Switzerland from gridded daily data. *Water Resources Research*, 53(8), 6612-6625.
- Ling, H., Ling, H., & Li, L. (2009a). Centrifuge Modeling of Slope Failure Induced by Rainfall. In *EGU General Assembly Conference Abstracts* (Vol. 11, p. 6730).
- Ling, H. I., Wu, M. H., Leshchinsky, D., & Leshchinsky, B. (2009b). Centrifuge modeling of slope instability. *Journal of Geotechnical and Geoenvironmental Engineering*, 135(6), 758-767.
- Liniger HP, Weingartner R. (1998). Mountains and freshwater supply. UNASILVA No. 195, Vol. 49, 1998/4, FAO, Rome.
- Lourenço, S. D., Sassa, K., & Fukuoka, H. (2006). Failure process and hydrologic response of a two layer physical model: implications for rainfall-induced landslides. *Geomorphology*, 73(1-2), 115-130.

- Low, T. H., Faisal, H. A., & Saravanan, M. (2000). Suction and infiltration measurement on cut slope in highly heterogeneous residual soil. In *Unsaturated soils for Asia. Proceedings of the Asian Conference on Unsaturated Soils, UNSAT-ASIA 2000, Singapore, 18-19 May, 2000* (pp. 807-811). AA Balkema.
- Lucas, D. R., Fankhauser, K., & Springman, S. M. (2017). Application of geotechnical and geophysical field measurements in an active alpine environment. *Engineering Geology*, 219, 32-51.
- Lumb, P. (1975). Slope failures in Hong Kong. *Quarterly Journal of Engineering Geology*, 8(1), 31-65.
- Mayne, P. W., Coop, M. R., Springman, S. M., Huang, A. B., & Zornberg, J. G. (2009, December). Geomaterial behavior and testing. In *17th International Conference on Soil Mechanics and Geotechnical Engineering, ICSMGE 2009* (pp. 2777-2872).
- Michlmayr, G., Chalari, A., Clarke, A., & Or, D. (2017). Fiber-optic high-resolution acoustic emission (AE) monitoring of slope failure. *Landslides*, 14(3), 1139-1146.
- Michlmayr, G., Cohen, D., & Or, D. (2012). Sources and characteristics of acoustic emissions from mechanically stressed geologic granular media—A review. *Earth-Science Reviews*, 112(3-4), 97-114.
- Mikoš, M., Četina, M., & Brilly, M. (2004). Hydrologic conditions responsible for triggering the Stože landslide, Slovenia. *Engineering Geology*, 73(3-4), 193-213.
- Milne, F. D., Brown, M. J., Knappett, J. A., & Davies, M. C. R. (2012). Centrifuge modelling of hillslope debris flow initiation. *Catena*, 92, 162-171.
- Mueller, R., & Loew, S. (2009). Predisposition and cause of the catastrophic landslides of August 2005 in Brienz (Switzerland). *Swiss Journal of Geosciences*, 102(2), 331-344.
- Ng, C. W., Wang, B., & Tung, Y. K. (2001). Three-dimensional numerical investigations of groundwater responses in an unsaturated slope subjected to various rainfall patterns. *Canadian Geotechnical Journal*, 38(5), 1049-1062.
- Oggier, N.C. (2011). Simulierung von Murgängen mit RAMMS am Beispiel des Meretschibachs. (Master Thesis); ETH Zürich und Forschungsanstalt für Wald Schnee und Landschaft (WSL), Switzerland.

- Ochiai, H., Okada, Y., Furuya, G., Okura, Y., Matsui, T., Sammori, T., Terajima, T. and Sassa, K. (2004). A fluidized landslide on a natural slope by artificial rainfall. *Landslides*, 1(3), 211-219.
- Ochiai, H., Sammori, T., & Okada, Y. (2007). Landslide experiments on artificial and natural slopes. *Progress in Landslide Science*. Springer, Berlin, Heidelberg, 209-226.
- Oki, T., & Kanae, S. (2006). Global hydrological cycles and world water resources. *science*, 313(5790), 1068-1072.
- Olivares, L., Damiano, E., Greco, R., Zeni, L., Picarelli, L., Minardo, A., Guida, A. & Bernini, R. (2009). An instrumented flume to investigate the mechanics of rainfall-induced landslides in unsaturated granular soils. *Geotechnical Testing Journal*, 32(2), 108-118.
- Pedrozzi, G. (2004). Triggering of landslides in Canton Ticino (Switzerland) and prediction by the rainfall intensity and duration method. *Bulletin of Engineering Geology and the Environment*, 63(4), 281-291.
- Petkovšek, A., Kočevár, M., Maček, M., Majes, B., & Mikoš, M. (2011). The Stogovce landslide in SW Slovenia triggered during the September 2010 extreme rainfall event. *Landslides*, 8(4), 499-506.
- Pierson, T. C. (1982). Classification and hydrological characteristics of scree slope deposits in the northern Craigieburn Range, New Zealand. *Journal of Hydrology New Zealand*, 21(1), 34-60.
- Raetzo, H., Lateltin, O., Bollinger, D., & Tripet, J. (2002). Hazard assessment in Switzerland—Codes of Practice for mass movements. *Bulletin of Engineering Geology and the Environment*, 61(3), 263-268.
- Rickli, C., & Graf, F. (2009). Effects of forests on shallow landslides—case studies in Switzerland. *Forest Snow and Landscape Research*, 82(1), 33-44.
- Rouse, C., Styles, P. & Wilson, S. (1991). Microseismic emissions from flowslide-type movements in south wales. *Engineering Geology*, 31, 91–110.
- Sassa, K., Tsuchiya, S., Ugai, K., Wakai, A., & Uchimura, T. (2009). Landslides: a review of achievements in the first 5 years (2004–2009). *Landslides*, 6(4), 275-286.

- Scheidegger, C. (2007). Analyse von Hangrutschungen in ungesättigten Böden. *IGT Diploma thesis*, ETH Zürich.
- Schmid, F., Fraefel, M., Hegg, C. (2004). Unwetterschäden in der Schweiz 1972–2002 (Financial Damage caused by Flooding and Landslides in Switzerland 1972–2002): Verteilung, Ursachen, Entwicklung. *Wasser, Energie und Luft*, Band 1/2, pp 21–28.
- Schulz, W. H., McKenna, J. P., Kibler, J. D., & Biavati, G. (2009). Relations between hydrology and velocity of a continuously moving landslide—evidence of pore-pressure feedback regulating landslide motion? *Landslides*, 6(3), 181-190.
- Seno, S., & Thüring, M. (2006). Large landslides in Ticino, Southern Switzerland: geometry and kinematics. *Engineering Geology*, 83(1-3), 109-119.
- Sitarenios, P., Casini, F., Askarinejad, A. & Springman, S.M. (2019). Hydro-mechanical analysis of a surficial landslide triggered by artificial rainfall: the Ruedlingen field experiment. *Géotechnique*. In Press.
- Springman, S. M., Jommi, C., & Teyssere, P. (2003). Instabilities on moraine slopes induced by loss of suction: a case history. *Géotechnique*, 53(1), 3-10.
- Springman, S.M. (2008). Einfache Hangstabilitätsanalyse mit Berücksichtigung ungesättigter Verhältnisse - Analyse TRAMM, *FAN Fachleute Naturgefahren Schweiz Agenda*, December 2/2008: 7-11.
- Springman, S., Kienzler, P., Casini, F., & Askarinejad, A. (2009). Landslide triggering experiment in a steep forested slope in Switzerland. In *17th International Conference on Soil Mechanics and Geotechnical Engineering, ICSMGE 2009*, Alexandria, Egypt, (Vol. 2, pp. 1698-1701). IOS Press.
- Springman, S. M., Laue, J., Boyle, R., White, J., & Zweidler, A. (2001). The ETH Zurich geotechnical drum centrifuge. *International Journal of Physical Modelling in Geotechnics*, 1(1), 59-70.
- Springman, S. M. (2011). Simple slope stability analyses while considering unsaturated behaviour/response. *Zbornik referatov*, 5-35.
- Springman, S., Askarinejad, A., Casini, F., Friedel, S., Kienzler, P., Teyssere, P., & Thielen, A. (2012). Lessons learnt from field tests in some potentially unstable slopes in Switzerland. *Acta Geotechnica Slovenica*, 1, 5-29.

- Springman, S. M., Lucas, D. R., Oggier, N., Kos, A., Fankhauser, K. & McArdell B. (2015). Study of the seasonal response of a scree slope and a debris flow catchment in the Swiss Alps. In *the XVI European Conference on Soil Mechanics and Geotechnical Engineering (XVI ECSMGE 2015)* (pp. 1897-1902). ICE Publishing.
- Statham, I. (1973). Scree slope development under conditions of surface particle movement. *Transactions of the Institute of British Geographers*, 41-53.
- Sweeney, D. J. (1982). Some in situ soil suction measurements in Hong Kong's residual soil slopes. In *Proceedings of the 7th Southeast Asian Regional Conference, Hong Kong* (Vol. 1, pp. 91-106).
- Szymczak, S., Bollschweiler, M., Stoffel, M., & Dikau, R. (2010). Debris-flow activity and snow avalanches in a steep watershed of the Valais Alps (Switzerland): dendrogeomorphic event reconstruction and identification of triggers. *Geomorphology*, 116(1-2), 107-114.
- T. & C. AG. (2002). Protection Concept Meretschibach, technical report.
- T. & C. AG. (2006). Meretschibach below Geschiebefang, summary report.
- T. & C. AG. (2010). Meretschibach, Technical Report on the executed building, and update of the hazard maps.
- Take, W. A., Bolton, M. D., Wong, P. C. P., & Yeung, F. J. (2004). Evaluation of landslide triggering mechanisms in model fill slopes. *Landslides*, 1(3), 173-184.
- Take, W. A. (2014). Physical modelling of instability and flow in loose granular slopes. In *ICPMG2014–Physical Modelling in Geotechnics: Proceedings of the 8th International Conference on Physical Modelling in Geotechnics* (pp. 113-124). CRC Press, Boca Raton, FL, USA.
- Take, W. A., & Beddoe, R. A. (2014). Base liquefaction: a mechanism for shear-induced failure of loose granular slopes. *Canadian Geotechnical Journal*, 51(5), 496-507.
- Take, W. A., Beddoe, R. A., Davoodi-Bilesavar, R., & Phillips, R. (2015). Effect of antecedent groundwater conditions on the triggering of static liquefaction landslides. *Landslides*, 12(3), 469-479.

- Tamate, S., Suemasa, N., & Katada, T. (2010). Simulating shallow failure in slopes due to heavy precipitation. In *7th International Conference of Physical Modelling in Geotechnics*, (pp. 1143-1149).
- Terrasense Switzerland A.G. (2016). Radar interferometric measurements Meretschibach debris flow catchment, Canton Wallis.
- Teufen, B. (1973). Vorprojekt zur Verbauung und Aufforstung des Erosionsgebietes Bochtür, Gemeinde Leuk und Agarn. Brig: Fachstelle Naturgefahren Wallis.
- Theler, D. (2010). Cartographie géomorphologique de la dynamique sédimentaire des bassins versants de montagne. Project Doctoral Thesis, University of Lausanne, Lausanne, Switzerland.
- Thielen, A. (2007). Einfluss der Bodensättigung auf die Stabilität von Hängen *ETH-Diss* Nr 17303, ETH Zürich.
- Timpong, S., Itoh, K., & Toyosawa, Y. (2007). Geotechnical centrifuge modelling of slope failure induced by ground water table change. *Landslides and Climate Change. London: Taylor and Francis Group*, 107-112.
- Varnes, D.J. (1978). Slope movement types and processes. In: Schuster RL, Krizek RJ (eds) *Landslides, analysis and control*, special report 176: Transportation Research Board, National Academy of Sciences, Washington, DC., pp. 11–33.
- Vaunat, J., & Olivella, S. (2002). Code-BRIGHT/GID: a 3D program for thermo-hydro-mechanical analysis in geological media. In *1st Conference on Advances and Applications of GiD. Publicació CIMNE N°-210. CIMNE* (Vol. 2002, pp. 91-94).
- Weingartner, R., & Pearson, C. (2001). A comparison of the hydrology of the Swiss Alps and the Southern Alps of New Zealand. *Mountain Research and Development*, 21(4), 370-382.
- Yagi, N., Yatabe, R., Yokota, K., & Bhandary, N. P. (2000). Suction measurement for the prediction of slope failure due to rainfall. In *Unsaturated soils for Asia. Proceedings of the Asian Conference on Unsaturated Soils, UNSAT-ASIA 2000, Singapore, 18-19 May, 2000* (pp. 847-851). AA Balkema.

Zeni, L., Picarelli, L., Avolio, B., Coscetta, A., Papa, R., Zeni, G., Di Maio, C., Vassallo, R. & Minardo, A. (2015). Brillouin optical time-domain analysis for geotechnical monitoring. *Journal of Rock Mechanics and Geotechnical Engineering*, 7(4), 458-462.

Zumhofen & Glenz AG. (1993). Correction of the Meretschibach.

2 Study of the seasonal response of a scree slope and debris flow catchment in the Swiss Alps

Sarah M. Springman

ETH Zürich, Institute for Geotechnical Engineering
Stefano-Franscini-Platz 5, 8093 Zürich, Switzerland
E-Mail address: sarah.springman@igt.baug.ethz.ch

Daisy Lucas

ETH Zürich, Institute for Geotechnical Engineering
Stefano-Franscini-Platz 5, 8093 Zürich, Switzerland
E-Mail address: daisy.lucas@igt.baug.ethz.ch

Nicole C. Oggier¹

ETH Zürich, Institute for Geotechnical Engineering
Stefano-Franscini-Platz 5, 8093 Zürich, Switzerland
E-Mail address: ing@wasserschneelawinen.ch

Andrew Kos²

ETH Zürich, Institute for Geotechnical Engineering
Stefano-Franscini-Platz 5, 8093 Zürich, Switzerland
E-Mail address: andrew.kos@terrasense.ch

Kerstin Fankhauser³

ETH Zürich, Institute for Geotechnical Engineering and Institute of Geophysics
Stefano-Franscini-Platz 5, 8093 Zürich, Switzerland
E-Mail address: kerstin.fankhauser@erdw.ethz.ch

Brian McArdell

Eidgenössische Forschungsanstalt für Wald, Schnee und Landschaft WSL

¹Current employer: wasser/schnee/lawinen-Ingenieurbüro A. Burkard AG
Sebastiansplatz 1, 3900 Brig-Glis, Switzerland

² Current employer: Terrasense Switzerland Ltd.
Churerstrasse 99, 9471 Buchs, Switzerland

³ Current employer: focusTerra ETH-Bibliothek
Sonneggstrasse 5, 8092 Zürich, Switzerland

Zürcherstrasse 111, 8903 Birmensdorf, Switzerland

E-Mail address: brian.mcardell@wsl.ch

Submitted to: XVI European Conference on Soil Mechanics and Geotechnical Engineering (XVI ECSMGE 2015), Edinburgh, UK, 13.-17.9.2015, 1897-1902.

Status: Published

Springman, S. M., Lukas, D. R., Oggier, N., Kos, A., & Fankhauser, K. (2015). Study of the seasonal response of a scree slope and a debris flow catchment in the Swiss Alps. In the XVI European Conference on Soil Mechanics and Geotechnical Engineering (XVI ECSMGE 2015) (pp. 1897-1902). ICE Publishing.

Abstract

The paper introduces the scope of a multidisciplinary project in the Swiss Alps, which will investigate the generation, mechanical production, storage and remobilization of rock debris triggered by meteorological and hydrological processes in steep slopes to identify the extent of the hazard such as volume, mobility and run out of debris, so that effective mitigation measures can be implemented.

The study is in the Bochtür area in the Meretschibach catchment above Agarn village, for which frequent slope instability events have been determined using repeated remote sensing campaigns. These instabilities manifest themselves more frequently, in the form of smaller events on the open partly vegetated scree slope, and less frequently, but with larger volume of sediment and greater run out, as debris flows in the catchment. The field and laboratory work, either in progress or planned, will be described briefly, with hints towards subsequent analyses and process understanding obtained from the field and from physical and numerical modelling.

List of Notation

Decagon	→	Capacitance sensor EC-5, Decagon Devices
ERT	→	Electrical resistivity tomography
GPR	→	Ground-based penetrating radar
GPRI	→	Ground-based radar interferometry
InSAR	→	Interferometric Synthetic Aperture Radar
IT	→	Instrumented Trench
LiDAR	→	Surveying method, light detection and ranging
MS1,2,3	→	Meteostation
TDR	→	Time domain reflectometry sensor, Campbell
ϕ'	→	Critical state friction angle

2.1 Introduction

The temporary storage and remobilization of sediment in a stream bed, and of rock debris on surrounding slopes at inclinations steeper than the critical angle of friction ϕ' , lead to ongoing slope instability and debris flow hazard in an active Alpine environment. This presents significant challenges to those responsible for protecting inhabitants and infrastructure located in the valley below, who are required to be able to predict the impact of extreme events.

The study area is the Meretschibach catchment (Canton Valais, Switzerland: Figures 2.1, 2.2 and 2.3), above Agarn village. This site is ideal because unpublished satellite InSAR displacement maps (Dr. Hugo Raetzo, 2012, FOEN, pers. comm.) show movements $>50\text{cm/year}$ in the catchment, which also experiences frequent debris flows (Teyssie & Candolfi 2006; Szymczak et al. 2010; Theler 2010; Oggier 2011), including a series during this summer.

Similarities exist between the Meretschibach and the neighbouring valley to the west, Illgraben, which has been a focus of debris flow research for many years (Hürlimann et al. 2003; McArdell et al. 2007; Schlunegger et al. 2009; Berger et al. 2010; 2011).

Although debris and sediment sources are located in different parts of a catchment, they can be subject to similar external climatic factors (rainfall, snowmelt), and the triggers for erosion or surficial failure may be different.

Spatio-temporal characteristics of the scree slope (Figure 2.2) and channel (Figure 2.3) response to cycles of infiltration, saturation & drainage are being investigated more frequently in an integrated way at complementary scales through remote sensing (catchment scale), in-situ characterisation (slope scale) and monitoring combined with centrifuge (laboratory scale) and numerical modelling. Rockfall (Figure 2.4) remains a prevalent hazard necessitating great care about safety.

2.2 Site characterisation

Site characterisation is an essential preliminary activity in order to be able to make decisions about where to install any monitoring devices. Further refinement of a ground model extends throughout the duration of the project. The goal is to obtain a clear delineation of the ground conditions at the site location, with quantification of relevant geotechnical parameters for subsequent geotechnical analysis.

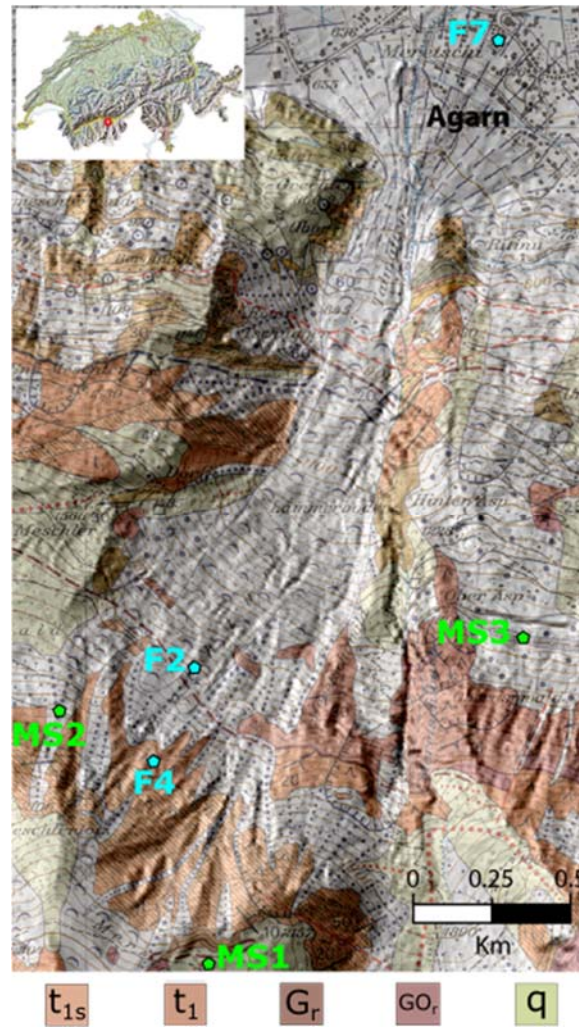


Figure 2.1. Geological map of the Meretschibach-Bochtür location with the positions of the weather stations (MS) and the photographs in other figures (Figures 2.2, 2.4 and 2.7), with North at the top. Legend from left to right: white quartzite (t_{1s}), green sericitized quartzite (t_1), albitic gneiss metharhyolite (G_r), Augen gneiss (GO_r), porphyritic granite (GO_r), surficial deposits (q) (from Gabus et al. 2008a).

2.2.1 Geology

Triassic aged sericitized quartzite and white quartzites of the Bruneggjoch formation (Gabus et al. 2008) form the main lithology in the release areas of the catchment. The quartzites appear disturbed, possibly as a result of tectonic processes and are highly susceptible to weathering, which occurs quickly after exposure of a fresh surface.

Surface morphological features in the steep upper slope of the catchment indicate previous deep-seated gravitational slope activity. Several terrace structures characterise the morphology, where bedrock landslides (and rockfalls) have occurred. The bedrock outcrops, slope and channel deposits can be observed from viewpoints appropriate for ground-based remote sensing.



Figure 2.2. Open scree slope, looking SE, location on Figure 2.1.

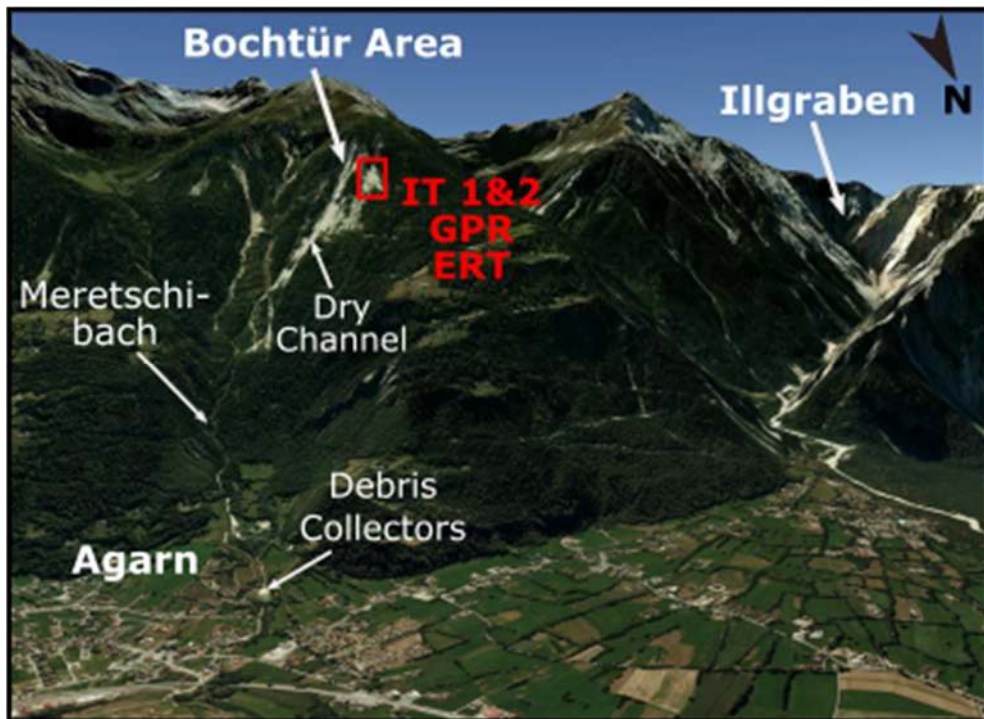


Figure 2.3. Debris flow catchment, looking South. The red rectangle encloses the scree slope on which the instrumented trenches (IT 1&2) are situated and the geophysical methods were conducted most intensively. For the exact location of the trenches and the ERT profile, see the close-up of the rectangular area in Figure 2.5.

2.2.2 Geotechnical characterisation

The scree slope may be characterised by sections that are on a ‘run-out cone’ from a weathering rock wall at the top of the slope, or where stunted vegetation has been able to gain some hold in a fine-grained clayey silty soil retained in the larger voids between the sandy, blocky, gravel (see Figure 2.2).

Trenches excavated (Figures 2.3 and 2.5) for installing devices to monitor infiltration and drainage processes, as they develop due to the environmental perturbations, have been used to extract samples for analysis and testing in the laboratory (Lucas et al. 2015). The next stage of characterisation includes an extensive programme of testing in the laboratory to determine the requisite geotechnical parameters in both saturated and unsaturated states.



Figure 2.4. Rockfall hazard, location on Figure 2.1.

2.2.3 Geophysics

Geotechnical experiments have been complemented by extensive geophysical measurements (Fankhauser 2014).

The depth of the bedrock was explored by ground-penetrating radar (GPR). Preliminary analyses of the GPR data indicate that the bedrock lies between 0.5-5 m below the surface of the scree slope. Temporal variations of the soil moisture content were

monitored with repeated electrical resistivity tomography (ERT) measurements (Figures 2.3 and 2.5). Results of two surveys, on the location delineated in Figure 2.5 are shown in Figure 2.6. The soil structures manifest themselves by decreased electrical resistivities compared with the underlying bedrock. The depth of the interface between soil and bedrock is broadly consistent with the GPR results. A comparison between geoelectrical tomograms obtained during a dry period in June, and after a period of heavy rainfall in July, reveals a significant reduction in the resistivities in the shallow subsurface. This can be attributed to the saturation of the soil.

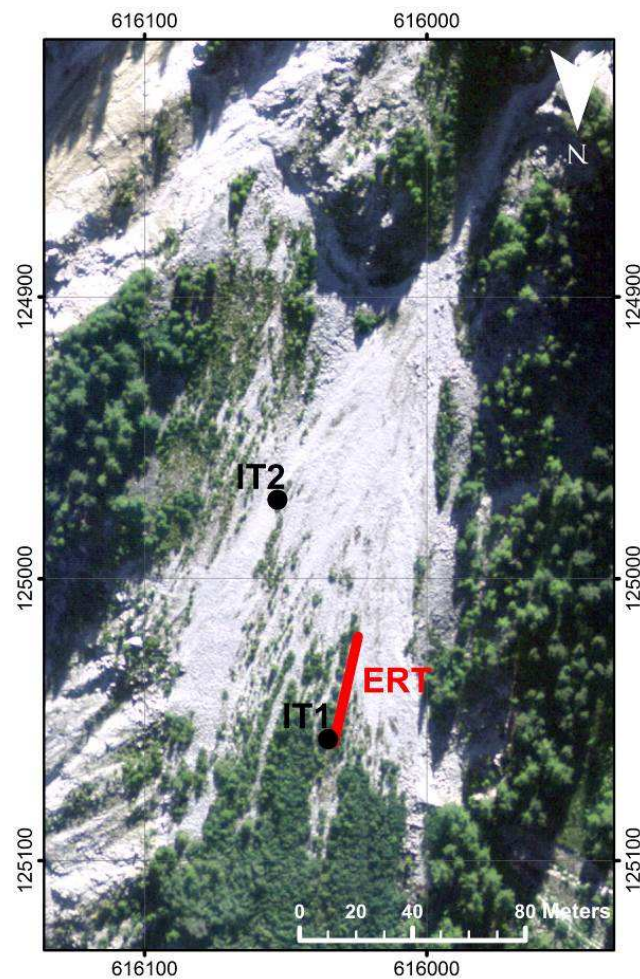


Figure 2.5. Instrumented trenches 1 and 2 (IT 1&2) and ERT profile location on the scree slope (see also Figure 2.3).

2.2.4 Monitoring

The steepness and coarseness of the scree slope and the irregular rockfall hazard complicates the way in which any monitoring location may be selected and installed. Consequently, remote sensing has proved to be exceptionally valuable in determining

where slope movements have taken place, as well as the degree of erosion or deposition. Monitoring can then be enhanced by recording the meteorological influences and the effect on saturation in back-filled trenches in the ground as well as through regular depiction of the surface of the catchment area.

2.2.4.1 Remote Sensing

The use and development of remote sensing methods, combined with geotechnical monitoring and field investigations to study rockslope failure processes and mechanisms, has become a focal point of recent research (Kos et al. 2010a&b). Hazard scenarios can be quantified through the combined use of field mapping, LiDAR and radar interferometric surveys. Ground-based portable radar interferometry (GPRI; Figure 2.7) has been successfully used to identify bedrock instabilities and to quantify displacements using continuous monitoring of the upper Illgraben catchment (Caduff et al. 2011) and is being used in this project to study the relationship between environmental forcing and the rate and extent of surface deformation. Additionally, signal coherence measured by the radar interferometer is being studied to understand how it changes in response to erosional processes.

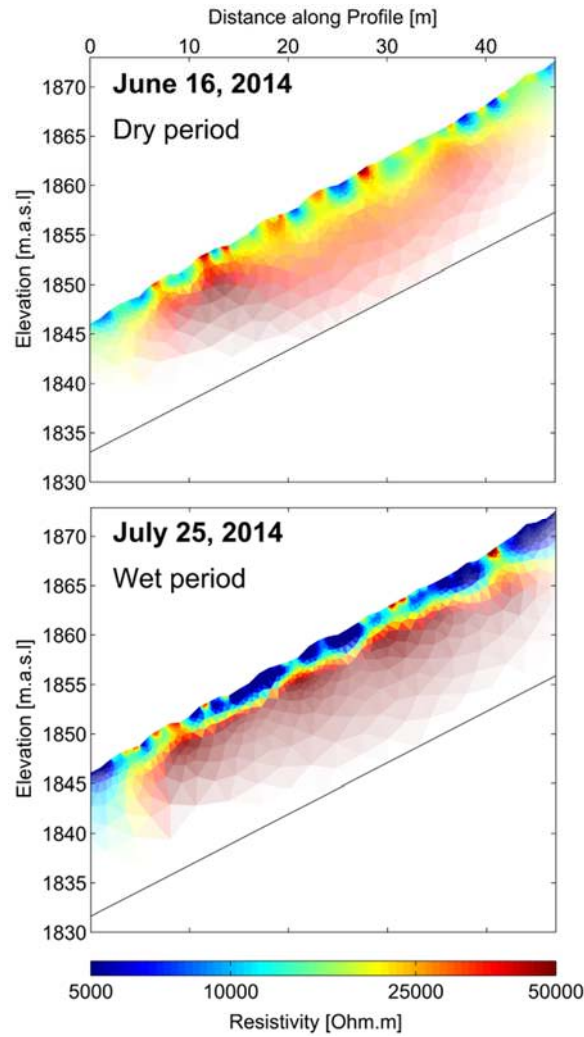


Figure 2.6. Geoelectrical tomograms obtained on the scree slope (Figure 2.5) during a dry period on June 16, 2014 (top) and after a period of heavy rain fall on July 25, 2014 (bottom).

2.2.4.2 Meteorology

Three meteorological stations have been installed at various times. MS1 has been located since October 2013 at 2220 m on the ridge above the scree slope (Figure 2.1), whereas MS2 was only installed for approximately 1 month, until it was damaged by rockfall. MS3 was installed in October 2014.

Station MS1 records rainfall, snowfall and temperature, MS2 measured temperature, rainfall and wind, while MS3 measures precipitation (liquid, solid and mixed, separately) as well as temperature.



Figure 2.7. Ground-based Portable Radar Interferometer (GPR) in front of Agarn church, location on Figure 2.1.

2.2.4.3 Instrumented trenches

Lucas et al. (2015) describe further details of two instrumented trenches (IT1, IT2; see Figures 2.3 and 2.5), which have been excavated in the scree slope in a gravelly soil with fines, overlying a coarser gravelly deposit (Figure 2.8). Following calibration in reconstituted host soil at various saturation degrees, selected devices have been installed at depths of roughly 15, 30, 45 cm to monitor:

- volumetric water content: TDRs, Decagons
- suctions: Jetfill tensiometers
- temperature: thermistors

Initial analyses based on data showing the changes of these quantities with time since installation in:

- IT1 (28th October 2013) and
- IT2 (25th June 2014)

are reported in a companion paper (Lucas et al. 2015).



Figure 2.8. Instrumented trench IT1 (location in Figure 2.5): slope, vegetation, data acquisition and covered trench showing sensors installed in the trench, and gravelly topsoil layer with roots overlying a coarser gravel in the inset.

2.2.5 Modelling & analysis

Various boundary value problems that represent scree slope instability (topsoil distribution, depth to rock, bedrock form, vegetation etc.) will be investigated in small scale physical models that will be tested at enhanced gravity in a geotechnical centrifuge (Springman et al. 2001). Artificial rainfall will be applied to specimens prepared in an environmental chamber, in a similar manner to that advanced by Askarinejad (2012) and vegetation will be modelled in some cases (Askarinejad & Springman, 2014). Subsequently, data from field and physical models will be compared with limit equilibrium analyses of surficial failure on an open slope (e.g. Springman et al. 2003). Moreover, the effect of partial saturation, vegetation and three dimensional failure mechanisms (Casini et al. 2013; Askarinejad et al. 2013) can be considered as well as hydromechanical analyses conducted with fully coupled numerical models (Askarinejad 2012).

2.3 Conclusions

This paper reports the background to a multidisciplinary project (geology, remote sensing, geotechnics and geophysics) that investigates ongoing slope instability and

debris flow hazard in an active Alpine environment. Some parts of the open scree slopes in the Meretschibach catchment that are subject to repeated and significant surface erosion, have been characterised and test pits have been excavated to install sensors to measure water content, suctions and temperature. In parallel, further monitoring is underway periodically from a ground-based portable radar interferometer combined with ongoing meteorological measurements and data from a range of sensors to determine the degree of saturation, suction and temperature in the ground at various locations on the slope.

Future plans for modelling and analysis are discussed briefly, in view of the challenges in predicting the impact of extreme events and protecting inhabitants and infrastructure located in the valley below.

2.4 Acknowledgements

The authors are most grateful for funding from the SNF Project No. 200021_144326/1 and Canton Valais, together with the Councils of Agarn and Leuk. In particular, we wish to acknowledge the support from Pascal Stoeber and Ernst Bleiker.

2.5 References

- Askarinejad, A. 2012. Failure mechanisms in unsaturated silty sand slopes triggered by rainfall, *ETH Dissertation* Nr. 21423.
- Askarinejad, A. Casini, F. Bischof, P. Beck, A. & Springman, S.M. 2013. Rainfall induced instabilities: a field experiment on a silty sand slope in northern Switzerland. *Rivista Italiana di Geotecnica* 3/2012 (luglio - settembre 2012): 9-30.
- Askarinejad, A. & Springman, S.M. 2014. Centrifuge modelling of the effects of vegetation on the responses of a silty sand slope subjected to rainfall. *14th International Conference of the International Association for Computer Methods and Advances in Geomechanics (14IACMAG), Kyoto, Japan*. (Eds: Oka, Murakami, Uzuoka & Kimoto), 1339-1344. Taylor & Francis Group, London, ISBN 978-1-138-00148-0.
- Berger, C. McArdell, B.W. & Schlunegger, F. 2010. Sediment transfer patterns at the Illgraben catchment, Switzerland: Implications for the time scales of debris flow activities, *Geomorphology* **125**, 421–432.
- Berger, C. McArdell, B.W. & Schlunegger, F. 2011. Direct measurement of channel erosion by debris flows, Illgraben, Switzerland, *J Geophys Res* **116**, F01002,

doi:10.1029/2010JF001722.

Caduff, R., Schlunegger, F., Kos, A., 2011. Assessment of precise spatial & temporal slope deformation w. Gamma Portable Radar Interferometer in the Illgraben debris flow catchment, Central Swiss Alps, *Geophys Res Abs* **13**.

Casini, F. Serri, V. & Springman, S.M. 2013. Hydromechanical behaviour of a silty sand from a steep slope triggered by artificial rainfall: from unsaturated to saturated conditions. *Canadian Geotechnical Journal* **50**(1): 28-40. <http://dx.doi.org/10.1139/cgj-2012-0095>.

Fankhauser, K. 2014. Geophysical Slope Characterization Using GPR and ERT in an Active Debris Flow Catchment. *Master Thesis*, EEG, ETH Zurich.

Gabus, J.H. Weidmann, M. Bugnon, P.C. Burri, M. Sartori, M. & Marthaler, M. 2008a. Feuille 1287 Sierre, *Atlas géologique Suisse*, 1:25'000, Carte 111.

Hürlimann, M., Rickenmann, D. & Graf, C. 2003. Field & monitoring data of debris flow events in the Swiss Alps, *Canadian Geotechnical Journal* **40**(1), 161-175.

Kos, A. Strozzi, T. Wiesmann, A. Amann, F. Tomkinson, W. & Conforti, D. 2010a. Spatial monitoring of large rock slopes instabilities at high resolution using a portable radar interferometer. *Proceedings, 3rd Int Dis & Risk Conf*, Davos.

Kos, A. Lunghi, D. Conforti, D. Tomkinson, W. Strozzi, T. & Wiesmann, A. 2010b. Integration of terrestrial Lidar and ground- based radar interferometry for monitoring rock slopes following blast mitigation. *Proceedings, IAEG, Auckland, NZ*.

Lucas, D. Askarinejad, A.A. Herzog, R. Bleiker, E. & Springman, S.M. 2015. Volumetric water content determination by TDR sensors and decagons in gravelly soils. *ECSMGE, Edinburgh*.

McArdell, B.W. Bartelt, P. & Kowalski, J. 2007. Field observations of basal forces and fluid pore pressure in a debris flow, *Geophys. Res. Lett.* **34**, L07406.

Oggier, N. 2011. Modelling of debris flows using RAMMS at the Meretschibach, Agarn, Wallis. *Master Thesis*, IGT, ETH Zurich.

Raetzo, H. 2012. FOEN, pers. comm.

Schlunegger, F. Badoux, A. McArdell, B.W. Gwerder, C. Schnydrig, D. Rieke-Zapp, D. &

Molnar, P. 2009. Limits of sediment transfer in an alpine debris-flow catchment, Illgraben, Switzerland, *Quat. Sci. Rev.* **28**, 1097-1105.

Springman, S.M. Laue, J. Boyle, R., White, J. & Zweidler, A. 2001. The ETH Zurich Geotechnical Drum Centrifuge, *Int. Journal of Physical Modelling in Geotechnics* **1**(1): 59-70.

Springman, S.M. Jommi, C. & Teyssere, P. 2003. Instabilities on moraine slopes induced by loss of suction: a case history. *Géotechnique* **53**(1): 3-10.

Szymczak, S. Bollschweiler, M. Stoffel, M. & Diku, R. 2010. Debris-flow activity & snow avalanches in a steep watershed of Valais Alps (Switzerland): dendrogeomorphic event reconstruction & identification of triggers, *Geomorphology* **116**, 107-114.

Teyssere & Candolfi AG. 2006. Meretschibach unterhalb Geschiebefang, *Bericht Nr. 1642a/3*, Visp.

Theler, D. 2010. Contribution à la cartographie géomorphologique de la dynamique sédimentaire des petits bassins versants torrentiels, *Thèse de doctorat*, Université de Lausanne, Faculté des géosciences et de l'environnement.

3 Volumetric water content determination by TDR sensors and Decagons in gravelly soils

Daisy Lucas

ETH Zürich, Institute for Geotechnical Engineering
Stefano-Franscini-Platz 5, 8093 Zürich, Switzerland
E-Mail address: daisy.lucas@igt.baug.ethz.ch

Amin Askarinejad

ETH Zürich, Institute for Geotechnical Engineering
Stefano-Franscini-Platz 5, 8093 Zürich, Switzerland
E-Mail address: A.Askarinejad@tudelft.nl

Ralf Herzog

ETH Zürich, Institute for Geotechnical Engineering
Stefano-Franscini-Platz 5, 8093 Zürich, Switzerland
E-Mail address: ralf.herzog@igt.baug.ethz.ch

Ernst Bleiker

ETH Zürich, Institute for Geotechnical Engineering
Stefano-Franscini-Platz 5, 8093 Zürich, Switzerland
E-Mail address: ernst.bleiker@igt.baug.ethz.ch

Sarah M. Springman

ETH Zürich, Institute for Geotechnical Engineering
Stefano-Franscini-Platz 5, 8093 Zürich, Switzerland
E-Mail address: sarah.springman@igt.baug.ethz.ch

Submitted to: XVI European Conference on Soil Mechanics and Geotechnical Engineering (XVI ECSMGE 2015), Edinburgh, UK, 13.-17.9.2015, 3565-3570.

Status: Published

Lucas, D., Askarinejad, A., Herzog, R., Bleiker, E., & Springman, S. M. (2015). Volumetric water content determination by TDR sensors and Decagons in gravelly soils. XVI ECSMGE Proceedings, 3565-3570.

Abstract

Debris flow and landslide events in an alpine environment depend on factors such as slope inclination, soil and rock mass characterization, vegetation, rainfall infiltration, ice degradation and snowmelt. If rain infiltrates into the ground, the degree of saturation will increase, with a subsequent decrease in suction, and effective stress in the soil. The shear resistance decreases accordingly, which can trigger failure in critical cases, although the loads that act in the soil may remain almost constant. A study site is located in a steep alpine slope of a lateral valley of the Rhone valley in Valais. This paper focuses on the preliminary geotechnical monitoring, which includes installation of thermistors, TDR (time domain reflectometry) sensors and Decagon (capacitance/frequency domain technology) sensors to measure the volumetric water content and recording of data to assess the effect of rainfall infiltration on the reduction of shear resistance in the soil. The process of laboratory calibration, placement of the sensors in gravelly soil in the field, and early results from the monitoring will be presented and discussed. Determination of the volumetric water content at discrete points in a slope will correlate to the degree of saturation, and can, through tensiometer measurements of the soil suction or a suitable Water Retention Curve, give valuable information to calculate the change in soil resistance.

List of Notation

C_c	→	Coefficient of curvature
C_u	→	Coefficient of uniformity
G_s	→	Specific gravity
Decagon	→	Capacitance sensor EC-5/10HS, Decagon Devices
InSAR	→	Interferometric Synthetic Aperture Radar
IT	→	Instrumented Trench
TDR	→	Time domain reflectometry
TP	→	Test pit
VWC	→	Volumetric Water Content
WSL	→	Swiss Federal Institute for Forest, Snow and Landscape Research

3.1 Introduction

Heavy rainfall events can trigger instabilities in natural slopes due to the rise in pore water pressure in the ground, followed by loss in suction that occurs during infiltration and saturation; this reduces the effective stress and therefore the shear resistance in soils. This process can trigger shallow landslides and the remobilization of material in a scree slope.

The study is carried out in the Bochtür area of the Meretschibach (Figures 3.1 and 3.2), above Agarn village in the Valais (Switzerland). Further details are given in a companion paper (Springman et al. 2015). The process of rock weathering has created extensive scree slopes between elevations of 1500-2000 m, with an inclination angle of approximately 40°. Data of movements recorded by satellite InSAR are of the order of 0.5 m/year at some places in the slope (unpublished data, Dr. Hugo Raetzo, 2012, Foen, pers. Comm.), which indicate that there is instability and potential risk.

Site monitoring is being developed to collect rainfall data, soil temperature, volumetric water content and suction in two trenches. These data represent the input parameters for physical and numerical modelling, simulating field conditions of the scree slope under intense rainfall events, and the triggering of failure mechanisms.

3.2 Location and soil characteristics

Figures 3.1 and 3.2 show the location of the research site, and where the soil samples were dug from test pits TP1 - TP3, only 3 - 5 m apart from each other. Instrumented trenches 1 and 2 (IT1 - IT2) and weather stations, including a new rainfall station planned for the end of 2014, are also shown in the Figure 3.2.

Samples were taken from TP1 - TP3 for grain size analysis at different depths, during dry summer weather conditions, with the following characteristics:

- the ground surface is considered to be 'depth zero' for each test pit,
- test pits were excavated to depths: 0.5 – 0.7 m,
- at least 4 kg were extracted for each sample,
- some cobbles and boulders were left at the site; and photographs were taken for documentation,
- roots were found in almost all of the samples.

The soil is classified (Table 3.1) according to USCS and Swiss standard classification SN 670 004-2NA as gravel with silt and sand GM.

3.2.1 Soil profile in IT1 and IT2

The soil found in instrumented trenches IT1 - IT2, at elevations of 1868 and 1890 m. respectively, is shown in Figure 3.3. The scree slope at these locations has a surficial layer of loose gravel and cobbles of approximately 10 - 15 cm thickness, followed by a layer of silty gravel of depth 25 - 30 cm. This is underlain by a layer of gravel, with an evident reduction of fines and loss of stability during excavation, this change is marked with a discontinuous red line in Figure 3.3.



Figure 3.1. Meretschibach Bochtür in the Valais from the north. Photograph Nicole Oggier (2014).

Table 3.1. Soil classification from test pits near IT1.

Test Pit	USCS Classification	Moisture content [%]	Percent of fines [%]	C _u [-]	C _c [-]	G _s [-]
TP1	GM	2.9-3.7	5.7-8.2	73.6-139.3	8.3-14.4	2.68
TP2	GM	3.0-5.4	5.5-10.8	33.3-105.1	7.9-11.2	
TP3	GM	3.7-4.3	6.7-16.4	72.8	9.1	

C_c: Coefficient of curvature; C_u: Coefficient of uniformity; G_s: Specific gravity

3.3 Methodology

Selected spots on the slopes (i.e. landslide source areas) are monitored *in situ* to measure water infiltration-suction characteristics in the ground, to provide time-series data about infiltration quantity and rate, and the effect on the inter-particle suction, which directly affects the in-situ effective stress. Suction is measured with tensiometers, providing complementary data to assess changing shear stress conditions.

Two vertical monitoring profiles have been installed (IT1-IT2), consisting of sets of co-located tensiometers, time domain reflectometry soil moisture (TDR) and temperature sensors. Freeze/thaw conditions, particularly during the crucial spring snowmelt period, can be identified through measurements of temperature, while the TDRs are calibrated to measure the volumetric water content. An SR50A Campbell weather station is installed and monitored within the study area (precipitation, ambient air temperature, humidity) by the Swiss Federal Institute for Forests, Snow and Landscape research, WSL.

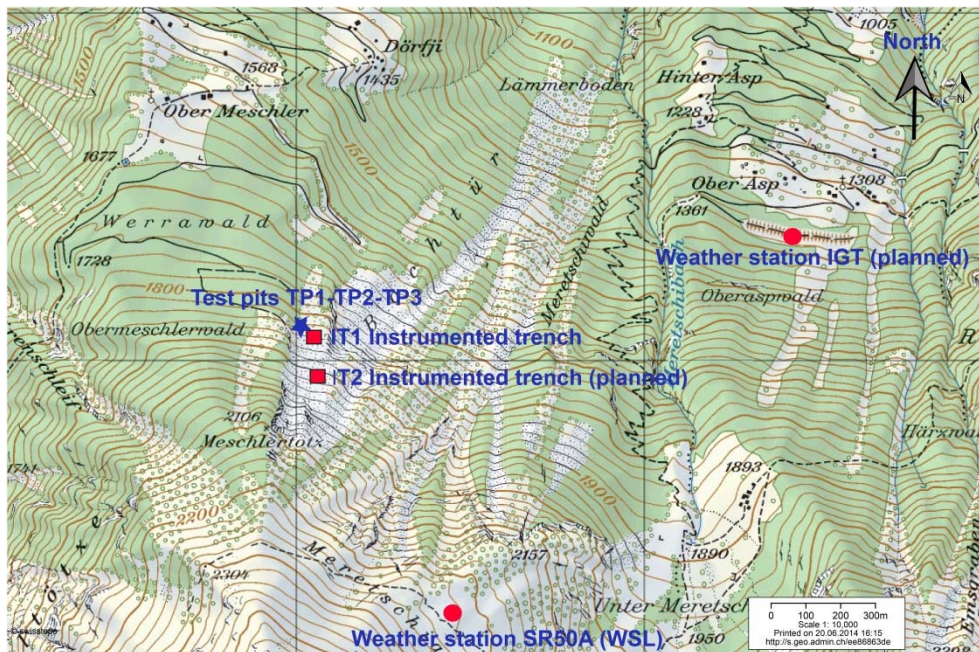


Figure 3.2. Map view of test pits and instrumentation trenches. Source <https://map.geo.admin.ch>.



Figure 3.3. Soil profile in instrumented trenches. Left IT1, right IT2.

3.4 Instrumentation

3.4.1 Sensors

The sensors used in this monitoring are: Tensiometers, decagon, Time domain Reflectometry (TDR) and temperature sensors. These have been described and used in previous landslide monitoring (Askarinejad 2013), see technical details in Table 3.2.

3.4.2 Sensor Calibration

TDR and Decagon sensors measure the volumetric water content of the soil in the field. General characteristics of the sensors are given in Table 3.2. By past experience (Askarinejad 2013; Teyssere 2005), TDR and Decagons have been used to measure the volumetric water content (VWC) in unsaturated silty sand, and alpine moraine with good results. The performance of both sensors will be compared in the field for gravelly soil. The Decagons and TDRs were calibrated using the soil from the field, over the range of volumetric water contents estimated for unsaturated conditions.

The soil was mixed homogeneously, with a defined amount of water for each of the three volumetric water contents desired, and placed in separate containers. Four calibration readings were taken at two different locations for each sensor. It was expected to experience some challenges in installing the instruments in the field because of the

presence of coarse gravel that could become trapped between the forks (Figure 3.4). However, this was managed quite well in practice, and the instruments have functioned.

Table 3.2. Technical information about the sensors installed.

Sensor	Name	Brand	Length	Measuring range
Decagon	EC-5	Decagon devices	0.089 m	Apparent dielectric permittivity ξ_a 1-50.
TDR	TDR100	Campbell Scientific	0.15 m	Apparent dielectric constant $K_a^{0.5}$.
Tensiometers	RTD	Keller AG Company	0.15,	80-85 centibar.
Temperature sensors	PT100		0.30, 0.45 m	-50 to 100 °C.

3.5 Instrumented trench construction

The following instrumentation was installed: TDR, Decagon and temperature sensors, at previously defined locations at depths of 15, 30, 45 cm. The proposed set up is shown in Figure 3.5. These positions were adapted in the field to the condition of soil while inserting the sensor.

3.5.1 Instrumentation

Every trench (Figures 3.5 and 3.6) contains: 2 TDRs, 4 Decagons and temperature sensors. A compact data logger (Figure 3.7) was placed downhill of the trench at a distance of approximately 1.5 - 2 m.

3.5.2 Installation

Both locations (trench and data logger) were cleaned of vegetation and an excavation of 1.1 x 1.0 m (in plan area) was started by teams of 1 - 2 people. A layer of gravel was found at depth of 30 - 40 cm in the excavation that made it extremely difficult to install the sensors at the target depths, so most of the sensors were located in the first 30 cm. Decagons were placed first, then TDRs and the temperature sensors were last of all. All locations were documented with a sketch and photographs (Figures 3.6 and 3.7).

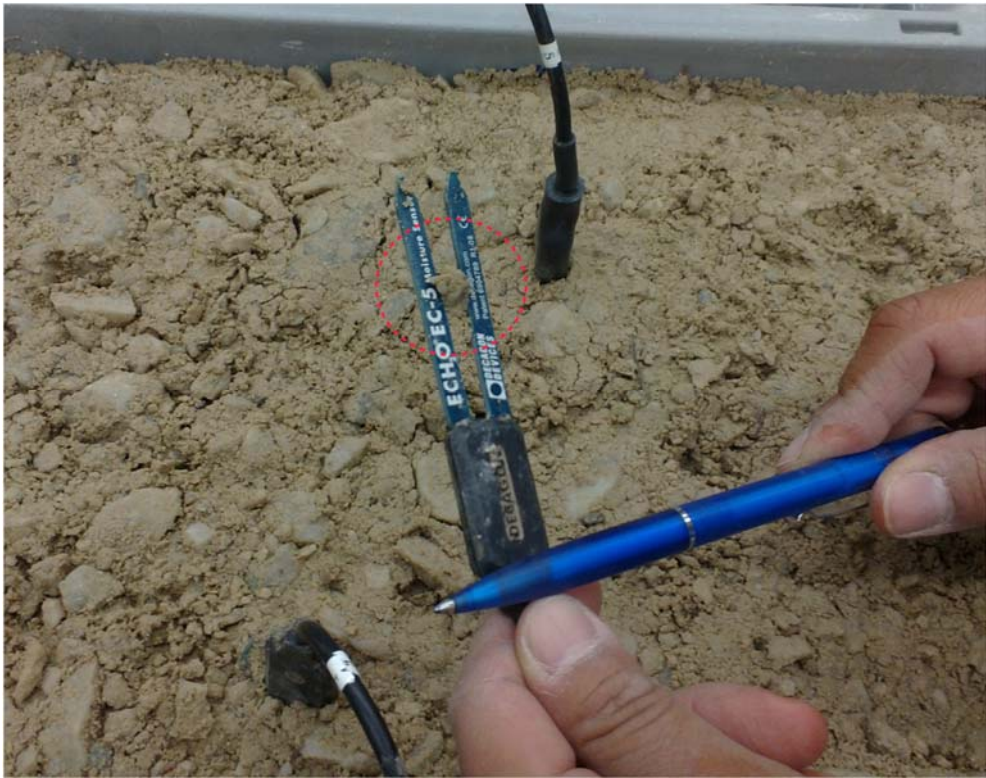


Figure 3.4. Gravel trapped in a Decagon fork during sensor calibration in the laboratory.

Depth			
15 cm	T1 □	TDR1 ○	Dec 1 ☆
30 cm	T2 □		Dec 2 ☆
45 cm	T3 □	TDR2 ○	Dec 3 ☆

Figure 3.5. Sensors set up in the field. Top frontal view arrangement, bottom lateral view.

Once the sensors were installed, the trench was refilled carefully with the same soil, trying to achieve the same density by using hand compaction. Some sensors were destabilised during the refilling procedures, and about 2 - 4 had to be relocated. Thereafter, it was possible to connect the instruments to the data logger, and an antenna was installed for remote data transfer.

3. Volumetric water content determination by TDR sensors and Decagons in gravelly soils



Figure 3.6. Sensor placement, with tags used for records.



Figure 3.7. Data logger located downhill of IT2.

3.6 Results

3.6.1 Instrumented trench IT1

Figure 3.8 show the data obtained from IT1, from the end of October 2013. The variation of volumetric water content at 25 cm depth shows agreement between the measurements from the TDRs and Decagons for the first 8 months. Values decrease to a minimum VWC during winter time, probably due to the low or non-existent rate of rain infiltration, and therefore the moisture content drops. This situation changes in April (spring season) through snow melt and rainfall. The Decagon readings differ from those from the TDR after the rockfall event (beginning of July), but it is not possible to affirm that the impact of the rockfall affected results at this depth. A comparison of the temperatures in the soil at 15 cm depth and in the data logger, which was considered to be the local exterior temperature, was plotted. Temperatures are around 0°C, with minimum variation, for both sensors during the winter season, and this trend continues until April 2014. The temperatures increase again in May, and stay mainly between 10 – 15°C until August (summer season).

A rockfall happened at the beginning of August 2014 (Figure 3.8) during a rain event, hitting the trench and breaking the stake and exposing the soil temperature sensor, causing some instability in the readings. The boulder was removed and the sensor placed in the trench again on 28th August 2014.

Figure 3.9 shows the variation of pore water pressure with precipitation (SR50A weather station), as recorded by the tensiometers, which were installed in June 2014 at depths of 15, 30 and 45 cm. The loss in suction due to rainfall events, during which the shallower tensiometers react more dynamically to rainfall than the deeper tensiometer at 45 cm, is clear in the figure.

3.6.2 Instrumented trench IT2

Temperature and VWC in IT2 are shown in Figure 3.10. The temperature in the data logger shows a greater range in the measurements from (25/6/2014-1/10/2014), since a rockfall strongly impacted the box (Figure 3.11), although the exact date of impact is unknown. The temperature sensors recorded similar readings after the box was fixed and protected in August, with the values from the ground being slightly lower than in the data logger (Figure 3.10).

The variation of VWC in the soil at IT2 is shown in Figure 3.10. They are similar to the magnitudes measured in IT1, since the sensors are relatively close to each other at 16, 20 and 25 cm depths. TDR1 responds slightly earlier than the deeper sensor, but records a lower saturation degree.

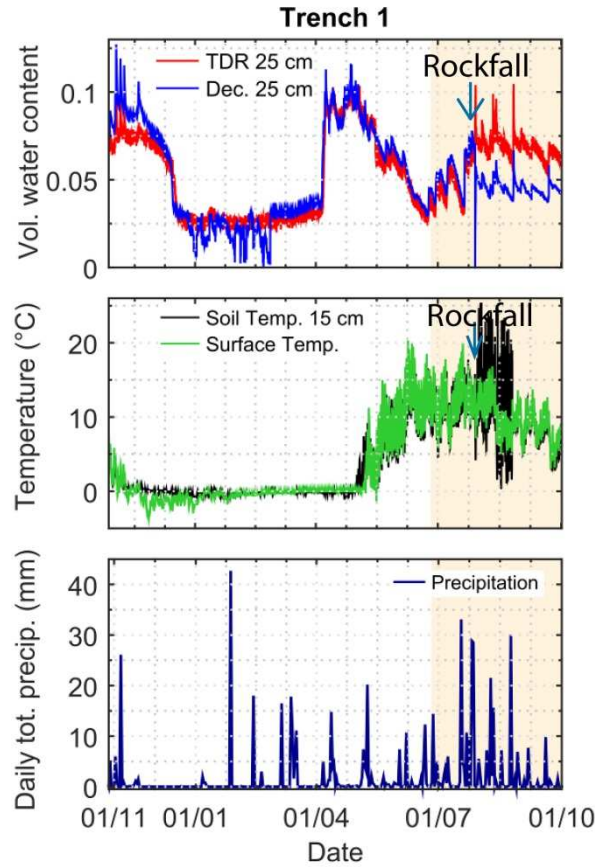


Figure 3.8. Volumetric water content at 25 cm depth; temperature at 15 cm depth and in the data logger; and daily total precipitation at IT1 (28/10/2013-1/10/2014). A rockfall happened at the beginning of August. Precipitation data supplied by WSL.

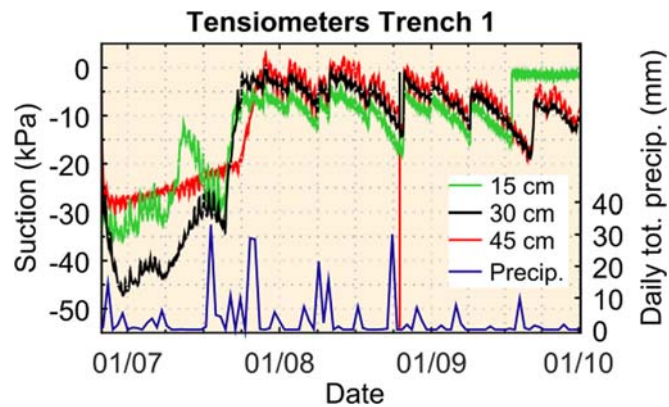


Figure 3.9. Tensiometer and precipitation data (25/6/2014-1/10/2014). Precipitation data supplied by WSL.

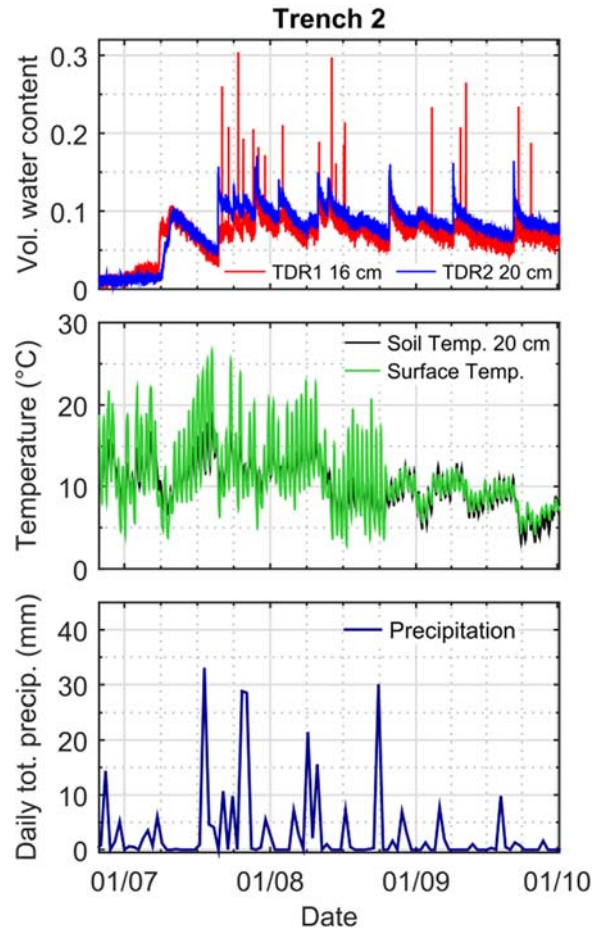


Figure 3.10. Temperature sensor, Volumetric water content reading and rain data; IT2 (25/6/2014-1/10/2014).



Figure 3.11: Left. Data logger after being hit by a rockfall. Right. Box and sensor connection repaired; IT2.

3.7 Conclusions

Temperature in the ground was recorded during four seasons at IT1. During the winter season, temperatures were near zero with very little variation during day and night, which was different to the summer season, where temperatures could change between 5 to 10 degrees per day. Variations were observed after a rockfall hit either the trench (IT1) or the data logger (IT2) but readings were still taken. Maintenance was carried on the IT2 data logger box to restore functionality.

TDR and Decagons reflect the increase of moisture content due to rain events and possible snow melting, with a good agreement in the gravelly soil in IT1. The measurement of volumetric water content recorded at 25 cm depth shows similar values for nine months (Oct-13 to July-14), with some variations in magnitude but similar trends from August 14th.

The reduction in suction after a rain event was recorded by three tensiometers at depths of 15 – 30 - 45 cm. They show a more dynamic response in the shallower locations.

Further work includes the installation of a rainfall station OTT Pluvio2 and the construction of a third instrumented trench IT3 in the scree slope.

3.8 Acknowledgements

The authors are most grateful for funding from the SNF Project No. 200021_144326/1 and Canton Valais, together with the Councils of Agarn and Leuk.

In particular, we wish to acknowledge the support from Pascal Stoebener, WSL, and specifically Nicole Oggier, for giving access to the rainfall data used in the analysis.

3.9 References

Askarinejad, A. 2013. Failure mechanisms in unsaturated silty sand slopes triggered by rainfall *ETH Dissertation* Nr. 21423.

Raetzo, H. 2012, FOEN, pers. Comm.

Springman, S.M., Lucas, D.R., Oggier, N.C., Kos, A., Fankhauser, A., McArdell, B., 2015. Study of the seasonal response of a scree slope and debris flow catchment in the Swiss Alps. ECSMGE, Edinburgh.

Teyssere, P. (2005). Geotechnische Eigenschaften von Möranen, *ETH Dissertation* Nr.16322.

[This page is intentionally left blank]

4 Study of the seasonal response of a scree slope and debris flow catchment in the Swiss Alps

Daisy Lucas

ETH Zürich, Institute for Geotechnical Engineering
Stefano-Franscini-Platz 5, 8093 Zürich, Switzerland
E-Mail address: daisy.lucas@igt.baug.ethz.ch

Kerstin Fankhauser¹

ETH Zürich, Institute for Geotechnical Engineering and Institute of Geophysics
Stefano-Franscini-Platz 5, 8093 Zürich, Switzerland
E-Mail address: kerstin.fankhauser@erdw.ethz.ch

Sarah M. Springman

ETH Zürich, Institute for Geotechnical Engineering
Stefano-Franscini-Platz 5, 8093 Zürich, Switzerland
E-Mail address: sarah.springman@igt.baug.ethz.ch

Submitted to Journal Engineering Geology

Status: Published

Lucas, D. R., Fankhauser, K., & Springman, S. M. (2017). Application of geotechnical and geophysical field measurements in an active alpine environment. *Engineering Geology*, 219, 32-51. <https://doi.org/10.1016/j.enggeo.2016.11.018>

¹ Current employer: focusTerra ETH-Bibliothek
Sonneggstrasse 5, 8092 Zürich, Switzerland

Abstract

A gravelly scree slope in the Meretschibach catchment, a location in the Swiss Alps in the vicinity of Agarn, canton Valais, has been observed to deform downslope at up to 0.5 m p.a. The potential instabilities at this site include surficial landslides, some of them originally thought to be triggered by an increase in pore water pressure with a subsequent loss of shear strength as a consequence of rainfall infiltration and rockfalls. A programme consisting of monitoring, laboratory testing and investigation was developed, to perform a thorough soil characterisation needed in order to produce a realistic ground model. The long-term geotechnical monitoring included in situ soil temperature, suction as well as volumetric water content measurements using dielectric permittivity and time domain reflectometry (TDR) sensors. This data was complemented by electrical resistivity tomography (ERT) to provide extensive knowledge on the depth to bedrock and to validate the volumetric water contents in specific locations. The datasets are completed by recordings from two nearby weather stations. Seasonal changes of precipitation and temperature were reflected in corresponding trends in all measurements. A comparison of volumetric water content records was obtained using capacitance and time domain reflectometry (TDR) sensors with ERT, yielding reasonable agreement. The resulting ground model, which integrates all currently available parameters, delivers the essential information and boundary conditions for predicting and validating slope instabilities in future using numerical and physical modelling.

List of Notation

a	→ Tortuosity factor
C_1 - C_4	→ Cameras
C_u	→ Coefficient of uniformity
C_c	→ Coefficient of curvature
CSD	→ Constant shear stress drained path
Dec	→ Dielectric permittivity sensor EC-5/10HS Decagon devices
D_1 - D_4	→ Densitometer measurements
EC-5	→ Capacitance sensor, Decagon Devices
ERT	→ Electrical resistivity tomography
G_s	→ Specific gravity
IGT	→ Institute of geotechnical engineering
IT	→ Instrumented Trench
K_a	→ Dielectric constant
m	→ Cementation factor
n	→ Coefficient of saturation
OTT Pluvio ²	→ Meteostation
S	→ Saturation
S_1 - S_2	→ Snow stakes 1,2
T_{surf}	→ Temperature in data logger
TDR	→ Time domain reflectometry sensor, Campbell Scientific
VWC	→ Volumetric water content
WSL	→ Swiss Federal Institute for Forest, Snow and Landscape Research
10HS	→ Capacitance sensor, Decagon Devices
ϕ'	→ Critical state friction angle
ρ	→ Resistivity of the porous soil
ρ_w	→ Resistivity of the pore filling
ρ_{ERT}	→ Electrical resistivity measured by ERT
Φ	→ Soil Porosity

4.1 Introduction

The Meretschibach catchment (Figure 4.1) situated in the Swiss Alps, canton Valais, near the village of Agarn (620 m.a.s.l.), has been investigated due to dynamic processes of erosion, deposition and remobilisation of debris, which can evolve into different kinds of mass movement. Debris flows have reached Agarn from an active channel and caused damage to infrastructure in the past. This has been well documented (Rickenmann and Zimmermann, 1993; Oggier, 2011). However, little has been published about slope instabilities triggered in gravelly soils in the adjacent scree slope, where surface movements of up to 0.5 m p.a. have been obtained from InSAR measurements (Dr. Hugo Raetzo, 2012, FOEN, pers. Comm.).

Three prevalent types of downslope movement were expected, either based on past research (Springman et al., 2003; Springman et al., 2012), or from observations made during the monitoring programme on the steep scree slope:

- shallow landslides triggered by an increase in pore water pressure that reduces soil suction and shear strength;
- boulders that topple, fragment, bounce and roll downslope from weathered rock walls at the top of the slope;
- ongoing surficial erosion, including destabilisation of the top ground layer through rainfall runoff and flow, movement of dry debris as well as small avalanches in winter.

Characterisation and long-term monitoring of this slope are necessary in order to gain more understanding of these processes, although this is complicated by slope inclinations of 33-43°, heterogeneous gravelly soil, patches of native vegetation, seasonal limitations and difficult accessibility due to the alpine location at 1840-2000 m.a.s.l. A realistic ground model can be established, defining extent of soil layers and depth to bedrock, as well determining relevant soil properties at different depths.

A long-term monitoring campaign, integrating geotechnical and geophysical methods together with laboratory analyses, allows a progressively more detailed calibration and validation of the ground model and relevant parameters, while observing and measuring the response of the scree slope to seasonal processes. Instrumentation was installed in the scree slope at shallow depths (<1 m) within four trenches (IT1-IT4), to perform real time monitoring of the volumetric water content (VWC), temperature and suction (Lucas

4. Study of the seasonal response of a scree slope and debris flow catchment in the Swiss Alps

et al., 2015; Springman et al., 2015). The VWC and the suction measurements provide valuable information to assess changes in soil shear resistance, particularly for soil in a partially saturated state and to enable a comparison between the VWC acquired by two different types of moisture sensors. Additionally, the precipitation in the area was measured with two weather stations located within a distance of 2 km, at elevations of 2220 and of 1370 m.a.s.l., respectively.

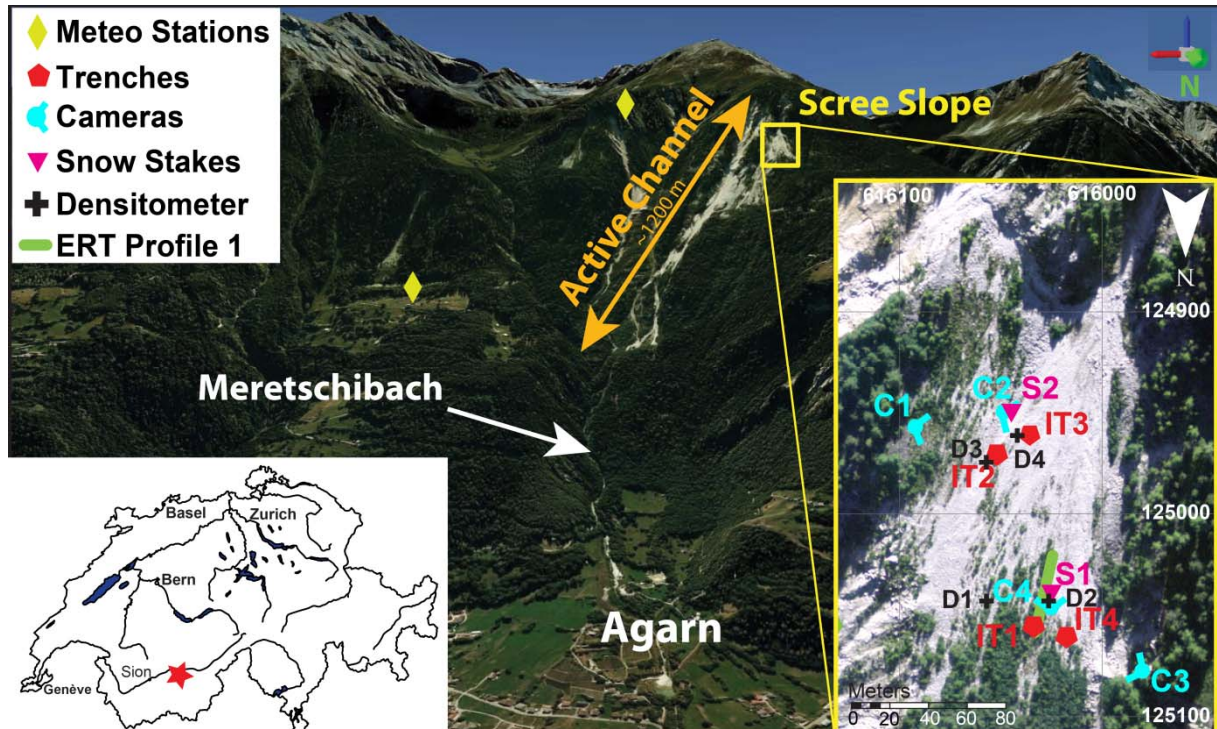


Figure 4.1. Overview of the field area, located in canton Valais, Switzerland (star on small map). The image looking south shows a view of Agarn, situated on the Rhone valley floor and the Meretschibach catchment on the mountain slopes behind. The most active area within the catchment can be divided into an active channel and a scree slope. The weather stations (yellow diamonds) are located at 1370 m.a.s.l. (IGT) and 2220 m.a.s.l. (WSL). The right image shows an enlargement of the scree slope (yellow rectangle) with the locations of the instrumented trenches (IT1-IT4), the ERT profile on which the monitoring was performed, snow stakes (S1-S2), densitometer measurements (D1-D4) and cameras (C1-C4).

Geophysical measurements complemented the long term soil monitoring, providing a convenient way to extend the knowledge of the subsurface to larger areas in the scree slope (Bogolovsky and Ogilvy, 1977; Hack, 2000; Bichler et al., 2004; Otto and Sass, 2006; Sass, 2007; Sass et al., 2008). Electrical resistivity tomography (ERT) measurements were conducted repeatedly throughout the spring and summer months of 2014, on a profile located close to IT1 (Fankhauser, 2014), allowing the insitu VWC recordings to be validated in specific locations using Archie's law (Archie, 1942; Friedel et al., 2006). Effective validation can demonstrate complementarity of geotechnical and

geophysical methods and provide a more widespread interpretation of the volumetric water content (VWC), leading to a more detailed characterisation of the scree slope.

The data presented here was acquired over a period of two years, and is analysed by seasons. Trends in summer and winter, and thawing/freezing processes in spring and autumn, are discussed further.

4.2 Soil ground characteristics

4.2.1 Soil classification

Figure 4.1 shows the location of the research site and, specifically, the instrumented trench sites IT1 – IT4. Samples were taken from test pits and trenches during dry summer weather conditions. The following characteristics were noted: the ground surface was considered to be ‘depth zero’ for each test pit; at least 4 kg of soil were extracted for each disturbed sample. Cobbles larger than 70 mm, and any boulders, were left at the site. Roots were found in almost all of the samples.

Grain size analyses were performed later in the laboratory. The soil is mostly gravel, with diverse percentages of sand and fines, and it is classified (Figures 4.2, 4.3 and Table 4.1) according to Swiss standard classification (SN 670 004-2NA), as poorly-graded gravel with silt and sand (GP-GM), silty gravel (GM), well-graded gravel with silt and sand (GW-GM), and well-graded gravel (GW). Figure 4.2 shows the soil profiles in the instrumented trenches.

Three common soil units are found in IT1, IT2 and IT4, but with different thicknesses: (A) gravel with fines and high root content; (B) gravel with fines, and less or no roots, (C) coarser gravel. An orange dashed line separates the gravel from a soil layer with greater fines content, considered here as more stable and suitable for instrumentation placement, from either coarser gravel layers or isolated lenses of coarser gravel that were more unstable for excavation (IT4). In contrast, IT3 consists of two different units described as finer gravel (D) and a transition to slightly coarser gravel (E).

4. Study of the seasonal response of a scree slope and debris flow catchment in the Swiss Alps

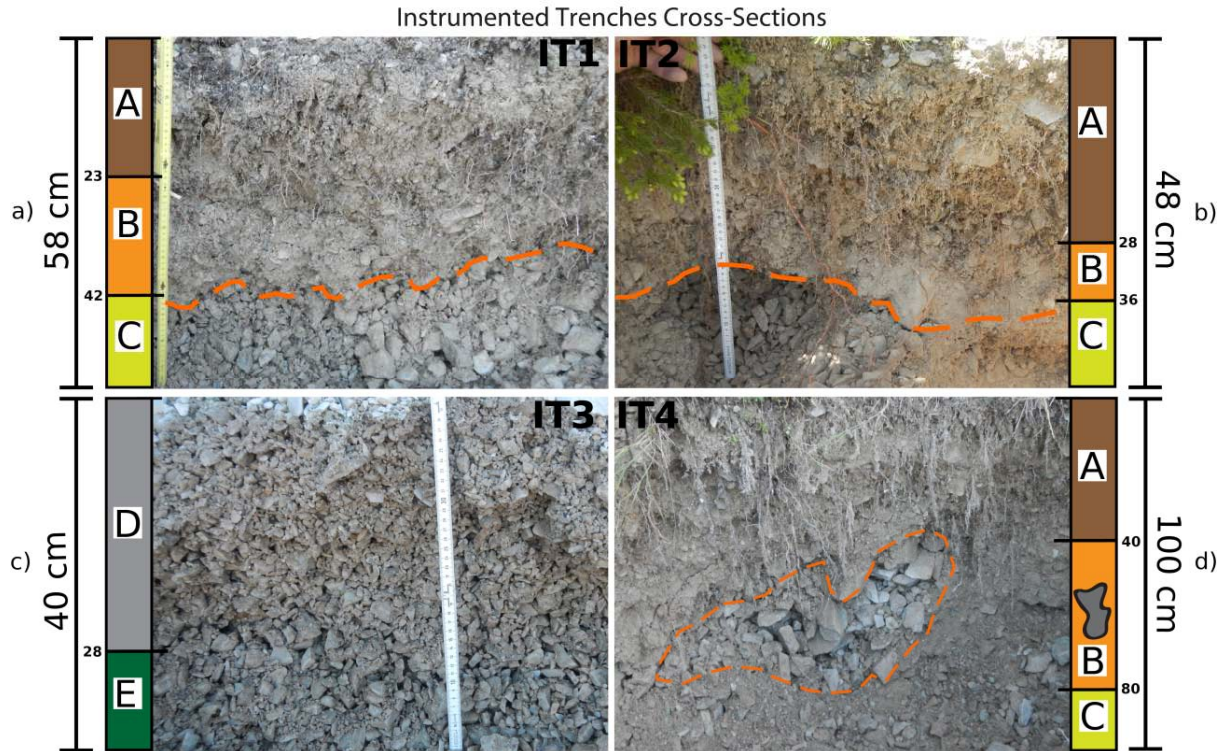


Figure 4.2. Soil profiles at instrumented trenches. a) IT1, b) IT2, c) IT3 and d) IT4. For IT1, IT2 and IT4: A (depth ~0-40 cm), gravel with silt, sand and some roots; B (depth ~25-40 cm), gravel with silt and sand; C (depth below ~40 cm), coarser gravel with less fines; IT3: D (depth ~0-25 cm), gravelly soil with little sand and silt content; E (depth below ~25 cm) change to a coarser gravel.

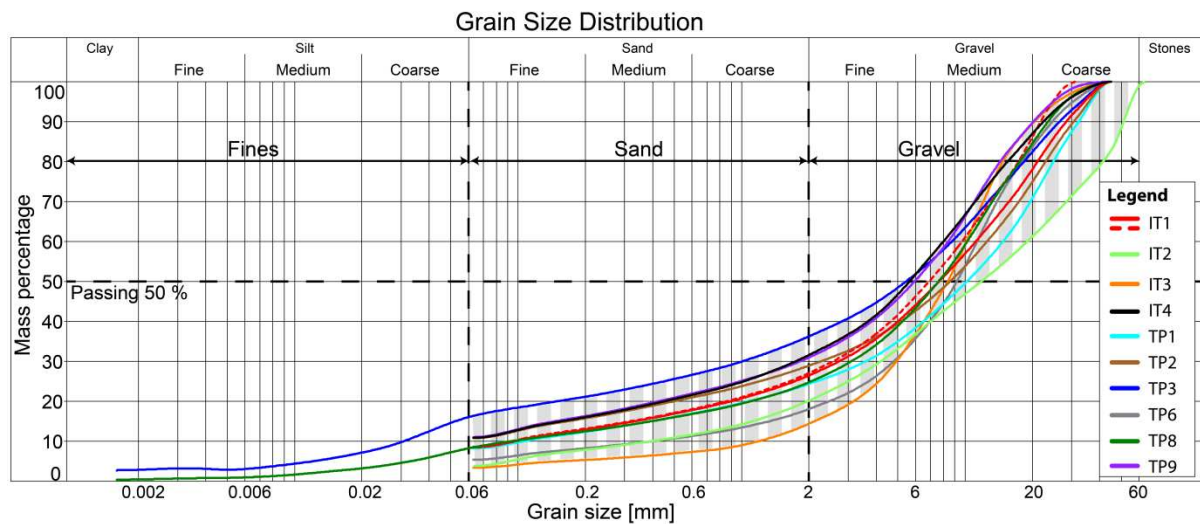


Figure 4.3. Grain size distribution: a selection from Meretschibach scree slope test pits TP 1-9 are plotted, together with IT1-IT4. The range is shaded in grey to illustrate the characteristics and content of fines for the entire set of samples.

4. Study of the seasonal response of a scree slope and debris flow catchment in the Swiss Alps

Table 4.1. Soil classification from test pits and instrumented trenches.

Test pit	Swiss Standard Classification (SN 670 004-2b NA)	Moisture content [%]	Percent of fines [%]	C_u [-]	C_c [-]	G_s [-]
TP1	GP-GM	2.9-3.7	5.7-8.2	73.6-139.3	8.3-14.4	2.68
TP2	GP-GM	3.0-5.4	5.5-10.8	33.3-105.1	7.9-11.2	
TP3	GM	3.7-4.3	6.7-16.4	72.8	9.1	
TP4/IT 1	GP-GM	-	7.7-9.2	98.2-115.3	6.2-8.2	
TP5	GP-GM	-	5.7	37.6	5.0	
TP6	GP-GM	-	5.4	28.7	5.1	
TP7	GP-GM	-	8.4	106.1	7.7	
TP8	GP-GM	-	8.5	110.2	10.1	
TP9		-	11.0	-	-	
TP10	GW-GM	-	11.7	94.9	2.2	
IT2	GW	2.2	4.0	46.9	2.32	
IT3	GW	-	3.4	8.4	1.9	
IT4	GP-GM	-	10.9	47.5	2.32	

C_u : Coefficient of uniformity, C_c : Coefficient of curvature; G_s : Specific gravity

4.2.2 In situ unit weight

The in situ unit weight was determined with a soil densitometer (Magdeburger Prüfgeräte GmbH (HMP)), which uses the balloon method (DIN 18125-2:2011-03) from which void ratio and porosity can be derived. It could be transported to alpine sites to carry out measurements in gravelly soil.

The unit weights calculated from the tests are presented in Table 4.2 and the test locations are shown in Figure 4.1. These values were in agreement with the void ratio range of 0.34-0.69, which was determined in the laboratory from test samples.

Table 4.2. Dry unit weight obtained with the soil densitometer method.

Measurement	Dry unit weight [kN/m ³]	Void ratio [-]	relative density [%]	Porosity [-]
D1	17.63	0.52	48.57	0.34
D2	16.98	0.58	31.43	0.37
D3	17.69	0.51	51.43	0.34
D4	16.09	0.66	8.57	0.40

4.2.3 Slope inclination

The slope inclination in the scree slope (Figure 4.4) was obtained using geographical information system (GIS) and processed by Fankhauser (2016, after Oggier 2013). The

most predominant angle of inclination in the scree slope is between 33 and 43°, although some steeper areas (mostly upslope) can be identified up to 43°.

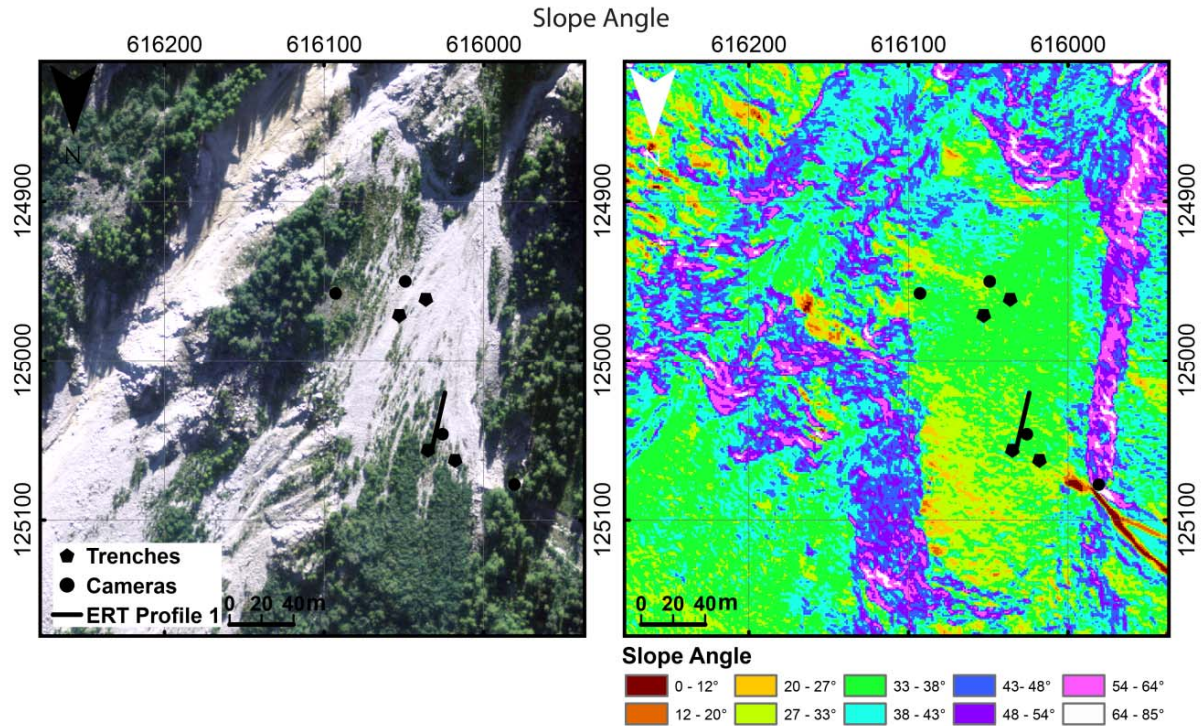


Figure 4.4. Left: Aerial photograph (SWISSIMAGE) of the scree slope and top part of the active channel; right: slope angle in °: of the same area. Black symbols show the location of instrumentation (see Figure 4.1 for comparison).

4.2.4 Instrumented trenches

Selected spots on the scree slope (i.e. landslide source areas) are monitored in situ to measure water infiltration-suction characteristics in the ground, to provide time-series data on infiltration quantities and rates, as well as the influence on the capillary suction, which directly affects the effective stress. Four monitoring profiles were installed (IT1-IT4, Figure 4.1 and 4.2), consisting of sets of dielectric permittivity sensors (EC-5 and 10HS), time domain reflectometry (TDR) soil moisture and temperature sensors (Table 4.3). Two trenches, IT1 and IT4, are supplemented by co-located tensiometers. All the sensors were installed in trenches up to 1 m depth and of minimum 1 m width, to minimise interference between sensors at similar depths.

Two weather stations were installed and are monitored within the study area, a SR50A Campbell weather station (precipitation, ambient air temperature, humidity) controlled by the Swiss Federal Institute for Forests, Snow and Landscape research (WSL), and an OTT Pluvio² device (precipitation, ambient air temperature, humidity and wind direction) installed by ETH (IGT). While the Campbell station is used to measure

precipitation in the form of rain when the ambient air temperature is higher than zero (no heater), the OTT Pluvio² is able to measure precipitation in the form of rain, snow, or a mixture of both during all seasons.

Environmental changes, including freezing/thawing conditions, particularly during the crucial autumn/spring snow-melt period, can be identified through ambient and soil temperature measurements. The TDRs and dielectric permittivity sensors (EC-5, 10HS) are calibrated to measure the volumetric water content (VWC).

4.2.4.1 Sensors and calibration

4.2.4.1.1 Sensors

Two types of sensor were installed to measure VWC (Table 4.3): time domain reflectometry (TDR100; Campbell Scientific) and capacitance sensors (EC-5 and 10HS; Decagon Devices), via the apparent dielectric constant /permittivity of the soil surrounding the probes.

The volume of sensitivity of the sensors (soil volume influenced during VWC measurement) becomes relevant while interpreting data in terms of first response to a saturation event. A representative VWC of gravel in the scree slope should reflect the range of particle sizes and the measurement volumes, with 181 (Onset, n.d.) and 1160 cm³ (ICT international, 2008) respectively for EC-5s and 10HSs (method after Sakaki et al., 2008), and 1.4 times the diameter of the rod spacing (2.1 cm) for TDRs (O'Connor and Dowding, 1999), leading to a volume of 101 cm³ (Table 4.3).

The suction was recorded with tensiometers (Jetfill 2725 in IT1 and Remote 2100F in IT4; Keller AG), paused in October before winter (to avoid freezing conditions) and restarted again in May. While the Jetfill were installed a few metres upslope of the trench, to a maximum depth of 0.45 m, the Remote were installed in the trench with the other instruments at different depths (up to 1 m).

Further information on all sensors can be found in supplementary material 4.7.

4.2.4.1.2 Calibration

The capacitance and TDR sensors were calibrated in the laboratory using poorly-graded gravel with silt and sand (GP-GM) from the field, over the range of VWCs estimated for the unsaturated conditions expected in situ. The specimens were prepared by moist

tamping, with void ratios in the range of $e = 0.53 - 0.69$, simulating suitable installation conditions with both medium and loose densities.

A linear calibration was fitted to the measured values in most cases, in which the coefficient of determination was $r^2=0.56-0.98$. In some cases, this could be improved by fitting a polynomial equation, and this was adopted, for instance, for IT2 capacitance sensor 10HS at 13 cm depth.

Although Topp's equation (Topp et al., 1980) allows prediction of VWC for grain sizes up to 2 mm, the VWC obtained were between factors of 2-3 smaller than for a site-specific linear calibration at 20°C using the soil from the field with a $d_{\max} \leq 31.5$ mm (albeit with a 8% content of fines). This significant difference could be due to effect of the texture, structure, and density on the electrical response in soils, as mentioned by Topp et al. (1980). These results confirm that a site specific calibration function is necessary when using poorly-graded gravel with silt and sand. While Topp's approach could not be completely applicable to the grain size distribution of the scree slope, the adjustment of the permittivity due to changes in temperature derived by Bogaen et al. (2007), using a liquid with known dielectric properties (2-isopropoxyethanol (i-C3E1) water mixtures) was tested against Bogaen's equation for loamy silt. This has a significant effect on the calculated VWC, which in many cases maps closely to the values of the site-specific calibration results. As the use of a site-specific calibration function has been recommended by other authors (e.g. Take et al., 2007 and Mittelbach et al., 2011), this has been adopted. A site-specific equation for the correction of permittivity due to temperature (applicable to capacitance sensors installed in scree soil) is advised for future studies.

Ultimately, the performance of a sensor type is directly related to the soil conditions in the field. Large stones and boulders, sometimes comparable to the size of the capacitance sensor prongs, complicate effective insertion of the probes into the soil. Heterogeneity contributes natural variability in density, void ratio and grain sizes that have impacted on the process of site-specific calibration and functionality of TDRs and capacitance sensors during monitoring.

4. Study of the seasonal response of a scree slope and debris flow catchment in the Swiss Alps

Table 4.3. Technical information about the sensors installed.

Sensor	Name	Brand	Length	Measuring range	Volume of influence [cm ³]	Accuracy	Temperature range [°C]
Capacitance	EC-5	Decagon Devices*	0.089 m	0-100 % VWC	240	±1-2% VWC with soil specific calibration	-40 to +50
	10 HS (only IT2)		0.145 m	0-57% VWC with polynomial	1320	using soil specific calibration, ± 0.02 m ³ /m ³ (± 2% VWC) in any soil	Survival Temperature: -40 - 50 Operating Temperature: 0 - 50
Time domain reflectometry	TDR100	Campbell Scientific **	0.15 m	0-100 % VWC	188.5	±1.5% VWC	-40 to +55
Tensiometers	Jetfill 2725 ARL	Keller AG Company ***	0.15, 0.30, 0.45 m	0-85 kPa	Direct contact	+/- 1.5%	Avoid freezing condition
	Remote 2100F	Keller PR23-S****	Installed at depths from 0.2 to 1 m.	0-85 kPa			
Temperature	RTD PT100	Heraeus	Installed at depths from 0.2 to 1 m.	-50 to 100 °C	Direct contact	+/- 0.05 °C	-50 to 100 °C

*http://manuals.decagon.com/Manuals/13876_EC-5_Web.pdf

**<https://s.campbellsci.com/documents/us/manuals/tdr100.pdf>

***http://www.soilmoisture.com/RESOURCE_INSTRUCTIONS-all_products/Resource_Instructions_0898-2725_2725%20Jet-Fill%20Tensiometers.pdf

****http://www.soilmoisture.com/RESOURCE_INSTRUCTIONS-all_products/Resource_Instructions_0898-2100_2100F%20Soilmoisture%20Probe.pdf

4.2.5 Electrical Resistivity Tomography (ERT)

A 2D electrical resistivity survey was carried out on a fixed profile line next to instrumented trench IT1 (Figure 4.1) to complement the point measurements from the TDRs and dielectric permittivity sensors, and achieving a more widespread characterisation of the subsurface. The basic principle of geoelectrical resistivity measurements, as well as the equipment and configurations used in this project, are briefly summarised in supplementary material A. Further details on acquisition, processing etc. can be found in Fankhauser (2014), Günther et al. (2013), Günther et al. (2006), Günther (2011), Rücker et al. (2006) and Lowrie (2007). A total of six ERT

measurements (three of which are presented here) were poorly-graded gravel with silt and sand (GP-GM) conducted in a monitoring phase from May to July 2014.

4.2.6 Archie's law

ERT measurements are highly susceptible to changes in the subsurface water content/saturation as the current injected during a geoelectrical survey flows mostly through the pore water. An empirical relationship between the resistivity of a porous medium to the amount of pores, their connectivity and saturation, as well as the resistivity of the pore filling fluids, was found by Archie (1942):

$$\rho = a\rho_w\Phi^{-m}S^{-n} \quad \text{with } S = \frac{\theta}{\Phi} \quad (4.1)$$

where ρ is the resistivity of the porous soil, ρ_w is the resistivity of the pore filling fluid, Φ is the soil porosity (typically n in a geotechnical context) and S the saturation, which can also be expressed as the ratio between the volumetric water content θ and the porosity. Furthermore, a is the tortuosity factor set to 1 for granular soils, m is the cementation factor and n is the coefficient of saturation. The latter two factors are assumed to be constant and, if taken from literature (e.g. Archie, 1942; Lowrie, 2007; Schön, 1983), are usually given as $m \cong 1.3$ and $n \cong 2$ for granular soil. Archie's law is considered to be valid in this case (without the need for any correction factors), as the soil consists mainly of gravel and sand and contains almost no fines, especially no clay (Figures 4.2 and 4.3, Table 4.1). The relationship can be used for effective comparisons between the geotechnical soil moisture measurements and ERT acquisitions (e.g. Brunet et al., 2010; Lehmann et al., 2013; Springman et al., 2013). For this purpose, the key parameters, Φ and ρ_w , were estimated from soil and water samples (small creeks and surface run-off near to the scree slope) extracted from the field, and analysed through laboratory and field experiments as $\Phi = 0.33 \pm 0.08$ and $\rho_w = 155 \pm 28 \Omega m$ (at 25 °C; for temperature corrections, the equation and the geophysical temperature compensation factor stated in Hayashi (2004) were used).

A convenient way to use the temporally varying soil resistivities (repeatedly measured ERT profile) is to calculate the saturation relative to a so-called baseline model (chosen here as the acquisition on 15th May 2014) and so avoid having to estimate many (uncertain) parameters in Archie's law. The resulting trend (Figure 4.16) can be compared relative to the readings obtained from TDR and dielectric permittivity sensors. This process is further described in supplementary material 4.7.

4.3 Results and discussion

4.3.1 VWC and temperature monitoring in instrumented trenches IT1-IT4

An overview of the data time series recorded since October 2013 is presented in Figure 4.5, where a set of two plots display the volumetric water content (VWC) and temperature versus time (in months at the bottom and the top, separated by dashed lines), in chronological order of installation for each of the instrumented trenches (from top to bottom: IT1-IT4).

The VWCs displayed in all of the plots range from 0 to 0.3 and the temperatures from -10 to 30 °C. The precipitation from the two weather stations (WSL and IGT) is shown at the bottom, over a range of 0 to 50 mm per day. Each coloured line represents a sensor installed at a given depth, as shown in each legend with the corresponding sensor name (Dec = dielectric permittivity sensor; T = temperature), as well as the depth (in centimetres below the surface) as a sub-index. The VWC from the three types of moisture sensors (dielectric permittivity sensors and TDRs) can be compared when they are at similar depths. T_{surf} is the temperature measured in the data logger at the surface, usually a few metres away from the trench. The background shading represents a definition of summer (yellow) and winter (blue), as the season during which fieldwork can be carried out and a time during which access to the site is not possible, respectively. Missing data due to loss of signals or eliminated data from a specific device are marked at the top of the plot by a cross of the same colour.

Clear and expected seasonal differences are observed between summer, winter and spring/autumn in terms of temperature and volumetric water content (VWC).

4.3.2 Seasonal response of the scree slope

4.3.2.1 Summer

Figures 4.6 and 4.7 represent the summers of 2014 and 2015, respectively at different locations of the scree slope (Figure 4.1, IT1-IT3). High temperatures in summer combined with precipitation in the form of rainfall, which infiltrates into the ground, produces almost immediate increases in VWC near the surface. The variation in magnitude of VWC between trenches IT1-3 (Figure 4.7) can be attributed to the different grain size distributions (GW: IT2-3; GP-GM: IT1,4). Two types of infiltration behaviour can be identified in trenches IT1-IT2, which can be seen when comparing the VWC in July 2014. The increase of VWC can either be gradual with a gradual convex drop-off as

the ground drains, or reach immediate peaks, followed by linear to concave decreases. The former were associated with periods of high suctions (especially in deeper tensiometers, and during periods of little to no rainfall), when the unsaturated hydraulic conductivity decreased, while immediate peaks occurs at higher degree of saturation. Furthermore, suctions reduced either in the same timeframe as the rain infiltration or marginally slower than the VWCs had increased. This is due to the radius of influence of the sensors, EC-5 has a greater radius of 20 mm and the tensiometers around 1 mm, therefore capacitance sensors react faster during infiltration (Beck, 2010). Sun exposure is higher in IT3, with temperature ranging from 0 to 27°C, and daily peaks close to ambient air temperature.

4.3.2.2 Winter

Temperatures are near or below 0 °C (Figure 4.8), so that precipitation occurs in the form of snowfall or mixed with rainfall. The pore water fluid is expected to freeze when temperatures are below 0°C, decreasing the permeability of the unsaturated soil even further. Snow can accumulate on, and insulate, the slope, reducing the rate and volume of water infiltration (Figure 4.8, camera 2, 28.12.2014, 10:00). These two processes explain the degree of saturation dropping to a minimum and the lack of variation in VWC with ongoing winter precipitation (Figure 4.8, December, beginning January), while infiltrating precipitation and snow-melt processes cause rising VWC when there is an increase from negative to positive temperatures (Figure 4.8, end December, beginning January). Episodes of freezing and snow melting are observed later in some trenches, because the ground temperature is dependent on sun exposure, which differs depending on the location on the scree slope (up- or downslope).

Patterson et al. (1981) proposed that K_a is not highly sensitive to ice content in partially saturated coarse sand samples, since the slight increment measured is a product of replacing air ($K_a=1$) by ice ($K_a=3-4$). Moreover, they measured K_a at negative temperatures in fine-grained soils (clay loam, silt loam), showing that the VWC for ice-water mixtures was within ($\pm 2.5\%$) of values calculated by Topp et al.'s (1980) equation, suggesting that it could be applicable, at least, to unfrozen and frozen fine-grained soils.

Considering Patterson's approach, with Topp's values of VWC compared to soil-specific calibration, and VWCs measured at sub-zero temperatures by capacitance and TDR sensors at different depths (Figure 4.8):

- IT1 TDR₂₂ and EC-5₂₅ show similar ranges of VWC, with EC-5 slightly lower,
- TDR₃₈ and EC-5₃₇ match well,
- as do IT2 TDR₂₀, 10HS₁₃ and IT3 TDR₁₅ and EC-5₁₅.

This issue has been further studied by Spaans and Baker (1995), who proposed improving VWC estimation by calibrating TDR sensors in frozen soil, dependent on VWC and temperature.

Frost heave causes change in structure and expansion of saturated fine-grained soils through ice lens formation in the frozen zone under sub-zero temperatures, accompanied by water migration from the unfrozen zone to the ice lenses (Miller, 1973; Taber, 1929; Taber, 1930). As thermodynamic equilibrium is required at the interface of the ice lens and the water, suction builds up, changing the VWC and therefore the hydraulic conductivity of the soil. Furthermore, frost heave in a steep slope can contribute to surficial movement, with surface debris rolling downslope (Matsuoka, 1998). This process is unlikely to have happened at the study site, even when soil reached sub-zero temperatures (Figures 4.5, 4.8), although there would have been more likelihood to occur, very locally in silty soil around roots of stunted vegetation in IT1 and IT4, due to the higher content (around 10%) of fines (Figure 4.3, Table 4.1).

4.3.2.3 Spring/Autumn

The spring snow-melt (Bayard et al., 2004) happens over conditions of sun exposure and higher temperatures during the day, producing a significant steady supply of water with more gradual infiltration. In combination with precipitation in the form of rainfall, water infiltrates through the partial insulation (e.g., remaining snow patches) into the ground, raising the VWC (Figures 4.9, 4.10). The decrease of temperatures in autumn set the conditions for snowfall and potential soil freezing, which results in reduced VWCs.

Figure 4.9 shows data from mid-April to mid-May 2015, including a larger scale plot of the most extreme precipitation event (2nd May 2015). The spring season shows the transition in soil temperature rising from minimum values, while the air temperature is already positive, with a daily variation of ~10°C. The temperatures rise earlier in IT2 and IT3 (upslope) respectively, whereas IT1 (downslope) follows days later, confirming the effect of sun exposure. The daily temperature variation in IT1 through IT3 is greater for shallower depths (15-20 cm; yellow), compared with deeper sensors (40-45 cm; red).

However, the magnitude of this variation in IT3 is much greater at depth than in any other trench.

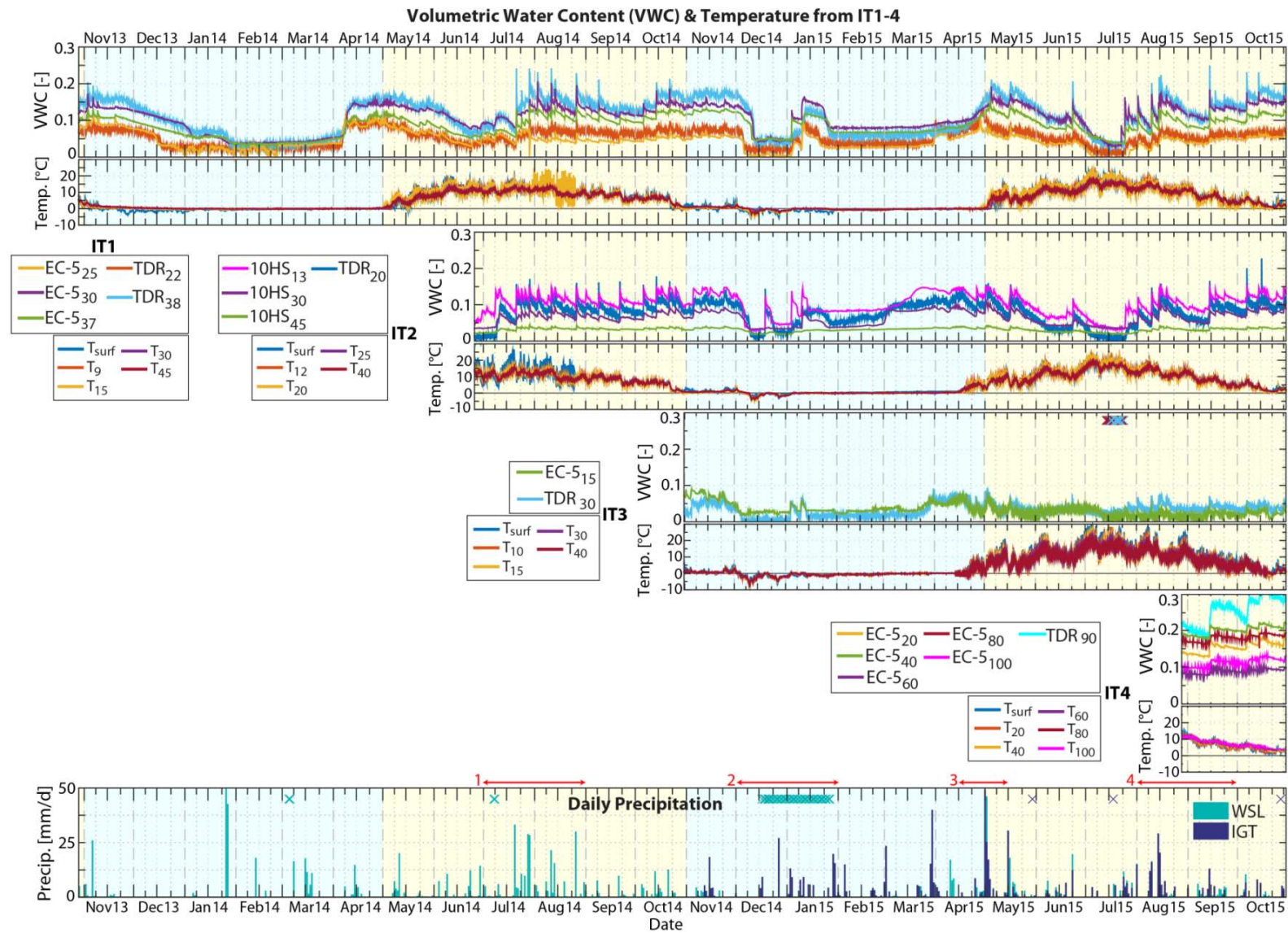


Figure 4.5. Overview of measurements at instrumented trenches. From top to bottom for each trench IT1-IT4: VWC, temperature; precipitation from WSL and IGT stations on the bottom.

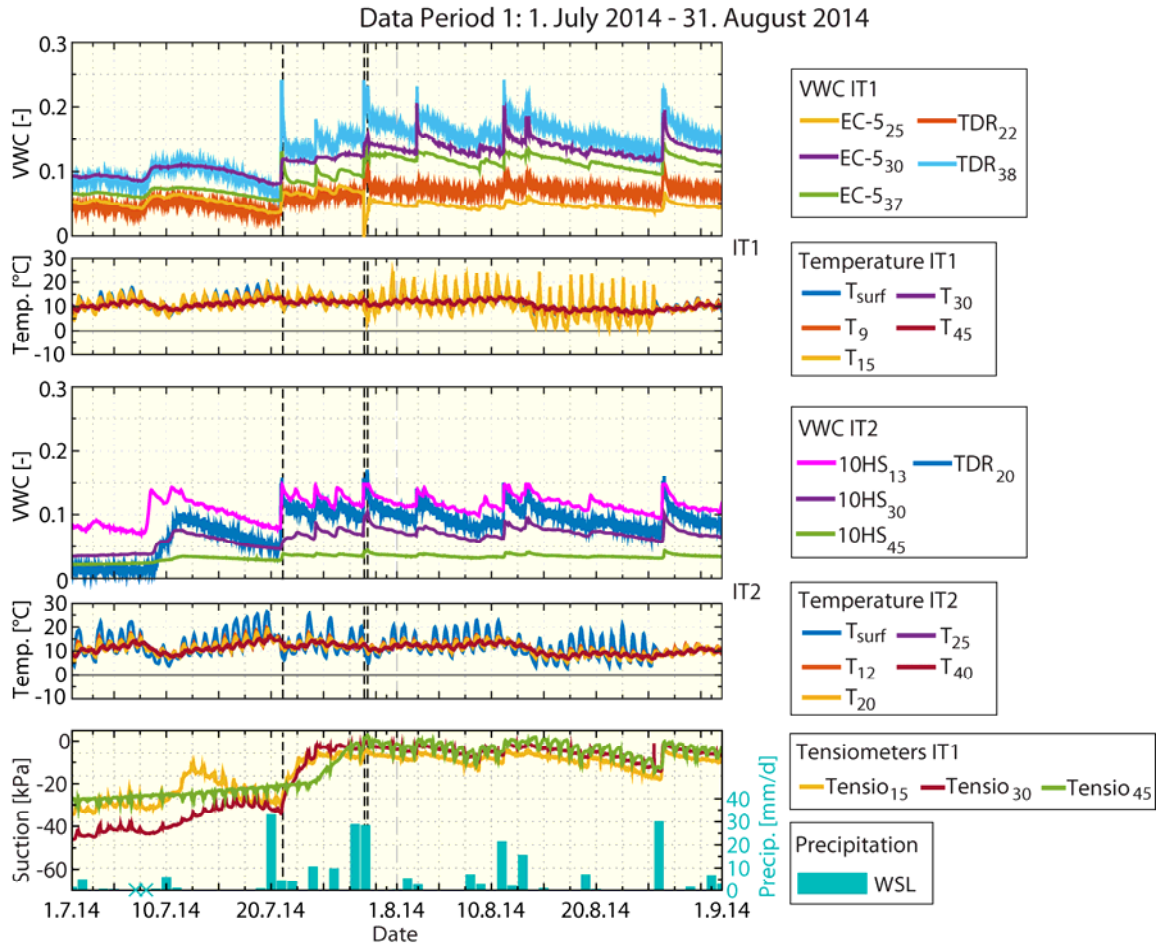


Figure 4.6. VWC, temperature and precipitation at IT1-IT2 and suction data at IT1 are displayed from 1st July 2014 to 31st August 2014. The debris flow events in the active channel (Figure 4.1) are marked with a dashed line each. The sub-index in the legend indicates the sensor depth in cm. Missing precipitation data are marked with a cross.

4.3.3 Tensiometers

The suction versus time was monitored at depth ranges equivalent to VWC measurements for IT1 and IT4 (Figures 4.11 and 4.12). The data are plotted to a monthly scale, separated by dashed lines, corresponding to the different periods. Missing or excluded data were marked by a continuous solid arrow at the top of each graph, using the colour trace for the malfunctioning sensor.

Figure 4.11 shows the suction measured in IT1 at 15, 30 and 45 cm depth, complemented by daily total precipitation in mm/day, plotted on a parallel y-axis and temperatures at different depths in a separate plot below. Periods run from the end of June to October 2014 and May to October 2015.

4. Study of the seasonal response of a scree slope and debris flow catchment in the Swiss Alps

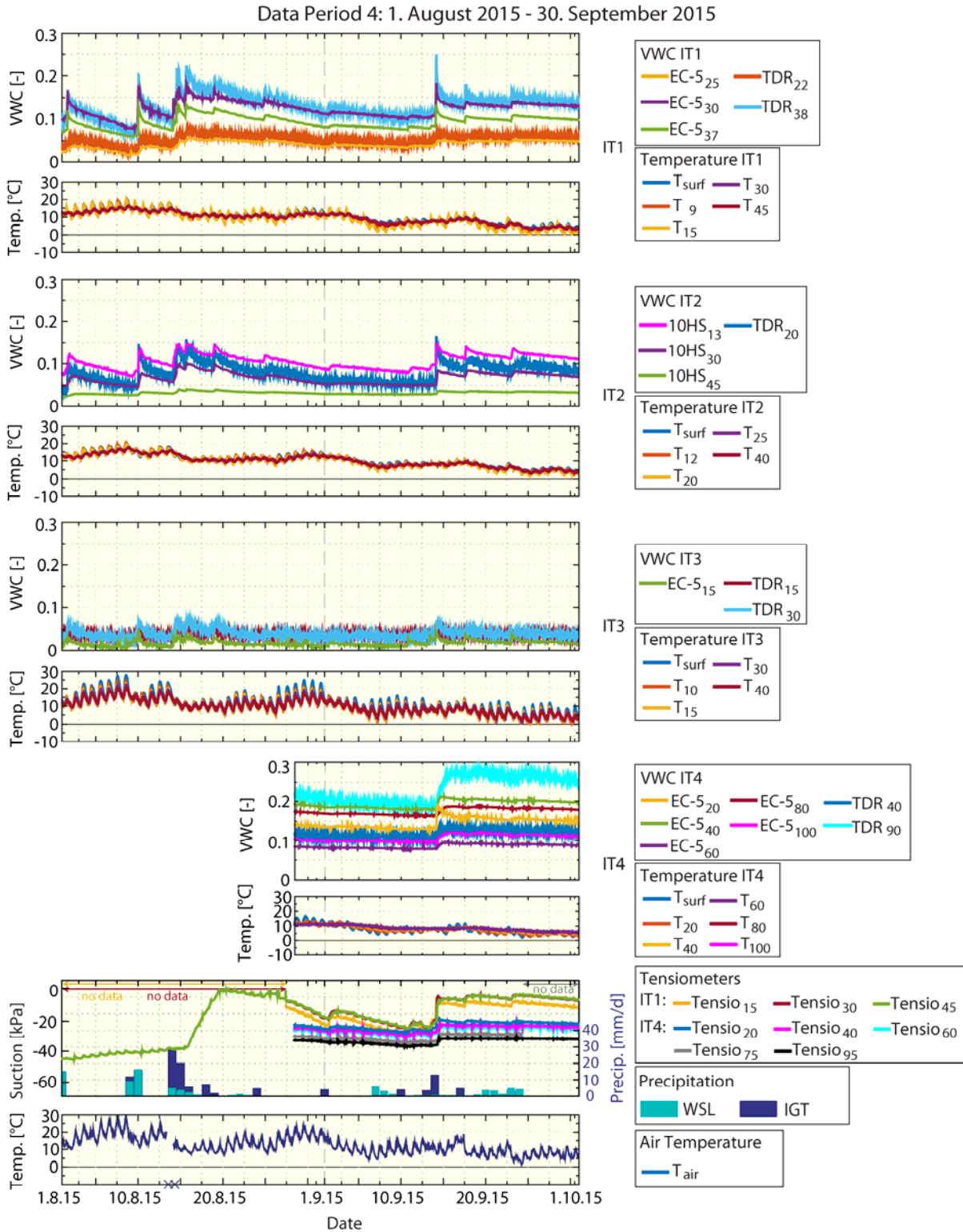


Figure 4.7. VWC, temperature and precipitation at IT1-IT4 and suction data from IT1 and IT4 are displayed from 1st August 2015 to 30th September 2015. In addition, the ambient air temperature recorded at the IGT weather station is shown on the bottom. The sub-index in the legend indicates the sensor depth in cm. Missing suction data are marked with an arrow in corresponding colour and missing air temperatures with crosses.

4. Study of the seasonal response of a scree slope and debris flow catchment in the Swiss Alps

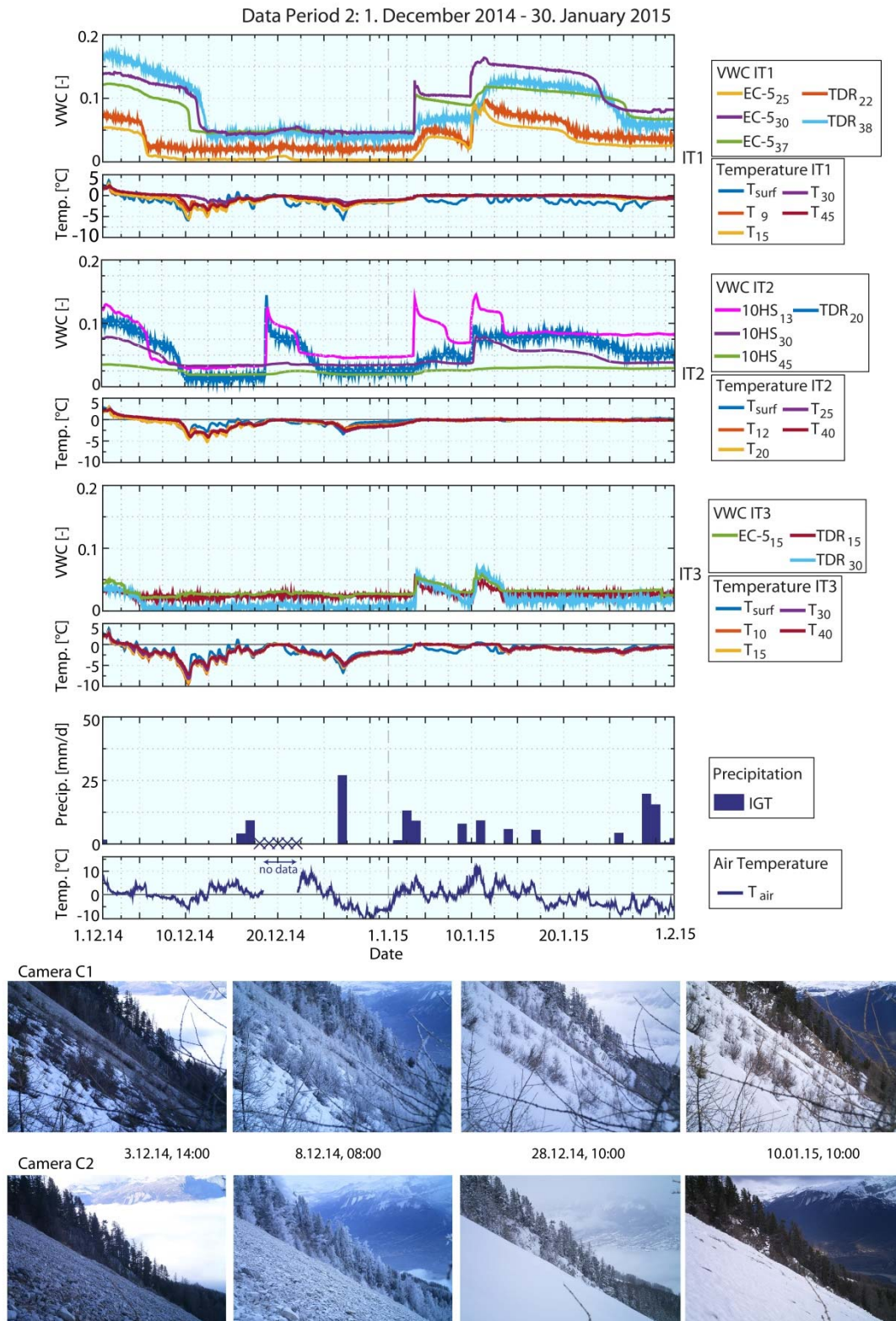


Figure 4.8. VWC, temperature and precipitation at IT1-IT3 from 1st December 2014 to 31st January 2015. The ambient air temperature recorded at the IGT weather station is shown below the other graphs. The sub-index in the legend indicates the sensor depth in cm. Missing data are marked with crosses. Photos from selected dates (cameras C1 and C2; Figure 4.1) are shown on the bottom.

4. Study of the seasonal response of a scree slope and debris flow catchment in the Swiss Alps

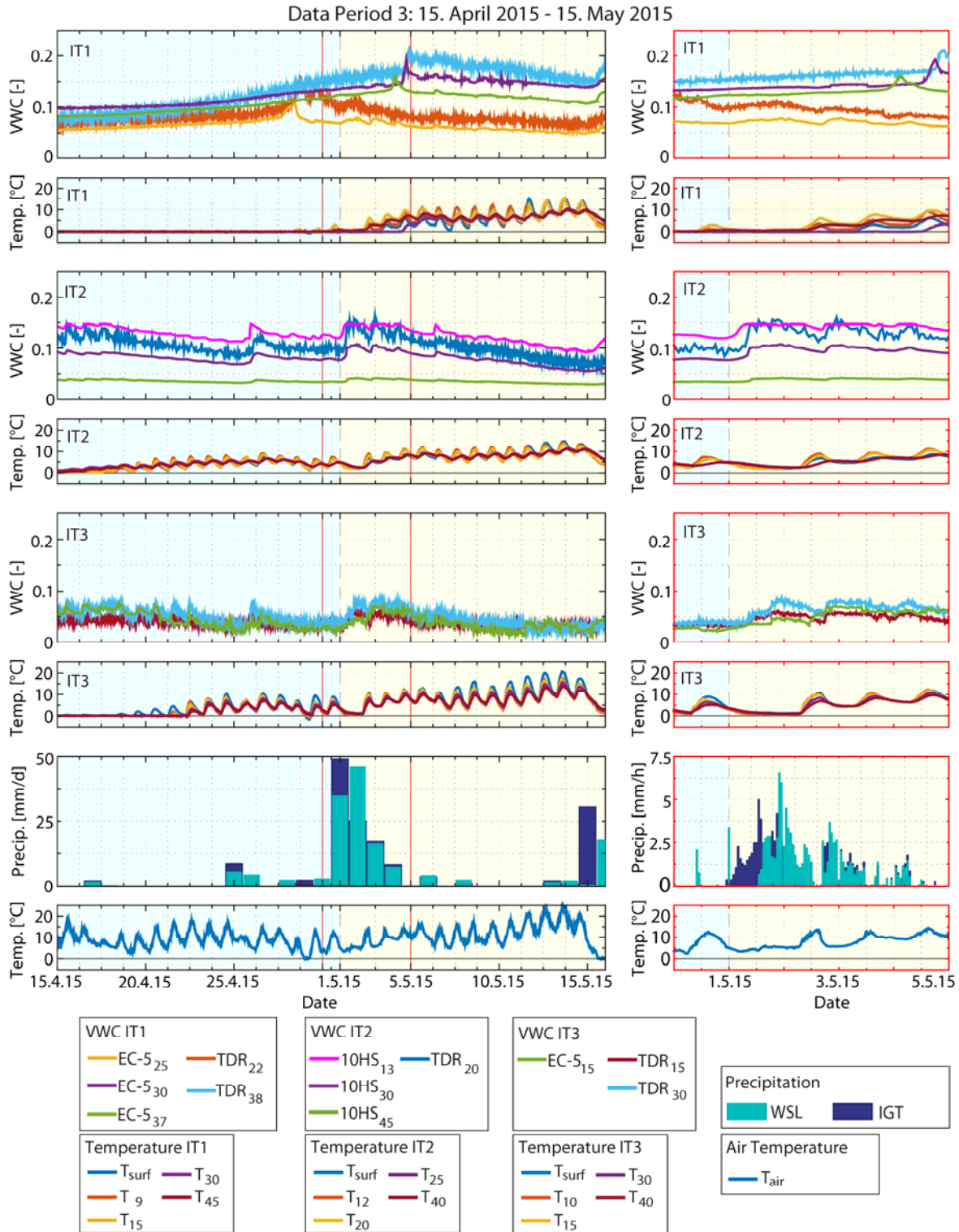


Figure 4.9. VWC, temperature and precipitation at IT1-IT3 from 15th April 2015 to 15th May 2015 on the left hand side and from 30th April 2015 to 5th May 2015 on the right hand side. The ambient air temperature recorded at the IGT weather station is shown on the bottom. The sub-index in the legend indicates the sensor depth in cm. Corresponding photographs is shown in Figure 4.10.

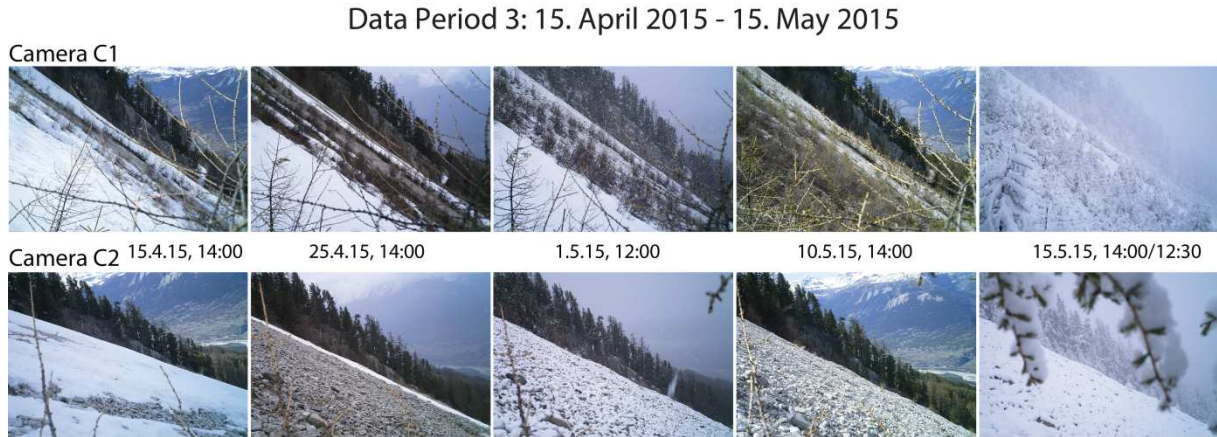


Figure 4.10. Photographs from cameras C1 and C2, illustrating the time series in Figure 4.9.

The three tensiometers at IT1 were installed in soil units, A, B, and C, (roots with gravel and fines, gravel with sand and fines, and coarser gravel respectively, GP-GM, section 4.2.1). Correlation between the loss in suction after rainfall events can clearly be observed, after all tensiometers show a significant increase in pore water pressure during periods of high precipitation in July 2014. In addition, shallower tensiometers react faster after a rainfall event than the deeper tensiometers, due to top-down infiltration.

The unsaturated hydraulic conductivity of the soil will decrease during July 2014 and 2015 (maximum annual temperatures) due to the higher suction level, resulting in a small variation of the suction, regardless of the rain events recorded. The soil only approaches saturation after a major rainfall event, leading to higher permeability and a more dynamic response to rain infiltration.

Figure 4.12 shows the suction measured in IT4 (GP-GM) at five depths (20-95 cm), complemented by daily total precipitation and temperatures. The period extends from the end of August to October 2015. Suctions increase with depth, indicating top-down infiltration through macro-voids after rain (September 15th), with gradual recovery of suction, which is surprising given the lenses of coarser gravel exposed in IT4 (Figure 4.2).

4.3.4 Temperature and VWC with depth

Figure 4.13 shows the temperature distribution with depth from 5th to 25th September 2015 for IT1-IT4, from top to bottom, respectively. The temperatures are indicated by colours (blue for colder, red for warmer), displayed in a colour bar on the right hand side.

4. Study of the seasonal response of a scree slope and debris flow catchment in the Swiss Alps

Dashed and solid (black and green) contour lines represent the boundaries at 10 °C, 5 °C and 2 °C respectively. Each depth label corresponds to a depth where sensors are located. The maximum plot depth represents the deepest sensor in each trench, ranging from 40 (IT2-IT3) to 100 cm (IT4). This 20-day autumn period (Figure 4.5) is characterised by a decreasing trend in temperatures, with fluctuations between 1 to 13 °C, while the volumetric water content responds dynamically to rain precipitation. Periods of warmer, colder and transition temperatures can be identified in the soil in IT1 (Figure 4.13), showing a significant response of the soil to variations in ambient air temperature, even though the general trend is decreasing.

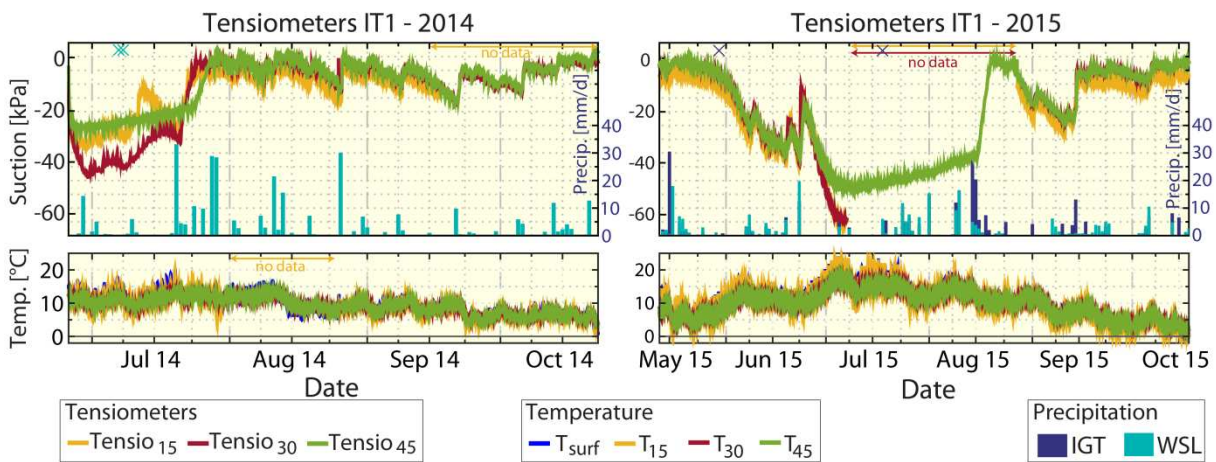


Figure 4.11. Tensiometer measurements at IT1, temperature and precipitation data for two summer seasons (25th June 2014 to 23rd October 2014 and 13th May 2015 to 18th October 2015).

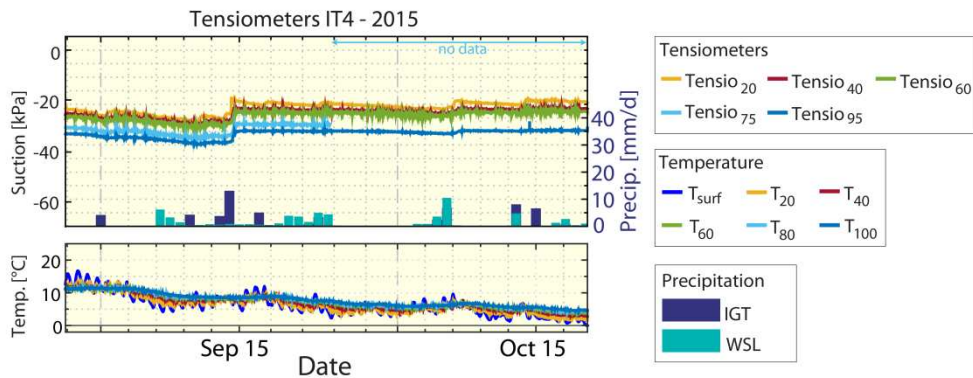


Figure 4.12. Tensiometer measurements at IT4: suction, precipitation and temperature data (28th August 2015 to 20th October 2015).

Reddish or blueish vertical ‘strips’ alternate daily. The response is more apparent at shallower depths (<20-25 cm) corresponding to GP-GM soils (Table 4.1), with nearby $e=0.52$ (D1, Table 4.2, Figure 4.1), the influence is less and temperatures lag behind in deeper, generally coarser, soil. The temperatures during warm and cold periods are

about 7-13°C and 1-5° C, respectively with transition zones of 3-7°C. The temperatures plotted as ground level (0 cm depth) correspond to a sensor installed in the data logger, situated on the surface a few meters from the trench and can be warmer than the temperatures measured in the soil particularly for the cold and transition times. The lowest daily temperatures over all trenches were recorded at 12 cm depth at IT1.

The soil temperatures are generally warmer in IT2 than IT1, because the soil is coarser (GW; Table 4.1), albeit with a similar $e=0.51$ (D3, Table 4.2, Figure 4.1). As in IT1, the influence of ambient air temperatures extends to the trench bottom, with greater variation in the top 25 cm. Periods of transition and cold are less evident due to greater thermal conductivity; this can be related to less vegetation and greater sun exposure than for IT1 (Figure 4.1), warmer periods are similar in both trenches. Ambient temperature variations in IT3 affect all depths at the same time. Heat is transferred into the soil more immediately and uniformly than for other trenches, due to coarser (GW, Table 4.1) more permeable soil (Figure 4.2c), and higher $e=0.66$ (D4, Table 4.2). Greater sun exposure (Figure 4.1) with generally lower values of VWC (Figure 4.5), contribute to these greater daily variations in soil temperature, with temperatures of 12°C and significant drops to 2°C over 24 hours (Figure 4.13, 7-9th September).

Poorly graded gravel (GP-GM) in IT4, with a similar content of fines to IT1 (Table 4.1), less vegetation and $e=0.58$ measured nearby (D2, Table 4.2), could explain the higher temperatures during cold and transition periods than IT1 at similar depths. Soil temperatures exhibit daily variations until depths of 40 cm, whereas sensors below this depth are less influenced, they exhibit a gradual transition to a colder season instead, with particularly cold trends noticeable between 5-13th and 18-23rd, starting at depths of 10 cm to the trench bottom (Figure 4.13).

Figure 4.14 shows the VWC distribution with depth for the same time period as for Figure 4.13, for IT1-IT4 from top to bottom, respectively. Colours ranging from yellow to blue (colour bar on the right hand side) represent increasing VWC. Each depth label corresponds to the depth where sensors are located. Maximum depths vary from 30 (IT3) to 100 cm (IT4) and the plots are scaled accordingly.

This VWC representation enhances the understanding of water infiltration into the soil. Precipitation events are clearly observable as ‘wet fronts’ in each of the trenches (e.g. on 14th September 2015). IT1 shows lower VWCs (0.05) over the top 28 cm and higher VWCs (0.1-0.2) below, during all periods of observation, with an increase during the rain

event (14th September) to 0.015, when four hours of rain intensity (1-5 mm/h) occurred. Since there is no visible sign of water infiltration and pore water pressure dissipation into the shallow depths, it is possible that lateral flow occurred in the scree slope through the coarser soil layer.

In all other trenches, water infiltrates during significant rainfall events, increasing the VWC to different degrees and depths. Drainage occurred from the top 30 cm in IT2 into the coarser underlying gravel. The narrowest range and lowest VWCs are exhibited in IT3, due to fast infiltration and dissipation of pore water pressure from the much coarser material, with exponentially decaying trends after each rain event (14th, 17th and 23rd September).

Higher VWCs and drainage at 60 cm depth into a coarser gravel layer typify data from IT4, located nearby IT1 (Figure 4.1). While a significant increase in saturation was observed in a 10 cm thick layer (depths of 0.9-1 m) after 15th September, and maintained for at least 10 days until the end of the period (25th September), the tensiometers above and below this layer (Tensio75, Tensio95; Figure 4.12) maintained suctions of between 30-40 kPa. This can be interpreted as pore water pressure build-up in a potential failure surface.

4.3.5 Sensor comparison: TDR vs. capacitance sensors

Figure 4.15 show the comparison between TDRs and capacitance sensors (EC-5, 10HS) at similar depths is shown, and complemented by measurements of temperature, suction, precipitation, soil and ambient air temperature. All VWC sensors consistently measure within a range of 0 to 0.3, which is expected, considering the given range of porosity (Section 4.2.2 and 4.2.6). Resulting time series from capacitance sensors and TDRs generally exhibit a similar dynamic response in VWC to rain infiltration.

Sensors at similar depths in the same trench, or similar depths in different locations, agree in terms of peak occurrence, but not in magnitude of variation, nor in increase and decay patterns.

Comparing sensors TDR₃₈ and EC-5₃₇ in IT1, the response on 14th September is immediate in both cases with a significant, sharp peak, and drainage in the coarser gravel represented by concave decay pattern due to high hydraulic conductivity. However, the magnitude of variation in VWC for the TDR is greater than for the EC-5. This can be attributed mostly to the heterogeneity of the soil, the volume of sensitivity,

because the EC-5 averages the VWC over a larger volume than the TDR and possibly to the dependency of the EC-5 sensors on temperature (section 4.2.4.1.2).

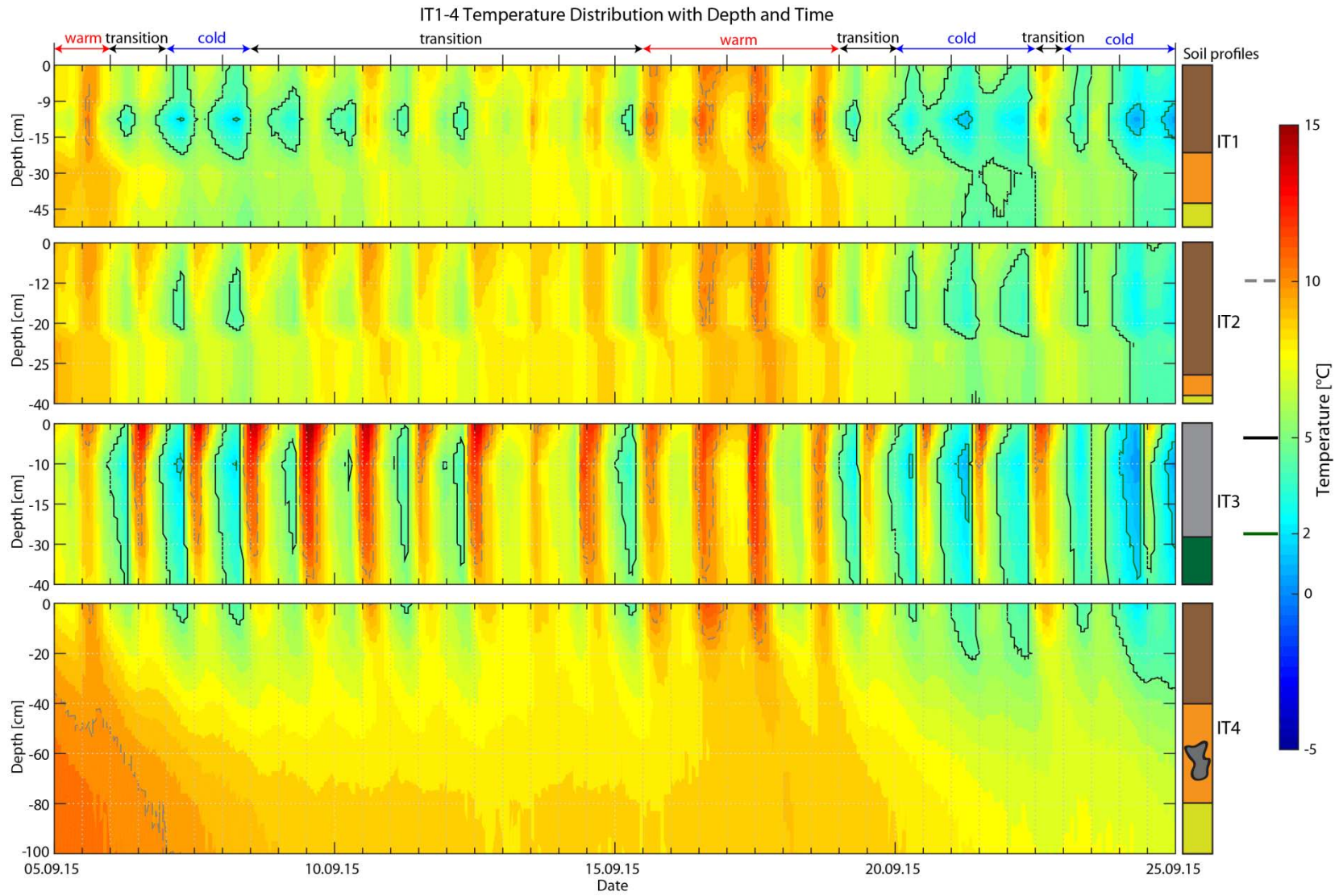
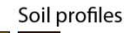


Figure 4.13. Temperature distribution with depth in September 2015. IT1-IT4 are shown from top to bottom with sensor depths labelled for each trench. Contour lines are drawn at 10 °C, 5 °C and 2 °C.



103

Even though, the daily temperature variation recorded at IT1 in T_{30} and T_{45} on 14th is actually smaller than in IT3 and other sensors in IT1 at shallower depths, the trend in temperatures vary between 4-8°C during these two weeks. For the same sensors, when compare at the rain events on 17th and 23rd, the difference in variation of magnitude of VWC is less, but different patterns of decay in VWC changes after rainfall. Sharp peaks develop with a concave decay profile (IT1, TDR₃₈) in contrast to softer shape peaks and convex decays (IT1, EC-5₃₇), that can be explained by the soil heterogeneity or a larger volume of sensitivity for the capacitance sensors. Two other sensors TDR₂₂ and EC-5₂₅ in IT1 at similar depth, show similar values of VWC and variations in VWC after a rain event, with slightly higher VWC recorded at TDR than EC-5, by the reasons explained before.

Capacitance sensors 10HS₁₃ and 10HS₃₀ and TDR₂₀ in IT2, located at different depths were compared as a reference. The sensors have similar time of reaction, with a slight lag from 10HS₃₀ on the 14th September (also observed for deeper sensors in other trenches), due to the initial smaller rain intensity (mm/h) (Figure 4.15) that probably infiltrated only to shallower depths. 10HS₃₀ and TDR₂₀ registered similar VWCs before the rain, with greater magnitude response for TDR₂₀, which remains at a higher VWC after that. Sensors installed nearby at the same reference depth (Figure 4.1) 10HS₃₀ (IT2) and TDR₃₀ (IT3) were also compared. Both sensors indicate similarly low VWCs (GW, Table 4.1), and VWC in TDR₃₀ (IT3, $e=0.66$) is lower than 10HS₃₀ (IT2, $e=0.51$) as would be expected. Mittelbach et al. (2011) also compared TDR and 10HS in clayey loam, and have preferred 10HS in medium to low VWC using site-specific calibration, because of the greater sensitivity and accuracy in this specific range.

Finally, corrections for temperature effects could be applied to account for some of the differences, whereas the remaining discrepancies can be due to laboratory calibration, imperfect installation, varying volumes of influence as well as the heterogeneity of the gravelly soil.

4.3.6 Electrical Resistivity Tomography (ERT)

The resulting geoelectrical tomograms in Figure 4.16a-c show the subsurface resistivities obtained from inversion of the ERT data acquired on 15th May, 16th June and 25th July, 2014. All models depict a two-layered subsurface: an upper, relatively low resistive layer, which can be attributed to the unsaturated gravelly soil and a highly resistive layer underneath, which is assumed to represent the quartzite bedrock.

The precipitation data before each of the acquisitions show that the conditions were relatively dry and undergoing a drainage phase for the first two campaigns, whereas the data acquired in July was recorded within a period of heavy rainfalls.

These seasonal variations are mostly reflected in resistivity changes within the soil layer, in particular as a significant reduction of resistivities in the July model. The saturation relative to the subsurface model obtained in May (Figure 4.16d-e) clearly reflects these conditions; there is a slight net near-surface decrease in saturation in June, whereas an increase in saturation is observed within the soil layer in July. This trend in near-surface soil saturation corresponds very well to the volumetric water content measurements (which are directly proportional to saturation; (Equation 4.1) from TDR and dielectric permittivity sensors installed at shallow depths within IT1.

Numeric VWC values calculated from resistivity measurements using Archie's law (Equation 4.1) are presented in Table 4.4. It should be noted, that values for VWC_{ERT} were calculated using different cementation factors m and coefficient of saturation n . For all calculations, the resulting VWC_{ERT} agree very well with the saturation trend and the magnitude measured by either type of moisture sensor: higher VWC values in May, lower values (relative decrease in saturation of the gravelly soil) during the dry period in June to higher values again during the period of heavy rainfalls (relative increase in the saturation of the soil) in July 2014. However, the VWC_{ERT} were systematically overestimated when using literature values for m and n . Determining m and n by matching the VWCs from the first acquisition (15th May 2014) and using them in subsequent calculations, a very good fit of the VWC_{ERT} to the VWC_{TDR} and the VWC_{Dec} was found for all of the acquisition dates.

Two pairs of m and n achieved this fit very well but even though estimation without soil specific laboratory measurements is difficult, $m = 1.5$ and $n = 1.3$ was discarded, because an increase in the cementation factor (from the literature value of 1.3 estimated for loose materials) would mean an increase in cementation, which is certainly not the case in this gravelly scree. Hence, the VWC_{ERT} are indicated as vertical error bars in Figure 4.16f, using the VWC_{ERT} calculated with $m = 1.05$ and $n = 1.75$. The resulting VWC_{ERT} fit best with the VWCs from the dielectric permittivity sensor at 37 cm and the TDR at 38 cm depth. The remaining differences (to other sensors) were most likely due to the following factors:

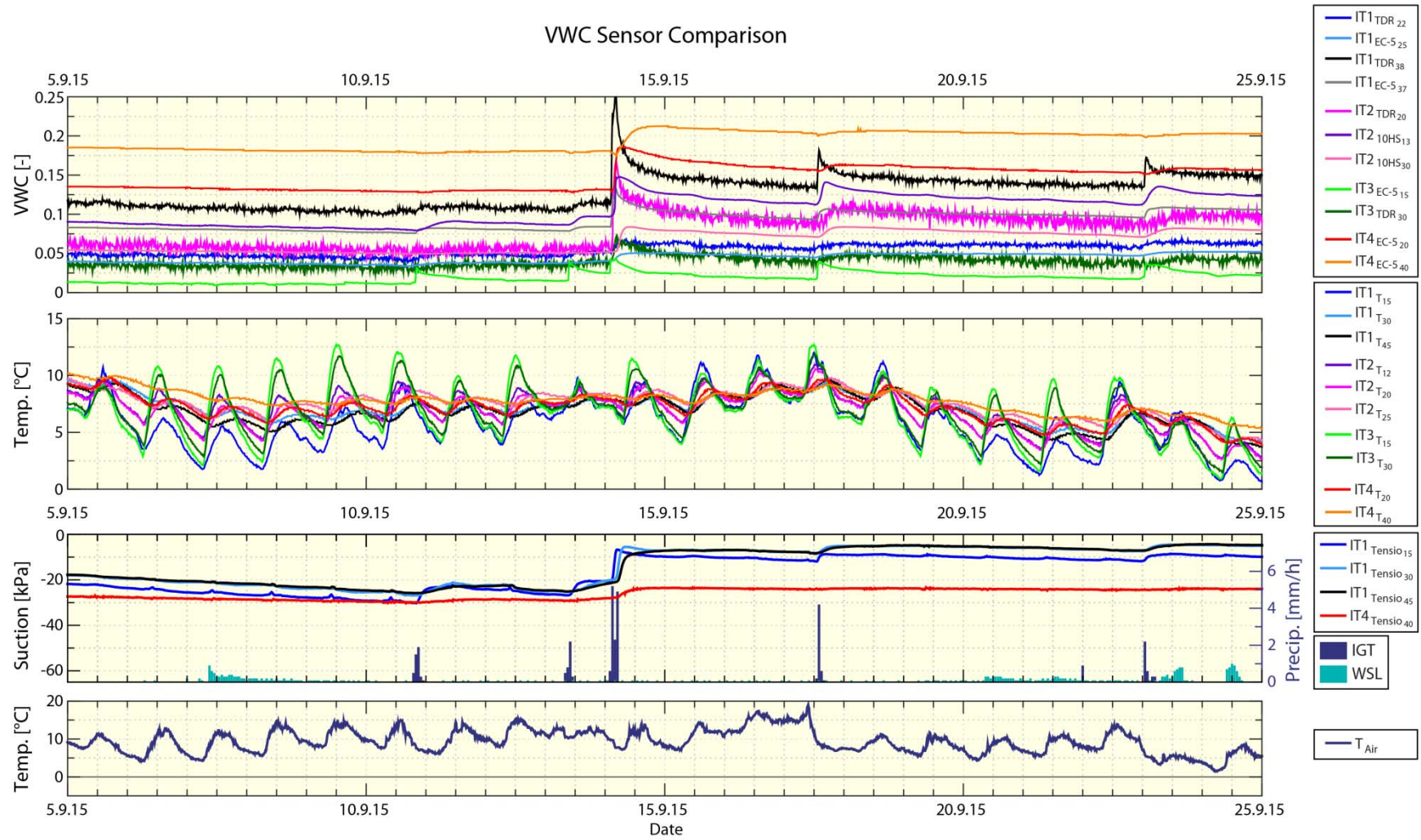


Figure 4.15. Comparison between TDRs and dielectric permittivity sensors for IT1-IT4 at similar depths. From top to bottom: VWC, temperatures, suction and precipitation, and ambient air temperature in a period from 5th – 25th September 2015.

- both methodologies of ‘measuring’ the VWC are indirect;
- tomograms consist of model cells larger than the cylinders of influence of individual moisture sensors in IT1 and hence an average (spatial) resistivity of surrounding cells was calculated for the comparison. In addition, the VWCs from TDR and dielectric permittivity sensors (Table 4.4) are also (temporal) averages, calculated over the duration of the ERT acquisition;
- parameters used in Archie’s law, such as the resistivity of the pore water and the porosity, were only inferred from preliminary measurements.
- the ERT profile 1 is representative of the specific area of measurement in IT1, but the heterogeneity of the soil has to be taken into account, when comparing recorded VWCs, because of the slight difference in location (Figure 4.1).

4.3.7 Slope characteristics

4.3.7.1 Sections of the slope

The variation of VWC by type of moisture sensor versus time and depth, within all of the trenches IT1-IT4, is shown in Figures 4.5, 4.14 and 4.15. The range of VWC recorded at IT2 and IT3, compared to IT1 and IT4, is remarkably narrow for the dielectric permittivity sensors as well as the TDR measurements. These differences in the range of VWC, in addition to the VWC and temperature trends observed, support splitting the slope into up- and down-slope sections, with the following characteristics:

4.3.7.1.1 Upper scree slope (upslope)

Volumetric water content:

- low range of VWC (e.g. IT2/IT3), Figure 4.5;
- Faster infiltration and drainage of water due to predominance of coarser soil with less fines. (e.g. IT3), Section 4.3.4, Figure 4.14;

Temperature:

- temperatures can rise earlier (by up to half a month) than in downslope locations, due to greater sun exposure, Figure 4.5;
- daily variations are higher and more pronounced for all sensor depths (e.g. IT3), section 4.3.4, Figure 4.13;
- extreme maximum values during winter and summer respectively (IT3) due to a coarser soil with higher permeability, Figure 4.5;

- earlier snow-melt caused by greater sun exposure (IT2/IT3).

4.3.7.1.2 Lower scree slope (downslope)

Volumetric water content:

- higher range of VWC (e.g. IT1/IT4), Figure 4.5, 4.14;
- VWC can rise due to infiltration and possible lateral flow of water downslope (IT1/IT4) section 4.3.4, Figure 4.14;

Temperature:

- more insulation and less sun exposure due to patches of vegetation, Figures 4.1, 4.5;
- daily variations influenced by ambient air temperature are greater than upslope in the first 20-30cm and less pronounced for deeper sensors (e.g. IT1/IT4), section 4.3.4, Figure 4.13.

Table 4.4. Comparison of VWCs from ERT to VWCs from TDRs and capacitance sensors (Dec) in IT1. “No.” refers to the number of readings taken by the moisture sensors during the recording of the ERT, as VWC_{TDR} and VWC_{Dec} are averaged over all measurements. ρ is the electrical resistivity measured by ERT.

Date	No.	Temperature [°C]	VWC_{TDR} [-]	VWC_{Dec} [-]	ρ_{ERT} [Ωm]	VWC_{ERT} [-]* m = 1.3; n = 2	VWC_{ERT} [-], m = 1.05; n = 1.75	VWC_{ERT} [-], m = 1.5; n = 1.3
15.5.2014	3	4.8	0.11	0.11	7217.9	0.14 \pm 0.01	0.11 \pm 0.01	0.11 \pm 0.01
16.6.2014	4	11.7	0.06	0.07	9003.4	0.11 \pm 0.01	0.08 \pm 0.01	0.07 \pm 0.01
25.7.2014	4	12.1	0.1	0.1	5363.7	0.14 \pm 0.02	0.10 \pm 0.01	0.10 \pm 0.01

* m and n taken from literature (e.g. Archie, 1942; Lowrie, 2007; Schön, 1983).

** m and n calibrated using the first measurement (15th May 2014), then used in subsequent calculations of VWC_{ERT} .

4. Study of the seasonal response of a scree slope and debris flow catchment in the Swiss Alps

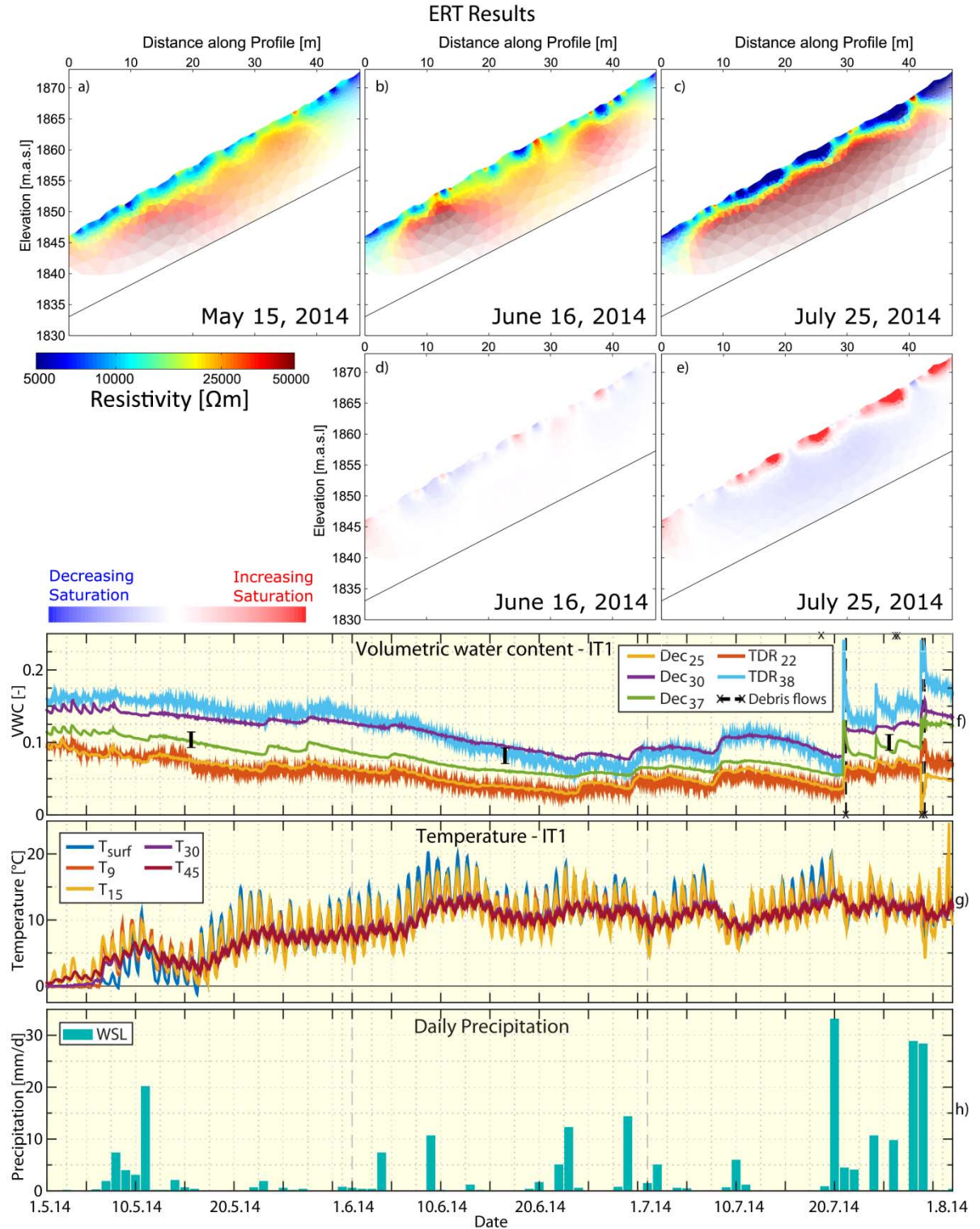


Figure 4.16. a-c: Geoelectrical tomograms from 15th May, 16th June and 25th July, 2014. The resistivity scale beneath the tomograms is the same for every acquisition. d-e: increasing and decreasing saturation, relative to the subsurface model obtained on 15th May (see Equation S4.A1 in supplementary material A for further information). Finally, the three acquisition dates are indicated as vertical error bars within the volumetric water content measurements from TDR and capacitance sensor instrumentation in IT1 (f), which is shown from 1st May to 1st August, 2014. The temperature (g) and the precipitation (h; in mm per day) are shown in the lower two time series plots.

4.3.7.2 Ground model

The ground model in Figure 4.17 (with parameters in Table 4.5) was derived from the ERT tomograms (hence showing only the lower part of the scree slope). The boundary between the upper soil layer and the highly resistive bedrock underneath can be seen on each of the recorded tomograms (Figure 4.16), however, it is clearest in the results obtained from the recordings on 25th July 2014. This measurement took place at the end of a rainy period and therefore current injected into the ground could penetrate more effectively and deeper into the saturated (more conductive) ground. Hence, the solid black line could be drawn in the ground model to divide the two layers.

All ERT surveys, but in particular those that were carried out during dry periods (e.g. 16th June, 2014), reveal (local) areas of high resistivity near the surface. Most of these were not consistently observed at the same spots along the profile, were limited in size and could be explained by the difficult ground coupling of an electrode in a dry and highly resistive soil in the respective area. A few of these “patches” were more extensive than others, and could be interpreted to extend down to the bedrock (marked with dashed, light grey lines in the ground model). These were particularly visible on the tomogram from 25th July. However, field observations, as well as GPR measurements on the lower part of the slope, indicate that it is rather unlikely that the bedrock rises to the surface. Furthermore, geological observations favour a series of “steps” at the soil-bedrock interface below ground, as nearby bedrock outcrops above ground exhibit rock layers inclined southward (into the slope) with 10-30° (see also Gabus et al., 2008a; 2008b). Assumed bedrock layers are therefore indicated in the ground model with dashed grey lines.

The highly resistive patches on the upper part of the profile, where there is less vegetation (mostly small trees, bushes and shrubs), are explicable by large boulders (estimated up to 0.5 m in diameter), which have been deposited on the surface and which also made electrode insertion difficult. Such boulders are not connected to the bedrock, but might produce a more extensive area of high resistivity. In addition, lenses consisting of larger cobbles and even boulders have been discovered within finer gravelly soil, e.g. during the excavation of IT4 (Figure 4.2). Such lenses could also be attributed to highly resistive areas.

Due to the shallow depth of the bedrock (1-3 m), it is very difficult to determine resistivity changes within the soil layer. Subtle differences in grain size distributions

4. Study of the seasonal response of a scree slope and debris flow catchment in the Swiss Alps

were seen from trench and soil excavations (Figures 4.2 and 4.3). Although these volumes are too small to be detected by ERT measurements (with an electrode spacing of 1 m), the soil is therefore depicted in the ground model as a uniform layer of gravel with sand and silt. However, a schematic description of the soil profiles in the trenches has been integrated as well, even though only IT1 is located along the ERT profile used for the ground model.

A friction angle of 41° was obtained using a constant shear drained triaxial stress path tests (CSD). A series of CSD triaxial tests were carried out in a medium (150 mm diameter) and large (250 mm diameter) scale apparatus using reconstituted specimens (for further information, see Grob, 2015).

Table 4.5. Geotechnical soil parameters used in the ground model.

Section	Classification (SN 670 004-2b NA)	Percentage of fines [%]	Friction angle critical state ϕ' [°]	Cohesion [kN/m ²]	G_s [-]
Downslope	GP-GM	5-10	41	0	2.68
Upslope	GW-GM	0-5	41	0	2.68

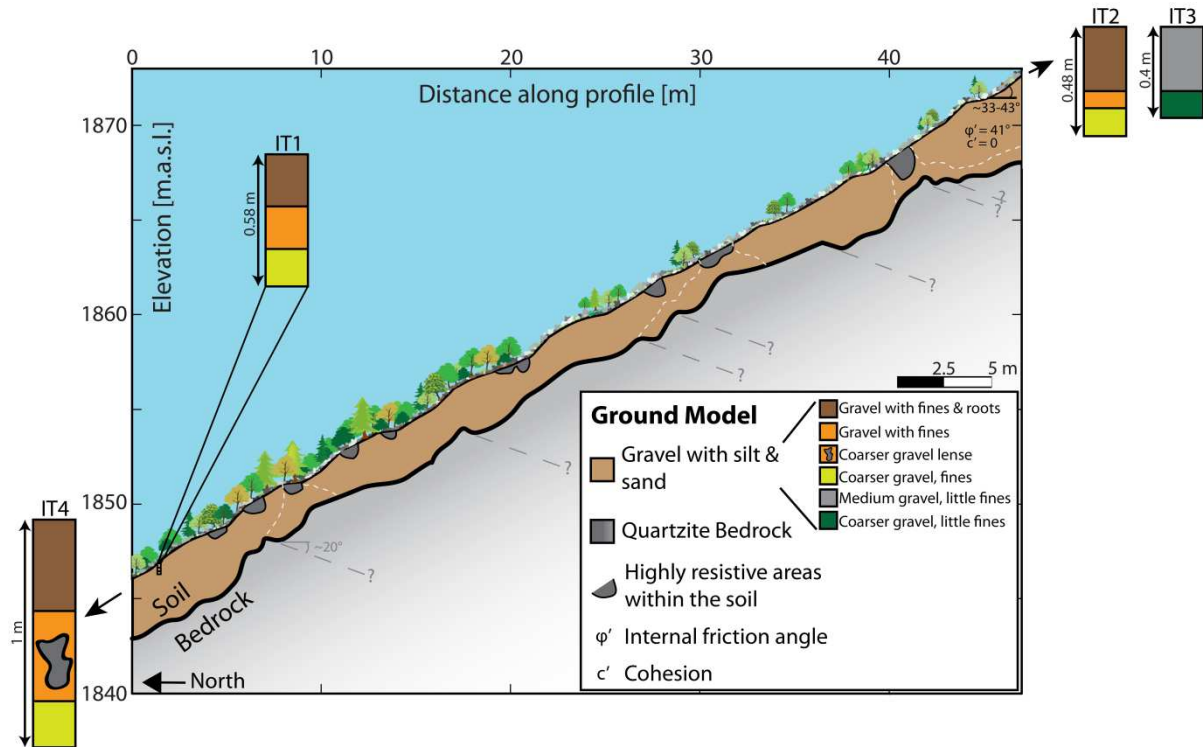


Figure 4.17. Ground model derived from ERT measurements on profile 1. A visual description of the soil observed in IT1-IT4 is included, as well as some of the most important parameters, such as the friction angle.

4.4 Conclusions

Combining geotechnical and geophysical techniques has led to greater insight about the characteristics of a steep alpine scree slope. A ground model that estimates soil thickness and depth to bedrock, strength parameters, and soil classification, can be used in a posterior analysis of slope response to environmental perturbations through physical and/or numerical modelling. Furthermore, natural hazards can be assessed more effectively to provide input to needs for early warning systems and any mitigation measures.

Long-term monitoring and extensive characterisation using instrumented trenches, geophysical surveys, meteorological data and photographic observation of the slope surface yielded complementary and therefore well integrable results and gave useful indications of processes that could cause three prevalent types of downslope movement and changed perceptions of the most likely events.

Initially, it had been hypothesised that the most likely failure mechanism would be through shallow landslides, triggered by rainfall infiltration and lateral flow in a saturating soil that is heterogeneous in terms of porosity and grading. Given that the slope angle was between $33\text{-}43^\circ$ and the friction angle is 41° , there remains some potential for small slips to occur if pore water pressures become positive over a significant layer that runs more or less parallel to the surface (as observed in 1 m depth in one of the trenches). However, the greatest number of downslope movements arise either from boulders falling and toppling downslope, being deposited temporarily in metastable positions, and remobilised either by repeated cycles of freezing and thawing, and snow-melting processes in winter or eroded by rainfall and runoff during the rest of the year.

Seasonal, daily and event driven patterns in changes of VWC, temperature and suction could be identified during the two years of monitoring and there is an agreement in trends of the VWC between dielectric permittivity sensors EC-5, 10HS and TDR in their response to rain infiltration, freezing and thawing processes. Correction factors could be applied in future for capacitance sensors (EC-5, 10HS) to allow for phase change between water and ice. Remaining differences in VWC from neighbouring devices, or similar depths, can be attributed to different installation locations and soil heterogeneity.

VWCs obtained from instrumentation were compared to values independently calculated from ERT measurements, conducted on different dates from May-July 2014. It was found that even though seasonal saturation trends agreed, VWC values were systematically overestimated by ERT, when using literature values for two parameters in Archie's law. A better fit was obtained, when these parameters were calibrated by matching one of the ERT acquisitions to the local trench measurements recorded at the same time. Hence, the agreement of VWCs from both types of measurements led to the conclusion that ERT indeed provides a convenient and fast way to infer VWC values over a larger area (spatial resolution), but has to be carefully calibrated using local VWC measurements, which in turn have the advantageous ability to more frequently record data (temporal resolution). "Small scale" trench instrumentation and "larger scale" ERT surveys complement each other very well and therefore, when combined and calibrated properly, can substantially enhance the characterization and monitoring of (steep) alpine scree slopes.

4.5 Acknowledgements

The authors are most grateful for funding from the SNF Project No. 200021_144326/1 and Canton Valais, together with the Councils of Agarn and Leuk. The project also contributes to the TRAMM2 programme of the Competence Centre of Environmental Sustainability. Furthermore, we wish to acknowledge, in particular, the support from Pascal Stoebener (WSL), Brian McArdell (WSL), Prof. Dr. Hansruedi Maurer (Exploration and Environmental Geophysics, EGG), Dr. Andrew Kos, Dipl. Ing. Ralf Herzog, Ernst Bleiker, Thomas Buchli, Reto Grob and Nicole Oggier. We would also like to thank Peter Molnar for providing us with insights regarding the recorded data series of rainfall. For the help with sensor-related problems, we would like to thank many employees of Decagon Devices.

4.6 References

- Archie, G. E. (1942). The electrical resistivity log as an aid in determining some reservoir characteristics. *Transactions of the AIME*, 146(01), 54-62.
- Bayard, D., Stähli, M., Parraiaux, A., & Flühler, H. (2004). The influence of seasonally frozen soil on the snowmelt runoff at two alpine sites in southern Switzerland. *Journal of Hydrology*, 309 (1), 66-84.
- Beck, A. (2010). Measurement of unsaturated hydraulic conductivity with the instantaneous profile method. Semester project ETH, Zurich, Switzerland.
- Bichler, A., Bobrowsky, P., Best, M., Douma, M., Hunter, J., Calvert, T., & Burns, R. (2004). Three-dimensional mapping of a landslide using a multi-geophysical approach: the Quesnel Forks landslide. *Landslides*, 1(1), 29-40.
- Bogena, H.R., Huisman, J.A., Oberdörster, C., & Vereecken H. (2007). Evaluation of a low-cost soil water content sensor for wireless network application. *Journal of Hydrology*, 344(1), 32-42.
- Bogoslovsky, V.A., & Ogilvy, A.A. (1977). Geophysical methods for the investigation of landslides. *Geophysics*, 42(3), 562-571.
- Brunet, P., Clément, R., & Bouvier, C. (2010). Monitoring soil water content and deficit using Electrical Resistivity Tomography (ERT) – a case study in the Cevennes area France. *Journal of Hydrology*, 380(1), 146-153.
- Fankhauser, K., 2014. Geophysical slope characterization using GPR and ERT in an active debris flow catchment. *Master Thesis*, EEG, ETH Zurich.
- Friedel, S., Thielen, A., & Springman, S. M. (2006). Investigation of a slope endangered by rainfall-induced landslides using 3D resistivity tomography and geotechnical testing. *Journal of Applied Geophysics*, 60(2), 100-114.
- Gabus, J. H., Weidmann, M., Burri, M., & Sartori M. (2008a). Feuille 1287 Sierre, *Atlas Géologique de la Suisse 1:25'000, Carte 111*, swisstopo, Wabern.
- Gabus, J. H., Weidmann, M., Burri, M., & Sartori M. (2008b). Feuille 1287 Sierre, *Atlas Géologique de la Suisse 1:25'000, Note explicative*, swisstopo, Wabern.
- Grob, R. (2015). Measurement of soil properties for gravels in a scree slope using large

scale triaxial testing. *Master Thesis*, IGT, ETH Zurich.

Günther, T. (2011). Timelapse ERT inversion approaches and their applications. *Geoelectric Monitoring*, 91-97.

Günther, T., & Rücker, C. (2013). Boundless electrical resistivity tomography - the user tutorial. Available at: www.resistivity.net.

Günther, T., Rücker, C., & Spitzer, K. (2006). Three-dimensional modelling and inversion of DC resistivity data incorporating topography - II. Inversion. *Geophysical Journal International*, 166(2), 506-517.

Hack, R. (2000). Geophysics for slope instability. *Surveys in Geophysics*, 21(4), 423-448.

Hayashi, M. (2004). Temperature-electrical conductivity relation of water for environmental monitoring and geophysical data inversion. *Environmental monitoring and assessment*, 96 (1-3), 119-128.

Lehmann, P., Gambazzi, F., Suski, B., Baron, L., Askarinejad, A., Springman, S. M., & Or D. (2013). Evolution of soil wetting patterns preceding a hydrologically induced landslide inferred from electrical resistivity survey and point measurements of volumetric water content and pore water pressure. *Water Resources Research*, 49(12), 7992-8004.

Lowrie, W. (2007). *Fundamentals of Geophysics*. Cambridge University Press.

Lucas, D. R., Askarinejad, A., Herzog, R., Bleiker, E., & Springman, S. M. (2015). Volumetric water content determination by TDR sensors and decagons in gravelly soils. In *XVI European Conference on Soil Mechanics and Geotechnical Engineering (XVI ECSMGE 2015)*, Edinburgh, UK, 13.-17.9.2015, 3565-3570. doi: 10.1680/ecsmge.60678.vol6.560

Matsuoka, N. (1998). The relationship between frost heave and downslope soil movement: field measurements in the Japanese Alps. *Permafrost and Periglacial Processes*, 9(2), 121-133.

Miller, R. D. (1973). Soil freezing in relation to pore water pressure and temperature. 1. In *International Conference on Permafrost, 2d, Yakutsk, Siberia, 1973. Papers*.

- Mittelbach, H., Casini, F., Lehner, I., Teuling, A. J., & Seneviratne, S. I. (2011). Soil moisture monitoring for climate research: Evaluation of a low-cost sensor in the framework of the Swiss Soil Moisture Experiment (SwissSMEX) campaign. *Journal of Geophysical Research: Atmospheres*, 116(D5).
- O'Connor, K. M., & Dowding, C. H. (1999). *Geomeasurements by pulsing TDR cables and probes*. CRC Press.
- Oggier, N. C. (2011). Simulierung von Murgängen mit RAMMS am Beispiel des Meretschibachs. *Master Thesis*, ETH Zürich und Forschungsanstalt für Wald Schnee und Landschaft (WSL).
- Otto, J.C., & Sass, O. (2006). Comparing geophysical methods for talus slope investigations in the Turtmann valley (Swiss Alps). *Geomorphology*, 76(3), 257-272.
- Patterson, D. E., & Smith, M. W. (1981). The measurement of unfrozen water content by time domain reflectometry: Results from laboratory tests. *Canadian Geotechnical Journal*, 18(1), 131-144.
- Rickenmann, D., & Zimmermann, M. (1993). The 1987 debris flows in Switzerland documentation and analysis. *Geomorphology*, 8(2), 175-189.
- Rücker, C., Günther, T., & Spitzer, K. (2006). Three-dimensional modelling of DC resistivity data incorporating topography - I. Modelling. *Geophysical Journal International*, 166(2), 495-505.
- Sakaki, T., Limsuwat, A., Smits, K. M., & Illangasekare, T. H. (2008). Empirical two-point α -mixing model for calibrating the ECH2O EC-5 soil moisture sensor in sands. *Water Resources Research*, 44(4).
- Sass, O. (2007). Bedrock detection and talus thickness assessment in the European Alps using geophysical methods. *Journal of Applied Geophysics*, 62, 254-269.
- Sass, O., Bell, R., & Glade, T. (2008). Comparison of GPR, 2D-resistivity and traditional techniques for the subsurface exploration of the Aeschingen landslide, Swabian Alb (Germany). *Geomorphology*, 93(1-2), 89-103.
- Schön, J. (1983). *Petrophysik Physikalische Eigenschaften von Gesteinen und Mineralen*. Berlin: Akademie-Verlag.

- Spaans, E. J., & Baker, J. M. (1995). Examining the use of time domain reflectometry for measuring liquid water content in frozen soil. *Water Resources Research*, 31(12), 2917-2925.
- Springman, S. M., Jommi, C., & Teyssie, P. (2003). Instabilities on moraine slopes induced by loss of suction: a case history. *Géotechnique*, 53(1), 3-10.
- Springman, S. M., Askarinejad, A., Casini, F., Friedel, S., Kienzler, P., Teyssie, P., & Thielen, A. (2012). Lessons learnt from field tests in some potentially unstable slopes in Switzerland. *Acta Geotechnica Slovenica*, 1, 5-29.
- Springman, S. M., Lucas, D. R., Oggier, N. C., Kos, A., Fankhauser, K., & McArdell, B. (2015). Study of the seasonal response of a scree slope and debris flow catchment in the Swiss alps. In *XVI European Conference on Soil Mechanics and Geotechnical Engineering (XVI ECSMGE 2015), Edinburgh, UK, 13.-17.9.2015*, 1897-1902. doi: 10.1680/ecsmge.60678.vol4.285
- Springman, S. M., Thielen, A., Kienzler, P., & Friedel, S. (2013). A long-term field study for the investigation of rainfall-induced landslides. *Géotechnique*, 63(14), 1177-93.
- Taber, S. (1929). Frost heaving. *The Journal of Geology*, 428-461.
- Taber, S. (1930). The mechanics of frost heaving. *The Journal of Geology*, 303-317.
- Take, W. A., Arneppalli, D. N., Brachman, R. W. I., & Rowe, R. K. (2007). Laboratory and field calibration of TDR probes for water content measurement. Kingston, Ontario, Canada: Queen's University, GeoEngineering Centre.
- Topp, G. C., Davis, J. L., & Annan, A. P. (1980). Electromagnetic determination of soil water content: Measurements in coaxial transmission lines. *Water Resources Research*, 16(3), 574-582.
- Onset Computer corporation. EC-5 Volume of Sensitivity Application Note. (n.d.). <<http://www.onsetcomp.com/files/15926-B%20EC-5%20Volume%20of%20Sensitivity.pdf>> Accessed 23.09.16.
- ICT International. 10HS Volumen of sensitivity. (2008). <<http://ictinternational.com/content/uploads/2014/03/10HS-Volume-of-Sensitivity.pdf>> Accessed 23.09.16.

4.7 Appendix: Supplementary data on sensors and calibration.

4.7.1 Moisture content sensors description

The time domain reflectometry sensor TDR100, manufactured by Campbell Scientific, uses a technique consisting of sending an electromagnetic pulse to the connecting cable and probe embedded in the soil. The returning signal reflected at the end of the probe is sampled and the travelling time is measured and is related to the apparent dielectric constant, which can be associated with the volumetric water content of the soil through linear or polynomial forms of equations (Topp et al., 1980). The probe consists of two rounded prongs of 150 mm length and 6 mm diameter, at a centre-to-centre spacing of 20.5 mm.

The dielectric permittivity sensors (Decagon) EC-5 and 10HS (used in IT2) measure the volumetric water content of the soil using the capacitance technique. The capacitance of the soil is related to the permittivity or charging time of an electromagnetic field, from which the volumetric water content can be inferred by a linear or polynomial form of equation. The probe dimensions are 8.9 x 1.8 x 0.7 cm, and 14.5 x 3.3 x 0.7 cm respectively.

Tensiometer JetFill 2725 ARL consists of a tube of 2.2 cm diameter with a porous ceramic tip at the bottom of 6 cm length and sealed water storage on top, connected to a pressure transducer (Range 0-85 kPa). The water can flow from the tube to the porous ceramic tip and the gauge will record the bonding between water and soil around the ceramic tip as negative pressure suction. Remote 2100F were used in IT4, (Range of 0-85 kPa). The ceramic is inserted in the ground in the wall face of the trench and backfilled carefully, paying special attention to a representative soil distribution around the other half of the tip and ensuring good contact between soil and ceramic. The water storage and pressure transducers are located in the ground adjacent to IT4.

4.7.2 Electrical resistivity tomography (ERT) and Archie's law

The basic principle of geoelectrical resistivity measurements is to inject current into the ground through a pair of electrodes and to measure the resulting potential in the form of a voltage difference, caused by current flow, at another pair of electrodes along the subsurface. 48 electrodes were planted along the profile line and the Syscal Pro system (IRIS instruments) was used for all measurements performed during the monitoring phase from May to July 2014. A Wenner configuration was selected for all acquisitions,

due to the highly resistive environment. The inversion was performed using the BERT (Boundless Electrical Resistivity Tomography) software package (for more detailed information on the processing of the ERT data from this project, see Fankhauser, 2014; Günther et al., 2013; Günther et al., 2006; Günther, 2011; Rücker et al., 2006).

Although Archie's Law (Archie, 1942) is considered to be valid in this case and can be used to calculate VWCs from the resistivities measured during the ERT acquisition, it is very difficult to get accurate estimates of the parameters involved in this law. Therefore another approach can be used to relate the temporal variation of soil resistivities along the repeatedly measured ERT profile to the temporal variation of soil saturation or water content (under the assumption that the porosity and the pore water resistivity remain constant) as:

$$\frac{\rho_t^{-\frac{1}{n}} - \rho_{t_0}^{-\frac{1}{n}}}{\rho_{t_0}^{-\frac{1}{n}}} = \left[\frac{\rho_t}{\rho_{t_0}} \right]^{-\frac{1}{n}} - 1 = \frac{S_t - S_{t_0}}{S_{t_0}} = \frac{\Delta S}{S_{t_0}} = \frac{\Delta \theta}{\theta_{t_0}} \quad (\text{S4.A1})$$

where ρ_{t_0} , S_{t_0} , θ_{t_0} and ρ_t , S_t represent the resistivity, saturation and water content at times t_0 and t respectively. ΔS and $\Delta \theta$ represent the differences in saturation and water content between these times. The profile measured on 15th May, 2014 was chosen as the baseline model (at time t_0) and variations in saturation in later acquisitions are presented relative to this profile. The advantage of this approach is that neither the constants (except for n) nor the porosity or the resistivity of the pore water need to be quantified to observe a seasonal variation in soil saturation.

4.7.3 Sensor operation difficulties

4.7.3.1 Operation difficulties

Issues with performance of the sensors can appear either during calibration in the laboratory, or installation and operation in the field. Indirect measurements such as TDR and capacitance sensors that measure the dielectric constant representative of the components in the soil, require a physical calibration to be able to calculate the VWC in the soil. Relevant issues for TDRs and dielectric permittivity sensors are:

During calibration:

- gravel became trapped in the fork during insertion, which could dominate the REV and lead to inaccurate readings;

4. Study of the seasonal response of a scree slope and debris flow catchment in the Swiss Alps

- specimens used in the laboratory might differ slightly from the grain size distribution present in the field. This affects the accuracy in the calculation of VWC.

During installation:

- gravel trapped in the fork during insertion: it is difficult to detect when this happens in the field;
- the sensor is not fully in contact with the soil, meaning air gaps could be filled by water or by air, altering the equivalent dielectric constant. This could be observed in the form of inconsistent spikes in the recorded data.

During operation:

- rockfalls: trenches IT1 and IT2 were hit by fragmenting boulders in 2014. The rockfall hit the trench at IT1 and affected the temperature sensor at 15 cm depth. The instrumentation was fixed at the end of August 2014 and performed normally after that. A slight shift between a TDR and dielectric permittivity sensors (25 and 22 cm depth) was observed after the rockfall; IT2 was installed in June 2014 and was also hit by a rockfall, a few days after its placement. Even though the data logger container was damaged and displaced by approximately 3 m, the sensors kept reading during this time, with the exception of one temperature sensor, which read normally again after the damage to the container was fixed;
- change in bulk density;
- change in voltage input.

All these issues can result in an under- and overestimation of the dielectric constant, affecting the calculation of VWC, or generating spikes in the data.

Relevant issues for tensiometers during operation include:

- insufficient storage water within the instrument's plastic tube and reservoir, resulting in inconsistent measurements;
- the range of measurement in the ceramic tip, specified by the manufacturer (80 kPa), is exceeded and data has to be disregarded due to cavitation.

Issues for the ERT encompass:

- insertion of electrodes: due to the gravelly nature of the soil, electrodes were difficult to insert, resulting in coupling issues at some locations. In most cases, the problem could be avoided by slightly shifting the electrode's position;

- coupling issues: insertion problems and/or the highly resistive nature of the (dry) soil led to electrodes that were not optimally coupled to the ground. The problem was reduced by using a very small amount of cat litter mixed with salt water around the affected electrodes.

4.8 Appendix: Annual temperature curves and profile of VWC and temperature vs depth

4.8.1 Temperatures

The average monthly temperatures are presented in Figures S4.8.1a-c for trenches IT1-3, for the years 2014 and 2015. The values of ambient air temperature (black), recorded at the IGT weather station in 2015, are also displayed. Three sensors are shown at three different depths (surface, 15 to 20 cm and 40 to 45 cm) for each trench. Each sensor is identified by one colour, which is darker for 2014 and lighter for 2015.

The average temperature during the summer (June to August) in 2015 was higher ($\sim 5^{\circ}\text{C}$) than the same season in 2014, which is clearly visible in IT1 and IT2 (Figures 4.13a and b). However, the autumn of 2015 was colder than in 2014.

The difference between the ambient air temperature and the soil temperature at 15-20 cm depth in 2015 is approximately constant in summer (~ 2 to 4°C), but varies during spring and autumn, where the difference can be larger or smaller. In addition, the air temperature was observed to be lower than any of the soil temperatures in winter.

As expected, the soil temperature decreases with depth during the summer months, in all of the trenches, but with different gradients, which suggests a significant dependency on trench location and hence sun exposure. The surface on the ground cools in the other seasons, although the deepest sensors continue to exhibit warmer temperatures because of the insulation created by the upper soil layer itself.

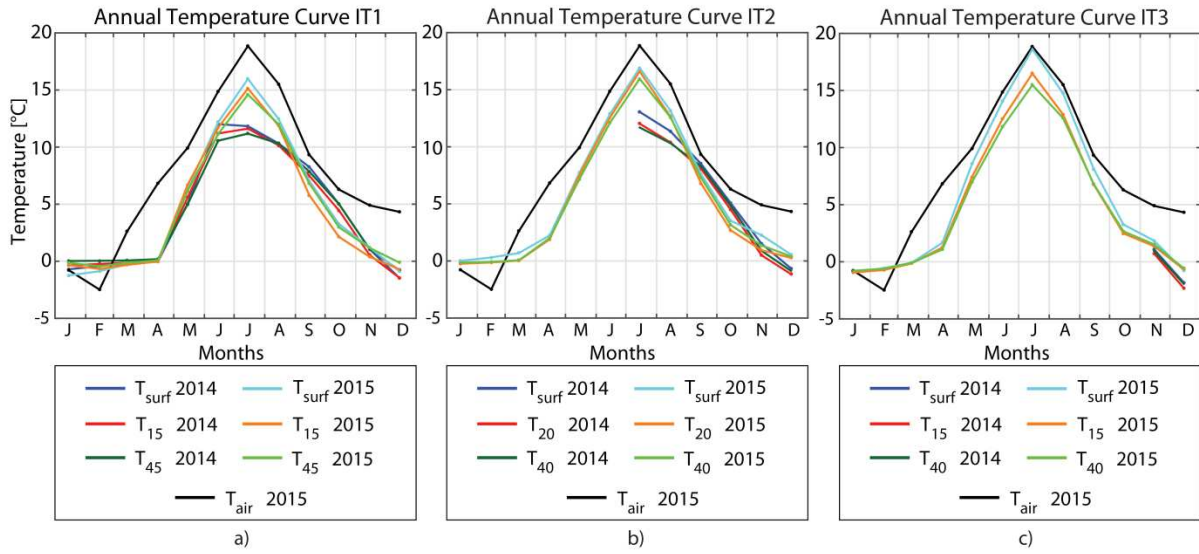


Figure S4.8.1. Monthly average temperatures for years 2014 -2015 for instrumented trenches: IT1 (left) to IT3 (right), with three sensors each, located at different depths.

4.8.2 VWC and Temperatures vs depth

Figure S4.8.2 shows the temperatures and VWCs with depth for three specific dates, the 10th, 15th and 20th of September 2015 at noon. This period corresponds to the transition season from summer to autumn and there was no rain recorded at these dates although rain events of different intensities were recorded between these dates (see Paper in Figure 4.14). Each colour represents the data recorded at each instrumented trench IT1-4 at their respective depths, with zero representing the ground level.

The figure shows a volumetric water content (VWC) in the scree slope varying approximately between 0.01 and a maximum of 0.28 for these dates, corresponding to the water content remaining from the past events. The variation of VWC with depth in all the trenches responds to the heterogeneity in the gravel, sand and fines content. For example, VWC for IT3 fluctuates in rather a low range due to the coarser soil with less fines and therefore fast drainage. The higher increase in VWC at IT4 at 90 cm depth also reflects a marked change in soil characteristics, showing a layer that can reach saturation faster, which is therefore susceptible to a sudden loss in shear strength triggered by rain events.

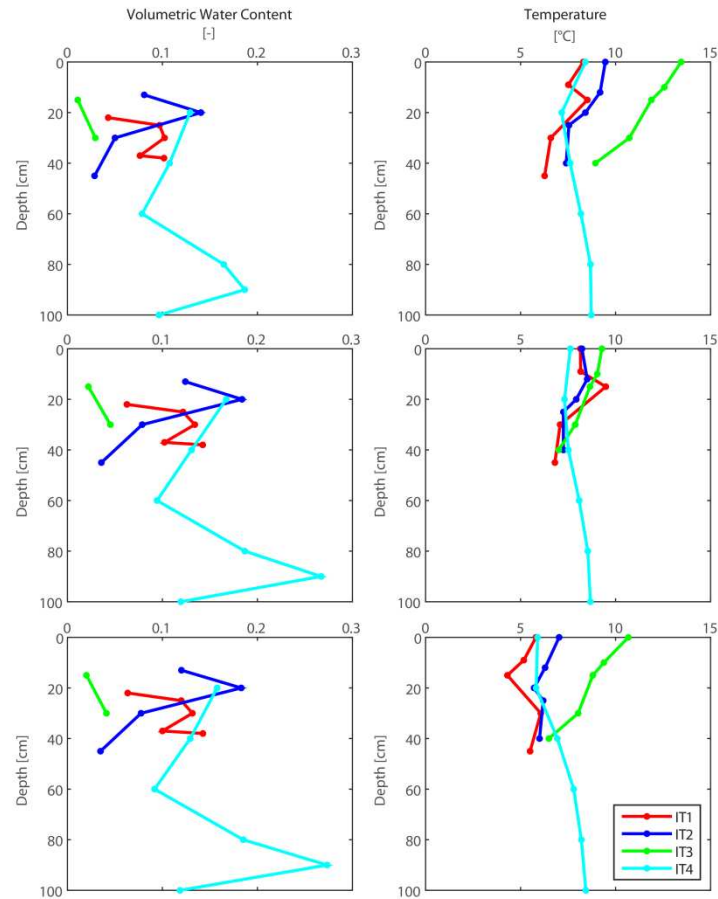


Figure S4.8.2. Temperature and VWC profiles 10th, 15th and 20th of September, 2015.

There is a trend of gradient decreasing with temperature for IT1-IT3, while IT4, which is located in the lower part of the scree slope, has only a small range of variation in temperatures with depth. IT2 and IT3 show the effect of sun exposure.

[This page is intentionally left blank]

5 Slope stability of a scree slope based on integrated characterisation and monitoring

Daisy Lucas

ETH Zürich, Institute for Geotechnical Engineering
Stefano-Franscini-Platz 5, 8093 Zürich, Switzerland
E-Mail address: daisy.lucas@igt.baug.ethz.ch

Kerstin Fankhauser¹

ETH Zürich, Institute for Geotechnical Engineering and Institute of Geophysics
Stefano-Franscini-Platz 5, 8093 Zürich, Switzerland
E-Mail address: kerstin.fankhauser@erdw.ethz.ch

Hansruedi Maurer

ETH Zürich, Institute of Geophysics
Sonneggstrasse 5, 8092 Zürich, Switzerland
E-Mail address: hansruedi.maurer@erdw.ethz.ch

Brian McArdell

Eidgenössische Forschungsanstalt für Wald, Schnee und Landschaft WSL
Zürcherstrasse 111, 8903 Birmensdorf, Switzerland
E-Mail address: brian.mcardell@wsl.ch

Reto Grob²

ETH Zürich, Institute for Geotechnical Engineering
Stefano-Franscini-Platz 5, 8093 Zürich, Switzerland
E-Mail address: reto.grob@flumgeo.ch

Ralf Herzog

ETH Zürich, Institute for Geotechnical Engineering
Stefano-Franscini-Platz 5, 8093 Zürich, Switzerland
E-Mail address: ralf.herzog@igt.baug.ethz.ch

¹ Current employer: focusTerra ETH-Bibliothek
Sonneggstrasse 5, 8092 Zürich, Switzerland

² Current employer: FlumGeo AG
Fuchsenstrasse 19, 9016, St. Gallen, Switzerland

Ernst Bleiker

ETH Zürich, Institute for Geotechnical Engineering
Stefano-Franscini-Platz 5, 8093 Zürich, Switzerland
E-Mail address: ernst.bleiker@igt.baug.ethz.ch

Sarah M. Springman

ETH Zürich, Institute for Geotechnical Engineering
Stefano-Franscini-Platz 5, 8093 Zürich, Switzerland
E-Mail address: sarah.springman@igt.baug.ethz.ch

Submitted to Special Issue "Water-Induced Landslides: Prediction and Control"
in Journal Water

Status: To submit by 15th November 2019.

Abstract

Three years of geotechnical monitoring including soil temperature, suction and volumetric water content plus geophysical measurements, lead to a preliminary ground model and assessment of slope stability for a steep scree slope in the Meretschibach catchment, near Agarn village in the Swiss Alps. Building on data reported in a previous paper, which focused on preliminary ground characterisation and monitoring, this current research aims to understand whether a surficial failure in the scree slope, triggered by rainfall and depending on bedrock conditions, would represent a relevant natural hazard for Agarn village. A final year of field data is included as well as site-specific sensor calibration, a GPR profile, and laboratory triaxial testing to provide strength parameters. A bedrock map is presented, based on GPR, with a realistic ground model of the entire scree slope. Furthermore, a preliminary numerical analysis, performed using SEEP-SLOPE/W, shows the influence of a bedrock outcrop observed in the field, for a specific soil thickness, strength parameters and rain intensity. The stability of a gravelly slope decreases with groundwater flow over a step in the bedrock, and the location of the failure will tend to move uphill of a bedrock outcrop at a shallow depth as flow increases.

Keywords: Landslide, monitoring, bedrock, scree slope, Ground Penetrating Radar, volumetric water content, natural hazard, triaxial stress path testing.

List of Notation

CSD	→	Constant shear stress drained path
CSL	→	Critical state line
CADCAL	→	Anisotropic consolidation-drained shear at constant axial load
ERT	→	Electrical resistivity tomography
EC-5	→	Capacitance sensor, Decagon Devices
F.S.	→	Factor of Safety
GSD	→	Grain size distribution
GPS	→	Global positioning system
GPR	→	Ground penetrating radar
ID	→	Intensity-duration threshold
IGT	→	Institute for geotechnical engineering
inSAR	→	Interferometric Synthetic Aperture Radar
IT	→	Instrumented Trench
PWP	→	Pore water pressure
TDR	→	Time domain reflectometry sensor, Campbell Scientific
VWC	→	Volumetric water content
WSL	→	Swiss Federal Institute for Forest, Snow and Landscape Research
C_c	→	Coefficient of curvature
C_u	→	Coefficient of uniformity
c'	→	Cohesion
D_i	→	$i\%$ of the particles are finer than this size
D_r	→	Relative density
e	→	Void ratio
ϵ_a	→	Axial strain
ϵ_v	→	Volumetric strain
K_c	→	Principal stress state ratio
$K_{\text{water,ice,soil}}$	→	Dielectric constant of (water/ice/soil)
p'	→	Mean effective stress
q	→	Deviatoric shear stress
Q	→	Input water Flow
10HS	→	Capacitance sensor, Decagon Devices
ϕ'	→	Critical state friction angle
γ_d	→	Dry unit weight

ψ → Dilatancy angle

σ'_i → Principal effective stress

5.1 Introduction

Scree slopes are formed in mountain areas by rock debris, which loses potential energy in falling from weathered and fractured bedrock walls, and follows a downslope trajectory until it decelerates and stops i.e. to zero kinetic energy once again. Typical dynamic processes occurring in an active scree slope are toppling failures [1], rockfalls; landslides (small or large mass movements); and the fragmenting and sorting of materials [2-4].

The scree slope at Meretschibach (Figure 5.1(a)) consists of a surficial layer of large boulders and cobbles underlain by a predominantly gravelly soil layer, with a mix of coarser, larger and finer sizes within a heterogeneous structure. The characteristics, in terms of geometry and particle arrangement, depend on the energy balances and rock crushing strength (e.g. in extremis as seen in rock slides and rock avalanches [5-12], this implies that particles of all sizes, and fractural dimensions are created during fragmentation, leading to a fabric where larger particles are immersed in a matrix of finer ones [7, 10, 13-15]. Furthermore, if the input energy is high, the rock may experience rock-burst [16], where highly stressed rock disintegrates suddenly, reaching high velocities (>10 m/sec) [9]. Additional factors are the bedrock slope and the climate environment.

Scree slopes that are under dynamic processes of debris deposition and remobilization, may suffer instabilities under hydrological events through intense periods of rainfall, or snow melting processes. Scree slope formation, processes and dynamics have been documented in the literature [2-4, 17-20]; although there is a lack of data on the slope instability and failure mechanisms.

A scree slope in the Meretschibach catchment in canton Valais in the south of Switzerland (Figure 5.1(a)) was characterised in order to improve understanding of the process phenomena in scree slopes and to investigate the potential hazard following initiation of landslides/debris flow with runout on to Agarn village. Frequent toppling and rockfall events were observed in the scree slope (Figure 5.1(b)), but their volume was too small (order of magnitude) to be considered as a hazard to the village. The most severe hazard that could be predicted after three years of field monitoring, apart from a deep-seated landslide, which was not investigated in this research, was identified as a surficial landslide. This could mobilise a significant volume of debris that could

eventually be deposited in an active channel and subsequently turn into a debris flow that could reach the community in Agarn.

Preliminary results from this research were presented in the paper ‘Application of geotechnical and geophysical field measurements in an active alpine environment’ [21] delivering two of years data of volumetric water content (VWC), temperature records at specific locations in the slope (Figure 5.1(c)), depth to bedrock (downslope) and characterisation of the gravelly soil. The data led to a better understanding of the response of the surficial soil in a scree slope, due to annual variations in weather conditions in an alpine environment.

This paper adds one more year of data to that already published, providing a complete overview of the finalised monitoring. Additionally, a soil-specific calibration was carried out for the VWC estimation in terms of temperature variation, accompanied by further analysis of GPR data (Figure 5.1(b)) and the shear strength analysis derived from stress-path triaxial testing of the gravelly soil.

The VWC distribution at a depth of 1 m [21], showed for a period of at least two weeks, that a thin layer of soil was near saturation in one location after successive rainfall events at the beginning of this period. Had there been additional severe events in the following fortnight, a surficial landslide could have occurred due increase in thickness of the saturated zone and further reduction in effective stress. Failure could be anticipated, should this change in saturation extend over a larger area of the slope (Figure 5.1(d)). In this scenario, some of the mobilised soil debris could be contained by the forest downslope, and the rest could fall into the active channel, accumulating there, and increasing the hazard of a debris flow in the future.

The results of the soil-specific calibration for temperature variation in the positive range showed that the VWC measurements at the different locations are more influenced by the heterogeneity of the silty gravel than by temperature changes. Application of the GPR led to a map of bedrock depth of scree slope, including steps in the profile. Subsequently, an estimation was made of the slope stability through simplified numerical models, based on strength parameters obtained by the triaxial stress path tests.

5.2 The Meretschibach-Böchtur scree slope experiment

5.2.1 Location and description of the site

The field site is located between 1840-1910 m.a.s.l. in a mountain slope of the Meretschibach catchment in canton Valais, Switzerland (Figure 5.1(a)). Agarn village has approximately 800 inhabitants and lies in the Rhone river valley at 637 m.a.s.l.. The catchment area of about 9.2 km² is divided into four subcatchments [22], from which Bochtür is observed as the most active debris channel in the area [22], and it is the most active in terms of rockfalls and debris flow events. It poses a persistent hazard for the Agarn community.

The bedrock slope is inclined mainly between 33-48° [21], and is the selected location for the geotechnical characterisation and lies on the west side of the Bochtür. The heavily jointed quartzite bedrock emerges at higher elevations as outcrops that are exposed to strong mechanical weathering, producing boulders of various sizes for rockfalls and toppling events. These impact in the slope and bounce, roll and fragment until they are deposited and subsequently remobilised along the scree slope, covering the underlying layer of gravelly soil. Geological observations suggest that the bedrock is stepped, with joints dipping southwards (into the slope) with an inclination of 10-30° [23, 24].

Stunted vegetation, like spruce (*Picea abies*) and low shrubs of less than 1 m height, are only present partially along the slope due to the active erosion and mass movements that impact on them and destroy them, increasing the risk of remobilisation of the debris. Some of the past mass movements have been summarised by Oggier [22] and Fankhauser [25].

5.2.2 Preliminary hazard assessment

The Bochtür hillslope is well known to local land-use planners for persistent rockfall and debris flow activity. Observations of the movement of the hillslope described herein are based on unpublished project reports from the Swiss Federal Institute for Forest, Snow and Landscape Research (WSL), summarised in McArdell [26].

InSAR measurements of displacement suggest that part of the Bochtür hillslope is underlain by a large landslide, with the head of the landslide corresponding roughly to the unvegetated areas at the uppermost part of the Bochtür hillslope and extending about 1.25 km downslope into the forest, with a width of up to about 0.5 km [27]. Photogrammetric analyses of the unvegetated portion of the Bochtür, made by WSL staff for the period between 1959 and 2010, suggest a somewhat incoherent movement pattern, with many areas exhibiting surficial movements of less than 0.1 m/year.

Locally large velocities (up to 0.4 m/year) have been measured, however it is unclear whether they represent surface creep on the talus, toppling movements of bedrock steps described above, or local differential landslide deformation. Differential GPS measurements of marked boulders on the surface of the slope (Figure 5.2(a)), made between 28 October 2013 and 30 May 2014 (e.g. the period when the slope was relatively wet), indicate annual movement rates of up to 0.4 m/year (Figure 5.2(b)). The presence of Sackung trench-scarp features indicated on the geological map [23-24] in the forest adjacent to the Bochtür, and in the vegetated area at the head of the Bochtür (Figure 5.3(a)), suggests that creep deformation is occurring within the bedrock. However, no additional information is available from borehole data or geophysical measurements to indicate the depth of a possible failure plane or planes (Figure 5.3(b)). Rock avalanche deposits can be observed in the adjacent Illgraben catchment to the west, and the hillslope to the east of the Bochtür is partially covered by large blocky debris, indicating that the possibility of rapid large-scale landslides should not be ignored at this site.

Six debris flows were observed in the Meretschibach torrent between July 2014 and Sept. 2015, during rainstorms with durations of less than one day to up to 5 days. It is not appropriate, in a statistical sense, to construct a rainfall intensity-duration threshold (ID) curve for only six debris flow events. However, it is worth noting that all of the points plot above the triggering threshold for the Illgraben catchment [28] and all plot lower than a general Swiss ID curve established by Zimmermann [29].

Rockfall activity at the Bochtür and the interaction with the forest was investigated by Eichenberger [30] along four transects through the forest downslope of the Bochtür, with observations on more than 1500 trees. They described both fresh rockfall deposits (individual stones and boulders) and dated the age of rockfall wounds on the trees. Boulders in the forest with a clear rockfall origin have a median volume of $\sim 0.1 \text{ m}^3$ with boulders of volumes up to 10 m^3 present ($n=204$ boulders measured along the transects). Although not all stones and boulders impacted trees and caused damage to them, a large number of rockfall scars could be dated, and most of them were less than 10 years old, and were concentrated, as would be expected at the upslope border of the forest.

5.2.3 Soil characterisation

ERT results from geophysical surveys, soil classification tests and field observations from instrumented trenches (IT) enabled a preliminary ground model to be presented in Lucas et al. [21], which forms the basis of this study. The soil is classified according to

the Swiss standard classification (SN 670 004-2NA) as poorly-graded gravel with silt and sand (GP-GM), silty gravel (GM), well-graded gravel with silt and sand (GW-GM), and well-graded gravel (GW).

The particles are coming mostly from the quartzite bedrock outcrop above the slope, which is heavily jointed and highly susceptible to weathering, leading to rockfalls, sliding, and toppling [22, 25].

ERT measurements performed by Fankhauser [25] and published in Lucas et al. [21] were used primarily to establish the depth to the bedrock down the scree slope (1-3 m). Additionally, they provided a means of VWC estimation, which agreed well with the values obtained using TDR and EC-5 sensors measured at IT1.

The soil characterisation provided in this study includes:

- soil strength parameters derived from triaxial stress path test results,
- additional curves of GSD for soil extracted from IT1-4;
- a new set of measurements for in-situ unit weight, which are used later in the soil specific calibration, and
- a contour line map with the depth bedrock in the scree slope, obtained through geophysical GPR techniques.

5.2.4 Seasonal monitoring

The seasonal alpine climate conditions directly affect the VWC and temperature measured in the soil. The seasonal response exhibited the following trends over the years of monitoring:

- soil temperature changes are more noticeable at shallow depths, with a higher diurnal variation in summer;
- as temperature drops in autumn, a winter regime develops with temperatures around 0°C (or lower), with VWC reaching minimum annual values (0-0.07), and a persistent snow layer in place over several months, which insulates the underlying gravel from temperature and VWC variations;
- as temperature increases in spring, leading to snow-melt, the ground resaturates and the VWC rises;

- subsequent VWC changes in the summer season are directly related to rainfall events, as well as the GSD of the trench location, and the unsaturated hydraulic conductivity of the soil.

Final results from the monitoring fieldwork are presented, now including the complete records of three years of VWC, temperature and precipitation, including a soil-specific site calibration for the estimation of the VWC under variations in temperature. A selection of data is used subsequently in the numerical preliminary simulation of slope instabilities using SLOPE-SEEP/ W [31] to evaluate the hazard.

5.3 Methodology

5.3.1 Characterisation

5.3.1.1 Soil unit weight and grain size distribution (GSD)

The unit weight obtained from in situ measurements in this research used the balloon method device (MagdeBurger Prüfgeräte GmbH (HMP), DIN 18125-2:2011-03)) described in [21]. The dry unit weight was determined using the calculated volume and the dry weight of the soil excavated. There was one preliminary measurement, followed by two campaigns (November 2015) [21], and a second test/series performed in November 2016. The results are presented herein.

The GSD test was performed according to Swiss standard classification (SN 670004-2NA) for each trench location at IT1-4, using soil samples of weight between 30-38 kg (Figure 5.4). The soil was then used for the site-specific recalibration of the VWC.

5.3.1.2 Triaxial stress path testing

Soil shear strength parameters

A slope stability analysis requires the study of the soil behaviour under the potential stress and stress path conditions that can lead to failure. Constant shear stress drained (CSD) triaxial tests (Figure 5.5(a)) on reconstituted specimens [32-33] reproduce the field conditions anticipated during infiltration and loss of effective stress [34] in terms of the saturation process in a steep slope, where the angle of inclination is close to the angle of repose. This allows stress path dependent critical state parameters of the gravel to be determined under saturated conditions. The initial principal stress state ratios K_c at point B in Figure 5.5(a) are based on the assumption of the principal stress orientation, as described in [35], for an infinite and planar slope. However, initial principal stresses

in the triaxial devices could not exactly reproduce field conditions, since they are limited to being axial and radial. The pre-shearing anisotropic consolidation plus, a CSD stress path, could increase the K_c until failure occurred (path B to C; Figure 5.5(a)).

A series of CSD triaxial tests were carried out using a prototype gravel mixture with a representative GSD [36], which is an average of the soil from IT1-4 (Figure 5.5(b)). The soil response was compared and discussed for different device scale to particle diameter ratios, leading to determination of appropriate shear strength parameters of the reconstituted gravelly scree soil.

Triaxial stress path testing

A constant shear stress drained path (CSD) under saturated conditions matches the process of water infiltration, by increasing the stress state ratio at constant deviator stress until failure occurs [34].

The initial anisotropic stress state ratio $K_c = (\sigma_1')/(\sigma_3')$ in a steep scree slope indicates that it is in an incipient state of failure [34, 37-38]. Pore water pressure (PWP) increases when water infiltrates into unsaturated soil, which occurs primarily under constant total stress, which reduces suction and hence the effective stresses. This can lead to failure under saturated or unsaturated conditions [34].

The analysis described herein has been applied in past slope stability studies e.g. [39-40], in helping to understand the failure mechanism. The constant shear stress drained path (CSD) is shown in Figure 5.5(a), and follows three phases: isotropic consolidation (A), anisotropic consolidation (B), and constant shear stress path to failure (C). The CSD stress path can be achieved in IGT apparatuses in two different ways:

- decreasing the mean effective stress $p' = (\sigma_1' + 2\sigma_3')/3$ at a constant rate, by reducing the total stresses, and keeping constant back-pressure and deviatoric shear stress $q = \sigma_1 - \sigma_3$ [41] for a 250 mm diameter specimen, after [34].
- increasing back pressure while total stresses are held constant.

The first method was used for the CSD in the large, and the second in the mid-scale, triaxial test. The loading piston can move independently in the large triaxial apparatus so that a decrease in cell pressure is possible, whereas the head plate is rigidly connected

to the loading piston in the mid-scale apparatus, so it is not possible to apply cell pressure changes to affect the vertical total stress.

An alternative stress path to CSD would be CADCAL, as applied by Casini [42] in a 50 mm diameter specimen of silty sand, where the consolidation phase is exclusively anisotropic, to an initial K_c (B in Figure 5.5(a)), with subsequent shearing at constant q , under stress controlled conditions.

Soil specimen preparation

The two types of specimens were reconstituted for mid- and large-scale triaxial apparatuses with natural soil using an adopted representative GSD (Figure 5.5(b)) suitable for each test diameter. The maximum particle size for the specimens followed the CEN ISO/TS 17892-9:2004 for soils with a coefficient of uniformity (C_u) larger than 5, which limited the maximum grain size to 1/6 of the specimen's diameters. Therefore, the maximum particle sizes allowed for the mid- and large-scale triaxial specimens were 25 and 41 mm, respectively. A maximum size was of 16 and 31.5 mm was adopted respectively in both medium (150 mm diameter) and large (250 mm diameter) scale triaxial apparatuses on reconstituted specimens [36].

Fractions of each grain size, excluding those larger than 16 and 31.5 mm, were mixed carefully to make the mid- and large scale specimens, respectively (Figure 5.5(b); Table 5.1). The specimens were prepared with initial moisture content of 3% at medium relative densities (27-60 %; Table 5.2), by moist tamping of 6 layers of 50 mm depth for the mid-scale and in 5 to 10 layers of 100 and 50 mm depth respectively for the large-scale.

Table 5.1. Soil characteristics for the reconstituted triaxial specimens.

Test	Mid-scale	Large scale
D_{10} [mm]	0.04	0.04
D_{30} [mm]	0.60	1.31
D_{60} [mm]	5.01	9.10
D_{max} [mm]	16.00	31.50
C_c [-]	1.90	4.70
C_u [-]	131.90	227.50
Percentage of fines [%]	14.9	11.7
Swiss Standard Classification (SN 670 004-2b NA)	GM	GM

Ratio $D_{\text{triaxial}}/D_{\text{max}}$	150/16 = 9.38	250/31.5 = 7.94
e_{min} [-]	0.269	0.341 ¹
e_{max} [-]	0.570	0.691 ¹

¹: $e_{\text{max, min}}$ from IT1 field soil.

Testing programme

The testing programme is presented in Table 5.2 and includes the characteristics of the stress paths for the mid-scale triaxial (mid) and the large-scale triaxial (large) devices. The initial conditions before consolidation are given by the void ratio (e_0) and relative density (D_r). The stresses are defined after each consolidation phase by p'_A and q_A for isotropic consolidation and by p'_B and q_B for anisotropic consolidation (Figure 5.5(a)). The calculated stress state ratio (K_c) captures the anisotropic stress state before the shearing phase starts.

Table 5.2. Triaxial testing programme on gravelly scree soil: specimen preparation.

Test	e_0 [-]	D_r [%]	$K_c = \sigma'_{1,B}/\sigma'_{3,B}$ [-]	q_A [kPa]	p'_A [kPa]	$\sigma'_{1,B}$ [kPa]	$\sigma'_{3,B}$ [kPa]	q_B [kPa]	p'_B [kPa]
mid_1	0.49	27	1.83	6.0	40.0	143.1	78.0	65.1	99.7
mid_2	0.52	17	1.94	6.0	19.0	72.6	37.4	35.2	49.1
mid_3	0.54	10	1.88	5.0	30.0	108.3	57.5	50.8	74.4
large_1	0.53	46	1.74	8.0	36.0	133.4	76.5	57.0	95.5
large_2	0.48	60	1.85	5.0	18.0	65.4	35.3	30.1	45.3
large_3	0.59	29	2.42	3.3	59.0	227.4	94.1	133.3	138.6

e_0 : initial void ratio; D_r : relative density; K_c : principal stress ratio

Dilatancy

According to Bolton [43] the dilatancy angle (ψ) in granular soils is represented by ϕ'_{max} where ϕ'_{max} is the peak friction angle, for triaxial can be calculated as:

$$\psi = 3 * I_R \quad (5.1)$$

with: $\psi[^\circ]$ = dilatancy angle

I_R = dilatancy index

Whereas the dilatancy index is:

$$I_R = I_D * (Q - \ln(p')) - 1 \quad (5.2)$$

with: I_R = dilatancy index

Q = natural logarithm of the mean stress p_c at which dense soil first reaches the normal consolidation line

I_D [-] = relative density

According to Bolton [44] Q can be estimated to 9.2. The relative density is determined with the void ratio as:

$$I_D = \frac{e_{\max} - e}{e_{\max} - e_{\min}} \quad (5.3)$$

with: e_{\max} [-] = maximum void ratio , e_{\min} [-] = minimum void ratio , e [-] = void ratio.

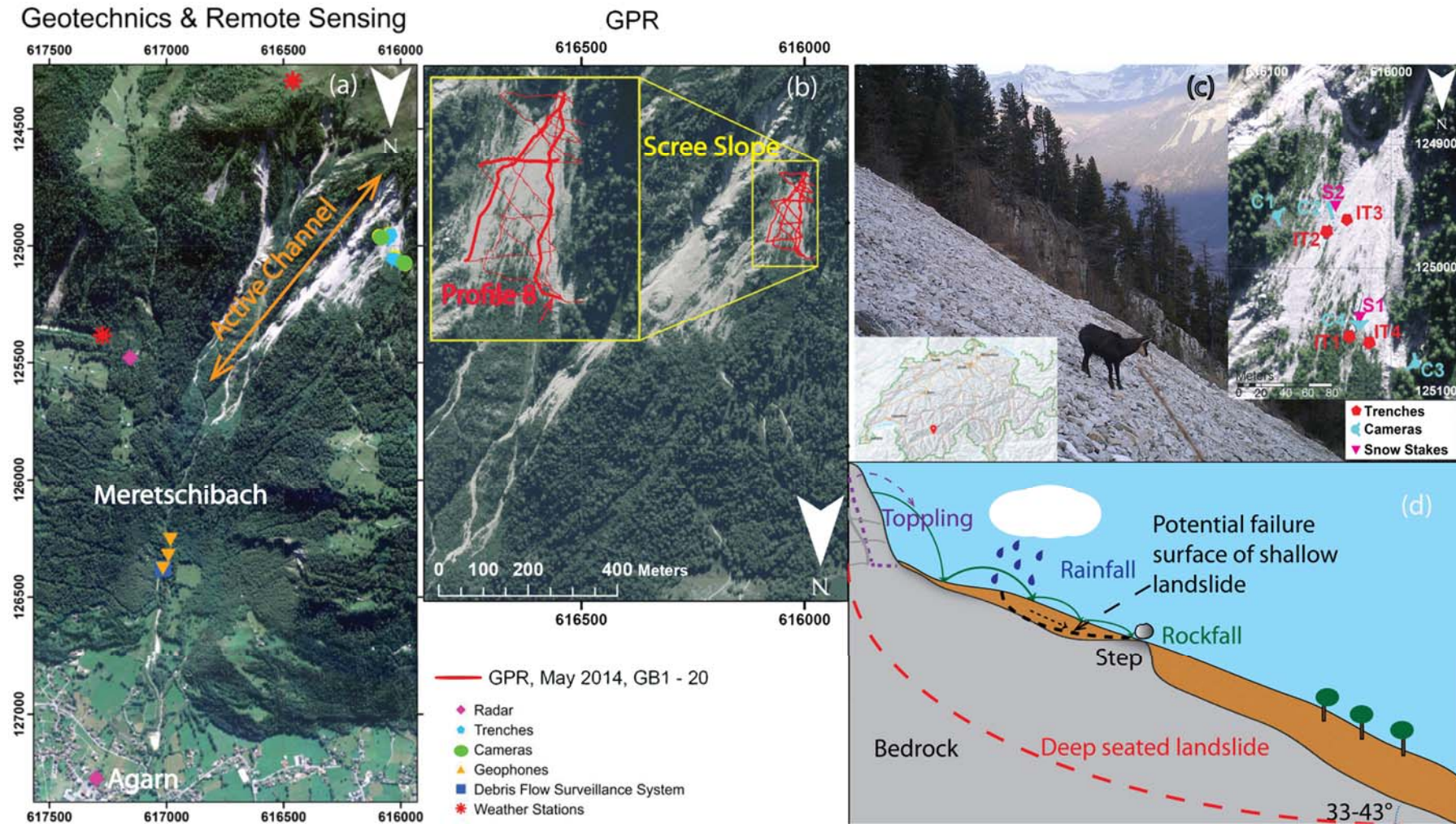


Figure 5.1. Field site located in canton Valais, Switzerland. (a) Location of geotechnical and remote sensing, (b) Geophysical measurements, extent of GPR with profile 8 (presented in Figure 5.9) indicated. Distances according to Swiss coordinate system CH1903 (in metres), (c) overview of the investigated area, (d) mass movement instabilities in the scree slope. The likely presence of a deep-seated landslide is indicated schematically with a red dashed line.

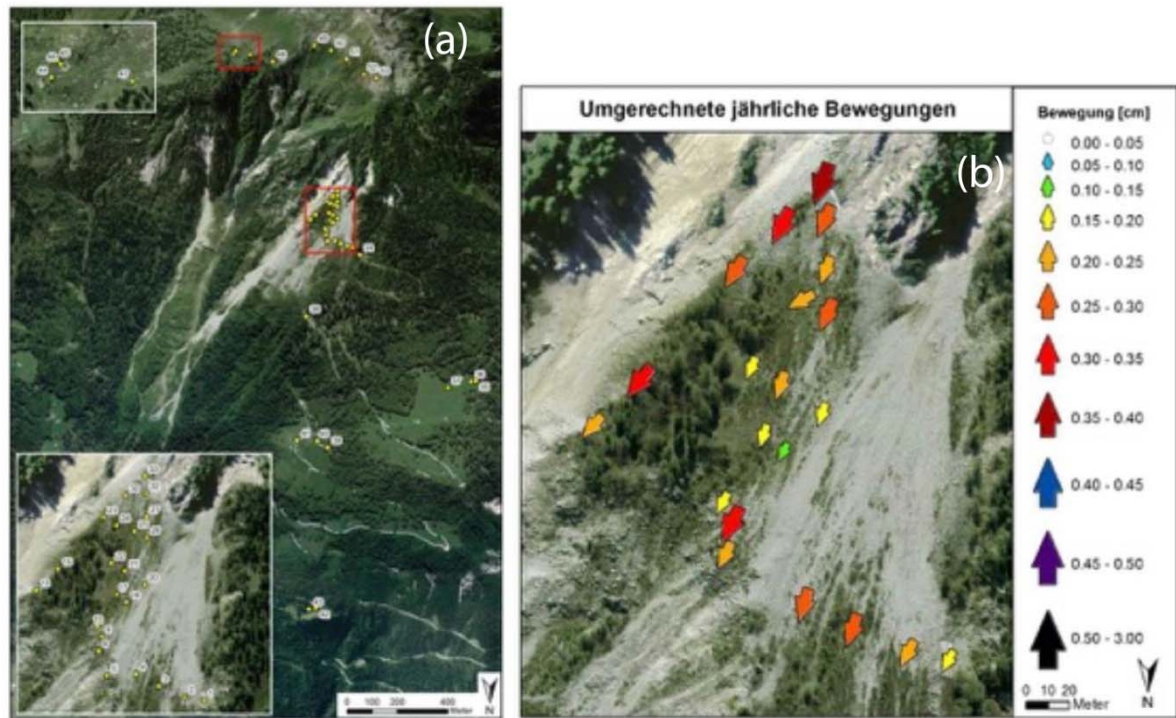


Figure 5.2. Meretschibach-Böchtur catchment. (a) Location of GPS points and (b) the annual hillslope movement rate between 28 Oct. 2013 and 30 May 2014. From Oggier and Thee (2015b, their Figures 6 and 7).



Figure 5.3. (a) Closed elongated depression at the top of the Böchtur hillslope, possibly indicating a Sackung-type failure of the bedrock, (b) local slope collapses near the bend of the road described in the text. Photos by B. McArdell, WSL.

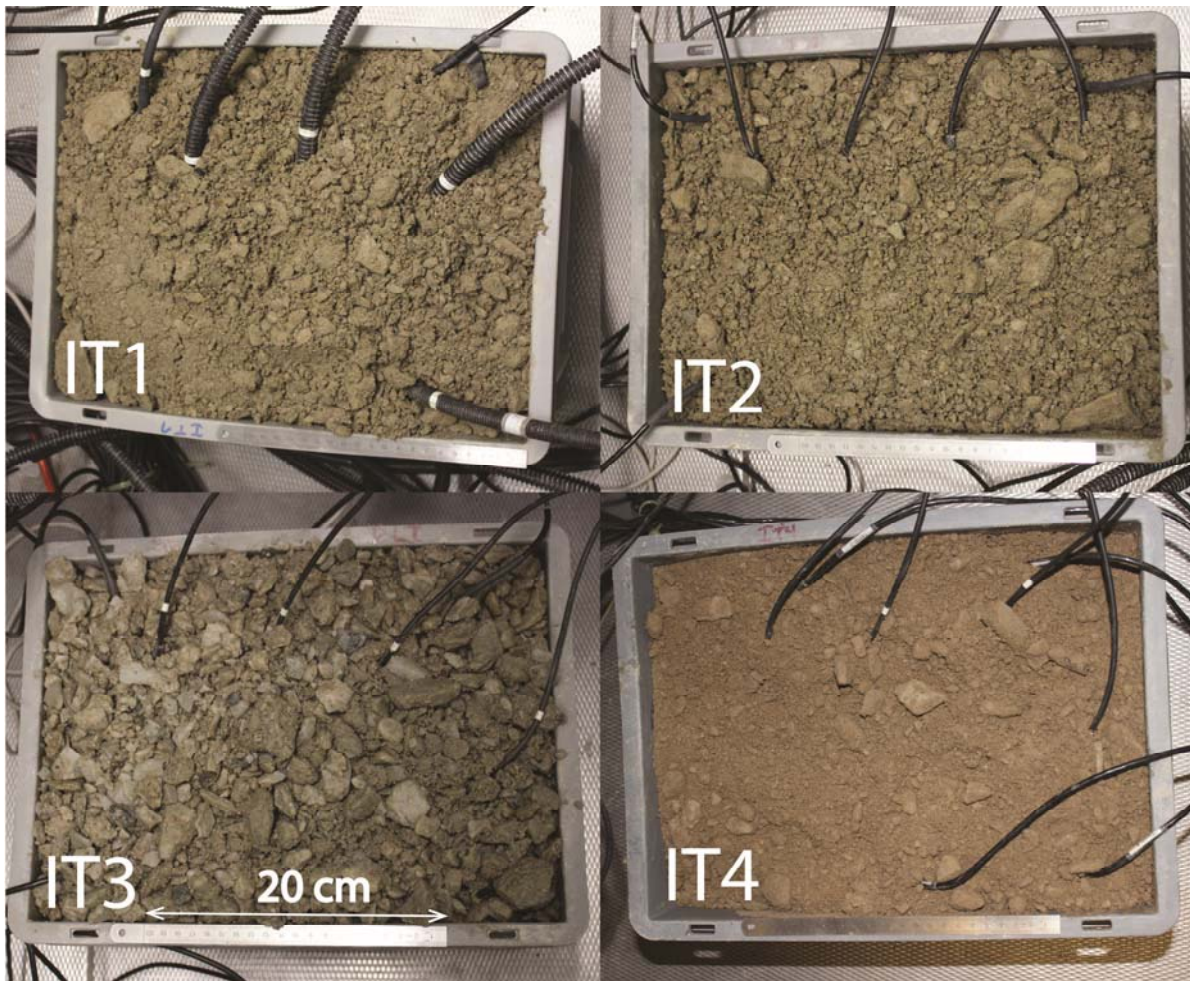


Figure 5.4. Recalibration of sensors: soil in reconstituted samples for IT1-4, with a moisture content is 8% at 1°C. The boxes have a length and width of 36 and 26 cm, respectively.

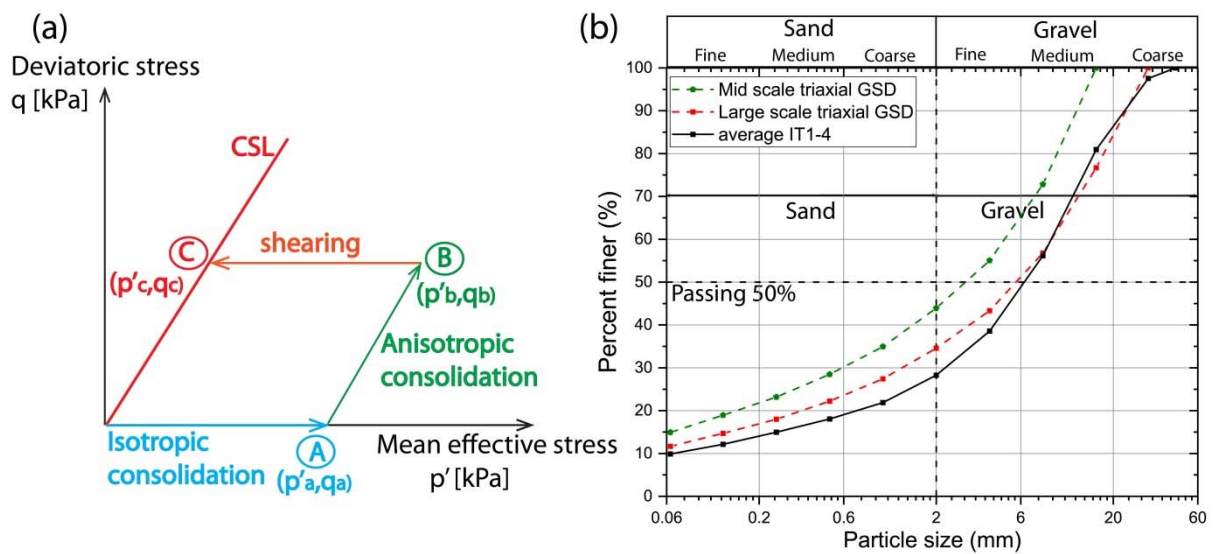


Figure 5.5. (a) Constant shear stress drained path (CSD). A is the point at the transition from isotropic to anisotropic consolidation, and B symbolises the transition from the latter to shearing as pore water pressures increases. Failure occurs at C, after shearing at constant deviatoric stress. (b) GSD of the sandy gravel specimen: mid-scale (150 mm diameter) and large scale (250 mm diameter) and the average GSD of the IT1-4.

5.3.1.3 Ground model: Ground penetrating radar (GPR)

Methodology, data acquisition, and data processing

Ground penetrating radar (GPR) was carried out to characterise the scree slope (Figure 5.1(b)) in the Bochtür area of the Meretschibach catchment. This geophysical method was used to complement the long-term geotechnical monitoring at this site.

GPR uses high frequency electromagnetic waves to map anomalous electrical structures in the subsurface. Transmitting and receiving antennas are kept at a fixed distance and are carried along the surface. Radar pulses are emitted into the ground by the transmitter, partly reflected and transmitted at discontinuities where electromagnetic properties (primarily the dielectric permittivity) of the subsurface material change (as is usually the case at the soil-bedrock interface). The reflected signal is captured by the receiver antenna. The time required for the signal to travel from the surface to the bedrock and back to the surface (two-way travel time) and can be converted to depth, using the propagation velocity of the GPR waves. More information on the GPR theory, resolution and penetration can be found in [45-49].

The choice of the antenna frequency is crucial to determine the penetration depth and resolution, which are always a trade-off: the higher the frequency, the higher the (vertical and horizontal) resolution, but this comes at the expense of a decreased penetration depths [45, 47-49]. The 250 MHz antenna from the PulseEKKO manufacturer was chosen for the main GPR acquisitions in this project, allowing for a vertical resolution of up to 0.1 m and a depth penetration of up to 10 m. The relevant acquisition parameters used during GPR surveys are provided in supplementary material Tables S5.9.2, S5.9.3 and [25].

GPR acquisition was carried out on 15th and 16th May 2014. The steepness of the terrain made walking difficult and the accessibility of the active channel proved to be too dangerous on foot. Therefore, 20 profiles (Figure 5.1(b)) were recorded on the scree slope using a large number of stacks (Table S5.9.2), because the slow walking ensured enough traces were recorded in each position.

A relatively standard processing workflow was applied to the GPR data acquired. It included (i) band-pass filtering to enhance the signal-to-noise ratio, (ii) removal of system ringing with singular value decomposition filter (e.g., [50]), (iii) trace binning for

obtaining equidistant traces (0.05 m), (iv) FX-deconvolution to enhance lateral continuity and (v) time-to-depth conversion using a velocity of 0.1 m/ns.

5.3.2 Field monitoring

5.3.2.1 Site-specific calibration

The VWC in the gravelly soil was monitored during three years, the first two years of data were presented in [21]; where some differences were observed in VWC measurements between capacitance and TDR sensors at similar depths and locations, were discussed but not yet investigated. The dielectric properties of the soil (related to the VWC) are strongly affected by the water content, soil structure and density [51], calibration of the sensor [52], input voltage [53], orientation and volume of measurement (depending of the type of sensor), and temperature [51, 54].

It was necessary to investigate whether there was any influence from fluctuations in daily temperatures, especially for surficial soil measurements, and for freezing and thawing [21]. The effect of temperature on the VWC has been already mentioned in the literature by several authors. On the one hand, Bogena [53], used an EC-5 in a known liquid permittivity at a range of temperatures (5-40°C) and found that the sensor generally showed an increase in VWC with an increase in temperature. On the other hand, Topp [51] measured the apparent dielectric constant (related to VWC) using a TDR in clay loam in a temperature range of (10-36°C) and stated that there was no significant temperature dependence. Pepin [55] used TDRs to study the effect of temperature in VWC in sand and peat and found that the dielectric constant decreased with increases in temperature, and suggested the use of empirical or theoretical relationship corrections due to temperature effects on the composite dielectric constant for higher VWCs. As no defined trend in the effect of temperature in the soil has been found and no one has referred to a gravelly soil, a site-specific calibration with maximum sizes passing the 45 mm sieve was carried out for the seasonal variation in temperature, which is presented here.

Monitoring instruments

Each instrumented trench contained time domain reflectometry (TDR100; Campbell Scientific) and capacitance sensors (EC-5/ 10HS; Decagon Devices) to determine the VWC by means of the measurement of the apparent dielectric constant /permittivity. The

VWC was complemented by temperature and precipitation data from two meteostations. Detailed information about the sensors and meteostations can be found in [21].

A site-specific calibration was performed (Figure 5.4) to verify whether the VWC values at similar depths and location will improve in terms of accuracy for each IT (1-4), when compared with the original calibration, which was done at room temperature with the soil from IT1 only. This recalibration used soil sampled from the field at each of the IT locations, and a temperature range variation (-5 °C to room ambient temperature).

Each sensor was calibrated in the laboratory after it had been removed from the field, under a programme of controlled moisture and temperature conditions, simulating the changes in weather conditions for every season. Although some of the sensors were broken after three years in the field, and some of them failed during the recalibration process back in the laboratory, it was possible to record information from the remainder (TDR, EC-5, 10HS) to analyse the effect of temperature changes in the sensor performance when these were installed in gravelly soil at similar relative densities.

Procedure

Samples were reconstituted in a rectangular box with base dimensions of 26x36cm (Figure 5.4), and with approximately 20 cm height, with soil collected from the field at each instrumented trench location. The dry unit weight from each IT1-4 was obtained from the in situ densitometer test, and used to reproduce the field conditions for each of the 4 laboratory samples.

The models were constructed with soil mixed homogeneously in four layers of 5 cm height. The TDR and capacitance sensors were inserted in the soil in horizontal and vertical directions, respectively allowing spacing between volumes of measurements. Air and soil temperature sensors, EC-5/10HS and TDR sensors were connected to the same data logger as in the field.

Moisture content and temperature conditions were maintained for 10-15 minutes at each stage and the rate of data recording was 0.04 Hz. The moisture content of the soil was increased from 0, 1, 3, 5, 8 % up to saturation, and measurements were recorded at the following temperatures: ambient room (17-23 °C), 10, 1 and -5 °C.

After each measurement at a defined temperature, the water content was determined and water added to reach the VWC target. Finally, a grain size analysis was performed

on the four model samples according to the Swiss standard classification (SN 670 004-2NA).

5.3.3 Preliminary numerical modelling

Preliminary numerical simulations into the slope stability were performed using the program SEEP-SLOPE/W [31] on a simplified prototype of the scree slope, consisting of a representative gravel layer and varied bedrock geometries which were then subjected to groundwater flow. The objective was to determine which bedrock geometry represents the most hazardous scenario under similar groundwater hydraulic conditions.

Model

The model (Figure 5.6) consisted of a unique layer of homogeneous gravel of 2.5 m thickness underlain by impermeable bedrock that could be either parallel to the slope or with a bedrock step. The gravel parameters were derived from the soil characterisation in this study (Table 5.3). Four different types of slope-bedrock geometry were tested: a) bedrock parallel to slope with toe, b) bedrock parallel to slope with no toe, c) bedrock with a single step and toe and, d) bedrock with a single step and no toe. Although the scree slope length is of the order of the 600 m (Figure 5.1(b)), the model was simplified to 50 m for this preliminary analysis, and the angle of inclination was selected as 40°, within the range of the slope inclination reported for the scree slope [21].

Hydraulic conditions

Input flow (Q) to trigger instability was applied to the top of the slope for each geometry case. This groundwater flow antecedent increased the saturation in the well-drained gravel in the steep slope and hence the PWP decreasing the effective stress of the soil. Although the variation of PWP due to water infiltration is a time dependent process, a simplified steady state analysis was conducted using SEEP/W with saturated/unsaturated analysis to impose the hydraulic condition for the further slope stability analysis.

Slope stability analysis

Slope stability simulations were performed in 2D using the SLOPE/W program based on the Morgenstern-Price method [31] and the hydraulic conditions imposed by SEEP/W. A slip surface failure is determined for a factor of safety ($F.S$) = 1. Due to the increase in

PWP, the effective confining stress in the slope decreases, triggering the failure. The results provided here corresponded to a preliminary and simplified analysis.

Table 5.3. Numerical simulation soil properties.

Parameter	Value
Soil classification	GP-GM
Internal friction angle ϕ'	41°
Specific density (kg/m ³)	2.68
Cohesion c' (kPa)	1
Hydraulic conductivity (m/s)	1.30×10^{-5}
Dry unit weight (kN/m ³)	19.42
Void ratio e (-)	0.38

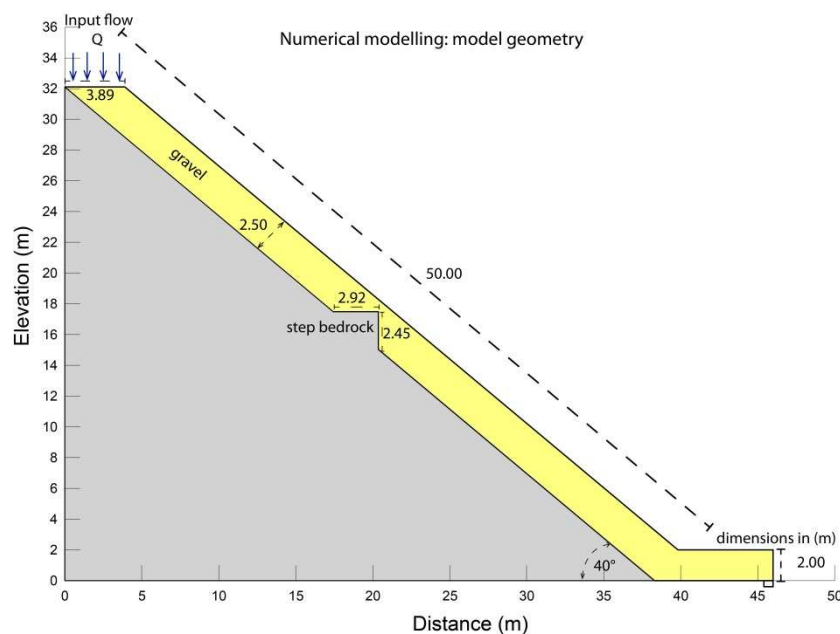


Figure 5.6. Model slope-bedrock geometry for the numerical modelling with bedrock step and toe (type c) with units in m.

5.4 Results

5.4.1 Characterisation

5.4.1.1 Dry unit weight

Two campaigns of in situ measurements were performed to determine dry unit weight, the first presented in [21], and the second performed in 2016 (Table 5.4). It was extremely challenging to carry out such tests in the field because of the steep slopes (mostly between 33-43°), which contained coarse gravel and cobbles, and which in many cases led to unstable walls when excavating the nominally cylindrical void. This volume often exhibited an irregular shape due to stones crossing the boundary of the nominal

circular ring around the excavation; therefore, the volume excavated was often less than that defined in the test specification.

Notwithstanding these challenges, sixteen densitometer tests were completed in total during the field monitoring programme. One single preliminary test was carried out prior to November 2015, a few metres downhill of IT4 in a relatively flat area, with a unit weight of 19.11 kN/m³. A second test in November 2015 was discarded, because of failure of the excavation during testing. Later, a campaign of 9 tests was performed in July 2016 [21] in the steep slope, which affected the volume of measurement due to the reasons mentioned previously. A final campaign of 5 tests was achieved in November 2016, after searching for suitable locations where the densitometer tests could be carried out closer to the norm, in terms of uniform volume cylinder. The results are presented in Table 5.4.

Table 5.4. Dry unit weight calculated from in situ testing.

	Final campaign November 2016		Dry unit weight used in site-specific recalibration		
	void ratio [-]	dry unit weight [kN/m ³]	void ratio [-]	dry unit weight [kN/m ³]	D _{max} [mm]
IT1	0.29	19.95	0.32	19.91	31.5
IT2	0.38	18.75	0.40	18.84	60.0
IT3	0.38	18.73	0.41	18.61	31.5
IT4	0.32	19.54	0.36	19.32	31.5

5.4.1.2 Grain Size Distribution (GSD)

The GSD of the soil extracted from each instrumented trench (IT1-4) was determined and used for the 4 sets of site-specific VWC sensor recalibrations, with the same GSD profile and a D_{max}= 31.5 mm and 60 mm for IT1, IT3-4 and IT2 respectively. The results and the GSD curves are presented in Figure 5.7 and the classification in Table 5.5, showing a mixture between poorly graded gravelly scree with sand and silt, with more fines in IT1 and IT4.

Table 5.5. Soil classification of scree soil from the instrumented trenches.

Trench	D ₁₀ [mm]	D ₃₀ [mm]	D ₆₀ [mm]	C _c [-]	C _u [-]	Percentage of fines [%]	Swiss Standard Classification (SN 670 004-2b NA)
IT1	<0.06	1.525	7.70	-	-	11.50	GP-GM
IT2	0.075	2.075	8.35	6.87	111.3	9.43	GP-GM

IT3	1.010	6.05	11.45	3.16	11.3	4.97	GP
IT4	<0.06	1.1	6.40	-	-	13.61	GM

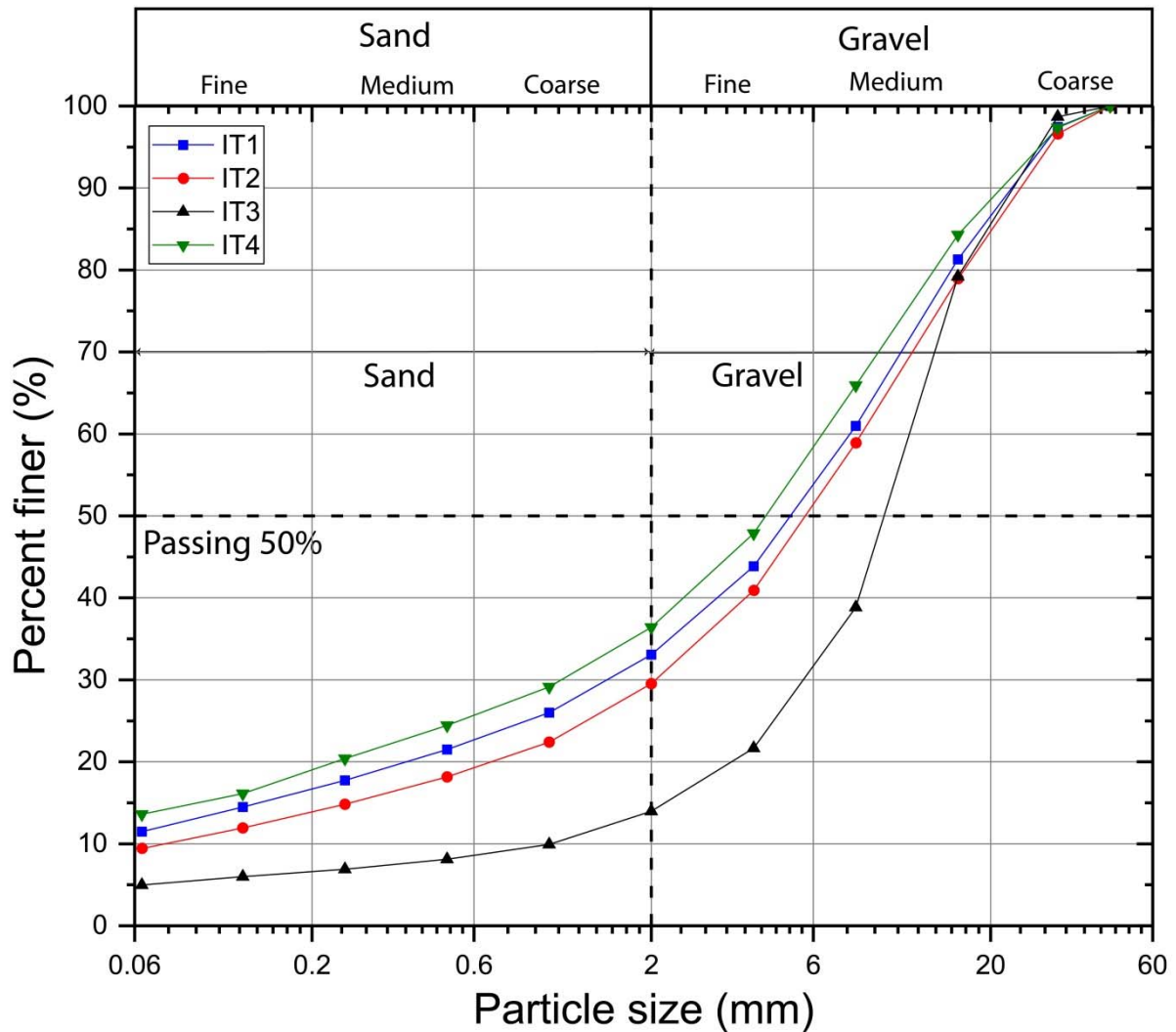


Figure 5.7. GSD site-specific calibration soil instrumented trenches IT1-IT4 after site-specific calibration process.

5.4.1.3 Triaxial stress path testing: CSD results

Results of the CSD tests are shown in Figure 5.8, in terms of ϵ_a versus p' , ϵ_v versus p' and q versus p' . Table 5.6, shows the stresses p'_F and q_F at failure, which were used together with the slope $M = (6\sin\phi')/(3 - \sin\phi')$, to obtain a friction angle at failure ϕ' of 42° and 41° , for the mid- and large-scale specimens respectively, with zero cohesion ($c' = 0$) in both cases.

Table 5.6. Summary of CSD triaxial stress path test results at failure from an adopted GSD of the gravelly scree.

Test	D_{ri} [%]	σ'_{1c} [kPa]	σ'_{3c} [kPa]	q_c [kPa]	p'_c [kPa]	ε_{ac} [%]	ε_{vc} [%]	M [-]	ϕ' [°]
mid_1	27	77.0	16.3	60.8	36.5	4.35	-0.66	1.66	41
mid_2	17	40.3	7.8	32.5	18.7	3.43	-0.53	1.74	42
mid_3	10	60.5	13.1	47.4	28.9	3.07	-0.35	1.71	42
large_1	46	61.2	8.7	52.5	26.2	4.21	-0.80	2.00	49*
large_2	60	32.8	2.1	29.7	12.0	1.41	-0.54	2.50	61*
large_3	29	156.5	32.0	124.5	73.5	6.32	-0.11	1.70	41

*: These values include dilatancy.

Figure 5.8 (a)-(d) illustrate steep increases of dilation and axial strain after the yield point of the gravel, followed by initiation of failure. The soil behaviour is dilative in most cases (Figures 5.8(c), (d)) with the exception of the test large_3, ($D_{ri}=29\%$) (Figure 5.8(d)), which contracts initially, and then dilates towards failure.

The stress paths shown in the $p' - q$ diagrams in Figures 5.8(e), (f), exhibit a horizontal constant deviator stress path until reaching failure, where the soil specimens no longer represent right cylinders and the calculated stresses decrease. A critical state line (CSL) was drawn through the origin and the stresses at failure in the mid- and large-scale tests Figures 5.8(e), (f). The mid-scale triaxial tests lead to derivation of a single CSL line, probably due to the finer soil grading (Table 5.1), which dominated the mobilisation of the soil strength. The large-scaled triaxial tests show different dashed lines (Figure 5.8(f)) of data representing the higher friction angles mobilised at low confining pressures, which are attributed to dilatancy (e.g. [43]) and the influence of the hardness of the coarser gravel on the shear strength. In this case the values reported in Table 5.8 for the tests large_1 and large_2 do not represent the critical state conditions [43].

The dilatancy angle (ψ) (equation (5.1),(5.2),(5.3)) was calculated for each of the triaxial tests (Table 5.7) in terms of the dilatancy index (I_R), mean effective stress (p') and relative density (I_D) according to Bolton [43] equation (5.1).

The dilatancy mobilised at nominal failure was found consistently to be larger at low confining pressures (Table 5.7). Theory suggests that the lower the confining stresses, the higher the relative density and grain crushing strength, the greater the I_R and hence ψ [43]. The small angle of dilation obtained in test large_3, carried out at higher

confining pressure, indicates the possibility of particle abrasion or crushing during testing [43, 56-59]. This assumption was confirmed by comparing the grain size distribution before and after shearing, where an increase of approximately 4 % in the fines content was observed in the post-test sieving due to shearing (Supplementary material).

Table 5.7. Calculated dilatancy in triaxial tests.

Test	e_0 [-]	I_{D0} [-]	e_B [-]	e_C [-]	I_{DC} [-]	p'_C [kPa]	I_R [-]	ψ [°]
mid_1	0.49	0.27	0.275	0.283	0.95	36.5	4.34	13.03
mid_2	0.52	0.17	0.323	0.330	0.80	18.7	4.00	12.00
mid_3	0.54	0.10	0.371	0.376	0.64	28.9	2.76	8.28
large_1	0.53	0.46	0.364	0.375	0.90	26.2	4.36	13.07
large_2	0.48	0.60	0.332	0.339	1.00	12.0	5.75	17.26
large_3	0.59	0.29	0.581	0.593	0.28	73.5	0.37	1.12

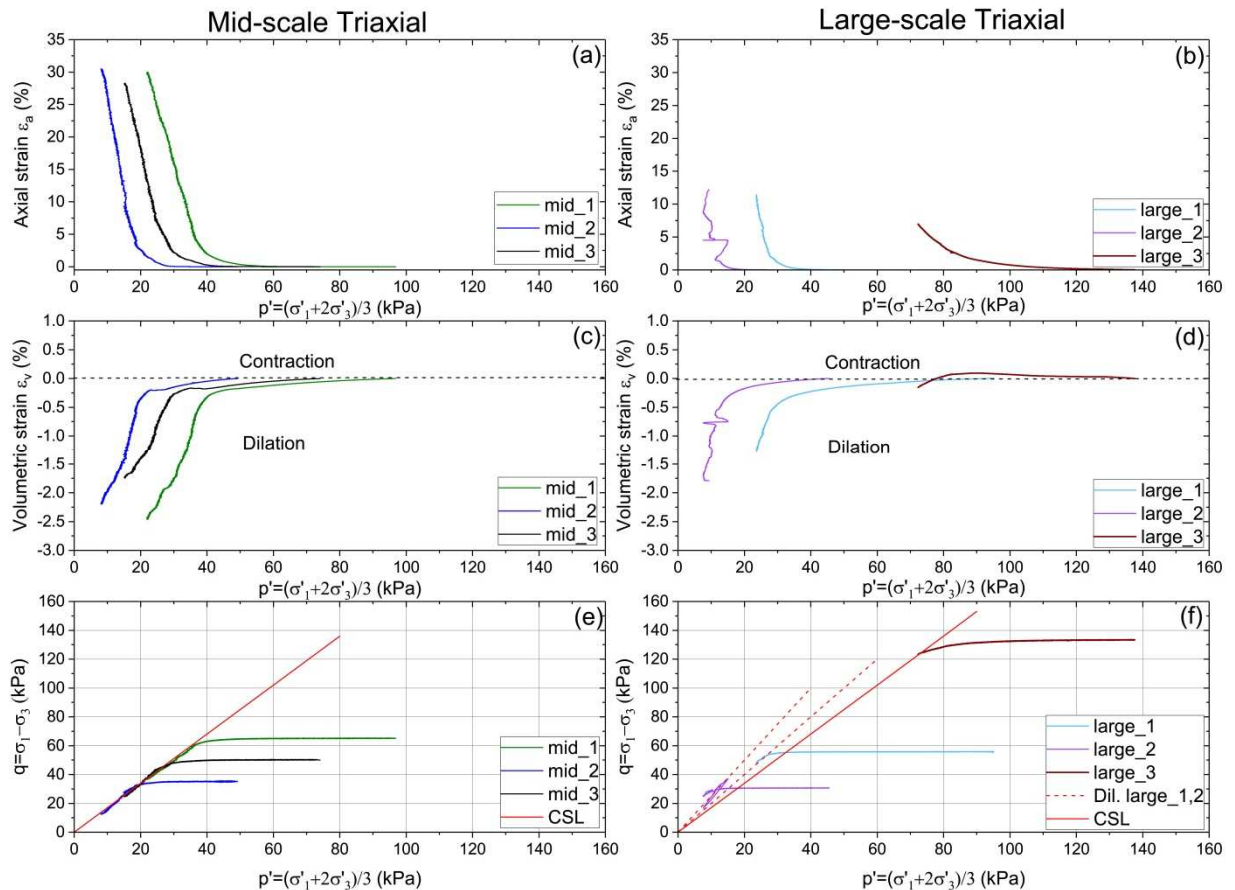


Figure 5.8. Constant shear stress drained test (CSD) results. (a), (b) axial strain versus mean effective stress; (c), (d) volumetric strain versus mean effective stress; (e), (f) shearing of gravelly scree soil (medium and large, with maximum particle size of 16 and 31.5 mm respectively) at constant deviator stress and showing the stress path and critical state line (CSL). The mid-scale triaxial test is on the left, the large-scale on the right.

5.4.1.4 GPR results

Figures 5.9(a),(b) shows an example of a processed GPR section. It is roughly parallel to the slope inclination (Figure 5.1(b)). Reflections from the bedrock interface can be identified quite clearly (blue arrows in Figure 5.9(b), although they cannot be traced continuously along the entire section. All reflected signals have been picked from all profiles and the corresponding bedrock depths have been interpolated across the entire scree slope covered by the GPR profiles.

The resulting contour line map is shown in Figure 5.10. Each colour represents an estimated depth of the bedrock, varying from 0.2 m (blue) to 2.8 m (red). The contour map shows that IT1-4 are located, where the bedrock depth is between 0.6 to 1.6 m, and that the deeper location of the bedrock is oriented to the mid-west, towards the uphill section of the scree slope. This result suggests that the maximum volume that could be mobilised in a potential landslide on this slope (of triangular area with average depth of 1.5 m) would be approximately $0.5 \times 100 \times 200 \times 1.5 = 15000 \text{ m}^3$.

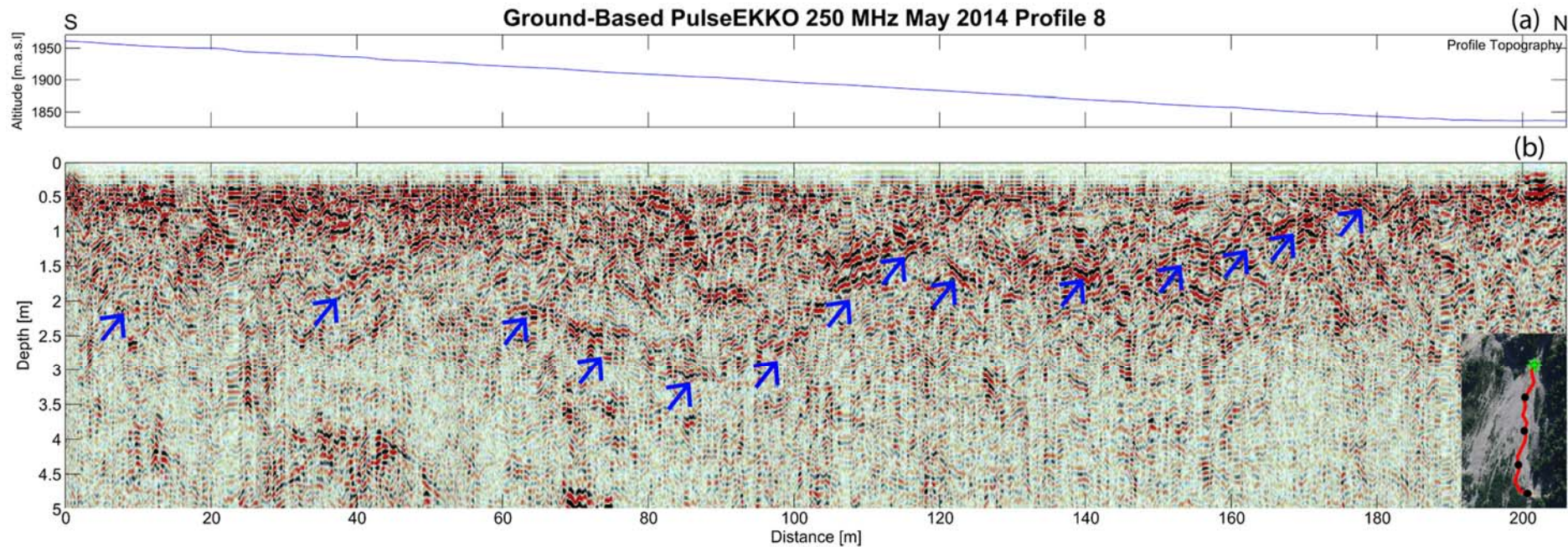


Figure 5.9. Resulting Ground-based GPR section from profile 8 (Figure 5.1(b)). (a) Ground elevation in longitudinal view; (b) Results after all processing steps were applied. Blue arrows indicate reflections from the bedrock interface.

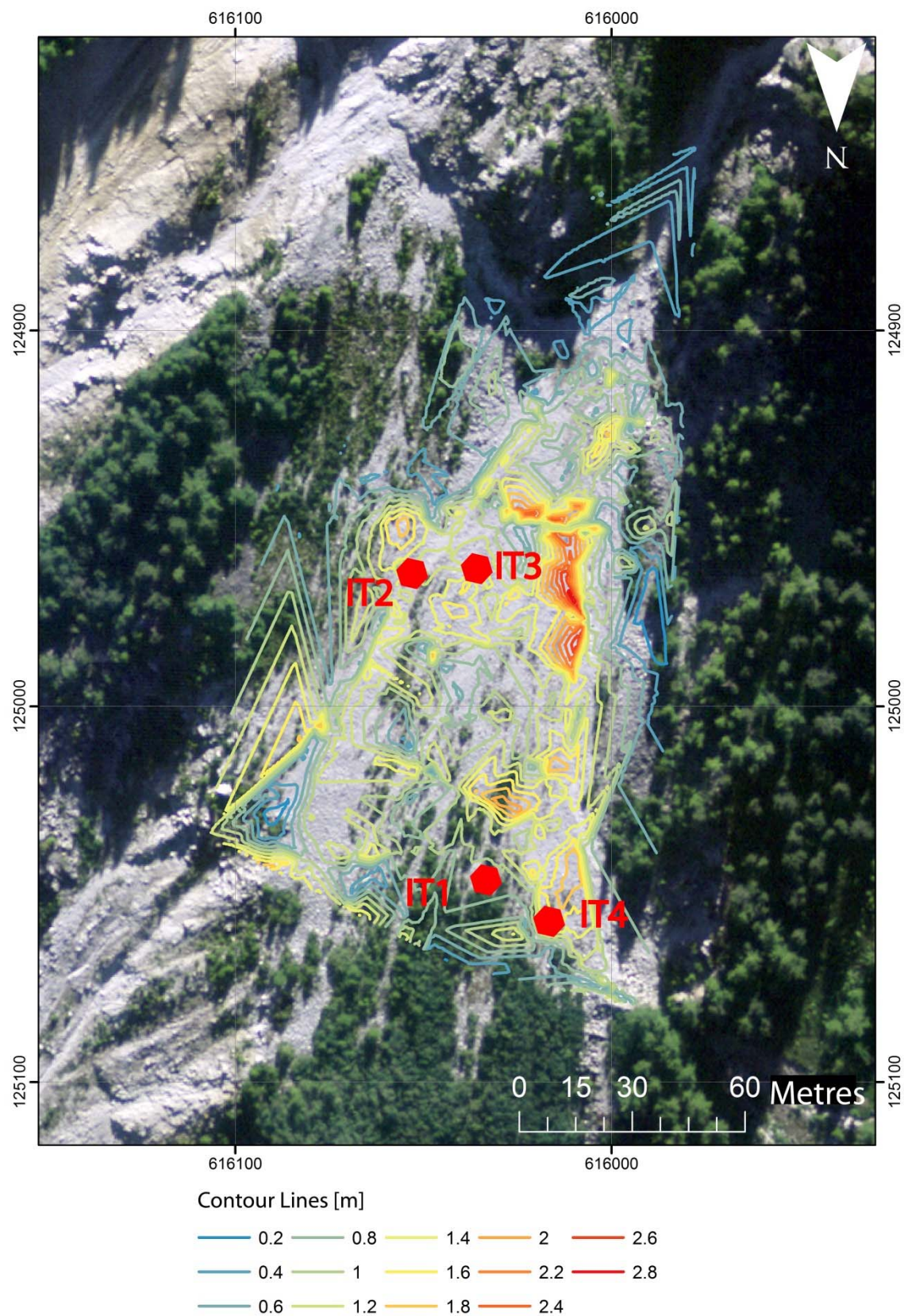


Figure 5.10. Contours lines of depth to bedrock in metres.

5.4.2 Monitoring

5.4.2.1 Overview

The VWC and temperature were measured at specific locations of the slope (IT1-4), and the data was complemented by the precipitation data from two meteostations. Figure 5.11 shows the data overview for VWC and temperature versus date measured in each trench (IT1-4) over a period of three years monitoring from November 2013 to October 2016. Each colour trace represents a VWC measured with a type of sensor (EC-5, 10HS and TDR), which has been recalibrated following reassessment of the relevant parameters. The depth was recorded in the sub-index for both VWC and temperature sensors. The plots are arranged in chronological order of installation and the precipitation recorded by two meteostations, IGT and WSL, is added at the bottom. Background colours of light blue and yellow differentiate between winter and summer regimes, respectively.

New data addition: November 2015-October 2016

Figure 5.12 (framed in blue in Figure 5.11) shows the new data (Nov. 2015-Oct. 2016), which completes three years of monitoring. Graphs of VWCs and temperature are shown consecutively for each trench, with the precipitation (rain/snow) and air temperature at the bottom.

A continuous minimum VWC was not observed in any IT during this winter period, and a sustained increase of VWC (January to March 2016) was noticeable in IT1-2. This could be attributed to periods of unusually high ambient air temperature, which were predominantly positive (green trace), alternating with intense snowfall (peak of over 60 mm/day after mid-January) and avalanche events (recorded by in situ cameras, which caused loss of data in IT4 from 21.11.2015 to 24.05.2016). Despite the soil temperature in all of the trenches being recorded as near or below 0 °C, this “short winter” combined with periods of warmer temperatures may have induced early snowmelt, removing the insulating snow layer, facilitating water infiltration and potentially causing surface erosion. The VWC recorded at IT4 during the summer season provided useful information, especially at deeper locations (up to 1 m), showing higher VWC with depth, and with peaks close to 0.5 in June indicating that the soil was near to saturation (1 m depth).

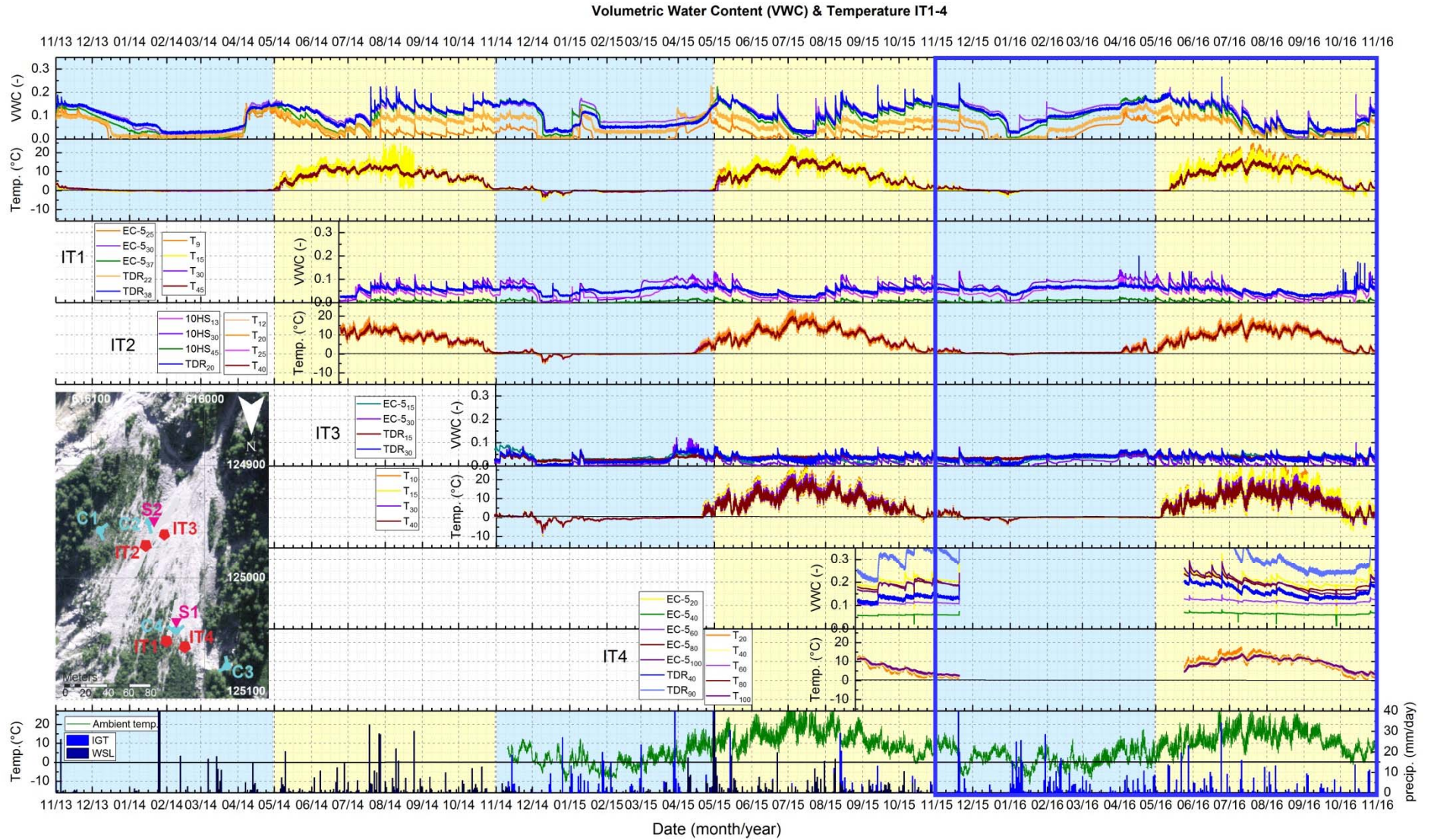


Figure 5.11. Overview of measurements at instrumented trenches IT1-4 in the Meretschibach catchment for three years duration of monitoring (November 2013–October 2016): VWC, temperature with precipitation data at the bottom.

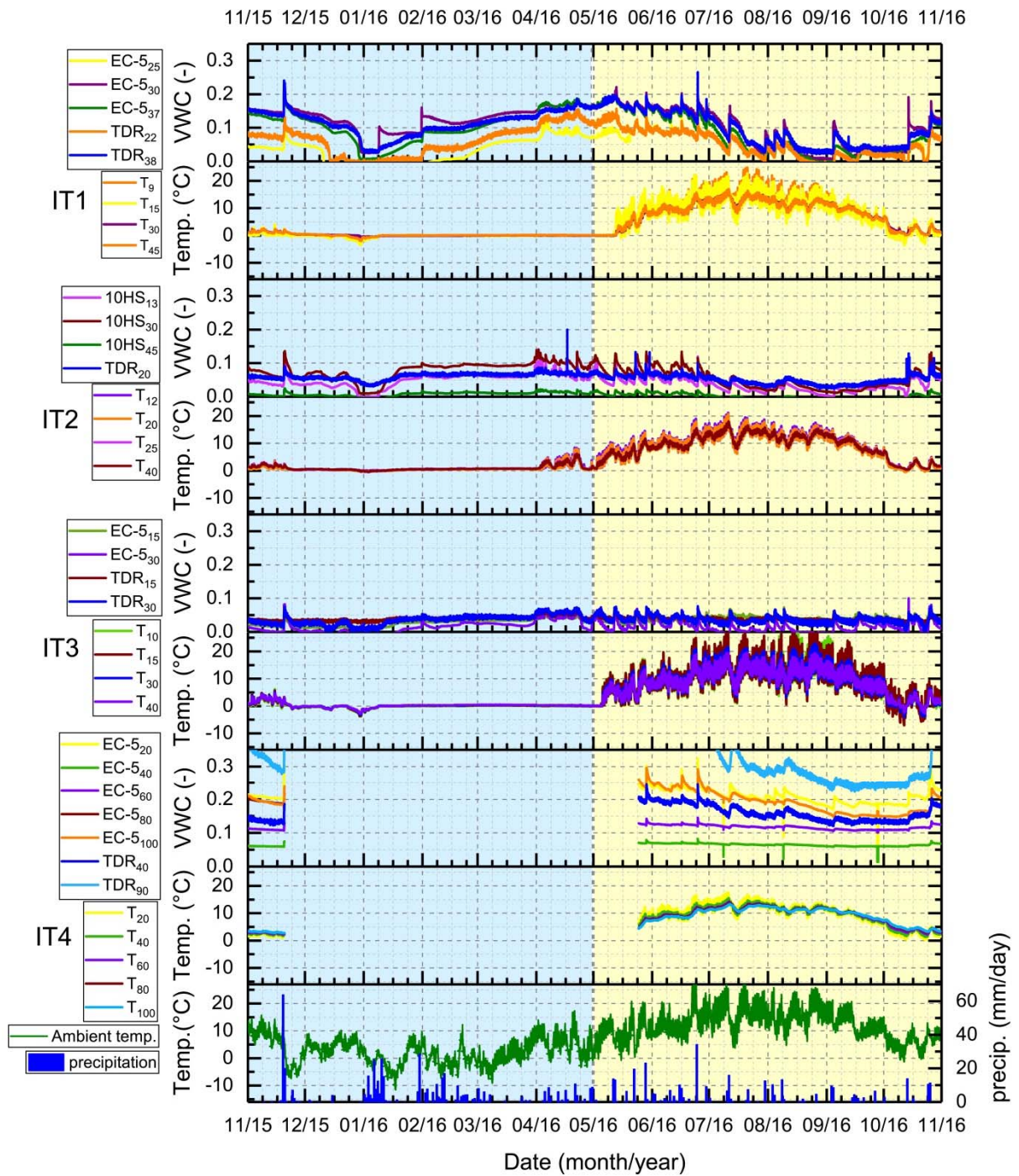


Figure 5.12. Measurements at instrumented trenches IT1-4 last year of monitoring (November 2015-October 2016): VWC, temperature with precipitation and ambient air data on the bottom.

5.4.2.2 Site-specific calibration

VWC measurements over a range of temperatures

The VWC sensors used in each trench were recalibrated in soil excavated from each IT (Figure 5.4, 5.7), which had been reconstituted at the field relative density (Table 5.4)

with different VWCs (moisture content of 0, 1, 3, 5, 8 % or up to saturation) and temperatures applied, varying from -5 °C to room temperature (17 to 23°C). A relationship was determined to calculate the VWC as a function of temperature.

Sensor measurements indicate soil temperatures ranging from -5° to 23°C. Figures 5.13(a)-(f) show the recalibration data and equations for IT1, IT2 and IT4. Each row corresponded to the VWC measured with capacitance sensors (EC-5/10HS, left) and TDR (right) respectively for the same trench. Each colour (blue, green, red) defines the target temperature (1°C, 10°C, room temperature), respectively. Data shown in orange corresponds to the initial calibration obtained using soil from IT1 with measurements at room temperature. The calibration equation to determine the VWC for each sensor was the best (linear or polynomial) fit to the data, with the highest value of R^2 .

The full record of data for each sensor in trenches (IT1-4) can be found in the supplementary material.

Sensor measurements at temperatures under 0 °C

In the case of an unfrozen soil, the VWC reflects the combined permittivity of air, ice and unfrozen water [60-63]. Data recorded in the laboratory at negative temperatures were excluded from the recalibration, since the VWC associated to the unfrozen water present in the soil was not measured. The measurements were low similar to those obtained from the original calibration with a range of VWC between 0-0.07 [21].

VWC sensor recalibration equation

Figure 5.14(a)-(f) shows a unique recalibration equation (in blue colour) for IT1, IT2 and IT4, which integrates all of the data presented in Figure 5.13 for temperatures >0°C. The advantage of this new recalibration over the original calibration (orange colour), is that these later measurements were performed with the soil excavated from the destination trench and reconstituted at the void ratio measured in the field.

Impact of maximum grain size

A sensor calibration was completed with a maximum grain size passing the 45 mm sieve, using a capacitance sensor EC-5 (at approximately 20°C) and in soil from IT1 sieved to the GSD (Figure 5.7). It shows that the VWC is underestimated at finer gradings, confirming a very significant effect of the GSD on the calibration factors.

5.4.2.3 Comparisons for seasonal responses of the scree slope

The VWC and temperature measurements by season are shown in Figures (5.15-5.18) with a VWC determined using the original calibration [21] in soil from IT1, and compared to the site-specific recalibration results (2018), performed with soil from each destination trench at an equivalent void ratio .

Summer

Figures 5.15 and 5.16 represent the summers of 2014 and 2015 respectively. Each colour represents the VWC measured with either a EC-5/10HS or a TDR sensor at a certain depth, using the original calibration, or the new site-specific recalibration.

Good agreement can be observed between the VWC measured with EC-5 in IT1 in Figures 5.15(a) and 5.16(a), since the original calibration and the re-calibration were performed with the same soil. A shift in the VWC in Figure 5.15(a) can be observed after a debris flow event (beginning of August), which could have happened due to a changed the local soil conditions in the volume of measurement or sensor performance.

The VWC calculated from the original calibration factors and those from the recalibration show more differentiation in IT2 and IT4 (Figures 5.15(c), 5.16(c) and 5.16(e) respectively), due probably to the different soils, IT1 for original calibration and from the respective trench in the recalibration, and void ratios adopted to represent field conditions in the calibration process. Sensors 10HS₁₃ and TDR₂₀ in IT2 Figure 5.15(c), appeared to agree better after recalibration, exhibiting notably lower values in VWC (0.05-0.1).

Winter

Figure 5.17(a), (c) shows a comparison of VWC determined using the original and recalibration equations for the winter period for IT1-2 respectively. A larger difference in the magnitude of VWC in EC-5₂₅ Figure 5.17(a) was observed after mid-December with negative values, which is not feasible (same sensor with shifted readings after the debris flow (Figure 5.15(a))). Furthermore, the soil voids contain air, ice and unfrozen water during the winter regime. The replacement of air by ice in the voids should increase the combined dielectric constant, and therefore VWC should be greater than dry soil with air ($K_{\text{air}}=1.0$; $K_{\text{water}}=78.5$ at 25°C; $K_{\text{ice}}=3.2$ and $K_{\text{soil}}=3-7$). This suggests that a polynomial calibration equation where the curve flattens at lower VWC, as shown in Figure 5.14(e)

would be a better fit for the determination of VWC during a winter regime. Some other differences between the original calibrations and the recalibration in IT2 (Figure 5.17(c)) could be attributable to the different soil and void ratio. The TDR₂₀ (Figure 5.17(c)) shows a greater range of magnitude in the VWC measurement than the 10HS₃₀. Finally, peaks in VWC in winter were observed due to precipitation of snow/rain combined with periods of ambient temperatures in a range of (-10 to 12°C).

Spring/Autumn

The variations in results for both calibrations are rather insignificant (in engineering terms) in Figure 5.18(a) for IT1, EC-5. The TDR data after recalibration displays a greater range in magnitude. IT2 10HS calibrations are similar, with some differences for 10HS₄₅ (Figure 5.18(c)).

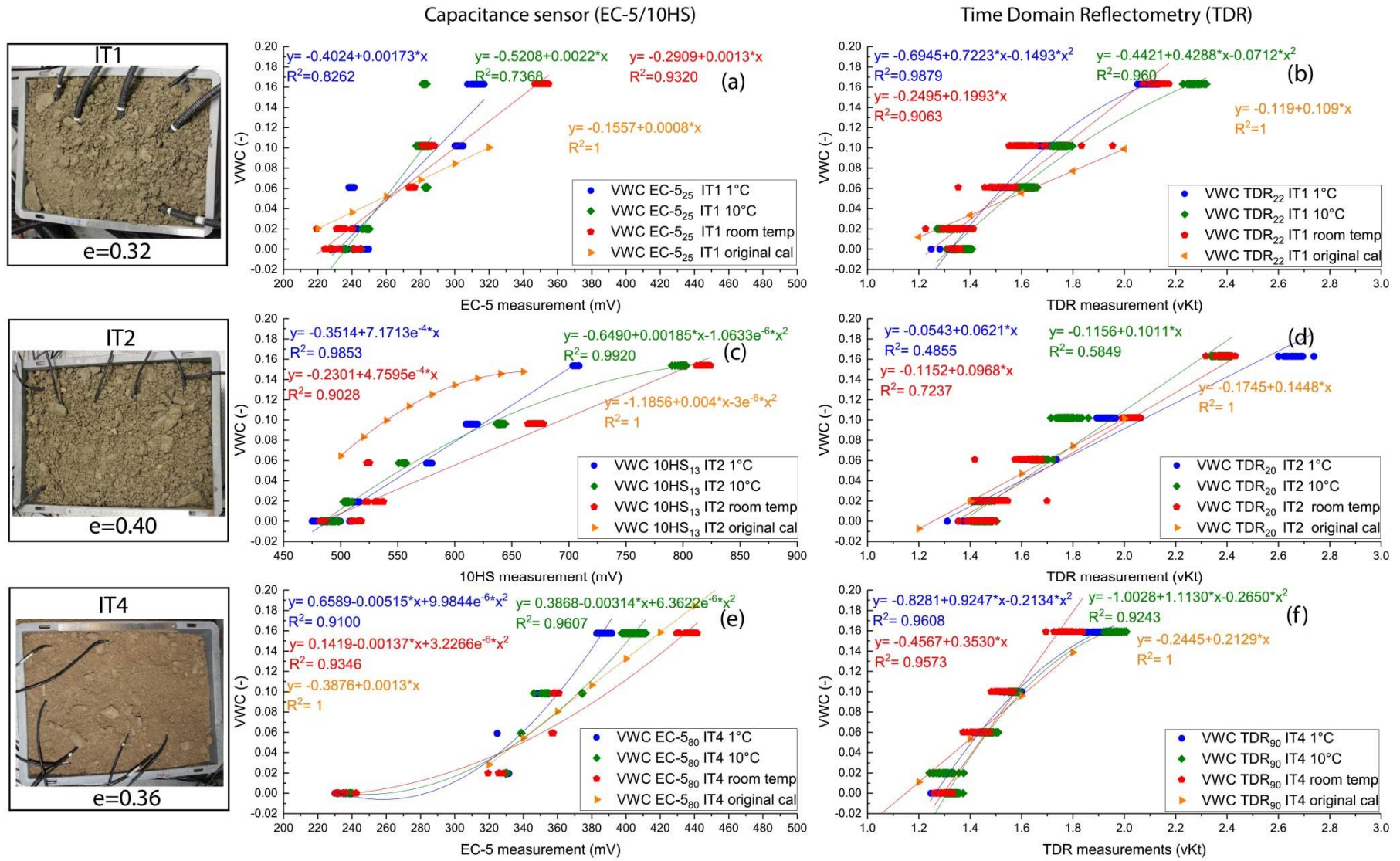


Figure 5.13. Site specific calibration of VWC sensors of IT1, IT2, IT4 and the effect of temperature. With the exception of TDR in IT2 where $R^2 < 0.5$, all $R^2 > 0.82$.

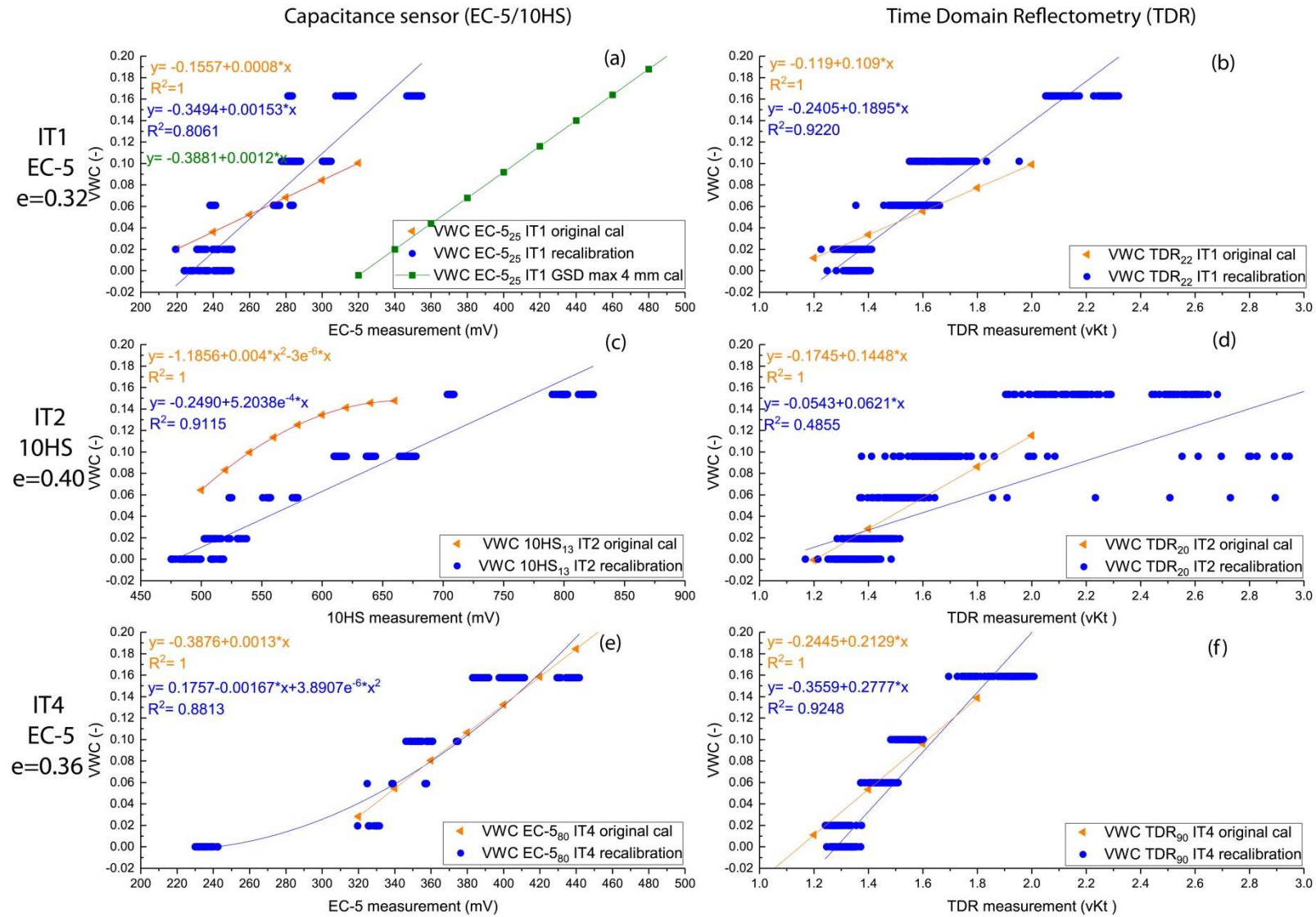


Figure 5.14. Site specific calibration for IT1, IT2 and IT4. For a range of temperature (1 to 23°C).

Data Period 1: 1. July 2014 - 31. August 2014

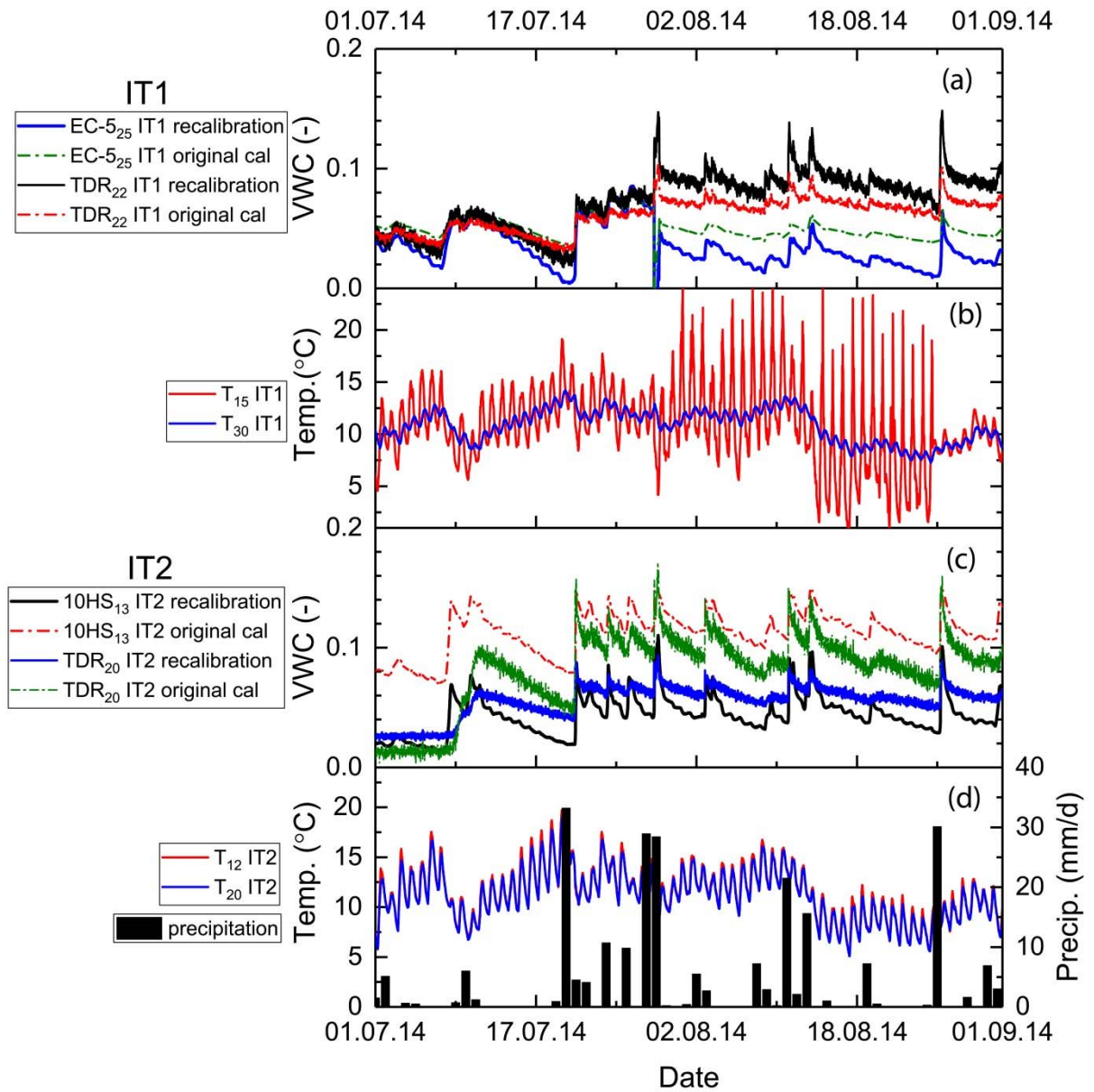


Figure 5.15. Site-specific calibration: comparison between data based on original calibration and the recalibration for the summer period.

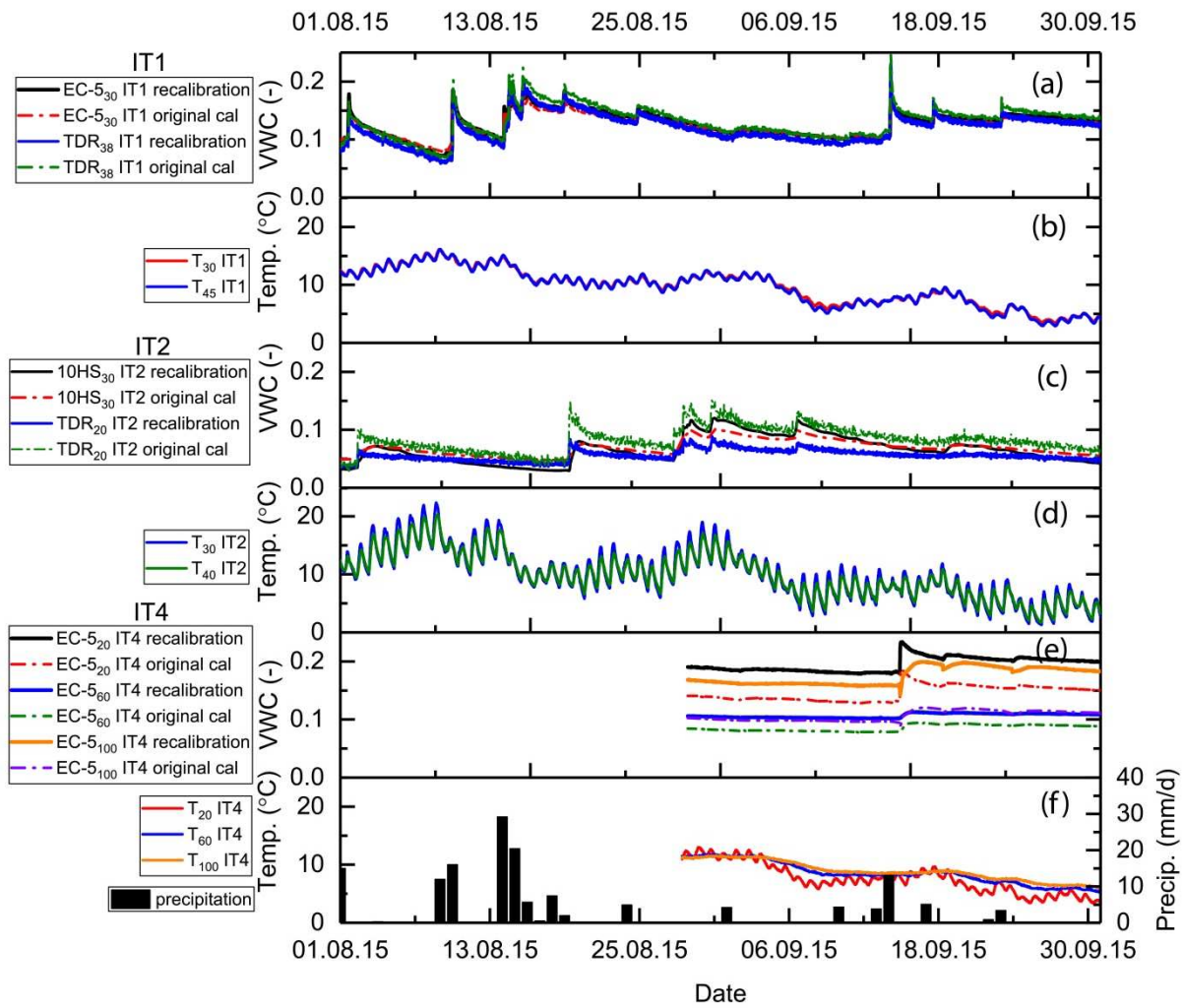
Data Period 4: 1. August 2015 - 30. September 2015


Figure 5.16. Site-specific calibration: comparison between data based on original calibration and the recalibration for the summer period.

Data Period 2: 1. December 2014 - 30. January 2015

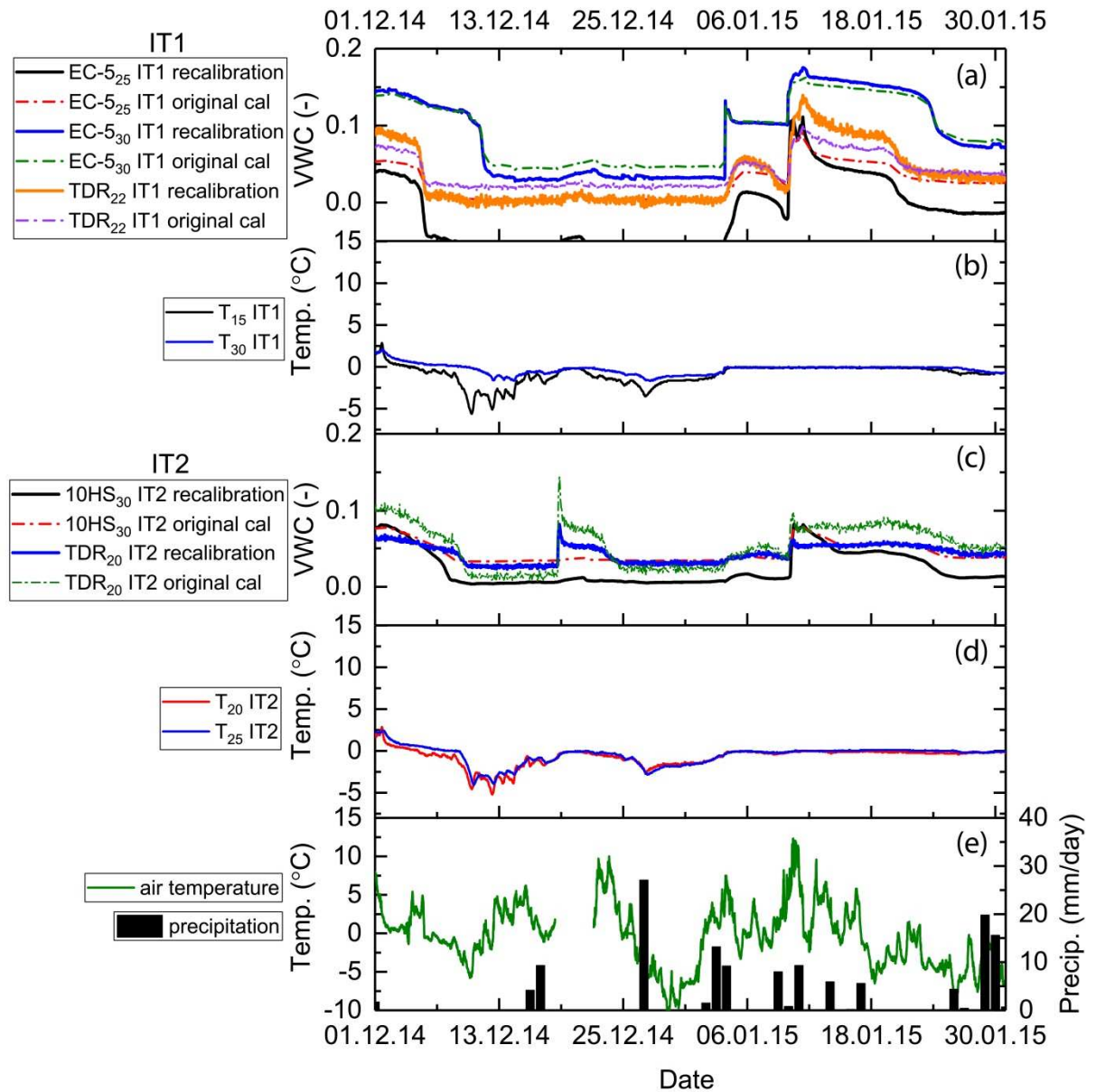


Figure 5.17. Site-specific calibration: comparison between data based on original calibration and the recalibration for the winter period.

Data Period 3: 15. April 2015 – 15. May 2015

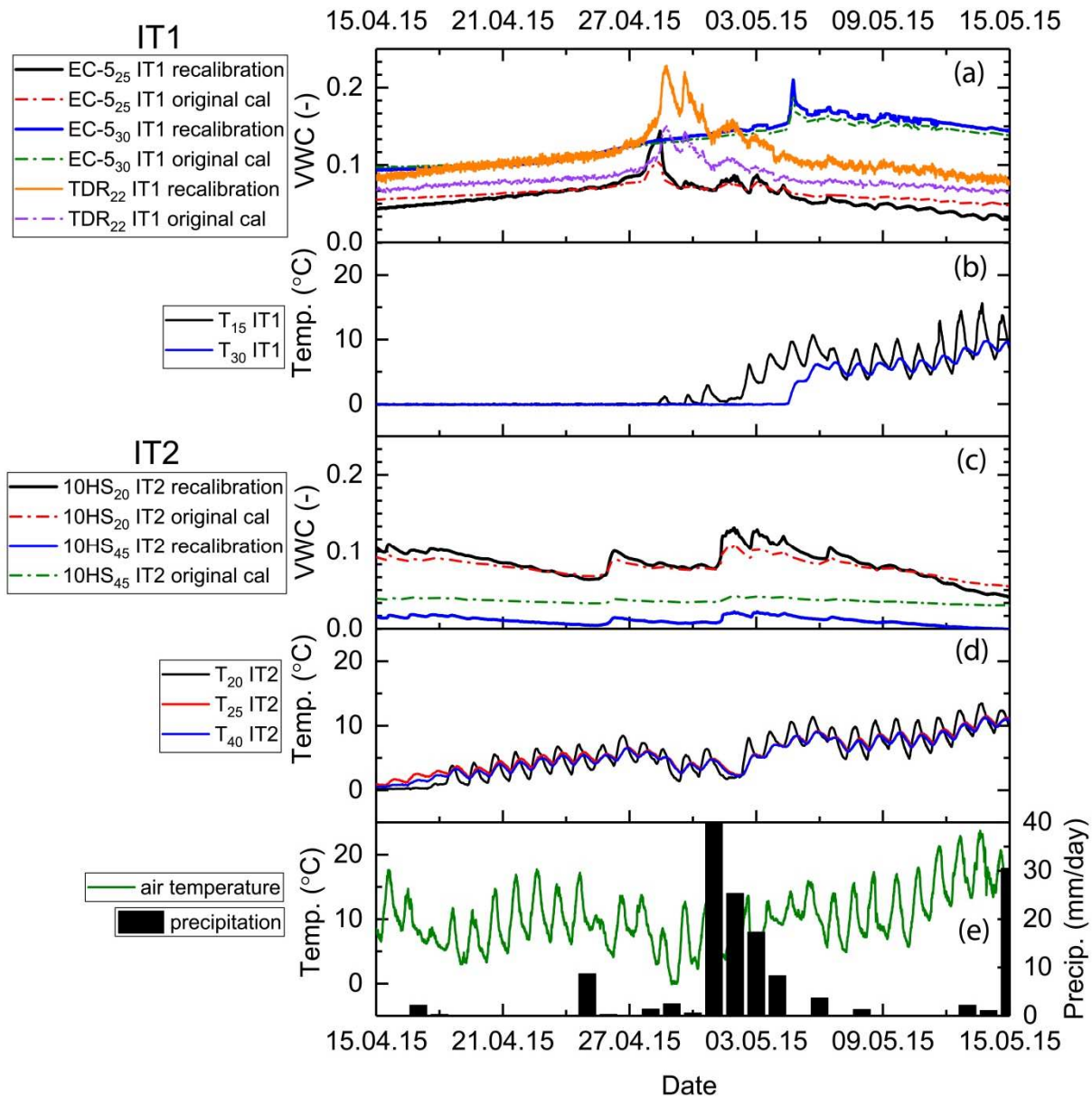


Figure 5.18. Site-specific calibration: comparison between data based on original calibration and the recalibration for the spring period.

5.4.3 Numerical modelling

Preliminary simulations of the instabilities caused by saturation of the ground through flow downslope were analysed using four different ground model geometries. Each of these four models represent a scenario of the scree slope (Figure 5.19), with (a) slope parallel to bedrock with toe, (b) slope parallel to bedrock no toe (c) bedrock step with toe and (d) bedrock step no toe. A phreatic water table was achieved by applying an input flow Q at the top of the slope to cause an instability with a $F.S=1$. The flow Q was determined for comparison of the hazard scenarios and given in Table 5.8.

A slip failure surface is shown in green with the water table plotted dashed in blue. The results show that the safest configuration under the imposed hydraulic conditions would be a) in that the flowrate at failure is significantly greater and the initial volume displaced is the smallest. Bedrock step case (d) requires the least water flow to fail, and is therefore the most hazardous although the differences (c) and (d) are small because they are affected primarily by the bedrock step. The role of the toe is important in that it prevents the water from emerging as a spring on the surface, leading to development of an initial local failure mechanism. The volume mobilized was greatest in case (b).

Table 5.8. Water flow input to cause slope instability ($F.S=1$) in a numerical model (Geoslope).

Case	Q [ml/min/m]	Volume estimated [m ³ /m]
(a) slope parallel to bedrock with toe	819.0	19.7
(b) slope parallel to bedrock no toe	585.0	56.6
(c) bedrock step with toe	562.0	34.0
(d) bedrock step no toe	515.0	28.3

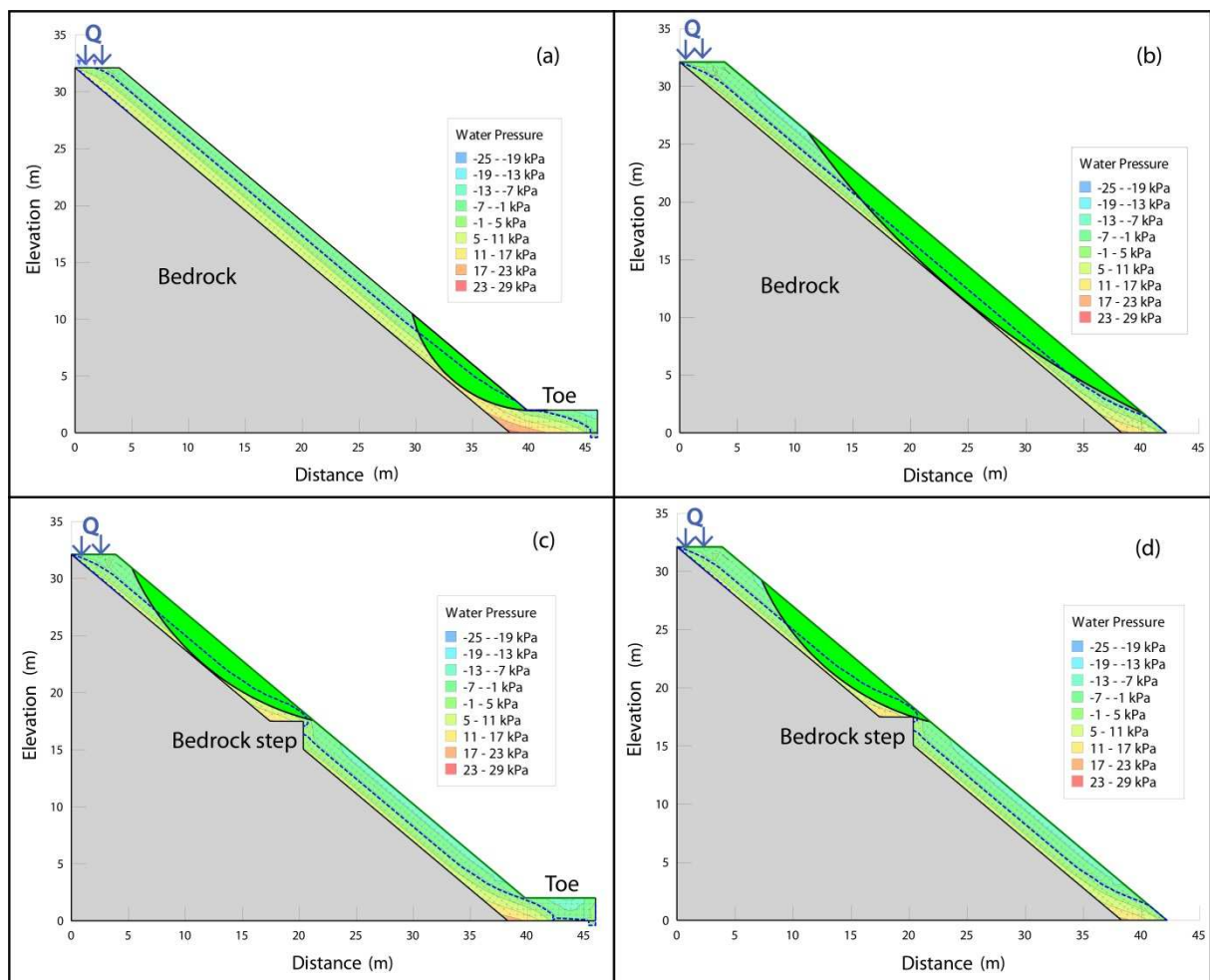


Figure 5.19. Preliminary numerical modelling of instabilities for four different slope bedrock geometry.

5.5 Interpretation and discussion

5.5.1 Characterisation

GSD

The GSD at IT1-4 was measured at the beginning (2014) and at the end of the monitoring (2016) with the same sampling techniques. Similar results are obtained ([21]; Figure 5.7). Although dynamic processes are affecting the scree slope, the composition of the gravelly soil did not show significant variations at these specific locations during the three years of monitoring, due to the self-sorting and gravitational processes. This confirms the observations from the in situ cameras that while surface movements and ravelling occurred, no massive mass movement event has taken place in these locations.

Unit weight

The in-situ unit weight measurement with the balloon method was challenging in the gravelly scree soil. Problems happened during excavation due to the heterogeneity and the larger grain sizes and because the angular gravel could damage the rubber balloon. Improved experience of the user allowed the technique to be applied more successfully after repeated measurements. The results in Table 5.6 could be grouped into downslope trenches (IT1-IT4) with a higher dry unit weight $>19 \text{ kN/m}^3$, and upslope trenches (IT2-IT3), with values around 18 kN/m^3 . This natural segmentation could be explained by the sorting processes along the scree slope. Larger stones move greater distances downslope than smaller particles [2], whereas suffusion [64] may cause finer sands and silts to be transported downslope by seepage, as observed in the GSD curves of IT1 and IT4 (Figure 5.7). This was corroborated during field observation of loose blocks upslope and soil inspection at the trenches.

Triaxial testing

The determination of soil strength parameters for the gravel was successfully performed by using a medium size and large size diameter triaxial devices and a stress path that simulates slope failure due to rainfall. The critical state friction angle was shown to be similar in both cases (41° and 42° respectively). Some relevant aspects of the testing were:

- Soil specimens were prepared successfully to loose to medium density by moist tamping with 3% moisture content (Table 5.2), based on an average of the GSD from IT1-4 (Figure 5.5(b)).
- The hydraulic gradient (around 1.0) applied during saturation (from bottom to top) could have favoured transportation of the fines (suffusion). This could explain the volume loss during saturation (with vacuum and CO₂ methods), which was significant in the mid-size specimen, although this could not be confirmed.
- Considering that soil in steep slopes experiences a highly anisotropic stress state [35, 38, 41], the tests were carried out with a $K_c=1.83$ to 2.42 (Table 5.2) which was still conservatively lower than $K_c=3.3-4.3$, calculated as one tenth of the slope angle (33-43°), (as used by Anderson [34] in a residual and colluvial soil).
- The CSD triaxial stress path reproduced the mechanism of failure due to rain infiltration, increasing the PWP and moving the stress path horizontally in a q-p' space to intersect the failure envelope (stress ratio K_p), which would cause soil elements to fail and could lead to a landslide.
- The gravel exhibited dilatant behaviour during shearing for both the medium and large triaxial specimens. Although the specimens were constructed at a loose-medium relative density ($e=0.49-0.59$), they densified during the saturation and consolidation stages to (0.27-0.58). Particle breakage was confirmed during one of the large triaxial tests (supplementary material) at the highest confining pressure of ($\sigma'_{1,B}=227.4$; $\sigma'_{3,B}=94.1$ kPa) by conducting GSD tests before making the specimen and after shearing.
- A unique critical state friction angle of 41° (no cohesion) was determined from tests in the medium size triaxial apparatus, whereas 42° was determined in the large triaxial, also with no cohesion. Dilatancy was enhanced at lower confining pressures because of the effect of particle interlocking and the GSD.

GPR

The GPR measurements were crucial for the soil characterisation and the definition of a ground model. The profiles set up were according to, and representative of, the scale of the scree slope covering the whole area of study. Reliable results were obtained. A

contour map showing the depth to bedrock was determined for selected criteria, and this was critical for the hazard assessment.

5.5.2 Field monitoring

Two years of monitoring have been reported in [21]. A third year of data is added to finalise the monitoring campaign and a new site recalibration was performed using the soil and void ratio corresponding to each instrumented trench in the field.

The main aspects to discuss about the field monitoring include the additional year of data and the site-specific recalibration of the sensors:

Additional year of monitoring

The last year of data included a winter and a summer period (2015 to 2016) and confirmed the trend of VWC and temperature measured in the soil during the entire three year period. Variations and ranges in VWC and temperature in the soil for each trench depended not only on the soil characteristics, but were particularly responsive to changes in climatic conditions (rain (summer), snow-melt and rain (spring/autumn), and snow fall combined with higher ambient temperatures (winter)) and location within the scree slope (inclination, sun exposure).

The addition of data at IT4 of up to and including 1 m depth was also valuable, since it showed a higher and wider range of VWC than the rest of the trenches, with peaks of saturation at greater depths (Figure 5.12), but drainage was fast due to the high permeability, similar to its neighbour IT1 (up to 0.5 m depth). The soil did not reach saturation at any season in the rest of the trenches during the entire three year period.

Site-specific recalibration sensors for determination of VWC

A site-specific recalibration was performed under laboratory-controlled conditions to determine the influence of the temperature variations in gravelly soil over a range of temperature of -6- 23°C. Some of the challenges and findings were:

- Obtaining recalibration data from the coarser soil in IT3, since it was not possible to establish an appropriate unique relationship (in terms of achieving a suitable value R^2) between the VWC and measurements in the laboratory. It is not clear if that was due to the GSD or sensor damage.

- Noting the small variations between VWC measurements (EC-5/10HS and TDR) and temperatures (1-23°C) (Figure 5.13), which agree with the results by Topp [51], who had tested TDRs in clay loam (10-36°C). Results reported by Davis [47] and Wobschall [65] for similar range of temperature variations (0-30°C) in clay and laboratory selected soils respectively, show a small difference between readings at different temperatures at lower VWCs [55].
- A relationship between the dielectric constant increase/decrease with temperature was not found. Pepin [55] said the dielectric constant in TDRs decreased with increased temperature (in sand), while Bogena [53] found that the permittivity in EC-5 sensors increased with increasing temperature (in a water solution).
- Finally, remaining differences between sensor measurements could be due to discrepancies between measurement volume and installation depth [53]. An additional factor is due to sensor installation, since the EC-5/10HS were inserted vertically in the soil model in the laboratory to create less disturbance, whereas they were installed horizontally in the field; while the TDRs were calibrated and installed horizontally. This could have more influence on the 10HS because of the larger volume of influence during measurement, compared to the EC-5 sensors.

5.5.3 Numerical modelling

As hypothesised, a berm is demonstrably helpful in managing the emergence of water outflow onto the slope without a bedrock step, whereas the presence of steps in the bedrock makes the situation more critical. The bedrock step forces the PWP to rise at the junction of the step and the bedrock slope, saturating the soil upslope, and reducing the effective stresses. If the bedrock step was close to the surface, water could outflow there, in a form of a spring, eroding the soil at this location and triggering a failure (Figure 5.19(c),(d)). The toe favoured an increase of the PWP and failure in the bottom section (Figure 5.19(a)), whereas a larger volume could be mobilised in a slope with no toe and bedrock step (Figure 5.19(b), Table 5.8).

5.5.4 Hazard

The results in this study focused on one of the possible hazards, specifically surficial landslides in the scree slope. The relevance of this type of hazard is that it could change the stability of the scree slope on a larger scale, and could also influence the occurrence of other hazards such as debris flow.

In terms of slope stability assessment and based on the results, the locations of the scree slope, which are more endangered, in terms of slope instabilities are locations:

- the bedrock outcrop approaches the ground surface (relatively shallow depths to bedrock (e.g. 1-1.5 m) (Figure 5.10). In this case, the groundwater flow can saturate the soil layer and potentially spring to the surface, causing the soil to fail;
- the slope location is more susceptible to erosion processes from snow melting and rainfall run off that can contribute to the remobilisation of debris in the slope.

5.6 Conclusion

A geotechnical characterisation of an alpine scree slope at the Swiss Alps in Switzerland, was conducted to provide the basis for the hazard assessment of shallow landslides triggered by rainfall combined with an antecedent of a high groundwater tables. The work presented used the basis of information that was already reported in a previous paper [21] and extended this knowledge by providing new data and key information including soil strength parameters, map of the bedrock depth, the long term field monitoring data was completed, and a preliminary analysis of the slope stability was carried out for four different cases of bedrock-slope geometry, which were investigated using numerical modelling.

The method of characterisation of the scree slope combined appropriate technologies for an alpine location, including geophysical measurement providing representative data for the problem scale. Testing techniques adopted for the long term monitoring and the study of the gravelly soil, proved to be adequate considering the heterogeneity and GSD of the soil. The application and results of these techniques was discussed for a gravelly soil scree slope influenced by weather seasonal changes. New findings were also discussed that could help to gain understanding of the mechanism of failure due to rainfall/groundwater in the scree slope.

A summary of the main findings are:

- The gravelly soil (GM-GP) was heterogeneous, with varying GSD and density, depending on the location in the steep scree slope, which was also affected by dynamic slope processes. Although the gravel may reach saturation (near 1 m depth) at the location of instrumented trench IT4 during rainfall events, the yearly

monitoring data revealed that the soil tends to stay in an unsaturated state at shallower depths, due to fast drainage in these mainly coarse granular soils.

- Soil strength parameters of the gravelly soil were obtained using large and mid-size triaxial testing devices on reconstituted specimens of two diameters (15 and 25 cm), adopting a constant shear drained stress path (CSD). The test simulated the anisotropic stresses in the slope and the shearing during failure under rainfall infiltration. Results of the mid and large triaxial tests provided critical state friction angles of 42° and 41° respectively, with zero cohesion. The soil specimens exhibited dilatancy associated with the interlocking of the coarser gravel, which was found consistently to be larger under low confining pressures.
- The use of ground penetrating radar (GPR) technology to find the depth to bedrock, proved not only to be effective in alpine environment but also key for the definition of a realistic ground model. A map of contour lines could be elaborated for the depth to bedrock for the entire scree slope. This result was a great asset for the hazard assessment of slope stability, enabling the estimation of potential volumes that could be mobilised, as well as localisation of where the bedrock is shallower and therefore the overlying soil layer is more likely to reach saturation.
- An additional year of data monitoring completed the three-year dataset. The trends in VWC and temperature in the soil confirmed regimes according to the weather seasons, with a low temperature and VWC in winter and a wider range in spring/autumn and summer, which was responsive to the climatic conditions. Although this trend confirmed throughout the three years of monitoring, the last winter monitoring data showed trends of sustained higher VWC, which could have been due to periods of warmer ambient temperatures combined with peaks of precipitation. Warmer temperatures could have anticipated the initiation of snow melting, and peaks in precipitation could have increase the snow pack volume, which combined with higher temperatures could have prolonged the snowmelting period. Field observations with in situ cameras suggested that these erosion processes and the potential remobilisation of surficial debris in the slope during winter and the transition season were enhanced by the occurrence of avalanches and snow melting in the scree slope.

- A site-specific recalibration was appropriate for obtaining relationships for the VWC using EC-5, 10HS and TDR sensors in the gravelly host soil from each monitoring location at their respective in-situ density and for variations in temperature. The effect of temperature in a range of (1-23°C) was not found to be critical for the sensor calibration due to the low range of VWC and the differences in VWC that could be attributable to the heterogeneity of the soil.
- Preliminary numerical modelling results showed that failures of the gravelly slope with these characteristics, are conditioned in terms of failure volume by the amount of groundwater infiltration (triggering factor), the geometry of the bedrock and the presence of a toe. Bedrock geometry with a step increases the likelihood (lower F.S) of a landslide because it requires less water flow to trigger an instability, compared to a slope parallel to the bedrock (no step). Moreover, these conditions influence the location of the failure and the debris volume. The failure is expected to happen upslope of the intersection of the bedrock slope in the case of bedrock step, and at the bottom by the toe in the case of a slope parallel to the bedrock.

5.7 Acknowledgments

The authors express their gratitude to the Councils of Leuk and Agarn, the local technicians, who collaborated during the field monitoring, to Nicole Oggier for her help during the first stages of the monitoring, and to the IGT technicians at the workshop for the tools created for the monitoring. The authors also wish to acknowledge assistance from Dr. Thomas Buchli and Dr. Alexandru Marin, for their collaboration in the fieldwork tests and tasks, to Prof. Amin Askarinejad for his instruction and feedback on instrumentation, as well as Dr. André Nuber, Dr. Fabienne Reiser, Dr. Marlies Vasmel and Dr. Melchior Grab for their help in the acquisition of the GPR data.

5.8 References

1. De Freitas, M. H.; Watters, R. J. Some field examples of toppling failure. *Géotechnique* **1973**, 23(4), 495-513.
2. Statham, I. Scree slope development under conditions of surface particle movement. *Trans. Inst. Br. Geogr.* **1973**, 41-53.
3. Gerber, E.; Scheidegger, A. E. On the dynamics of scree slopes. *Rock Mech. Rock Eng.* **1974**, 6(1), 25-38.

4. Evans, S. G.; Hungr, O. The assessment of rockfall hazard at the base of talus slopes. *Can. Geotech. J.* **1993**, 30(4), 620-636.
5. McDowell G. R.; Bolton M. D. On the micromechanics of crushable aggregates. *Géotechnique* **1998**, 48(5), 667–679.
6. McSaveney, M. J.; Davies, T. R. H. Inferences from the morphology and internal structure of rockslides and rock avalanches rapid rock mass flow with dynamic fragmentation. In: *Landslides from Massive Rock Slope Failure*. Springer, Dordrecht, **2006**. 285-304.
7. Einav, I. Breakage mechanics—part I: theory. *J. Mech. Phys. Solids* **2007**, 55(6), 1274-1297.
8. Imre, B.; Räbsamen, S.; Springman, S. M. A coefficient of restitution of rock materials. *Comput. Geosci.* **2008**, 34(4), 339-350. doi: 10.1016/j.cageo.2007.04.004.
9. Imre, B.; Laue, J.; Springman, S. M. Fractal fragmentation of rocks within sturzstroms: insight derived from physical experiments within the ETH geotechnical drum centrifuge. *Granul. Matter* **2010**, 12(3), 267-285. doi: 10.1007/s10035-009-0163-1.
10. Imre, B.; Wildhaber, B.; Springman, S. M. A physical analogue material to simulate sturzstroms. *Int. J. Phys. Model Geo.* **2011**, 11(2), 69-86. doi:10.1680/ijpmg.2011.11.2.69.
11. Strom, A. L. Mechanism of stratification and abnormal crushing of rockslide deposits. In *Proc. 7th International Association for Engineering Geology and the Environment IAEG Congress* **1994**, 3, 1287-1295. Balkema Rotterdam.
12. Strom, A. L. Morphology and internal structure of rockslides and rock avalanches: grounds and constraints for their modelling. In *Landslides from Massive Rock Slope Failure* **2006**. Eds. Evans SG, Mugnozza G.S., Strom A. and Hermanns R.L., 305-326, Springer, Dordrecht, The Netherlands.
13. Sammis, C.; King, G.; Biegel, R. The kinematics of gouge deformation. *Pure Appl. Geophys.* **1987**, 125(5), 777-812.

14. McDowell, G. R.; Daniell, C. M. Fractal compression of soil. *Géotechnique* **2001**, 51(2), 173-176.
15. Einav, I. Breakage mechanics—Part II: Modelling granular materials. *J. Mech. Phys. Solids* **2007**, 55(6), 1298-1320.
16. Linkov, A. M. Rockbursts and the instability of rock masses. *Int. J. Rock Mech. Min. Sci. abstracts* **1996**, 33 (7), 727-732. Pergamon.
17. Statham, I. A scree slope rockfall model. *Earth Surf. Process. Landf.* **1976**, 1(1), 43-62.
18. Carson, M. A. Angles of repose, angles of shearing resistance and angles of talus slopes. *Earth Surf. Process. Landf.* **1977**, 2(4), 363-380.
19. Blijenberg, H. M. In-situ strength tests of coarse, cohesionless debris on scree slopes. *Eng. Geol.* **1995**, 39(3-4), 137-146.
20. Pierson, T. C. Classification and hydrological characteristics of scree slope deposits in the northern Craigieburn Range, New Zealand. *J. Hydrol.* **1982**, 21, 34-60.
21. Lucas, D. R.; Fankhauser, K.; Springman, S. M. Application of geotechnical and geophysical field measurements in an active alpine environment. *Eng. Geol.* **2017**, 219, 32-51. <https://doi.org/10.1016/j.enggeo.2016.11.018>
22. Oggier, N.C. Simulierung von Murgängen mit RAMMS am Beispiel des Meretschibachs. (Master Thesis); ETH Zürich und Forschungsanstalt für Wald Schnee und Landschaft (WSL), Switzerland, **2011**.
23. Gabus, J. H.; Weidmann, M.; Burri, M.; Sartori M. Feuille 1287 Sierre, Atlas Géologique de la Suisse 1:25'000, Carte 111, swisstopo, Wabern, Switzerland, **2008**.
24. Gabus, J. H.; Weidmann M.; Burri, M.; Sartori M. Feuille 1287 Sierre, Atlas Géologique de la Suisse 1:25'000 Note explicative; swisstopo, Wabern; Switzerland; **2008**.
25. Fankhauser, K. Geophysical slope characterization using GPR and ERT in an active debris flow catchment (Master Thesis); EEG, ETH Zurich, **2014**.

26. McArdell B. Unpublished; Forschungsanstalt für Wald Schnee und Landschaft (WSL), Switzerland , **2018**.
27. Raetzo H.; Caduff R. Personal communication.
28. Badoux, A.; Graf, C.; Rhyner, J.; Kuntner, R.; McArdell, B. W. A debris-flow alarm system for the alpine Illgraben catchment: design and performance. *Nat. Hazards* **2009**, 49(3), 517-539.
29. Zimmermann, M; Mani, P; Gamma, P. Murganggefahr und Klimaänderung – ein GIS-basierter Ansatz. vdf Hochschulverlag AG at ETH Zurich, **1997**.
30. Eichenberger, V.; McArdell, B.; Christen, M.; Trappmann, D.; Stoffel, M. Wenn Baumwunden dazu beitragen, Steinschlagmodelle weiterzuentwickeln. *Schweizerische Zeitschrift für Forstwesen* **2017**, 168(2), 84-91.
31. GEO-SLOPE User's Guide, and SEEP/W. 2018. Geo-Slope International Ltd, Calgary, Alberta, Canada. Available: <https://www.geoslope.com>
32. Vaid, Y. P.; Negussey, D. Preparation of reconstituted sand specimens. In Advanced Triaxial Testing of Soil and Rock. ASTM International, **1988**.
33. Ishihara, K. Liquefaction and flow failure during earthquakes. *Géotechnique* **1993**, 43(3), 351-451.
34. Anderson, S. A.; Sitar, N. Analysis of rainfall-induced debris flows. *J. Geotech. Eng.* **1995**, 121(7), 544-552.
35. Vaughan, P. R.; Kwan, C. W. Weathering Structure and in Situ Stress in Residual Soils. *Géotechnique* **1984**, 34(1), 43-59.
36. Grob, R. Measurement of soil properties for gravels in a scree slope using large scale triaxial testing, (Master Thesis), IGT, ETH Zürich, Switzerland, **2015**.
37. Lowe, J. Stability analysis of embankments. *J. Soil Mech. Found. Div.* **1967**, 93(4), 1-33.
38. Zhu, J. H.; Anderson, S. A. Determination of shear strength of Hawaiian residual soil subjected to rainfall-induced landslides. *Géotechnique* **1998**, 48(1), 73-82.

39. Teyssere, P. Geotechnische Eigenschaften von Moränen, ETH Dissertation No. 16322, IGT ETH Zürich, Switzerland, **2005**.
40. Casini, F.; Serri, V.; Springman, S. M. Hydromechanical behaviour of a silty sand from a steep slope triggered by artificial rainfall: from unsaturated to saturated conditions. *Can. Geotech. J.* **2012**, *50*(1), 28-40.
41. Springman, S. M.; Jommi, C.; Teyssere, P. Instabilities on moraine slopes induced by loss of suction: a case history. *Géotechnique* **2003**, *53*(1), 3-10.
42. Casini, F.; Jommi, C.; Springman, S. A Laboratory investigation on an undisturbed silty sand from a slope prone to landsliding. *Granul. Matter* **2010**, *12*(3), 303-316.
43. Bolton, M. D. Strength and Dilatancy of Sands. *Géotechnique* **1986**, *36*(1), 65-78.
44. Bolton, M. D. Personal communication, **2005**.
45. Annan, A. P. GPR Methods for hydrogeological studies, *Hydrogeophysics*, **2005**, 185-213.
46. Annan, A. P. Electromagnetic principles of ground penetrating radar; Ground penetrating radar: Theory and applications. Elsevier Science, Amsterdam, **2009**.
47. Davis, J. L.; Annan, A. P. Ground-Penetrating Radar for High-Resolution Mapping of Soil and Rock Stratigraphy 1. *Geophys. Prospect.* **1989**, *37*(5), 531-551.
48. Reynolds, J. M. An Introduction to Applied and Environmental Geophysics. Wiley, Chichester, **1997**.
49. Parasnis, D. S. Principles of Applied Geophysics: Chapman and Hall. London, 5th edition, 1997.
50. Grab, M.; Bauder, A.; Ammann, F.; Langhammer, L.; Hellmann, S.; Church, G.; Schmid, L.; Rabenstein, L.; Maurer, H. Ice volume estimates of Swiss glaciers using helicopter-borne GPR—an example from the Glacier de la Plaine Morte. 17th International Conference on Ground Penetrating Radar (GPR), **2018**, 1-4.

51. Topp, G. C.; Davis, J. L.; Annan, A. P. Electromagnetic determination of soil water content: measurements in coaxial transmission lines. *Water Resour. Res.* **1980**, 16 (3), 574–582.
52. Mittelbach, H.; Casini, F.; Lehner, I.; Teuling, A. J.; Seneviratne, S. I. Soil moisture monitoring for climate research: evaluation of a low-cost sensor in the framework of the Swiss soil moisture experiment (SwissSMEX) campaign. *J. Geophys. Res. Atmos.* **2011**, 116(D5), D05111. doi.org/10.1029/2010JD014907
53. Bogaen, H. R.; Huisman, J. A.; Oberdörster, C.; Vereecken, H. Evaluation of a low-cost soil water content sensor for wireless network applications. *J. Hydrol.* **2007**, 344(1-2), 32-42.
54. Wraith, J. M.; Or, D. Temperature effects on soil bulk dielectric permittivity measured by time domain reflectometry: experimental evidence and hypothesis development. *Water Resour. Res.* **1999**, 35(2), 361-369.
55. Pepin, S.; Livingston, N. J.; Hook, W. R. Temperature-dependent measurement errors in time domain reflectometry determinations of soil water. *Soil Sci. Soc. Am J.* **1995**, 59(1), 38-43.
56. Bishop, A. W. Shear strength parameters for undisturbed and remoulded soil specimens. In stress-strain behaviour of soils, **1972**, 3-58 (ed. R. H. G. Parry). London: Foulis.
57. Billam, J. Some Aspects of the Behaviour of Granular Materials at High Pressures. In stress strain behaviour of soils **1972**, DD. 69-80 (ed. R. H. G. Parry). London: Foulis.
58. Vesic, A. S.; Clough, G. W. Behaviour of Granular Materials Under High Stresses. *J. Soil Mech. Fdns Div. Am. Soc. Civ. Engrs.* **1968**, 94, SM3, 661-688.
59. Casini, F.; Viggiani, G. M.; Springman, S. M. Breakage of an artificial crushable material under loading. *Granul. Matter* **2013**, 15(5), 661-673.
60. Spaans, E. J.; Baker, J. M. The Soil Freezing Characteristic: Its Measurement and Similarity to the Soil Moisture Characteristic. *Soil Sci. Soc. Am J.* **1996**, 60(1), 13-19.

61. Stähli, M.; Jansson, P. E.; Lundin, L. C. Soil moisture redistribution and infiltration in frozen sandy soils. *Water Resour. Res.* **1999**, *35*(1), 95-103.
62. Stähli, M. Freezing and Thawing Phenomena in Soils; Encyclopedia of Hydrological Sciences, 2006.
63. Arenson, L.; Azmatch, T.; Sego D.; Biggar K. A new hypothesis on ice lens formation in frost-susceptible soils. Proceedings of the Ninth International Conference on Permafrost, Fairbanks, Alaska, 2008, 1. 59-64.
64. Kenny, T. C.; Lau, D. Internal stability of granular soils. *Can. Geotech. J.* **1985**, *21*, 634-643.
65. Wobschall, D. A Frequency shift dielectric soil moisture sensor; IEEE Transactions on Geoscience Electronics 1978, 16. 112-118, doi: 10.1109/TGE.1978.294573

5.9 Appendix. Supplementary Material

5.9.1 Characterisation

Soil unit weight method

A clean and flat surface was prepared for the support aluminium plate (designed by IGT), which contains the base ring. Soil was excavated to 5 cm depth, removed and discarded. The densitometer, containing approx. 6 litres of water (mixed with a lubricant to reduce piston friction), was placed on the base ring, and the piston was pushed until water filled the hole up to the two calibrating marks in the tube. The initial position L_0 was read, before the densitometer was removed and the soil was excavated to 20 cm depth, with walls as vertical as possible. The soil was stored and the measurement with densitometer (L_1) was repeated. The volume of the bottom hole V is equal to the volume of liquid displaced by the device piston between the two readings L_0 and L_1 readings. The dry unit weight was determined using the calculated volume and the dry weight of the soil excavated.

Triaxial testing

Triaxial apparatus

The tests were carried out using two different triaxial apparatuses (a mid- and large scale) at the Institute for Geotechnical Engineering (IGT), ETH Zurich.

Mid-scale triaxial apparatus

The mid-scale triaxial (Figure S5.9.1) is described in detail by Buchheister (2012). It consists of an adapted hollow cylinder in which a specimen with a diameter of 150 mm and a height of 300 mm can be placed inside a cylindrical pressure chamber, and loaded by a triaxial press. The apparatus is controlled electronically and is able to apply static and dynamic loads and to perform load-controlled tests (Table S5.9.1). Vertical forces and torques are applied by the use of two independent hydraulic cylinders. The applied force is measured by a load cell with a maximum of 63 kN. The displacement can reach a maximum of 100 mm and is measured by an integrated sensor within the hydraulic cylinders.

Large scale triaxial apparatus

The large scale triaxial apparatus (Figure S5.9.1) is described by Guldenfels (1996). The electronically regulated system is able to apply static, quasi static, dynamic axial loads

and to perform tests under controlled force or deformation. The axial load is transmitted by a hydraulic cylinder and measured by a load cell, with a maximum capacity of 160 kN. The axial deformation is measured by a sensor integrated within the hydraulic cylinder, with a maximum displacement of 100 mm. The specimen for this apparatus has a diameter of 250 mm, and a height of 500 mm.

Table S5.9.1. Specifications of the triaxial apparatuses.

Test	Type	Maximum axial displacement [mm]	Capacity of axial loading device [kN]	Diameter of specimen [mm]	Height of specimen [mm]
Mid-scale	HCA	±50	63	150	300
Large scale	Schenk	±50	160	250	500



Figure S5.9.1. Triaxial testing apparatuses. Left: mid-scale; right: large scale, (photograph: R. Grob, 2015).

Grain size distribution post shearing

Figure S5.9.2 shows the GSD after shearing, of a large triaxial testing sample. There is increase of the fines content percentage and in the sand fraction, which suggest the crushing of particles during testing at higher confining pressures.

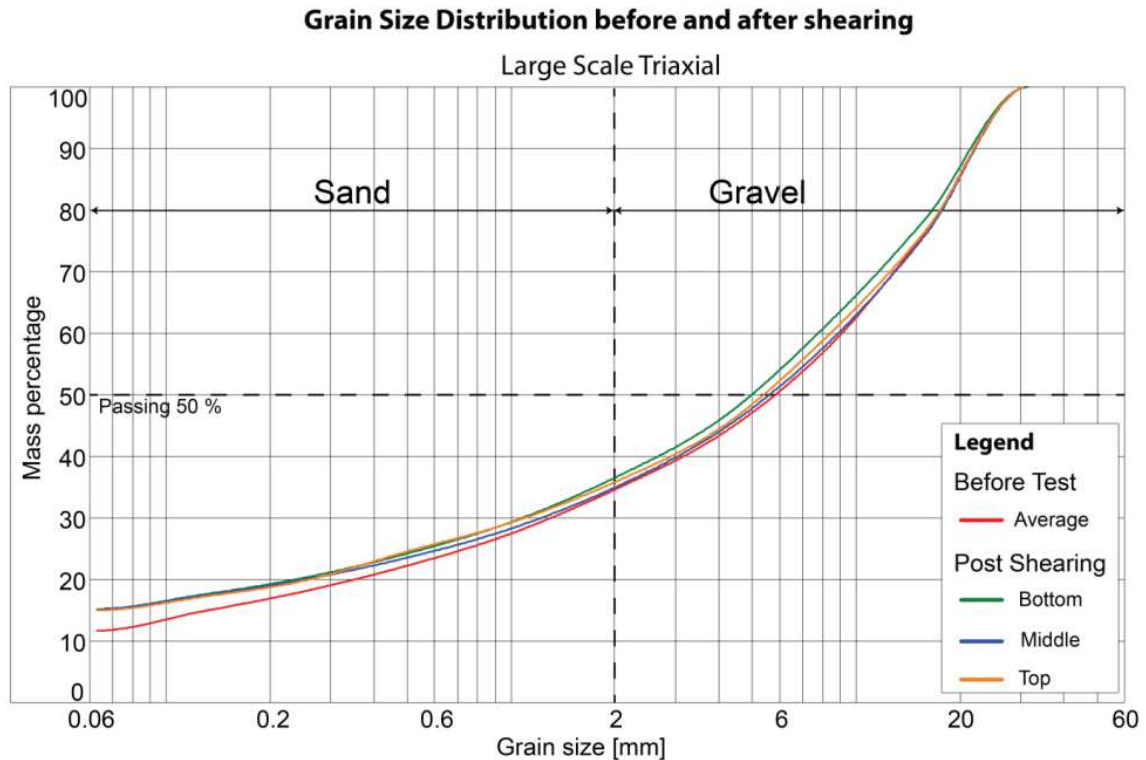


Figure S5.9.2. Grain size distribution before testing and after shearing for large scale test_3. The post-shearing curves from the bottom, middle and top of the specimen show the crushing of particles.

Ground-based penetrating radar.

An overview of all the relevant acquisition parameters used during GPR surveys are provided in Table S5.9.2 and S5.9.3.

Table S5.9.2. Overview of all acquisition parameters used during GPR surveys. “PE” stands for PulseEKKO, and “GB” for ground-based acquisition. The sampling interval was chosen as 0.4 ns, according to the specifications from the manufacturer. Two values are presented for the number of samples and the recorded time, as they were adjusted during the acquisition. Corresponding profile lines are shown in Figure 5.1(b).

System	Type	Date (dd.mm.yyyy)	Frequenc y (MHz)	Temporal sampling interval (ns)	Number of samples/trace	Time window (ns)	Stacks
PE	GB	15/16.05.2014	250	0.4	1000/625	400/250	8

Table S5.9.3 gives an overview of all processing steps that were applied for GPR data, including the most important selected parameters, selection criteria and amounts of eliminated data. GPR data from ground-based acquisition were processed using the same workflow, including all processing steps, which are commonly applied to GPR data [1-3].

Table S5.9.3. Selected processing parameters for each GPR acquisition

System	Type	Selected time window (ns)	Band Pass Filter (MHz)	Single value decomposition (SVD) filter length (ns)	Deconvolution filter length (ns)	Bin size (m)	Radar pulse velocity in soil (m/ns)
PEMay14	GB	200	100/600	30	20	0.05	0.1

5.9.2 Monitoring

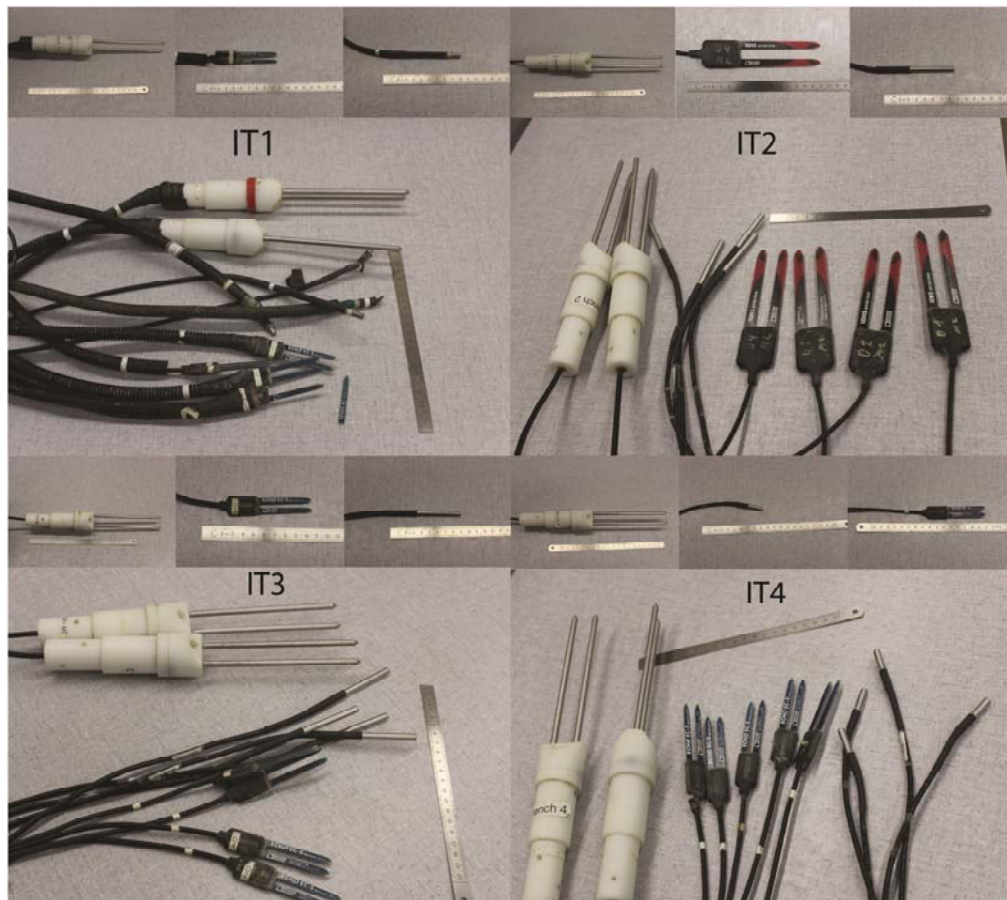


Figure S5.9.3. Sensors for each instrumented trenches IT1-4



Figure S5.9.4. Controlled room temperature at IGT ETH Zürich.



Figure S5.9.5. Soil in reconstituted samples for calibrating sensors from IT1-4

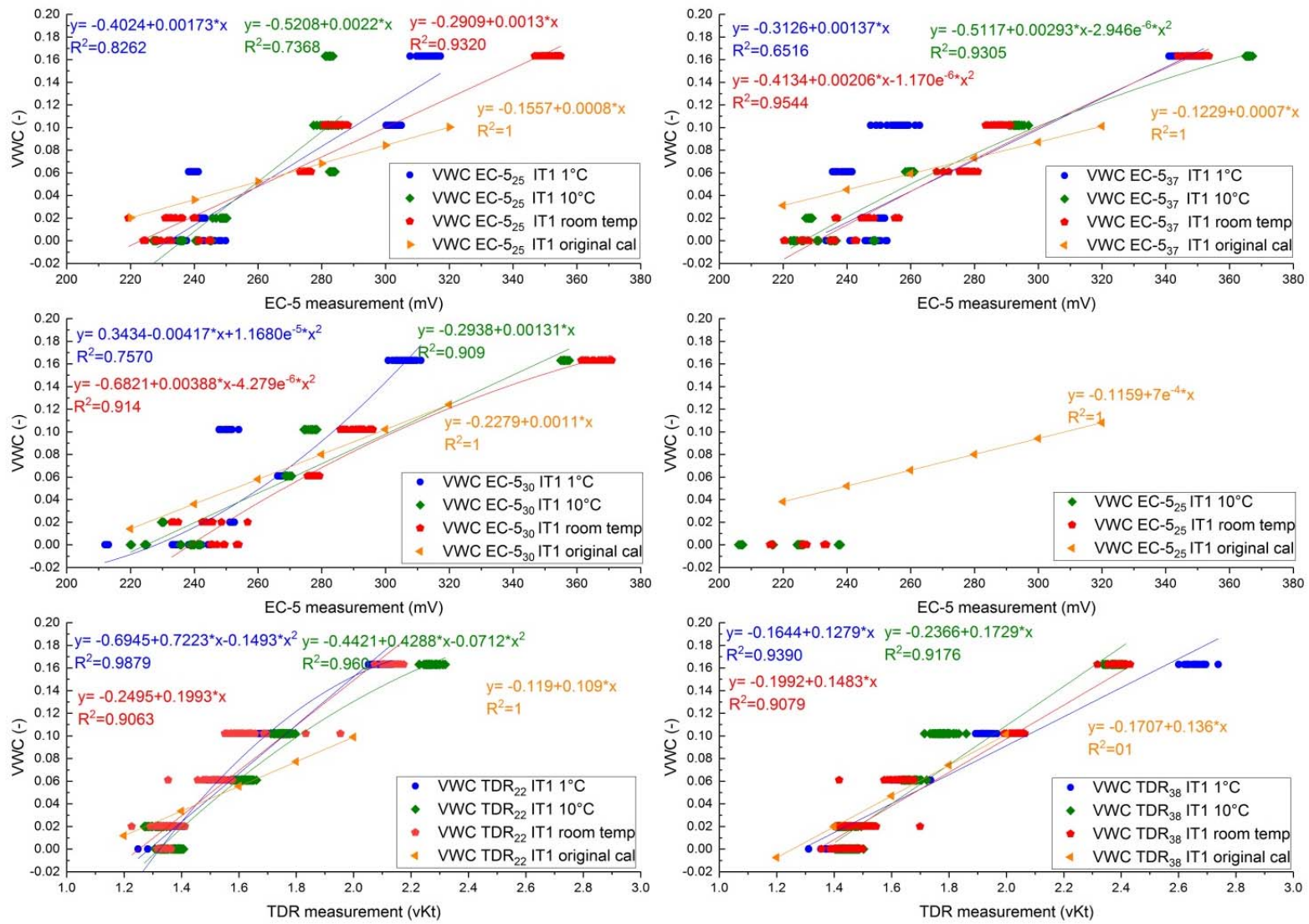


Figure S5.9.6. Specific site calibration of TDR and EC-5 sensors in terms of temperature IT1.

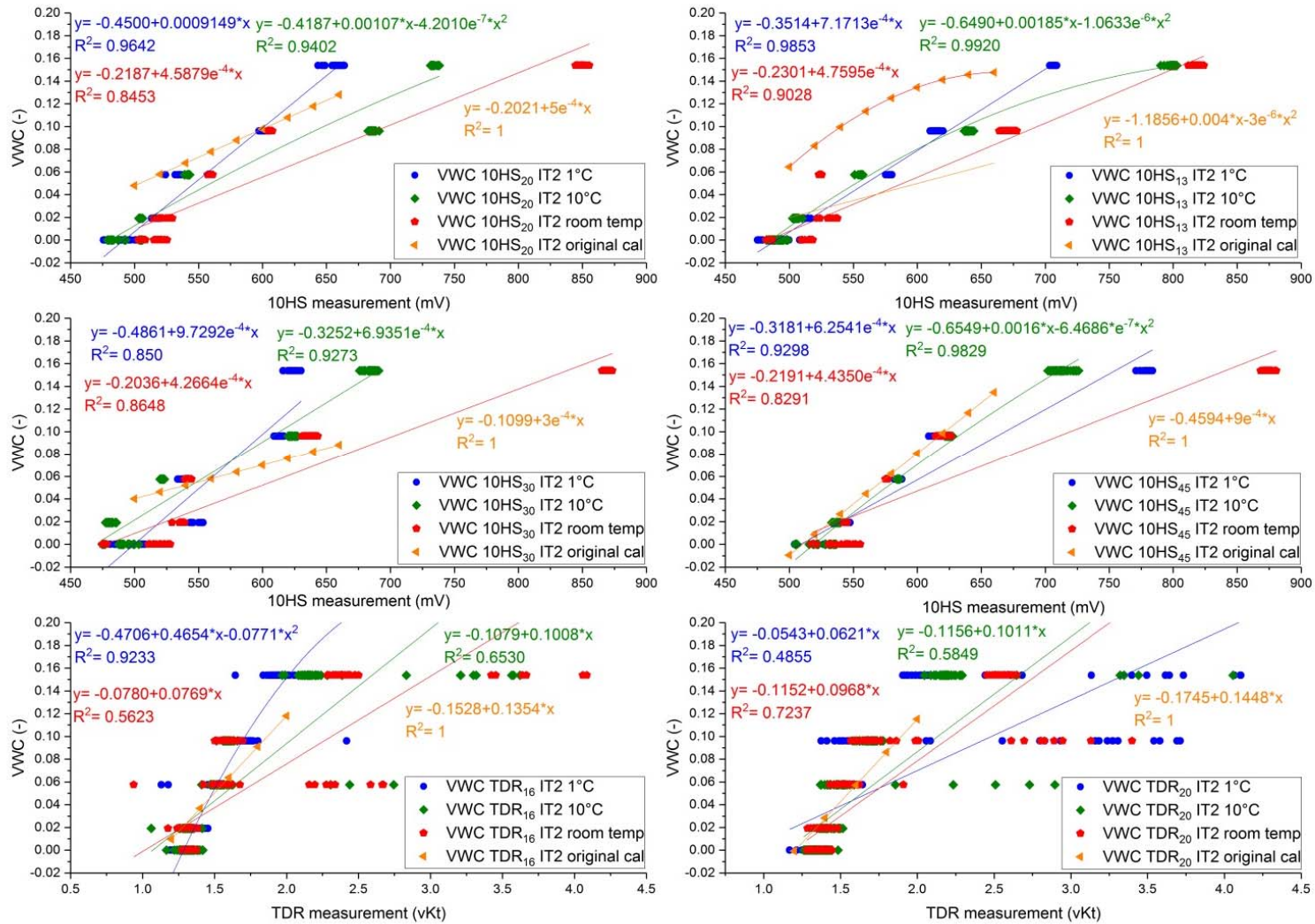


Figure S5.9.7. Site specific calibration of TDR and 10HS sensors in terms of temperature, IT2.

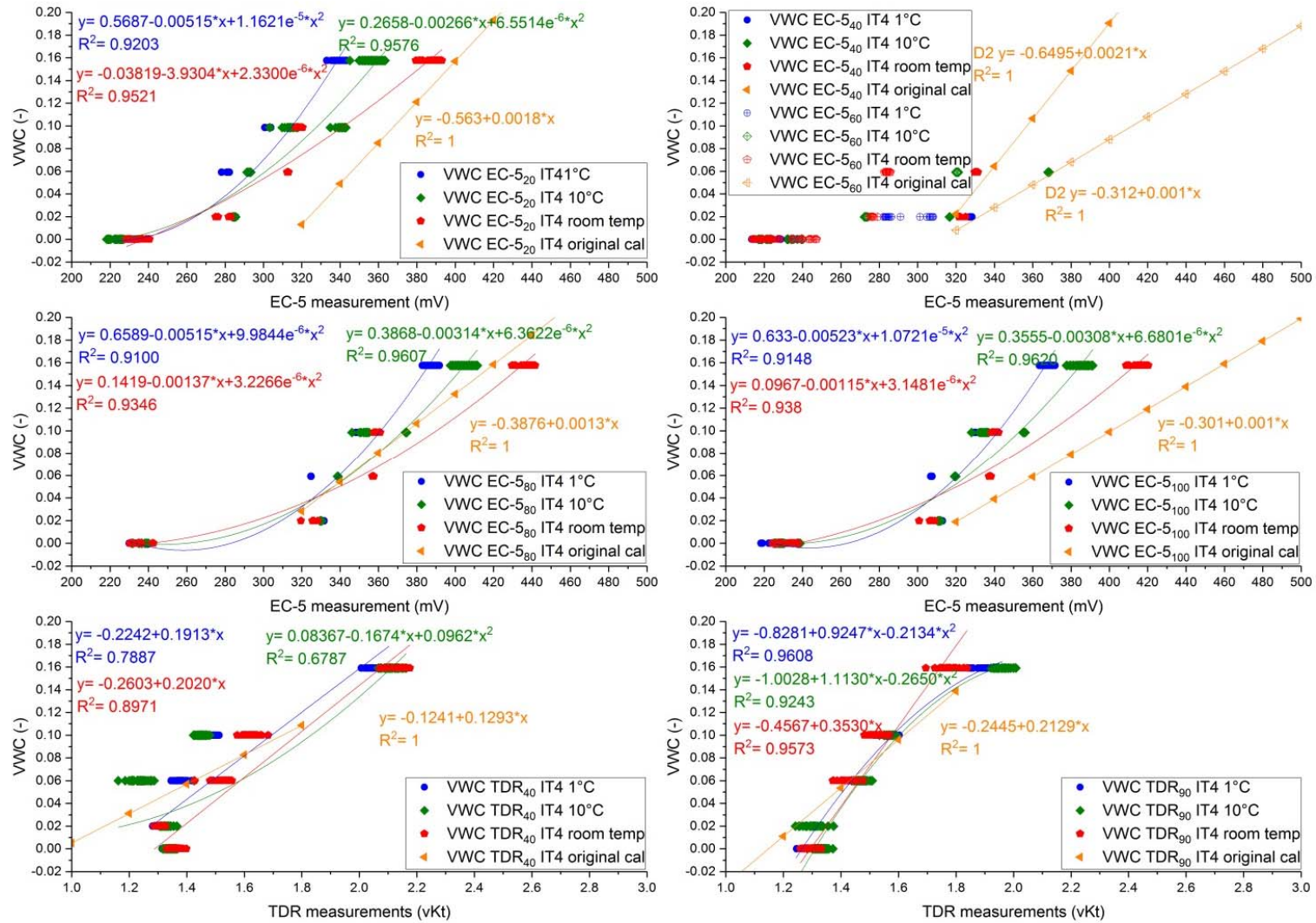


Figure S5.9.8. Site specific calibration of TDR and EC-5 sensors in terms of temperature, IT4.

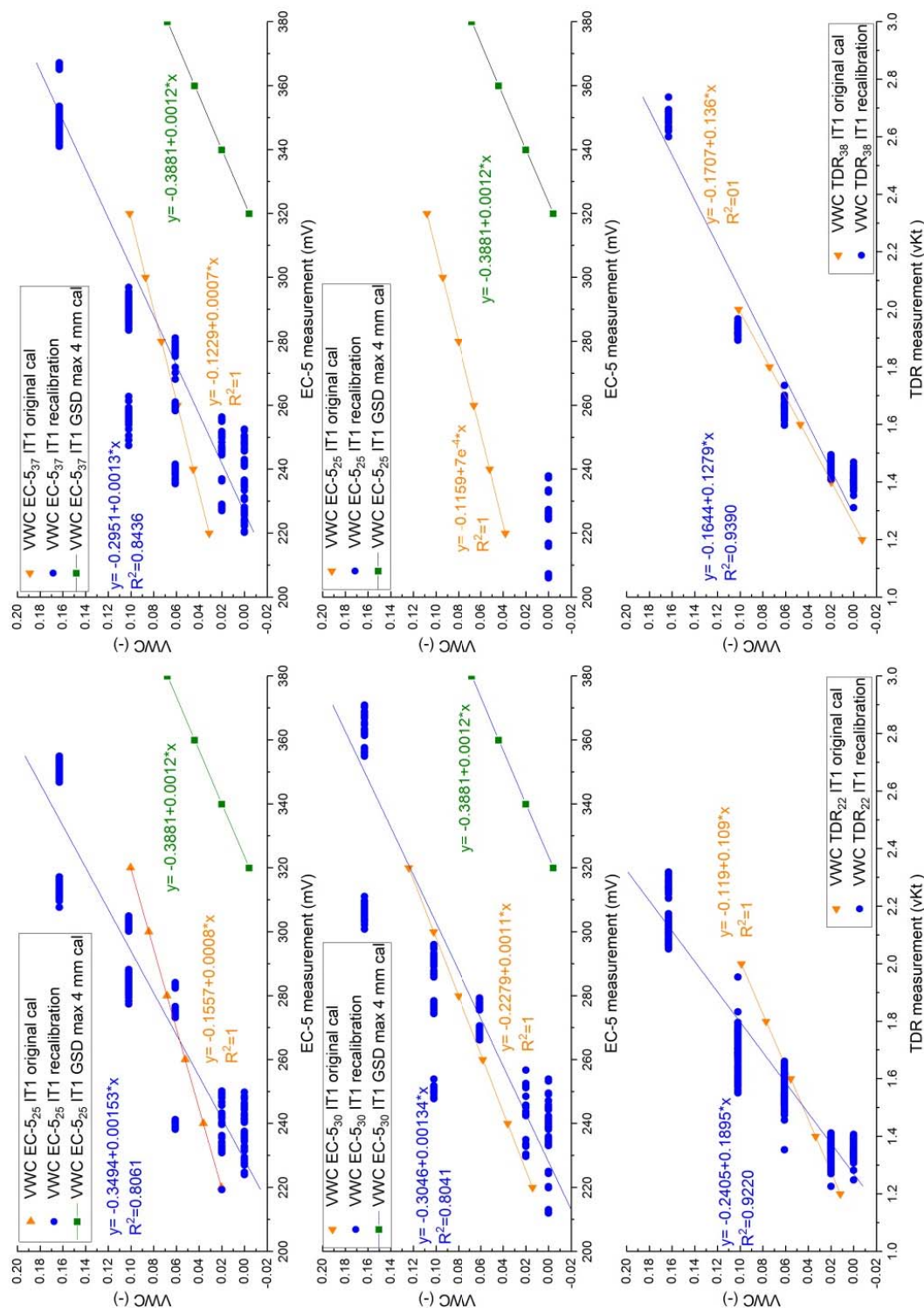


Figure S5.9.9. Site specific calibration for positive temperatures, IT1.

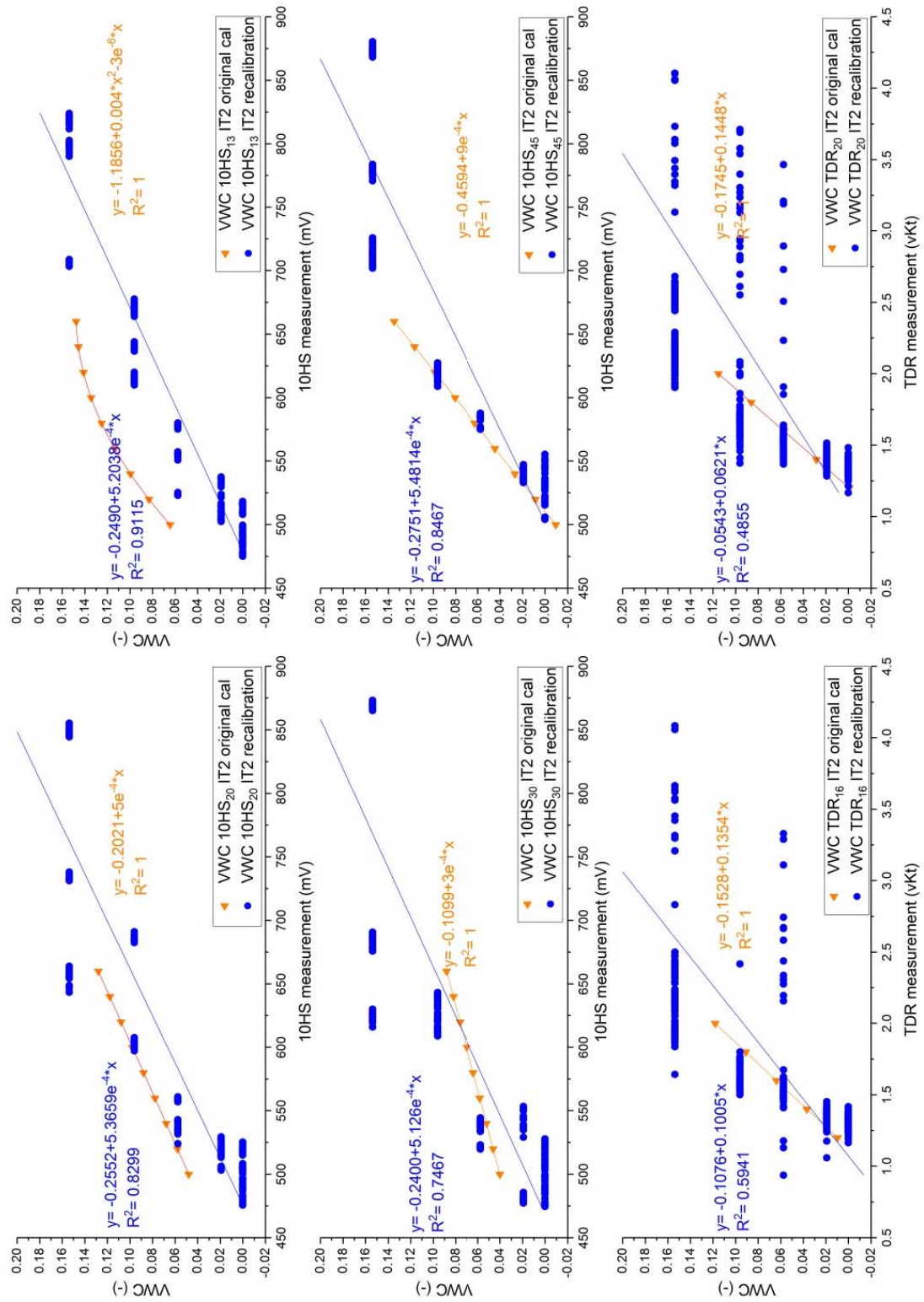


Figure S5.9.10. Site specific calibration for positive temperatures, IT2.

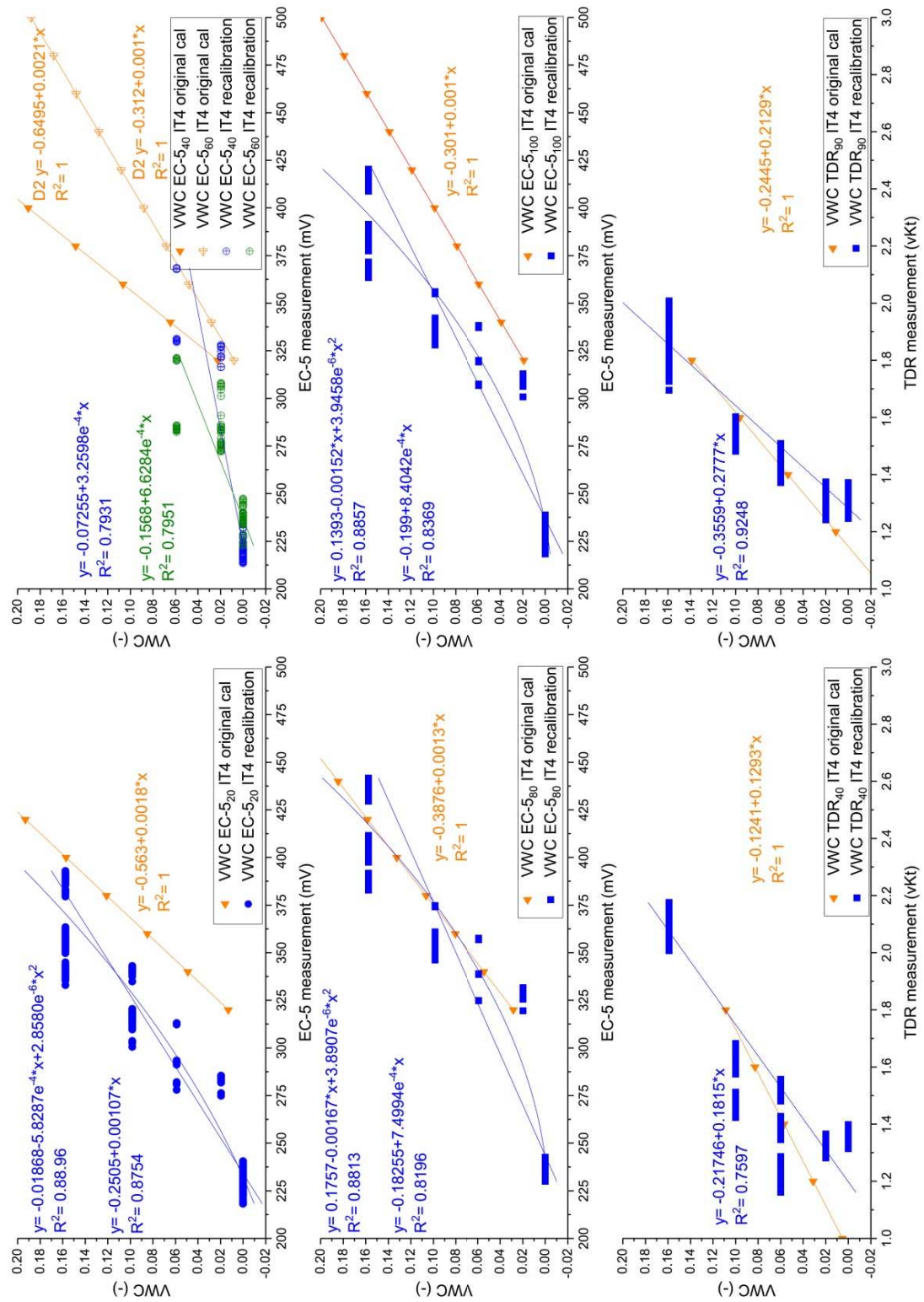


Figure S5.9.11. Site specific calibration for positive temperatures, IT4.

5.9.3 References.

1. Annan, A. P. GPR Methods for hydrogeological studies, *Hydrogeophysics*, **2005**, 185-213.
2. Annan, A. P. Electromagnetic principles of ground penetrating radar; Ground penetrating radar: Theory and applications. Elsevier Science, Amsterdam, **2009**.
3. Neal, A. Ground-penetrating radar and its use in sedimentology: principles, problems and progress. *Earth Sci. Rev.* **2004**, 66(3-4), 261-330.

6 Modelling of landslides in a scree slope induced by groundwater and rainfall

Daisy Lucas

ETH Zürich, Institute for Geotechnical Engineering
Stefano-Franscini-Platz 5, 8093 Zürich, Switzerland
E-Mail address: daisy.lucas@igt.baug.ethz.ch

Ralf Herzog

ETH Zürich, Institute for Geotechnical Engineering
Stefano-Franscini-Platz 5, 8093 Zürich, Switzerland
E-Mail address: ralf.herzog@igt.baug.ethz.ch

Markus Iten

ETH Zürich, Institute for Geotechnical Engineering
Stefano-Franscini-Platz 5, 8093 Zürich, Switzerland
E-Mail address: markus.iten@igt.baug.ethz.ch

Heinz Buschor

ETH Zürich, Institute for Geotechnical Engineering
Stefano-Franscini-Platz 5, 8093 Zürich, Switzerland
E-Mail address: markus.iten@igt.baug.ethz.ch

Andreas Kieper

ETH Zürich, Institute for Geotechnical Engineering
Stefano-Franscini-Platz 5, 8093 Zürich, Switzerland
E-Mail address: markus.iten@igt.baug.ethz.ch

Amin Askarinejad

Faculty of Civil Engineering and Geosciences, TUDelft
Building 23, Stevinweg 1 / PO-box 5048, 2628 CN Delft / 2600 GA Delft, The Netherlands
E-Mail address: A.Askarinejad@tudelft.nl

Sarah M. Springman

ETH Zürich, Institute for Geotechnical Engineering

Stefano-Franscini-Platz 5, 8093 Zürich, Switzerland

E-Mail address: sarah.springman@igt.baug.ethz.ch

**Submitted to themed issue of International Journal of Physical Modelling in
Geotechnics on Physical modelling of landslides**

Status: Published.

Abstract

Predicting the trigger of a slope failure of a steep Alpine scree slope in south-west Switzerland is challenging. The groundwater (GW) flow from snow-melting and rainfall infiltration during summer changes the susceptibility to surficial failure, which also depends on the slope angle, bedrock geometry, stratigraphy and the shear strength of the soil. Surficial failure mechanisms are investigated using prototype ground models that integrate input from field monitoring, geological observations, soil properties and account for relevant factors and constraints for physical and numerical modelling. Shallow scree deposits overlying various bedrock configurations (parallel to the slope, with and without a step) were tested under two hydrological regimes: GW flow, and combined with additional intense rainfall. Numerical modelling was used to study the parameter combinations that would lead to failure, and worst case scenarios were defined in terms of the bedrock geometry and hydraulic perturbations. These results were verified using advanced physical modelling techniques in a geotechnical drum centrifuge. Physical modelling results indicated that, for a given GW condition, slope stability decreases (a) as the depth of the soil cover over the bedrock decreases and (b) the higher the bedrock step. Furthermore, a bedrock step impacts the volume and the location of the triggered failure. Rainfall exacerbates the situation.

Keywords

Landslides, numerical modelling, centrifuge modelling.

List of notation

c'	→ Cohesion
h	→ Soil thickness
N	→ Scaling factor in the centrifuge
p'	→ mean effective stress $(2\sigma'_3 + \sigma'_1)/3$
Q	→ input flow rate
q	→ deviatoric stress $(\sigma'_1 - \sigma'_3)$
X_1	→ top length of bedrock step
X_2	→ length base of bedrock step
y	→ height of bedrock step
σ'_1	→ axial effective stress
σ'_3	→ lateral effective stress
ϕ'	→ angle of internal friction

6.1 Introduction

A project was developed by ETH Zürich in collaboration with the Agarn community, Canton Wallis to quantify the hazard associated with the surficial failure of an extensive north-facing Alpine scree slope in the Meretschibach catchment (Lucas et al., 2017; Springman et al., 2015). The 33–43° inclined scree slope (Figure 6.1(a)) is located at the top of the mountain slope (1840–1910 m a.s.l. (metres above sea level)), next to a highly eroded debris-flow channel path, which collects a portion of mobilised soil and rock debris, ‘harvested’ from above and from the neighbouring slopes. The potential source of material, which could accumulate prior to triggering as a debris flow, could eventually reach the community of Agarn (620 m a.s.l.), located downstream of the eroded channel bed, in more extreme cases (Frank et al., 2017; Lucas et al., 2017; Oggier, 2011). The dynamics and growing changes in the geomorphology of the catchment may imply new hazards in terms of slope instability in the future, and therefore it is important to understand when and how the slope could fail, and what the triggers would be. The stratigraphy of the slope was characterised (Lucas et al., 2017) and a ground model was defined (Figure 6.1(b)) for use in the physical and numerical simulations. A field monitoring campaign reported by Lucas et al. (2017), was carried out over a duration of 3 years, with instrumentation installed to record temperature, volumetric water content (VWC), suction and precipitation (additional information in Lucas et al., 2017 and supplementary material). These data sets were complemented by a series of triaxial stress path tests in the laboratory on reconstituted specimens extracted from sampling in test pits in the slope, and were combined with geophysical measurement techniques (electrical resistivity tomography (ERT), ground penetrating radar (GPR)) to determine the depth of bedrock (Fankhauser, 2014).

It was confirmed that the degree of saturation in an Alpine scree slope at Meretschibach is strongly related to the seasonal weather changes (Lucas et al., 2017). The slope is subjected to precipitation in the form of snow in winter, when temperatures are negative or near zero, which provides insulation against variations in the local air temperature and prevents significant changes in the VWC. The temperature increases in spring and the snow-melt infiltrates into the ground. Additional precipitation can be in the form of snow or rain, due to daily temperature variations. Finally, rainfall precipitation in summer increases the soil saturation, hence decreasing suction and effective stress in the soil.

The soil became fully saturated only in one location (of the four investigated) in a coarser layer at 1 m depth, after a period of intense rainfall (Lucas et al., 2017). This reinforces a hypothesis that the most unfavourable conditions for the slope stability could be very local and occur in spring–summer time, when rainfall infiltration combined with groundwater (GW) flow from snow-melting reduces the effective stress and hence the shear strength of the soil.

Additionally, a series of bedrock strata at the soil–bedrock interface, inclined southwards with a 10–30° dip (Gabus et al., 2008a, 2008b), were identified from geological observations as outcrops or ‘steps’ in the bedrock above the ground, which are expected to affect the local slope stability (Lucas et al., 2017).

Based on the reported information of field monitoring, laboratory testing and geological observation, it was predicted that a scree saturated above a steeply inclined shallow bedrock could become unstable. Furthermore, should there be a step in the bedrock that outcrops at the surface, failure would occur upslope of the outcrop, depending on step geometry (height/length). A slope failure was thought less likely to happen if the bedrock was parallel to the slope with no bedrock step, albeit that the lower part of the slope would then be more endangered, where GW could emerge at the surface (Take and Beddoe, 2014). Intermediate cases would be determined by the height (y) and length of a step in the bedrock (X_2), and would lie between these two failure mechanisms, which should be explored through physical and numerical modelling. The hypothesis was explored using a ground model that integrates findings from field monitoring and data from laboratory testing, by varying soil thickness and bedrock step geometry. Numerical simulations were conducted first in two dimensions, using Seep-Slope/W software from GeoStudio (Krahn, 2004a, 2004b) to analyse key influences. These were then investigated in the subsequent physical modelling programme, in which a plane prototype geometry and model soil were tested in parametric analyses under 50–52g in the ETH geotechnical drum centrifuge (Springman et al., 2001). The results show convincing evidence of the effect of the bedrock step geometry on the landslide triggering and the respective mechanisms of failure.

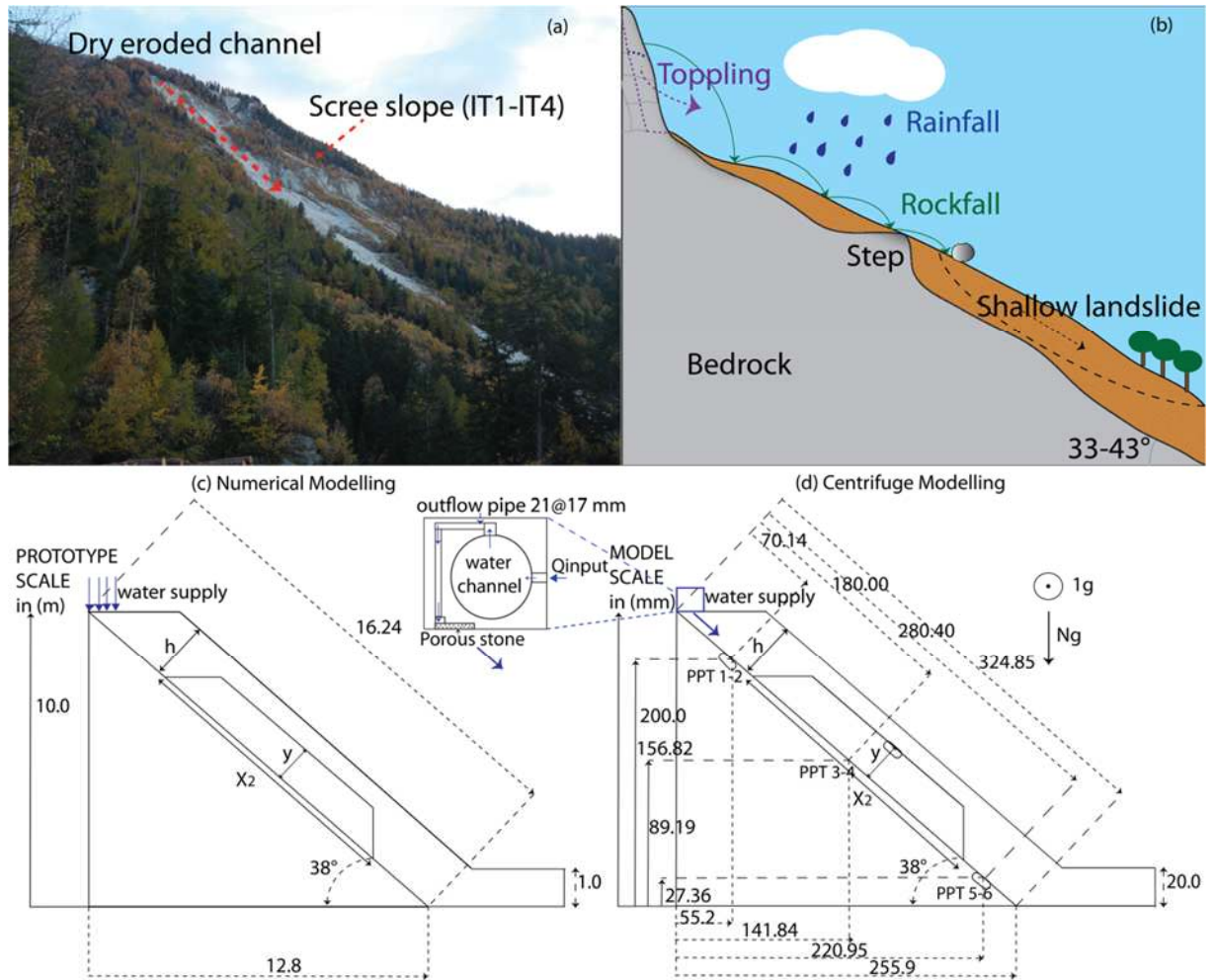


Figure 6.1. Scree slope in the Meretschibach catchment, Bochtür area: (a) scree slope and dry eroded debris flow channel, (b) simplified schematic ground model, (c) prototype and numerical model in metres and (d) scaled centrifuge physical model in millimetres. The direction of the Earth's gravity acts out of the paper towards the reader. IT, instrumented soil trench; PPT, pore pressure transducer

6.2 Methodology

The physical and numerical modelling are complementary and allow different aspects to be investigated using parametric analyses. The centrifuge modelling captures

- cracking and failure initiation (moment of mobilisation of soil and water as the debris runs out)
- timing and run out (to be considered with respect to scaling effects)
- transient pore water pressure (PWP) processes, derived from GW flow and rainfall in three dimensions (3D).

The numerical model represents

- idealisation as a decoupled steady-state analysis of flow, combined with
- a simplified two-dimensional (2D) analysis of state at failure of homogeneous, rigid–perfectly plastic soil
- and it does not consider transient behaviour, pre-failure deformations, three-dimensional (3D) influences (on flow or failure) or the effects of tensile cracking on macro-permeability, form of the failure surface or a variable and/or strain-dependent shear resistance mobilised along a failure surface and so on.

This is important, on one hand, because the rigid–perfectly plastic soil response, modelled in the slip surface analysis is generally considered to be conservative, given that the contributions of the side shear surfaces to the total shear resistance are not included. This is why it can be argued that it is an acceptable approximation (e.g. Askarinejad et al., 2012; Springman et al., 2003). On the other hand, creating opportunities for water to ingress easily through tension cracks to greater depth causes rapid saturation and potentially swifter ‘fluidisation’ of the failing landmass with reduced shear strength, leading to earlier failure, a different form of the failed mass and most likely a far greater run-out. This is more risky for inhabitants living below such a failing slope.

Therefore, running both types of analyses allows a richer understanding to be obtained of the response of a slope to GW flow combined with rainfall. Furthermore, checks can be made on whether there are secondary or tertiary effects that will change the expected behaviour considerably.

Two types of hydrological regimes were applied in numerical models, followed by a series of 17 centrifuge model tests (Table 6.1), in which soil thicknesses and bedrock step geometry were varied. Slope stability under GW flow released at the top of the slope was investigated initially, followed by an antecedent of GW flow combined with intense rainfall.

A variety of cases were run in the numerical simulations, which helped to select critical combinations of soil thickness and bedrock step geometry. These were then studied in the centrifuge tests to identify slope failure triggering mechanisms.

Centrifuge technology has been used for slope stability analysis since the 1960s (Taylor, 1995). The challenge of trying to represent a prototype slope with a small model has confronted many researchers over the years, often through the establishment of a reference model, with appropriate stress history and heterogeneity in the slope. Increasing radius, measured from the centrifuge axis, from top to bottom of the slope affects the nominal g-level imposed on the model, leading to challenging testing conditions (Bryant et al., 2015; Park, 2013; Schofield, 1980). Recent results on the simulation of landslides induced by rainfall using centrifuge technology have been promising (Askarinejad, 2013; Askarinejad et al., 2014a, 2014b; Craig, 2014; Lee and Bolton, 2006; Ling and Ling, 2012; Schofield, 1978; Take, 2014; Take and Beddoe, 2014; Timpong et al., 2007). However, there are still challenges in modelling such events in a geotechnical centrifuge. This contribution offers some additional original ideas and solutions.

6.2.1 Test soil properties

The scree slope (Figure 6.2, Table 6.2) is mainly a silty gravel (GP-GM) with <10% fines (Lucas et al., 2017). The field soil grain size distribution (GSD) (Figure 6.2) is an average of gradings obtained from samples from four instrumented trenches (IT1–4). There were less fines in the gravel at higher locations (1900 m a.s.l.), as shown for IT3 (GP) (Figure 6.2). The critical state angle of friction of the soil was determined as 41° from constant shear drained (CSD) stress path tests on reconstituted specimens at an equivalent relative density of 41–59% (Grob, 2015). The ‘scaled soil’ grading is $\approx 1/50$ th of the prototype soil (for centrifuge tests performed at 50g), to maintain the grain-size-structural element dimensional ratio in the small-scale model – that is, the bedrock steps and the overall dimensions of the strong box should not influence the model slope response due to unwanted particle-size effects.

The soil used in the centrifuge tests (mixed scaled soil: Table 6.2, Figure 6.2) is a mixture of 90% Hostun sand (HN31) with 10% Minisil B1, classified according to Swiss standard classification (SN 670004-2NA), as poorly graded sand with silt (SP-SM). The maximum and minimum void ratios are 0.6 and 0.9, respectively. The matrix soil Hostun sand is angular with a (peak) friction angle of 36° determined by drained consolidated triaxial testing at a relative density of 73% and a maximum stress ratio (q/p') of 1.46 (Alber, 2017). Although the friction angle is lower than the 41° obtained from the scree on steep

slopes up to 43° inclination, it represents a marginally conservative situation for the model slope, which was set at 38° (Askarinejad, 2013).

At prototype scale (Ng), the mixed scaled soil reverts to a prototype mixed (GP) (Table 6.2, Figure 6.2). Using silty sand for the centrifuge testing allowed a comparison to be made between different model tests in terms of pore-water pressure (PWP) development and failure location, focusing on the failure mechanism due to rain, GW and the effect of stepped bedrock.

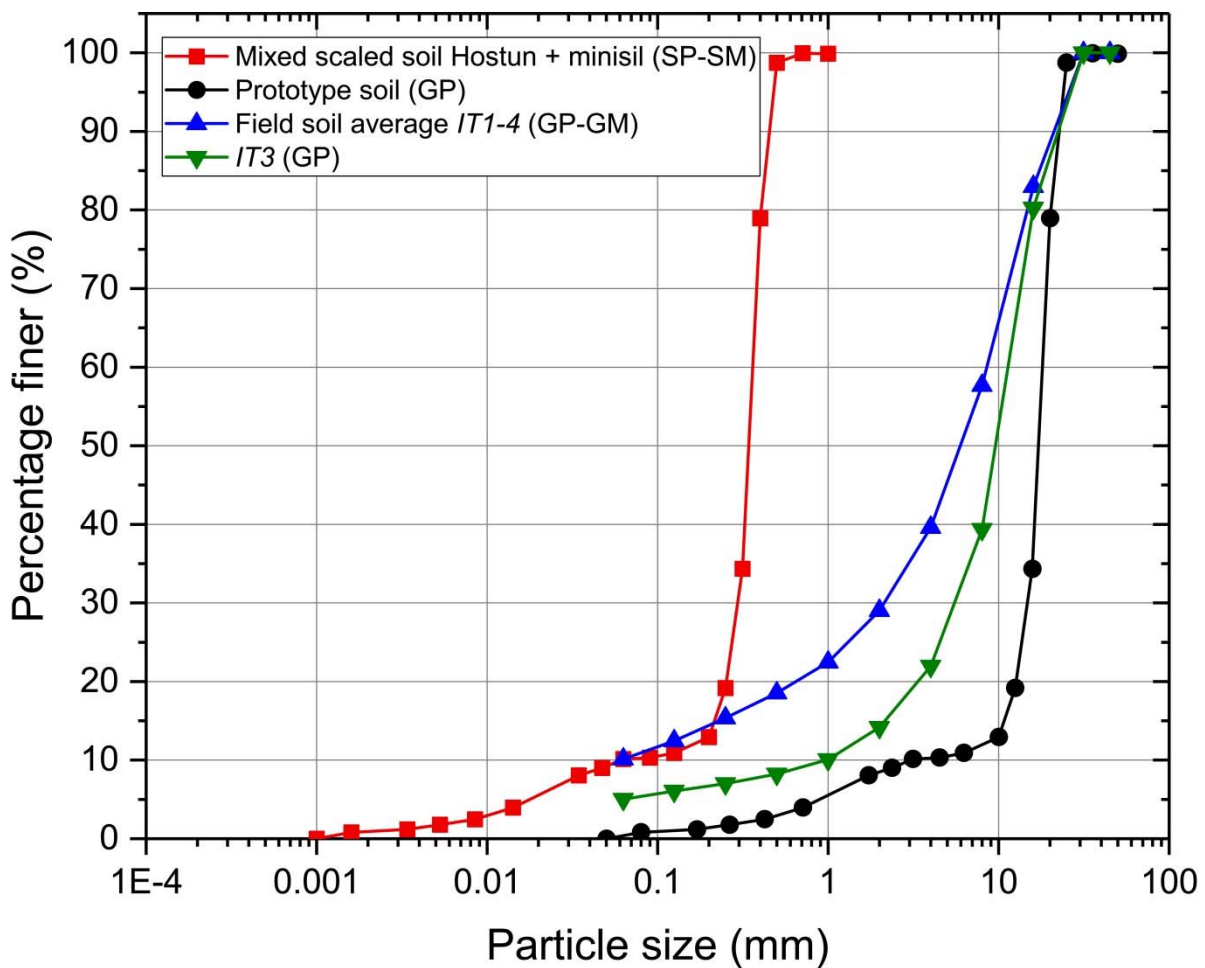


Figure 6.2. GSDs: average grading curve for field gravel from IT1–IT4 (GP-GM) and gravel IT3 (GP), silty sand mixed scaled soil (SP-SM); prototype gravelly soil (GP)

6.2.2 Model geometry and hydraulic conditions

The main features of the ground model were provided by Lucas et al. (2017) and were integrated into the physical and numerical models. The model slope angle is 38° , with soil thickness (h) varying between 1 and 3 m in depth (prototype). A simplified geometry

of the step in the bedrock was added with two different values of height (y) and length (X_2) (Figures 6.1(c) and 6.1(d), Table 6.1). The interior angles formed between step slope bedrock are 36° (near pore-pressure transducer (PPT) A) and 52° (near PPT C).

6.2.3 Hydraulic regime

Two GW conditions were implemented

(a) water flow applied at the top of the slope through a hydraulic boundary condition in the numerical model and a porous stone at the base of a water distribution cylinder in the centrifuge (see inset, Figures 6.1(c) and 6.1(d), further details in supplementary information)

(b) rainfall sprinkled above the slope in the centrifuge (see Askarinejad, 2013, Sections 6.2/6.3).

Water infiltrates from the top of the slope and seeps nominally parallel to the slope, causing the PWP to rise (a). Additional water infiltrates into the slope through rainfall, to reduce suction enough to trigger a slope failure (a) plus (b).

Table 6.1. Programme for the numerical simulations (those chosen for centrifuge testing are in bold)

Test #	Name of test	Soil thickness h (m)	Bedrock step height y (m)	y/h (m)	Bedrock step length X_2 (m)	Ground model figure	Centrifuge test descriptor
1	GP_1.0_0_0	1.0	0	0	0		
2	GP_1.0_0.25_8.5	1.0	0.25	0.25	8.5		
3	GP_1.0_0.5_8.5	1.0	0.5	0.5	8.5		
4	GP_1.0_0.6_8.5	1.0	0.6	0.6	8.5		
5	GP_1.0_0.75_8.5	1.0	0.75	0.75	8.5		4.a (Fig S6.9.24)
6	GP_1.25_0_0	1.25	0	0	0		8.b (Fig. S6.9.28)
7	GP_1.25_0.25_3	1.25	0.31	0.25	3.0		
8	GP_1.25_0.5_3	1.25	0.63	0.5	3.0		
9	GP_1.25_0.6_3	1.25	0.75	0.6	3.0		7.b (Fig. S6.9.27)
10	GP_1.25_0.75_3	1.25	0.94	0.75	3.0		
11	GP_1.25_0.25_8.5	1.25	0.31	0.25	8.5		

12	GP_1.25_0.5_8.5	1.25	0.63	0.5	8.5		
13	GP_1.25_0.6_8.5	1.25	0.75	0.6	8.5		7.a, 8.a (Fig. 6.15)
14	GP_1.25_0.75_8.5	1.25	0.94	0.75	8.5		
15	GP_1.5_0_0	1.5	0	0	0	6(a)	1.b, 6.b (Fig. 6.12)
16	GP_1.5_0.25_3	1.5	0.38	0.25	3.0	5(a),6(b)	
17	GP_1.5_0.5_3	1.5	0.75	0.5	3.0	5(b),6(c)	5.b (Fig.S6.9.25)
18	GP_1.5_0.75_3	1.5	1.125	0.75	3.0	5(c),6(d)	2.b, 3.b, 4.b (Fig. 6.13, S6.9.23)
19	GP_1.5_0.25_8.5	1.5	0.38	0.25	8.5	5(d),6(e)	
20	GP_1.5_0.5_8.5	1.5	0.75	0.5	8.5	5(e),6(f)	2. a, 3.a (Fig. S6.9.22)
21	GP_1.5_0.75_8.5	1.5	1.125	0.75	8.5	5(f),6(g)	1.a, 5.a, Proof. (Fig. 6.14, S6.9.21)
22	GP_3.0_0_0	3.0	0	0	0	6(h)	
23	GP_3.0_0.25_8.5	3.0	0.75	0.25	8.5	6(i)	
24	GP_3.0_0.375_8.5	3.0	1.125	0.375	8.5	5(g)	6.a (Fig. S6.9.26)
25	GP_3.0_0.5_8.5	3.0	1.5	0.5	8.5	6(j)	
26	GP_3.0_0.75_8.5	3.0	2.25	0.75	8.5	6(k)	

All dimensions in prototype scale

GP_h_y/h_X₂: Poorly graded gravel (GP)_soil thickness (h)_height step/soil thickness, y/h_length step, (X₂).

Dimensions in prototype scale.

Table 6.2. Properties of field gravel (GP-GM), mixed scaled soil (SP-SM), scaled up again at 50g (GP).

Property	Field soil (GP-GM)	Mixed scaled soil (SP-SM)	Prototype mixed (GP)
e _{max}	0.690	0.899	-
e _{min}	0.340	0.609	-
D ₅₀ (mm)	6.400	0.345	17.300
D ₁₀ (mm)	0.065	0.060	3.000

$C_u (D_{60}/D_{10})$	138.4	6.0	6.033
$C_c ((D_{30}^2/D_{10})D_{60})$	9.0	4.2	4.2
G_s	2.680	2.650	2.650
k (cm/sec)	1.3E-03 ($e=0.57$)	4.52E-04 ($e=0.84$)	4.1E-01 ($e=0.57$)
Friction angle, ϕ' (°)	41.0 ¹	-	40.0 ²
Fines content (%)	9.87	10.0	0.0
Cohesion c' (kPa)	0.0	-	1.0 ²
Sand content (%)	18.38	90	8.13

Notes: e , void ratio; D_{10} , D_{30} , D_{50} , D_{60} , soil particle diameter where the 10, 30, 50 and 60% of the sample is finer; k , coefficient of permeability by Kozeny-Carman (Carrier, 2003). Void ratio $e=0.57$ average from field data IT1-4 (Lucas et al., 2017).⁽¹⁾: derived from triaxial stress path test, ⁽²⁾: values adopted for numerical modelling.

6.2.4 Numerical model

GeoStudio programs Seep/W and Slope/W were used to investigate a variety of scenarios to explore the relevance of soil thickness and bedrock geometry for the assessment of the stability of a steep slope during GW flow. Preliminary results were obtained using an estimated hydraulic conductivity and a saturated/unsaturated model.

The geometry of the numerical model is shown in Figure 6.1(c). The slope bedrock is of 16 m length and 10 m height, with an inclination of 38°. Soil thickness variations are $h = 1.0, 1.25, 1.5, 3.0$ m. The gravel (GP) properties include $\phi'=40^\circ$; $c'=1$ kPa (Table 6.2, Figure 6.2), which were selected as representative of the soil used in the centrifuge at prototype scale.

Constant GW flow (Q) was applied from the top of the slope, and the model response was analysed using Seep/W (GeoStudio, 2016), assuming steady-state seepage. The development of PWP and the location of the GW table provided the parental conditions for the slope stability analysis using Slope/W. 2D limit-equilibrium analysis was performed using the Morgenstern and Price (1965) method, with the slip surface limited to passing through the soil layer.

Numerical modelling explored how the soil thickness (h) and bedrock step geometry (height (y); basal width (X_2)) affect the global factor of safety (F.S.) for slope stability under steady-state GW flow. The normalised GW flow rate ($Q_{\text{step}} / Q_{\text{no bedrock step}}$) necessary to trigger failure was plotted as a function of bedrock step height (y) and soil thickness

(h) (Figure 6.1(c)). The stability ($F.S._{step}/F.S._{no\ bedrock\ step}$) was also investigated under a specific GW flow rate (Q) to identify which model geometry was more susceptible to causing a surficial landslide. The detailed testing programme is given in Table 6.1.

6.2.5 Physical model

The testing programme was carried out in the ETH Zürich geotechnical drum centrifuge (Figure 6.3). The 2.2 m diameter centrifuge can spin at 600 r/min to deliver a maximum acceleration of 440g, testing two diametrically opposed models (models a and b, in Figure 6.3) simultaneously (Springman et al., 2001).

6.2.5.1 Geometry slope and soil characteristics

Nine different model types were studied in a programme of 17 centrifuge tests (bold in Table 6.1) to investigate the effects of soil thickness and bedrock step in a scree slope under two hydraulic regimes: GW and GW plus rainfall. The slope geometry is shown in Figures 6.1(d), 6.4 and 6.5, with a slope inclination angle of 38° . The bedrock and steps were made of aluminium and fine sand was sprayed onto a layer of glue to simulate frictional contact. The joints between bedrock slope and steps were sealed with Hylomar M and are considered impermeable. The soil thicknesses tested in the scaled model were $h=2.0, 2.5, 3.0$ and 6.0 cm equivalent to $h=1.0, 1.25, 1.5$ and 3 m at the prototype scale, respectively. All models were provided with a toe berm of 2 cm (model scale) in height to prevent local erosion. Take and Beddoe (2014) reported that the omission of such a feature would affect, and probably advance, the initiation of failure in some cases.

Soil layers, maximum 2 cm high, with 5% moisture content, were tamped to ensure model stability at 1g between model placement in the drum centrifuge (requiring rotation through 90°) and testing at 50g. The slope was cut with an aluminium frame guide and plate, which could be adjusted for different soil layer thicknesses.

The model is contained by an aluminium box of 40x40x20 cm dimensions (Figure 6.4), with one Plexiglas side window and two water drainage outlets at the corners. The box is covered by a multi-purpose aluminium box (Figure 6.3), which contains four to six rain nozzles, either three (model a, Figure 6.3) or one (model b, Figure 6.3) photogrammetry camera(s) (Askarinejad et al., 2012), and the newly designed GW distribution system, located at the top of the slope (Figure 6.1(d)).

The water supply is shown in the inset of Figure 6.1(d) and represents a cylindrical pipe and a porous stone that runs the width of the model box, whereas the input flow is located in the middle. There are 21 equally spaced outflow pipes (additional information in supplementary material).

It was a challenge to reproduce a uniform distribution of the GW flow along the top of the slope, due to the radial acceleration in a drum centrifuge with a radius of <1 m. Several tests were performed with different model orientations and modifications to the set-up to reduce the influence of the radial acceleration field, Coriolis effects and Earth's gravity (Caicedo and Thorel, 2014; Schofield, 1980), which caused water to flow markedly to the model's sides, producing undesirable failures by erosion at the model's edge. The difference in the radius of the model at the top (0.83 m) and bottom (1.00 m) of the slope causes a nominal variation in g level from 45.1g to 54.7g. The component of the Earth's gravity, which acts from the back of the box towards the window, has a significant effect on the flow regime. The porous stone was inclined to achieve a uniform water flow across the width of the slope, and the bedrock geometry was tilted and re-designed as a 3D form (Figure 6.4), taking the influence of Earth's gravity with increasing distance from the centre of rotation into consideration. All manufacturing was done in house by the centrifuge and workshop team.

6.2.5.2 Set-up in drum centrifuge and instrumentation

Figure 6.3 shows the centrifuge set-up, which was adapted to apply the two hydraulic conditions. All devices were designed to operate safely inside the drum at an acceleration of at least 65g. The GW flow supply system consisted of an external source of water flowing continuously inside the drum to a perimetral channel at the top of the drum wall (Springman et al., 2001). The channel was connected to two lateral water tanks (each of 5 litre capacity), so that the inflow was supplied at 1000 ml/min. The two tanks were instrumented with a PPT to monitor water storage and were connected together with a discharge outlet, in case they should overflow at maximum capacity. Water was extracted from each tank and supplied to each model at a predefined rate by a pump (Reglo-Z, Analog Z-140, Ismatec), and was measured by a magnetic inductive flow sensor (SM4100). A series of tests were performed to check the pipe diameter (inner diameter 8 mm), the water filling system time and refill rates and the calibration of the pumps and flowmeter, which were connected to the centrifuge computer located under the baseplate to the central water tank (CWT) and controlled from the centrifuge control room.

The rainfall was supplied by a CWT of 24.6 litre capacity, containing water pressurised from an air tank to a maximum of 1000 kPa, with an output pressure of 300 kPa (Figure 6.3). Water was supplied to the inner and outer pipe channels milled in the top plates of the climate chamber (Askarinejad, 2013; Figure 6.3, see further details in supplementary information) and distributed to the nozzles. The rainfall was sprayed into the chamber through aluminium extension tubes of 5–10 cm in length, so that the rainwater emerged as a spray within a range of 18.9–26.7 and 13.9–21.7 cm, respectively, above the ground surface. The rain intensity per nozzle was calculated measuring their respective flow (ml/min) and area, depending at the distance of the nozzle–soil (see further details in supplementary material). Assuming that each nozzle rain spray overlapped the soil surface, the total rainfall intensity on the model scale (mm/h) is estimated as the addition of all intensities. On applying scaling laws, the rain intensity at the prototype was estimated as N times smaller than the model scale (Askarinejad, 2013). PWP was measured by Druck PDCR81 PPTs and Keller 2Mi (measurement range varying from 35 to 700 kPa) in six locations at three heights (Figures 6.1(d) and 6.4(b)): upstream, on top of and downstream of the bedrock step. The sensors were fitted with porous stones, and saturated and calibrated in the laboratory. Sampling rates were 10 Hz for model a: PPT1–2, and PPT4, and model b: PPT1–2, PPT4 and PPT6 and 1 Hz for model a: PPT3–6 and model b: PPT2–3 and PPT5. Slope movements were monitored using cameras IDS uEye UI-6240 C with a resolution of 1.3 megapixel. Three cameras were placed in the strongbox lid of model a, and one for model b: each with a sampling rate of 0.5–1 Hz.

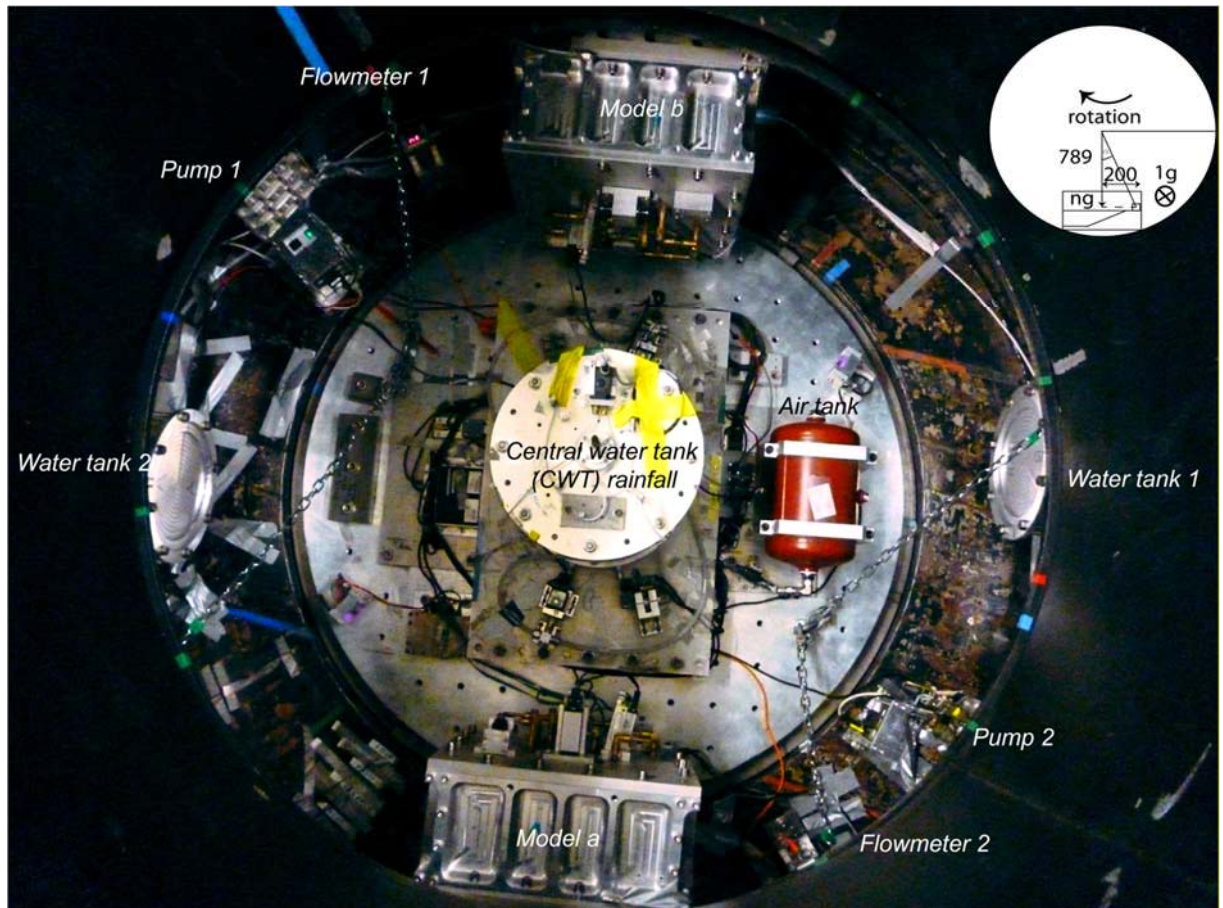


Figure 6.3. Overview of the set up in the drum centrifuge, with two models for slope stability, model a and b, only the “upper box” (climate chamber) is visible in this photograph. The “lower” boxes (Figure 6.4(a)) are located behind the “upper” boxes in the drum), flowmeter & pump 2, flowmeter & pump 1, two connected lateral water tanks (1, 2) to supply GW flow and the air pressure cylinder. The CWT is located at the centre of the tool platform to supply rain. The dimensions in the sketch (above right) are in mm.

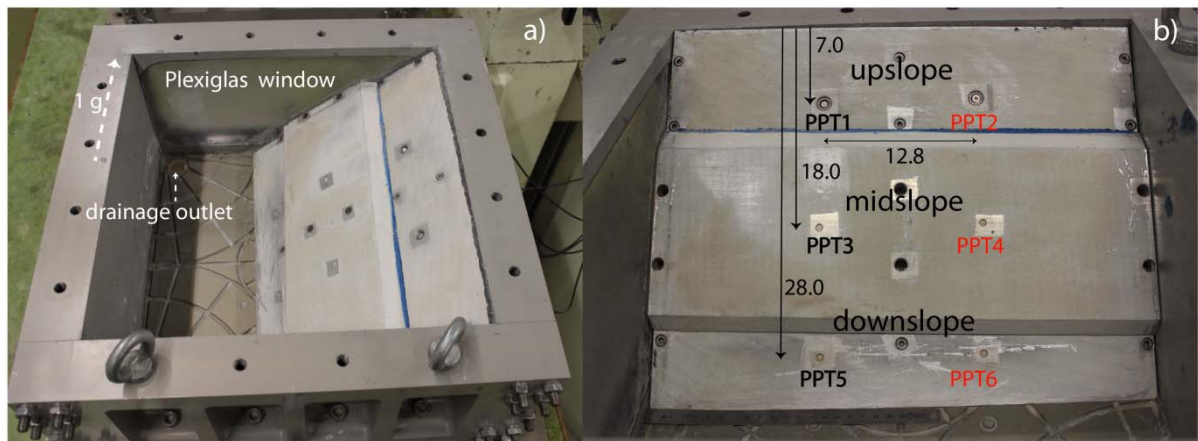


Figure 6.4. (a) Centrifuge model lower box (40X40X20 cm) with step bedrock and with a plexiglas window on the left and two water drainage outlets at the base at each corner of the box, (b) bedrock aluminium plate with PPTs and bedrock step. The direction of earth’s gravity acts out from the bottom to top in Figure 6.4(a) and right to left in Figure 6.4(b). Distances in centimetres. Detailed geometry of bedrock and PPT geometry and location are given in supplementary material.

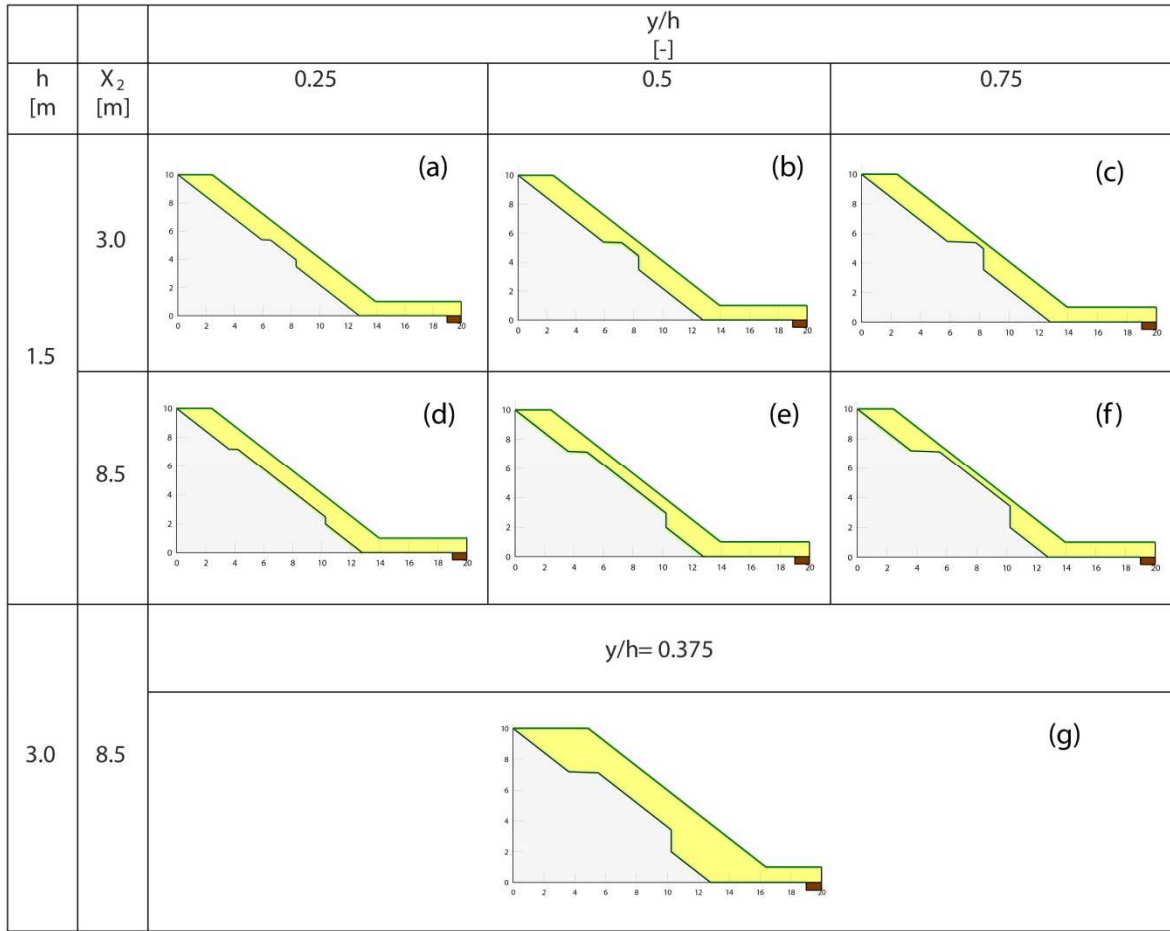


Figure 6.5. Elevation view of the bedrock and soil layer geometry used in numerical and physical modelling. Slope height is 10 m and the width of the drawing is 20 m. The drainage outlet is shown in brown at the bottom right of each slope (h is the soil thickness, y/h is the height bedrock step/soil thickness and X₂ is the length of the bedrock step).

6.3 Results

6.3.1 Numerical modelling

An overview of all plane-strain failure mechanisms is given in Figures 6.6(a)–6.6(k) and will be discussed throughout the following sections. Figures 6.7(a) and 6.7(b) show the GW flow rate required to induce failure under two variations of bedrock step geometry: (a) soil thickness (h) and (b) bedrock step length (X₂), with (y/h) as the height of bedrock step normalised by soil thickness (ranging from 0 to 0.75: Figure 6.5). The normalised GW flow rate $Q_{\text{step}}/Q_{\text{no bedrock step}}$ is calculated to establish what flow is necessary to induce failure. In both cases, the Q required to cause failure decreases as the size of the bedrock step increases, either with an increase of height or length.

Two soil thicknesses $h=1.5$ and 3.0 m, both representative of field conditions, were compared in Figure 6.7(a) for the longest bedrock step ($X_2=8.5$ m). Soil depth variation clearly affects the flow rate required to trigger failure, although the effect is smaller and similar to the case of the slope with no bedrock step ($y/h=0$), for steps $y/h<0.4$. The flow rate required decreases to 50% of the case without a bedrock step for $y/h=0.75$, for both models with $h=1.5$ and 3 m. The soil above the shorter step was more stable under equivalent flows (Figure 6.7(b)), as it has less capacity to pond the seepage flow (Figures 6.6(b), 6.6(e) and 6.6(i)).

Figures 6.8(a) and 6.8(b) show the effect of bedrock step length X_2 variation on the normalised GW flow rate required for slope failure simulation, for $h=1.25$ and 1.5 m. The normalised GW flow rate to trigger failure does not change much for $y/h=0.25$ compared to a slope with no bedrock step. The effect of step length is significant when $y/h \geq 0.6$, when the required GW flow rate to cause failure is roughly halved. An intermediate response is shown at $y/h=0.5$ for $X_2=3.0$ and 8.5 m, whereby significantly higher flow rates, similar to those for $X_2=0$, are necessary to cause failure for the shorter step. Soil depth plays a minor role here too, when comparing both depths at $X_2=3.0$ m. Greatly reduced flows are needed for $y/h \geq 0.6$, for $X_2=8.5$ m. A longer step can affect the slope stability more during GW flow than a minor change in soil thickness. $Q_{\text{step}}/Q_{\text{no bedrock step}}$ at failure for $0.25 < y/h \leq 0.75$ decreases as the step height (y) increases, while it is similar or equal to 1 for $y/h < 0.25$.

Figure 6.9 shows the normalised bedrock step height (y/h) plotted against a normalised F.S. ($F.S._{\text{step}}/F.S._{\text{no bedrock step}}$) for a specific flow rate. The F.S. does not change much for $h < 1.5$ m (Figure 6.9(a)), with a smaller step length of $X_2=3$ m (20% of the length of the slope) and decreases only when $y/h \geq 0.5$, typically by 10% for the highest step ($y/h = 0.75$). The deeper the soil depth, the greater the flow needed to saturate the soil layer upstream of the step to cause instability, whereas water can flow over the short step in the bedrock, reducing the F.S., but again, only by 10%.

Four different soil thicknesses are compared in Figure 6.9(b), all with a defined step length of $X_2=8.5$ m: the most unfavourable case in these analyses. A combination of a longer step with a higher step reduces the F.S. of the slope for all soil thicknesses simulated: by 40% when h is between 1.0 and 1.5 m. F.S. decreases as y increases for a

defined flow input Q . Likewise (Figure 6.9), F.S. decreases as y increases and h decreases (Figure 6.10).

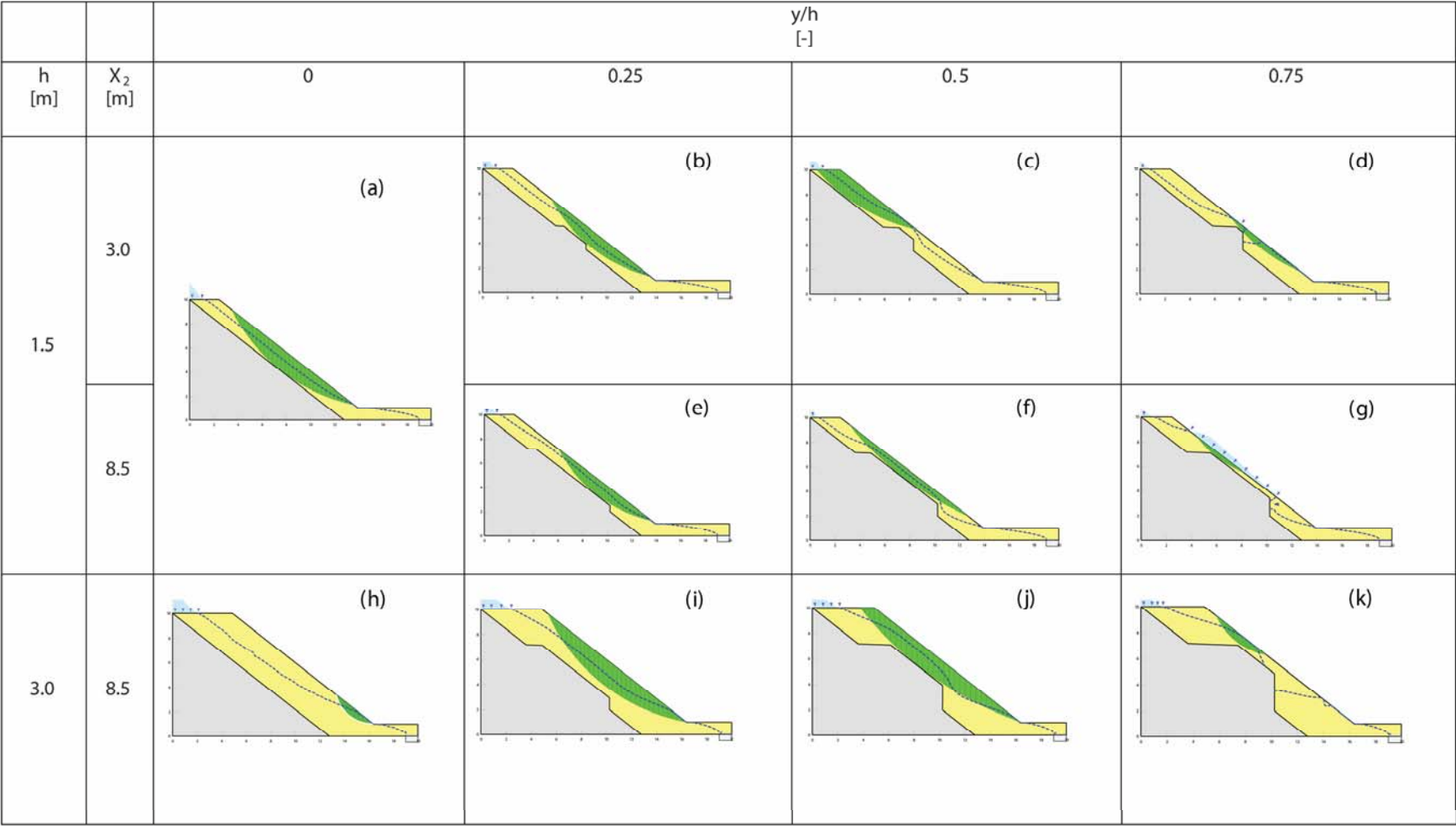


Figure 6.6. Slip surfaces at failure for numerical simulation with GeoStudio. Hydraulic conditions of *GW* flow were defined with SEEP/W, and slope stability by SLOPE/W.

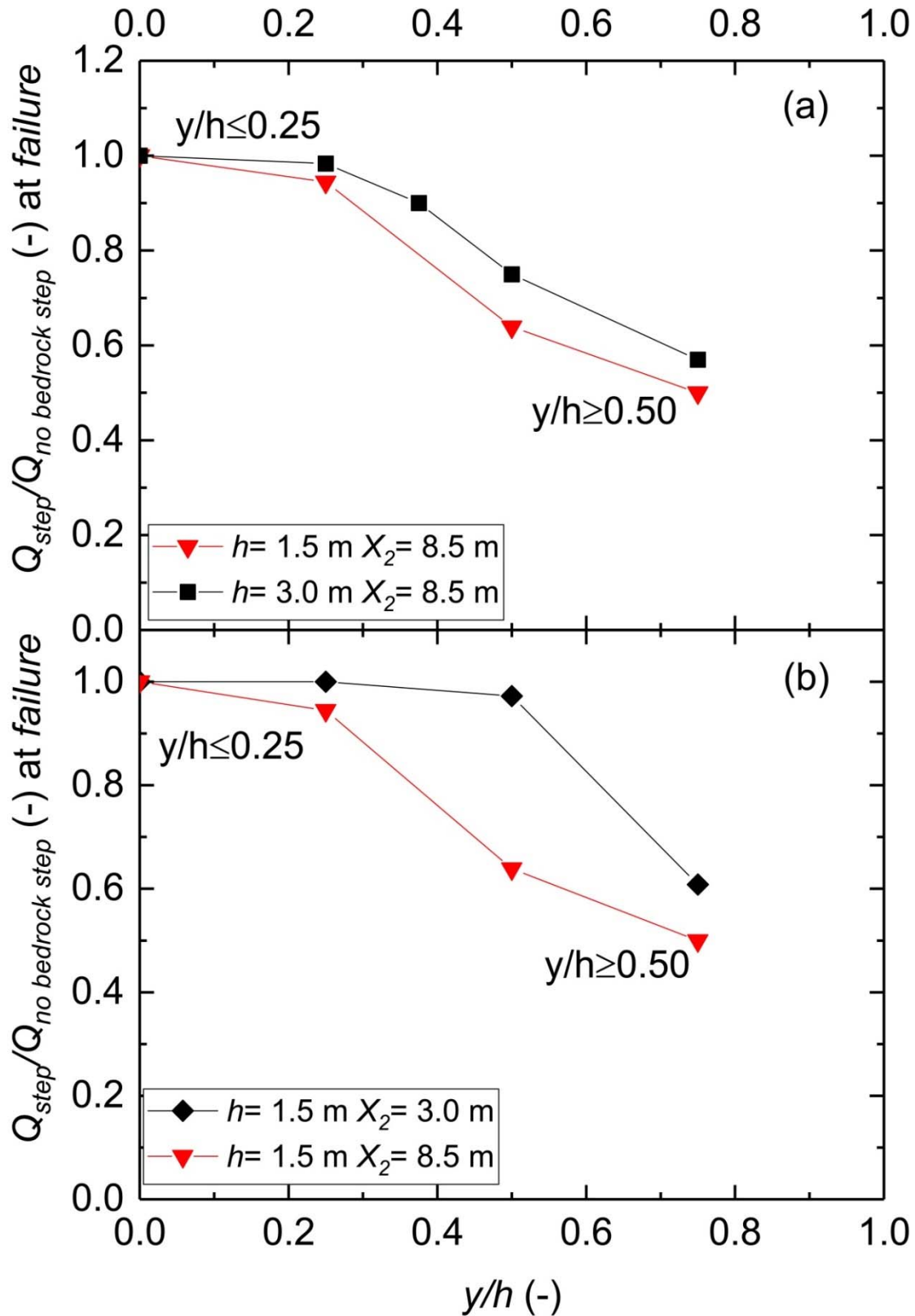


Figure 6.7. Numerical modelling: (a) effect of soil thickness and step height (y/h) on the flow required for failure, (b) effect of the bedrock step length (X_2) on the flow required for failure. y : height of bedrock step, h : soil thickness, Q is the GW flow rate.

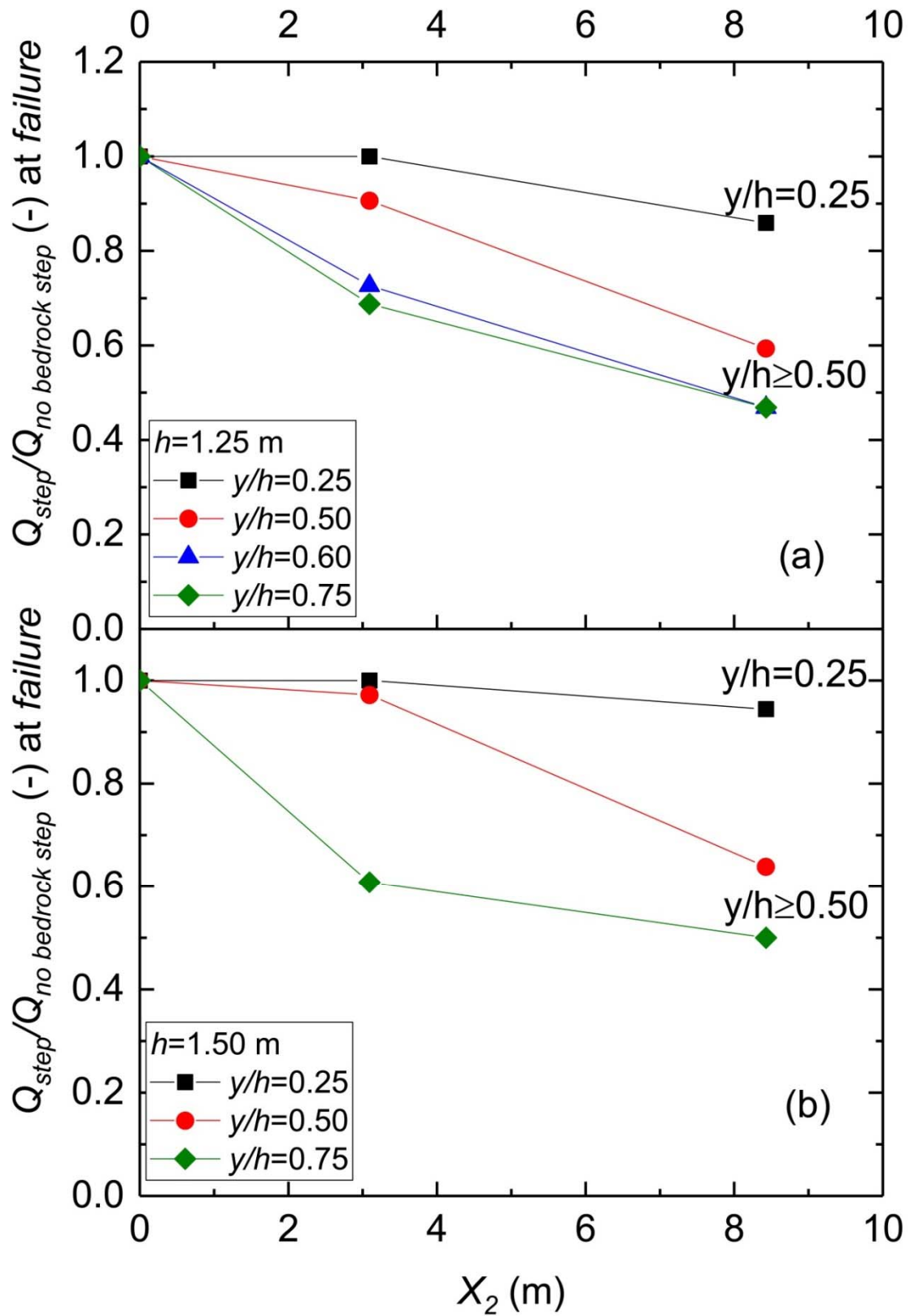


Figure 6.8. Effect of bedrock step (y/h) and bedrock length X_2 versus normalised flow required for a slope failure for soil thicknesses of (a) $h=1.25$ m and (b) $h=1.5$ m

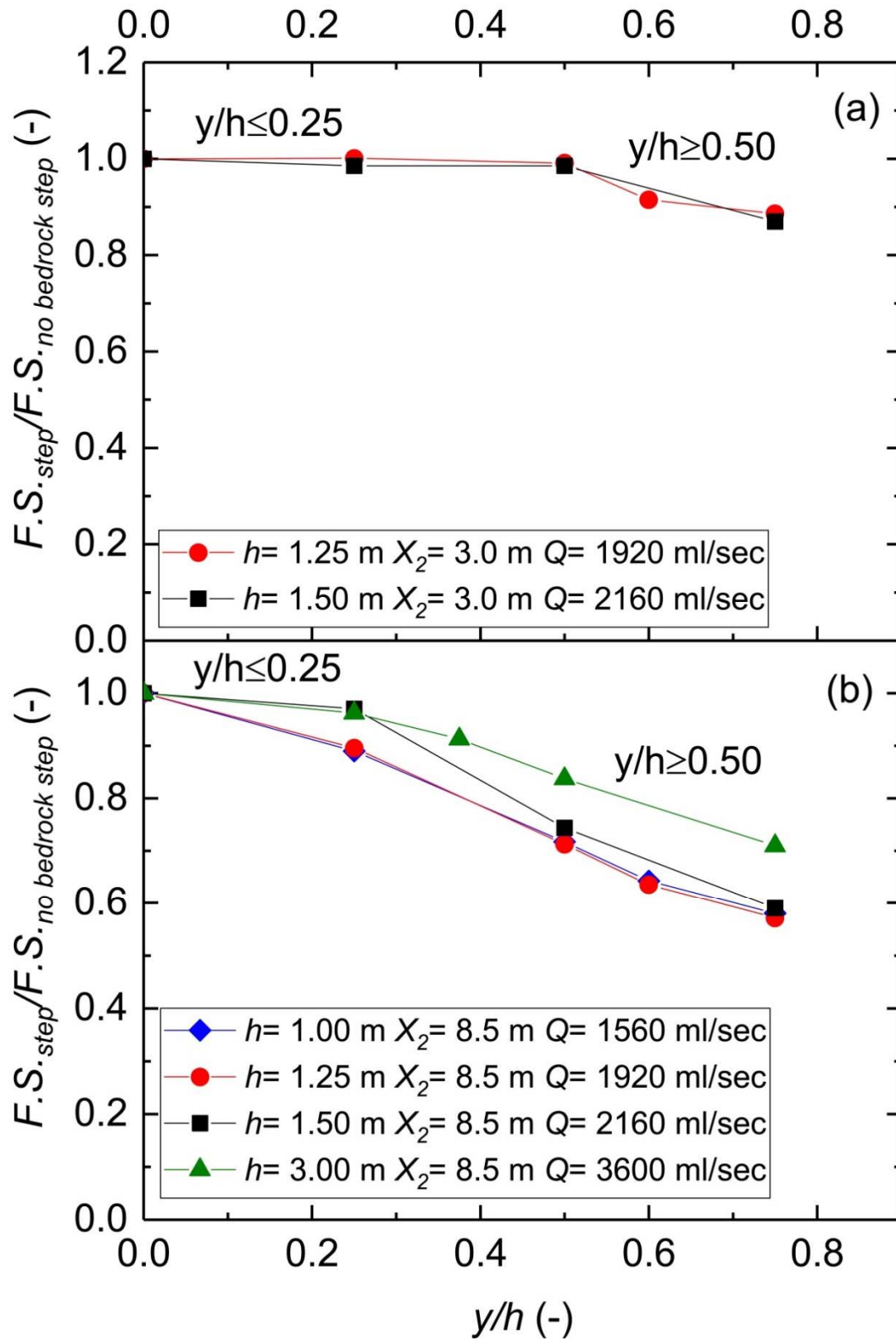


Figure 6.9. Effect of soil thickness (h) on the normalised F.S. for equal bedrock step length X_2 and different GW flows (a): $X_2=3$ m and (b) $X_2=8.5$ m.

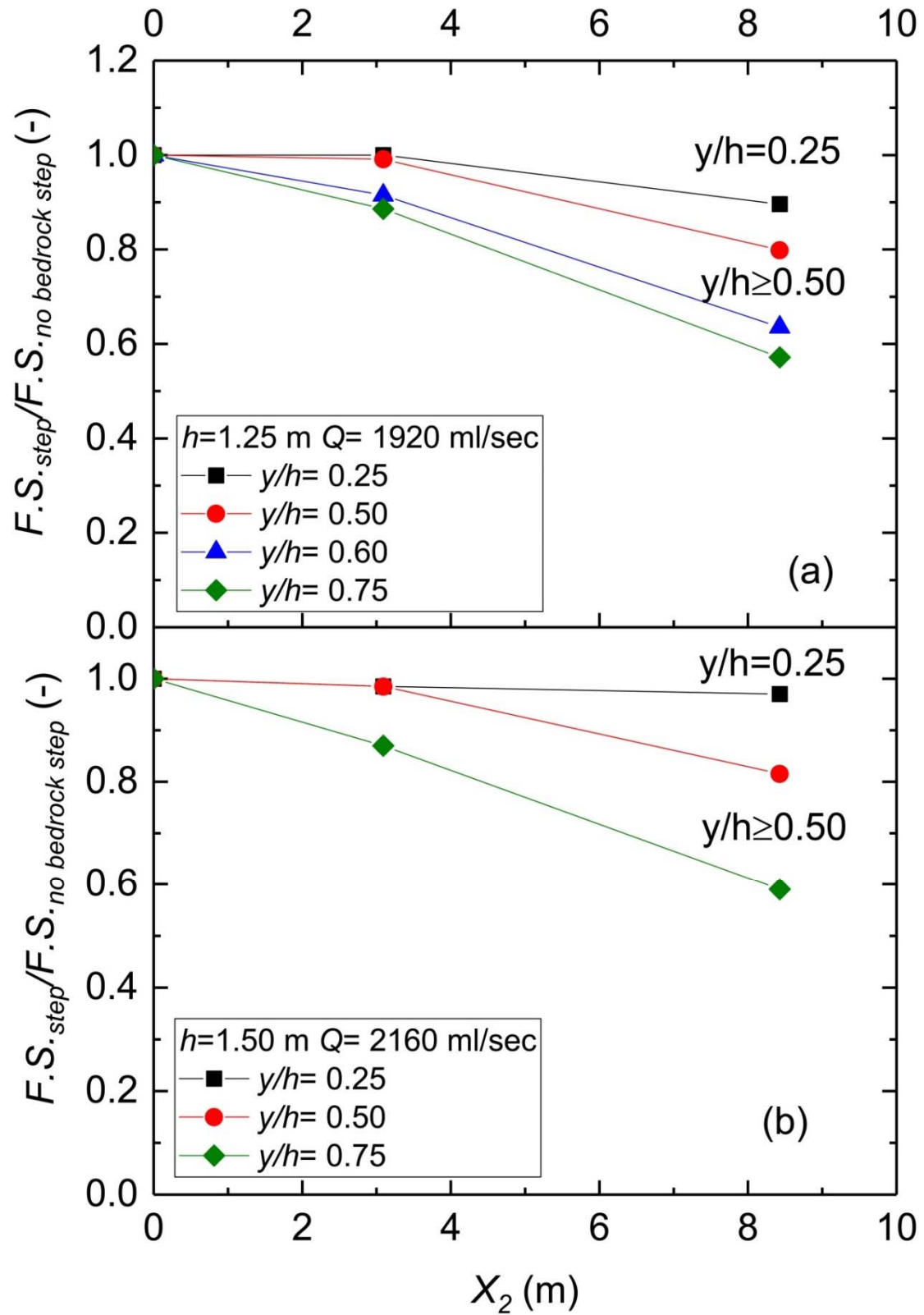


Figure 6.10. Effect of the length of bedrock step X_2 on the normalised F.S. for different soil thickness and a specific GW flow. (a) For $h=1.25$ m and (b) for $h=1.5$ m.

6.3.2 Physical modelling

Selected results from 17 centrifuge tests, performed on nine physical models, with three different soil thicknesses and two different bedrock step geometries (Table 6.1, Figure 6.5) are shown in this section. The rest can be found in the supplementary material.

An overview of all failure events is given in Figures 6.11(a)–6.11(h) and will be discussed in the following sections.

Figure 6.12 shows PWP development against time upslope, midslope and downslope. Each line dashed or solid represents a PPT location (Figures 6.1(d) and 6.4(b)). The rate of GW flow applied on top of the slope against time (model scale) is given at the bottom. GW and rainfall were combined in some later cycles (Figure 6.12(b)).

The Q was increased in steps in both tests 1.b and 6.b because the tank was refilled after it was emptied at flow rates >1000 ml/min. The nominal pump capacity was 3290 ml/min but the maximum flow possible at 50g was calibrated at about 2500 ml/min.

PWP sensors at similar elevations show different initial PWP, due either to the model position in the drum at 1g prior to testing or a zero offset reading variation affected by the atmospheric pressure. In addition, despite taking all precautions, it could be due to the marginally incomplete saturation of the porous stone.

The increased PWP in both tests fluctuated between 3 and 7.5 kPa, with dissipation occurring immediately following the pause in the GW flow, due to the high drainage capacity of the soil. Continuous rain was applied in test 6.b (Figure 6.12(b)) at 1379 ml/min, equivalent to a rainfall infiltration 215 mm/h at model scale and 4.3 mm/h in the prototype (Section 6.2.2, see further details in supplementary material). The rainfall helped to increase the pore pressure by an additional 2 kPa. Slope failures were not observed in these tests.

Figure 6.13 shows the effect of a higher ($y/h=0.75$) bedrock step with $X_2=3$ m. The rise in PWP was similar in test 2.b (Figure 6.13(a)) for all PPTs, varying between 2 and 5

kPa, and was dissipated swiftly between flow cycles. A failure occurred over the step bedrock ($Q=2500$ ml/min), initiated by an increase in PWP at the top junction of the bedrock step and the slope, which produced a tension crack. A small volume was mobilised and bulged over the top of the step, remaining in place for the test duration without any run out (Figure 6.11(a)). Increased PWP was between 3 and 5 kPa in the upper slope in test 3.b and decreased to 2–4 kPa at mid-slope and 1–3 kPa at the bottom. The PWP was slightly higher on the Plexiglas side (1g direction). Test 3.b (Figure 6.13(b)) combined rain of 613 ml/min equivalent to a rainfall intensity of 142 mm/h on the model scale and 2.8 mm/h in prototype from four nozzles (see further detail in supplementary material) from the last 5 min of GW flow rate of 1000 ml/min. The slope did not fail surficially, although significant erosion occurred on the Plexiglas side (Figure 6.11(b)).

A later test 4.b (supplementary material), with the same model, combined higher rain of 1379 ml/min equivalent to a rainfall intensity of 215 mm/h on the model scale (4.3 mm/h prototype), the soil bulged over the top of the step (1500 ml/min GW flow), similar to the failure mechanism in test 2.b (Figure 6.11(a)), although intense rain mobilised the soil downslope (Figure 6.11(c)).

Tests 1.a and 5.a (Figure 6.14) represented the model with the most unfavourable conditions for stability, given the highest and longest bedrock step. The soil exhibited suction initially in test 1.a (Figure 6.14(a)), which decreased as PWP built up during continuous GW flow, increasing from 500 to 2000 ml/min. The top PPTs were located upslope of the bedrock step, where the increased PWP was higher with 2–8 kPa on the Plexiglas side (PPT1) and 1–4 kPa nearer the wall (PPT2). Increased PWP at mid-slope and the bottom of the slope were similar with values between 1 and 4 kPa.

Failure was initiated at the top of the slope with a GW flow rate of 1500 ml/min, where the water could pond, before flowing up and over the bedrock step. Cracking was observed and the soil volume mobilised was greater than in test 2.b (Figure 6.11(d)),

with run-out occurring later, as the GW flow rate increased to 2000 ml/min. A proof test of the same model was performed with similar results in terms of the type, location and dimension of the failure, which confirms the reproducibility of the phenomena (Figure 6.11(e)), although the run-out almost reached the bottom of the slope in this case. PWP increase is higher on the Plexiglas side (PPT1) and varies between 2 and 6 kPa for the PPT at the top, and 1–2 kPa for the mid-slope and downslope locations in test 5.a (Figure 6.14(b)), as well as test 1.a. Failure occurred in test 5.a at GW flow of 1000 ml/min, when adding intense rainfall of 1479 ml/min (equivalent to 231 mm/h at model scale; 4.6 mm/h prototype), as expected from test 1.a, which failed after a GW flow rate of 1500 ml/min. Failure was similar to test 1.a and was located upslope of the bedrock step (Figure 6.11(f)).

Soil thickness of 1.25 m with a mid-height bedrock step of $y/h = 0.6$ and the longest step length $X_2 = 8.5$ m were represented in tests 7.a and 8.a (Figure 6.15). The increased PWP was similar on both sides and for all elevations, varying between 2.5 and 7.5 kPa at the top of the slope in test 7.a (Figure 6.15(a)), reducing to 2.5–4.5 kPa at mid-slope and 2–3 kPa for the bottom of the slope. Failure was triggered by a GW flow rate of 2000 ml/min (Figure 6.11(g)) with a similar failure mechanism to that described in test 1.a (Figure 6.14(a)), starting at the junction of bedrock and slope, mobilising one quarter of the width of the slope with a run-out reaching the bottom of the slope. Erosion on the Plexiglas side probably induced the failed volume to move in this direction.

The model for test 8.a (Figure 6.15(b)) responded similarly to that for test 7.a, with increased PWP at the top of the slope between 2 and 7.5 kPa, with 1–3.5 kPa at mid-slope and 0.5–1.5 kPa at the bottom. This last higher PWP was due to the ponding of water due to GW flow and rainfall of 1479 ml/min (equivalent to 231 mm/h at model scale and 4.6 mm/h prototype). Failure happened, as expected, for a GW flow of 1500 ml/min plus intense rain, initiated at the same location of test 7.a, but more in the centre (no erosion), mobilising the full soil thickness over the step, with run-out that reached the bottom of the slope (Figure 6.11(h)).

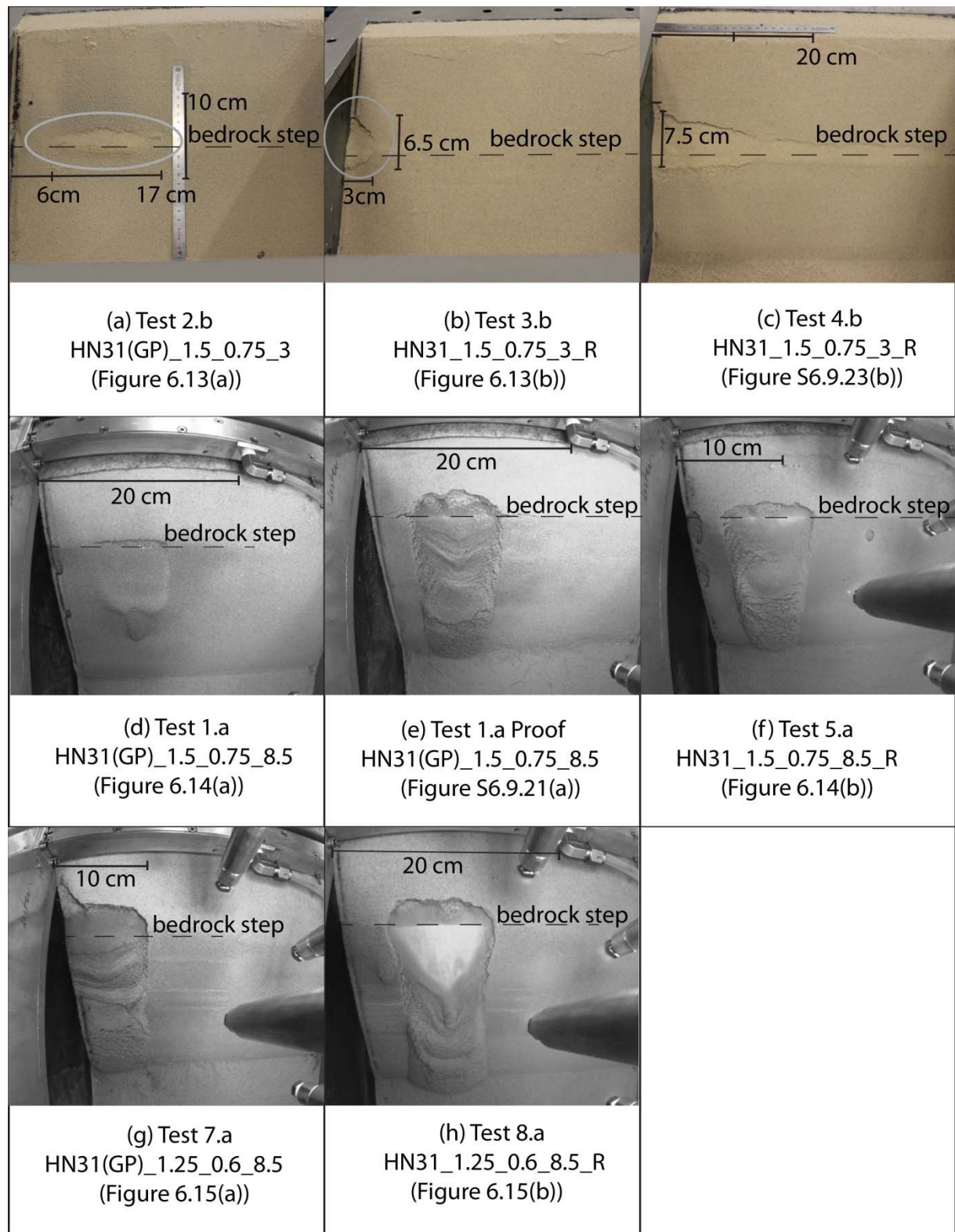


Figure 6.11. Physical modelling photographs captured after slope failure. (a) Test 2.b, (b) test 3.b, (c), and during failure: test 4.b, (d) test 1.a, (e) test 1.a proof, (f) test 5.a, (g) test 7.a and (h) test 8.a

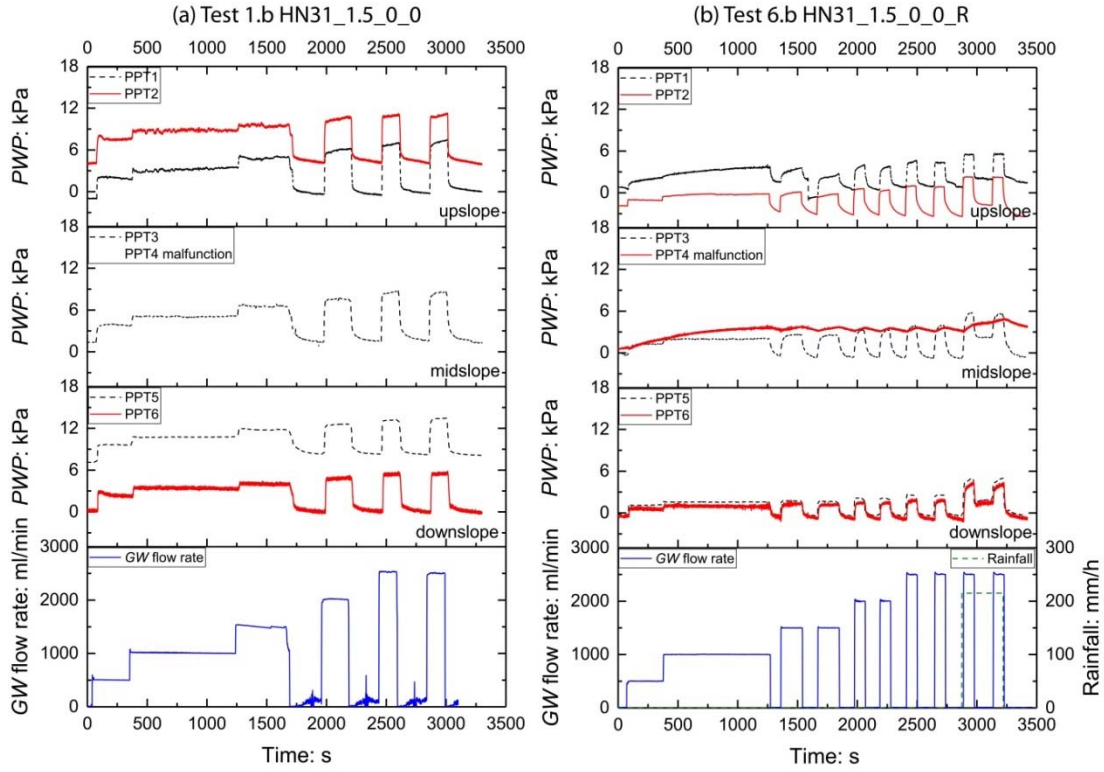


Figure 6.12. PWP and GW flow rate against time for tests 1.b and 6.b, which are identical models of 1.5 m soil thickness with slope with no bedrock step ($y = 0$), (a) 1.b HN31_1.5_0_0 under GW flow infiltration and (b) 6.b HN31_1.5_0_0_R GW flow combined with rainfall.

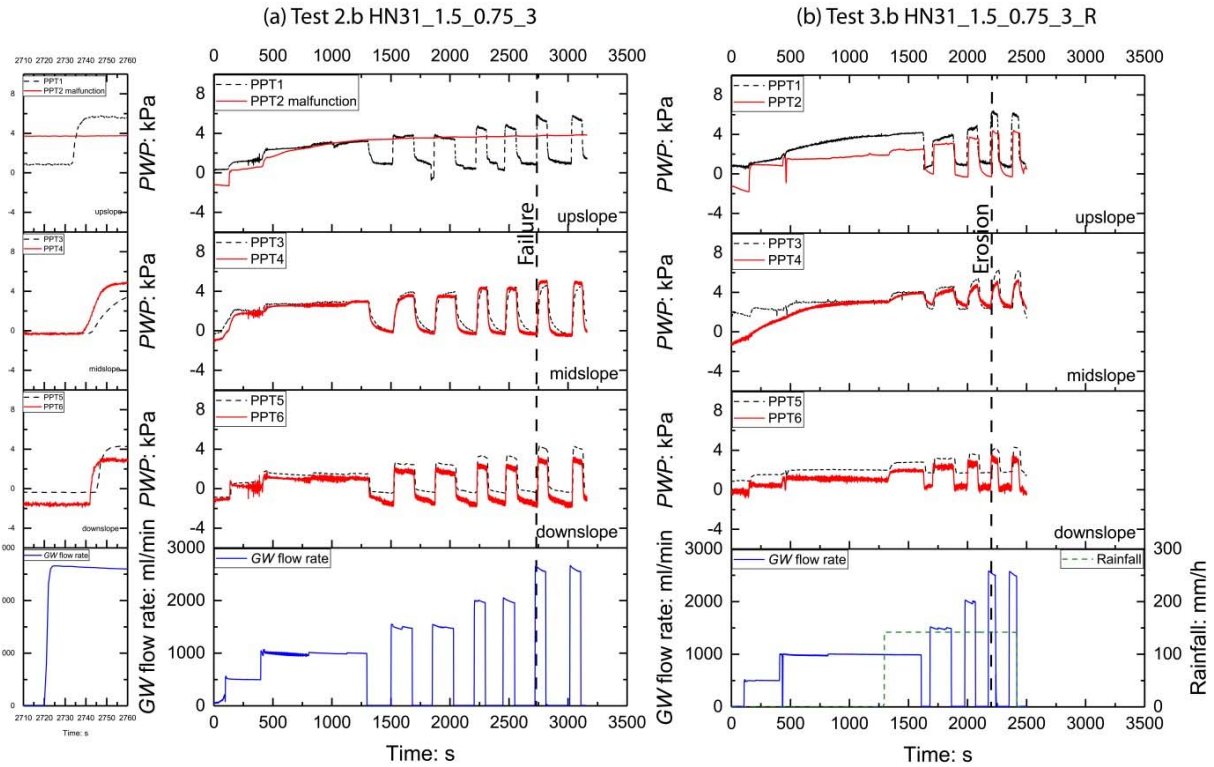


Figure 6.13. PWP and GW flow rate against time for identical models with $h = 1.5$ m, and bedrock step $y/h = 0.75$ and with step length $X_2 = 3$ m (prototype) for (a) test 2.b HN31_1.5_0.75_3 (the vertical dashed line shows the time of failure and a zoom figure at the left) and (b) test 3.b HN31_1.5_0.75_3_R.

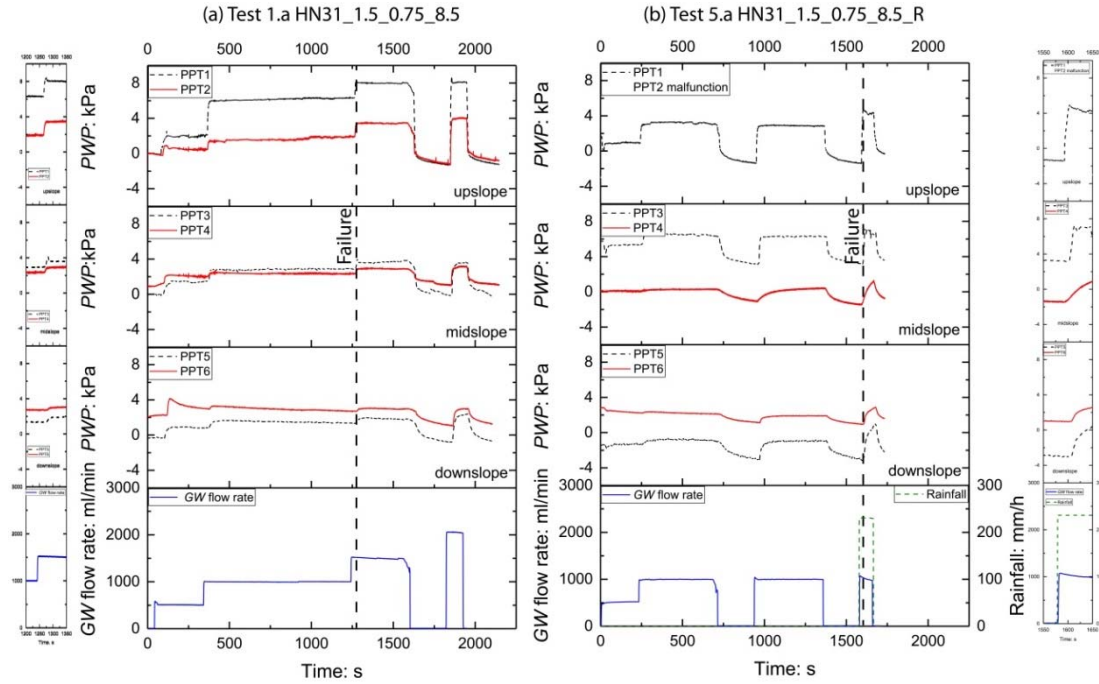


Figure 6.14. PWP and GW flow rate against time for identical models with $h = 1.5$ m soil thickness, bedrock step $y/h = 0.75$ with a step length $X_2 = 8.5$ m (prototype). A black dashed line shows the time of failure. (a) Test 1.a HN31_1.5_0.75_8.5 and (b) test 5.a HN31_1.5_0.75_8.5_R. A zoom of the PWP during failure is shown for each case at left and right, respectively.

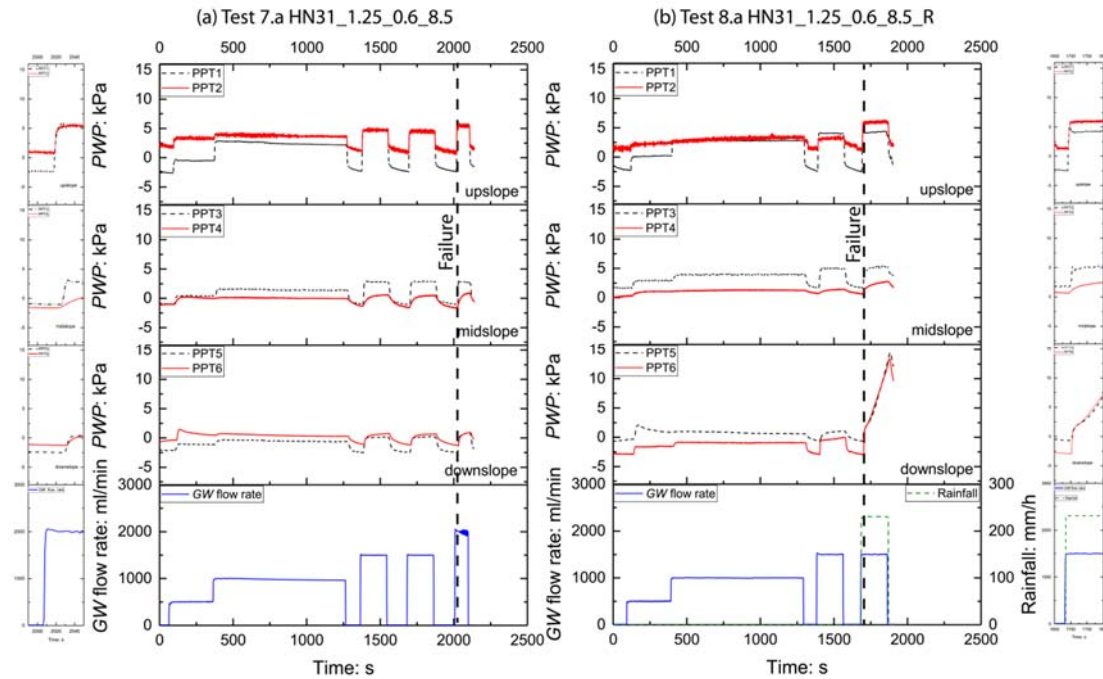


Figure 6.15. PWP and GW flow rate against time for identical models with $h = 1.25$ m, and bedrock step $y/h = 0.6$ with step length $X_2 = 8.5$ m (prototype). A vertical dashed line shows the time of failure. (a) Test 7.a HN31_1.25_0.6_8.5 and (b) test 8.a HN31_1.25_0.6_8.5_R. A zoom of the PWP during failure is shown for each case at left and right, respectively.

6.4 Discussion

6.4.1 Representation of field conditions

The field ground model was taken as the basis for parametric studies using numerical simulations and centrifuge tests to investigate simplified hydrological conditions, combining GW and rainfall necessary to cause surficial landslides in the models. The geometry and scaled soil (SP-SM) were simplified and a berm was introduced at the base of the slope, to prevent excessive erosion at the toe; nonetheless, it affected failure initiation in six out of 11 cases (Figure 6.6). GW flow was more local in the field, but was applied uniformly across the models, assuming a plane-strain condition.

6.4.2 Numerical versus physical modelling results

The numerical modelling results confirmed that a bedrock step increased the potential of a shallow landslide (Section 6.3). The F.S. decreased as the bedrock step increased in height (y) and length (X_2). Furthermore, an increase in bedrock step length (X_2) had a greater impact than an increase of y/h in decreasing the GW flow rate necessary to cause failure. Slopes without a bedrock step ($y/h = 0$), with high hydraulic gradient, required a larger amount of GW flow/rainfall to induce failure and this would initiate at the location where the water ponds at the berm of the slope. The PWP development, the order of magnitude of the GW flow discharge at failure, the failure mechanism, as well as the effect on the slope stability of the GW flow obtained from the nine centrifuge models, generally agreed with the findings from the numerical modelling. The locations of the failure scarps were similar for comparable models, whereas differences were observed in the extension of the failure mechanism, since the soil is able to run out in the centrifuge test, but this is not possible in the numerical models. An overview of the combined findings, as well as comments on the hypothesis presented in the introduction, is discussed in this section.

6.4.3 Triggering of surficial landslides

Various bedrock geometries were investigated in numerical models. The slopes were subjected to different GW flow discharge levels. Moreover, the hydrological regime was extended with rainfall in the centrifuge tests. Both modelling types supported the hypothesis that GW flow and rainfall infiltration increase the PWP, reduce suction and increase the potential for surficial instabilities and that this is affected by varying soil thickness and bedrock step geometry. Antecedent GW flow combined with intense rainfall in centrifuge tests led to both bottom-up and top-down saturation modes (Kienzler, 2007), which decreased suction and increased the unsaturated hydraulic conductivity of the soil. This promoted faster rainfall infiltration (Elia et al., 2017; Ng and Shi, 1998), leading to a more sudden and greater increase of PWP, which was distributed along the slope, especially over the bedrock step. This increases the hazard considerably (Askarinejad et al., 2018).

Variation in bedrock geometry with higher and longer bedrock steps, and less soil thickness would reduce the GW flow rate required at failure (Askarinejad et al., 2014b). Excess PWPs were dissipated quickly in physical models when the discontinuous GW flow applied was at a lower rate than the GW flow rate required at failure (Figures 6.12 6.15). This was also observed in measurements of VWC during field monitoring (Lucas et al., 2017).

A critical intensity of GW flow to trigger surficial failure, for each slope geometry at prototype scale (50g) (Figure 6.16), could be estimated from numerical simulations. An expected water table was predicted (Figure 6.6). This critical flow was then converted using centrifugal scaling relationships (Askarinejad, 2013; Dell'Avanzi and Zornberg, 2002).

The magnitude of GW flow required to cause a slope failure for various shapes of the bedrock, predicted using numerical and centrifuge modelling, is summarised in Figure 6.16. The results from numerical models show that the height of the bedrock step has a

major influence on the minimum required hydro-geological discharge to trigger a slope failure; the higher the step, the lower the required GW flow rate to trigger a failure. This observation is valid for all of the bedrock step lengths.

A comparison of the results from centrifuge tests to the numerical modelling results indicates a difference between the two values for the same bedrock geometry (Figure 6.16, Table 6.3). The minimum magnitude of GW discharge to cause a failure predicted by the centrifuge models is generally higher than that calculated from the numerical models (by factors of 1.16 for test 1.a, 1.59 for test 2.b, 1.26 for test 7.a). Reasons for this discrepancy could be that the hydro-mechanical properties of the soil defined for the numerical soil model are not exactly the same as those of the soil used for the centrifuge models. Additionally, the GW flow rate applied in the centrifuge increases by discrete steps (500, 1000, 1500 ml/min).

More specifically, the permeability used for the numerical soil model is expected to be higher than that of the soil used in the centrifuge tests, under comparable states. Furthermore, the 3D shape of the failures in the centrifuge tests also contributes to the slightly more stable behaviour, compared to the assumed 2D plane-strain numerical models, although tension cracking could counter some of these effects.

6.4.4 Failure mechanisms

The extension of the slip surfaces obtained from numerical and physical models agreed for the tests under GW flow and showed that failure would be conditioned to step geometry, developing upstream of the bedrock step in the most unfavourable case. Numerical simulations and physical modelling results at failure are shown in Figures 6.6 and 6.11, respectively, indicating that the mechanism is initiated where GW emerges at the ground surface (Figure 6.17). If the bedrock step is low, no spring emerges, and failure starts at the junction between the slope and the horizontal berm, mobilising the greatest volumes of soil for the entire test series. This is also dependent on soil depth for

example, Figure 6.6 cases (a), (b), (e), (i) and (j); however, retrogressive failures could occur in reality when a spring emerges on the slope.

When the soil depth is thicker (case (h)), a local failure has occurred at the bottom of the slope. Progressive failure is expected to follow here too, which would lead to the mobilisation of a larger failure mass, with successive releases at different times.

Figures 6.11(d)–6.11(h) and Figures 6.6(c), 6.6(g) and 6.6(k) show that the combination of water table springs directly above the step lead to smaller mobilised volumes and failure above the bedrock step, whereas the other cases 6.6(f), (d) are somewhat mixed and indicate intermediate failure volumes.

Tension cracks were observed in centrifuge model tests (with GW and GW plus rain) to develop at the crest of the slope, where water accumulated behind the bedrock step. Evidence of partial liquefaction of the soil can be seen in the form of apparently fluidised tongues, showing significant displacement and greater run out (Figures 6.11(d), 6.11(e), 6.11(f) and 6.11(h)). Table 6.4 includes the PWP, effective stresses in the slope at the time of failure as well the excess PWP ratio ($R_u = u/\gamma z$, with u is the pore pressure and γz is the total vertical stress) for tests 1.a, 2.b, 5.a, 7.a and 8.a. R_u increases during the PWP build-up phase and reaches 1.0 if liquefaction occurs. The highest values were found for PPTs 3 and 4, in tests 1.a and 2.b, but these were still below $R_u = 0.6$.

A combination of GW flow plus intense rainfall, for bedrock steps with $y/h > 0.6$, caused sudden landslides and run-out, which reached the berm (Figures 6.11(f) and 6.11(h)). This indicates greater hazard. A longer slope would probably experience either a local failure with multiple progressive failures, as expected in Figure 6.6(h), or a much longer translational mechanism that would destabilise a greater volume of debris on the slope.

Table 6.3. Comparison of GW flow rates calculated/observed to cause a slope failure.

Case	Numerical test	GW flow rate numerical (mL/min)	Physical test	GW flow rate physical (mL/min)	difference factor %
1	GP_1.5_0.75_8.5	1296.0	1.a	1500.0	15.7
2	GP_1.5_0.75_3.0	1576.8	2.b	2500.0	58.5
3	GP_1.25_0.6_3.0	1584.0	7.a	2000.0	26.3

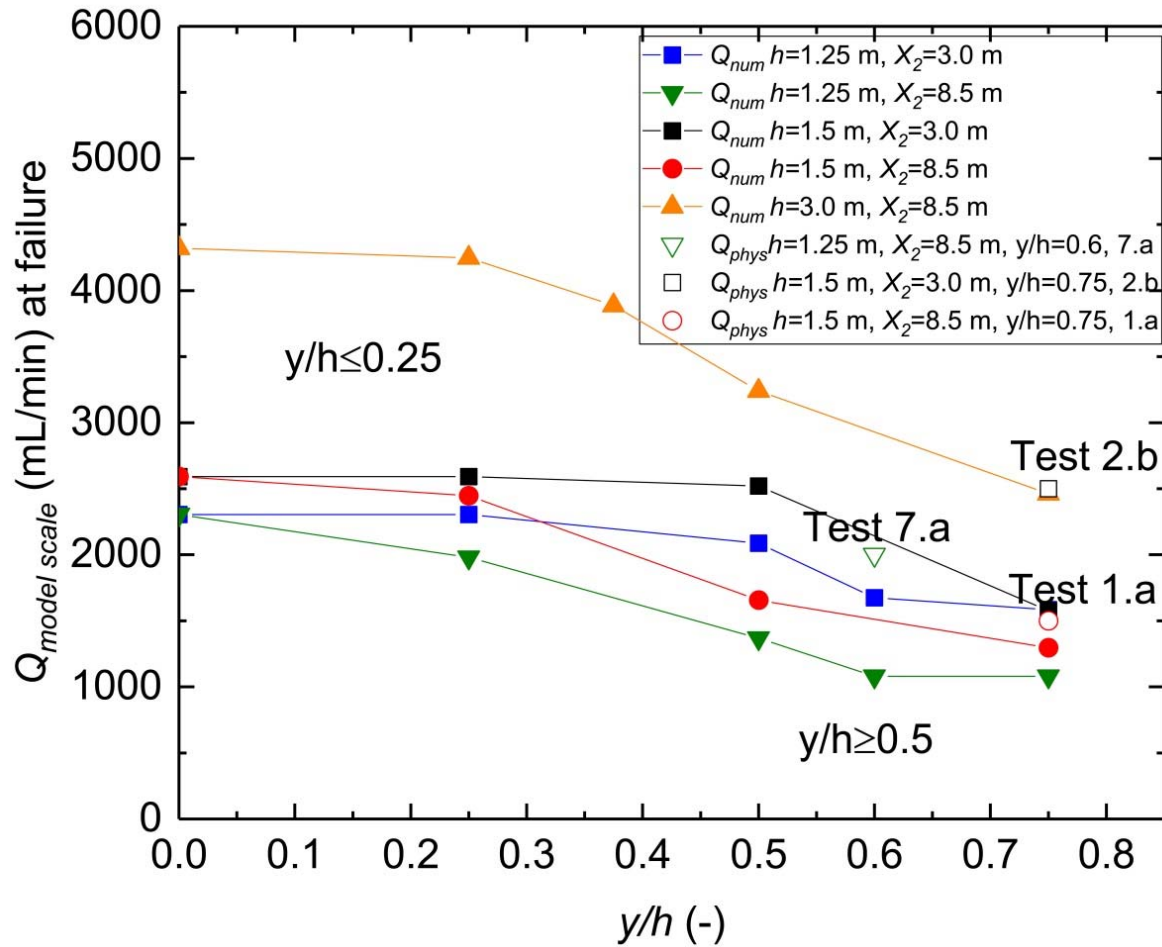


Figure 6.16. GW flow rate Q_{num} predicted by numerical modelling for the scaled centrifuge model to trigger a surficial failure at 50g level for different heights of bedrock step and GW Q_{phys} flow rate recorded at failure in centrifuge testing against y/h .

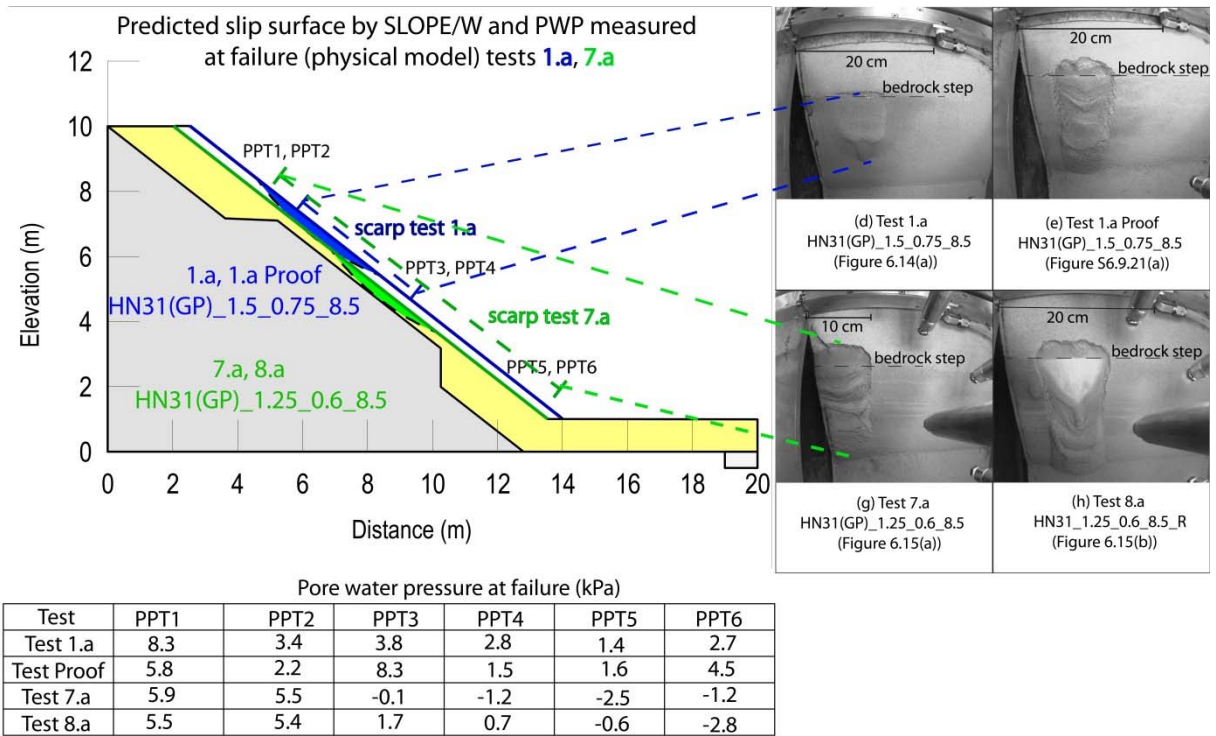


Figure 6.17. Failure slip surface predicted by numerical models (solid fill) $h = 1.25$ m, $y/h = 0.6$, $X_2 = 8.5$ m and $h = 1.5$ m, $y/h = 0.75$, $X_2 = 8.5$ m, failure scarp extension from centrifuge tests 1.a, 7.a and PWP measured in centrifuge tests 1.a, proof 1.a, 7.a and 8.a.

Table 6.4. Effective stress at failure determined at the locations of PPTs 1-6: centrifuge models HN31_1.5_0.75_8.5 (Test 1.a), HN31_1.5_0.75_3 (Test 2.b), HN31_1.5_0.75_8.5_R (Test 5.a), HN31_1.25_0.6_3 (Test 7.a) and HN31_1.25_0.6_8.5_R (Test 8.a).

		PPT					
		1	2	3	4	5	6
O_v ($Y=17$ kN/m ³) (kPa)	1.a, 2.b, 5.a	32.50	32.50	8.10	8.10	32.50	32.50
	7.a, 8.a	27.00	27.00	10.80	10.80	27.00	27.00
u (kPa)	1.a	8.39	3.46	3.86	2.83	1.40	2.72
	2.b	5.72	-	2.72	4.74	4.24	3.08
	5.a	4.95	-	3.74	-0.94	-3.01	0.98
	7.a	5.97	5.52	-0.05	-1.26	-2.50	-1.26
	8.a	5.55	5.48	1.70	0.79	-0.68	-2.89
O'_v (kPa)	1.a	24.11	29.04	4.24	5.27	31.10	29.78
	2.b	26.78	-	5.38	3.36	28.26	29.42
	5.a	27.55	-	4.36	9.04	35.51	31.52
	7.a	21.03	21.48	10.85	12.06	29.50	28.26
	8.a	21.45	21.52	9.10	10.01	27.68	29.89
R_u (-)	1.a	0.26	0.11	0.48	0.35	0.04	0.08
	2.b	0.18	-	0.34	0.59	0.13	0.09
	5.a	0.15	-	0.46	<0	<0	0.03
	7.a	0.22	0.20	0.00	<0	<0	<0
	8.a	0.21	0.20	0.16	0.07	<0	<0

6.5 Summary and conclusions

A combination of physical and numerical modelling using a prototype ground model of a steep scree slope, which integrated together field monitoring data and soil characterisation from previous studies, has exposed likely mechanisms of failure and how these are triggered. Each simulation method can complement one another so that the following statements can be made about the landslide hazard

- Prediction of the behaviour of unsaturated granular material in steep slopes subjected to hydraulic perturbations and their mechanical interactions with the underlying bedrock using numerical simulations requires a rigorous hydro-mechanical coupled analysis, accompanied by various assumptions and simplifications regarding the material constitutive model and input parameters. Moreover, features such as the failure timing, run-out extent and 3D effects cannot be readily predicted, numerically. Therefore, an advanced, state-of-the-art physical modelling technique was used to study the impacts of rain and GW flow, coupled with the shape of the bedrock, on the response of the slope. The observations from the physical modelling were supported using the simplified uncoupled hydro (Seep/W) and mechanical (LEM: Slope/W) numerical modelling.
- Numerical simulation was useful in studying a wide variety of cases and helped select the worst-case scenarios to be investigated further, and quantified, using centrifuge modelling. Different types of bedrock geometry and soil thicknesses, under combined effects of GW flow and rainfall, were simulated in some of the physical models. A steady-state condition for the hydraulic processes was assumed in the numerical models and the results of pore pressure distribution were applied in a 2D limit equilibrium stability analysis to provide a prediction for the failure location and volume.
- Centrifuge tests were used to verify numerical results, and provided insights into the development of PWP in the scree slopes subjected to GW flow and rainfall, as a

function of time. Location and triggering of the shallow failures were monitored in the centrifuge tests and detailed features of the extent and timing of tension cracking and displacement regime of the mobilised mass were recorded. The results of the centrifuge tests in terms of the thresholds for GW flow discharge for the triggering of a landslide, as well as the shape and location of the failure surfaces, were compared to those derived from numerical modelling.

- Results from both approaches supported the hypothesis that, under similar methodological and hydrological boundary conditions, slopes with no steps in the bedrock are more stable than slopes with shallow bedrock combined with a bedrock step, and the larger the step, the lower the flow rate required to cause the slope failure.
- The grain-size distribution (GSD) of the soil used in the centrifuge tests differed from that of the field, due to the limitations imposed by the scale effects. Therefore, the exact values of the rain intensity, and GW flow discharge leading to instabilities cannot be directly compared with the field data. Moreover, it should be mentioned that these investigations were done as parametric studies and naturally, the geometrical parameters of the steps in the bedrock were extremely idealised in the centrifuge and numerical models, compared to the field conditions. Therefore, the centrifuge test results cannot be directly used as class A prediction tools for the field measurements, although they can be applied to define the potentially critical combinations of the bedrock shape and hydraulic input.
- The landslide potential of a slope subjected to a hydraulic regime of GW flow and or rainfall increases when water can pond uphill over higher and longer bedrock steps. Ponding of water locally increases the PWP in the soil mass and subsequently results in a reduction of the effective stress and hence the shear strength, leading to a shallow landslide. However, it was observed that these landslides are generally smaller in volume and have less run-out extent compared to those that are triggered

in 'long' slopes with no steps in the bedrock. However, the hydraulic triggering threshold for a slope with no bedrock step is generally higher than that of a slope with a stepped bedrock under similar conditions.

6.6 Practical relevance and potential applications

The hypothesis presented in this study is based on observations and measurements collected from a steep scree slope, for a period of 3 years. The ground model has been designed as a prototype, based on geophysical measurements and laboratory testing. The results from this study can be used as a reference to address failure mechanisms in steep gravelly slopes that are under the influence of seasonal precipitation and hydrogeological changes. The challenges and solutions presented here, especially for the physical modelling of landslides using a drum centrifuge, could be relevant for future studies of complex interactive hydro-mechanical processes leading to mass movements.

6.7 Acknowledgements

The authors are most grateful for the funding from the SNF Project number 200021_144326/1 and Canton Valais, together with the Councils of Agarn and Leuk. The project also contributed to the TRAMM2 programme of the ETH Competence Centre of Environmental Sustainability. Furthermore, the authors acknowledge, in particular, the support and advice from Professor Dr. Andy Take, Kerstin Fankhauser, Ernst Bleiker, Reto Grob, Dr. Brian McArdell and Dr. Mario Sartori. They are also grateful to the reviewers for their constructive comments and valuable suggestions, which have helped them improve this paper.

6.8 References

- Alber S (2017) *Investigation of 3D Printed Geomaterials. Master Thesis*, IGT, ETH Zurich, Zürich, Switzerland.
- Askarinejad A (2013) *Failure mechanisms in unsaturated silty sand slopes triggered by rainfall*. ETH Dissertation, Nr. 21423, <https://doi.org/10.3929/ethz-a-010002526>.
- Askarinejad A, Laue J, Zweidler A, Iten M, Bleiker E, Buschor H and Springman SM (2012) Physical modelling of rainfall induced landslides under controlled climatic conditions. In *Proceedings of the conference Eurofuge 2012*, Delft, Netherlands, Delft University of technology and Deltares, Delft, Netherlands, CD-ROM
- Askarinejad A, Beck A and Springman SM (2014a) Scaling law of static liquefaction mechanism in a geocentrifuge and corresponding hydromechanical characterization of an unsaturated silty sand having a viscous pore fluid. *Canadian Geotechnical Journal*, 52(6): 708-720, doi:10.1139/cgj-2014-0237.
- Askarinejad A, Laue J and Springman SM (2014b) Effect of bedrock shape and drainage properties on the stability of slopes. In *Proceedings of the 8th International Conference on Physical Modelling in Geotechnics 2014, ICPMG 2014*, Perth, Australia (Gaudin C and White D (eds)). Taylor & Francis, London, UK, vol. 2, pp. 1211–1217.
- Askarinejad A, Akca D and Springman SM (2018) Precursors of instability in a natural slope due to rainfall: a full-scale experiment. *Landslides* 15(9): 1745–1759, <https://doi.org/10.1007/s10346-018-0994-0>.
- Bryant S K, Take WA, Bowman ET and Millen MDL (2015) Physical and numerical modelling of dry granular flows under Coriolis conditions. *Géotechnique*, 65(3), 188-200, <https://doi.org/10.1680/geot.13.P.208>.
- Caicedo B and Thorel L (2014) Centrifuge modelling of unsaturated soils. *Journal of Geo-Engineering Sciences*, 2(1-2), 83-103.

Carrier III WD (2003) Goodbye, Hazen; hello, Kozeny-Carman. *Journal of Geotechnical and Geoenvironmental Engineering*, 129(11), 1054-1056.

Craig WH (2014) Modelling slope failures by ‘gravity turn-on’. In *8th International Conference on Physical Modelling in geotechnics, Perth, Australia* (Gaudin C and White D (eds)). Taylor & Francis, London, UK, pp. 1203–1209.

Dell’Avanzi E and Zornberg JG (2002) Scale Factors for Centrifuge Modeling of Unsaturated Flow. *Proceedings of the Third International Conference on Unsaturated Soils UNSAT 2002, Recife, Brazil, March 10–13* (Jucá JFT, de Campos T and Marinho F (eds)). Swets & Zeitlinger, A.A. Balkema, Lisse, the Netherlands, vol. 1, pp. 425–430.

Elia G, Cotecchia F, Pedone G et al. (2017) Numerical modelling of slope–vegetation–atmosphere interaction: an overview. *Quarterly Journal of Engineering Geology and Hydrogeology* 50(30): 249–270, <https://doi.org/10.1144/qjegh2016-079>.

Fankhauser K (2014) *Geophysical Slope Characterization using GPR and ERT in an Active Debris Flow Catchment. Master Thesis*, EEG, ETH Zurich, Zürich, Switzerland.

Frank F, McArdell BW, Oggier N, Baer P, Christen M, and Vieli A (2017) Debris-flow modeling at Meretschibach and Bondasca catchments, Switzerland: sensitivity testing of field-data-based entrainment model. *Natural Hazards and Earth System Sciences*, 17(5), 801-815.

Gabus JH, Weidmann M, Burri M and Sartori M (2008a) Feuille 1287 Sierre, Atlas Géologique de la Suisse 1:25’000, Carte 111, swisstopo, Wabern, Switzerland.

Gabus JH, Weidmann M, Burri M and Sartori M (2008b) Feuille 1287 Sierre, Atlas Géologique de la Suisse 1:25’000, Note explicative, swisstopo, Wabern, Switzerland.

Grob R (2015) *Measurement of Soil Properties for Gravels in a Scree Slope Using Large Scale Triaxial Testing. Master Thesis*, IGT, ETH Zurich, Zürich, Switzerland.

Kienzler P (2007) *Experimental Study of Subsurface Stormflow Formation*. ETH Dissertation, Nr. 17330, ETH Zürich, Zürich, Switzerland, <https://doi.org/10.3929/ethz-a-005477823>.

Krahn J (2004a) *Seepage Modelling with SEEP/W: An Engineering Methodology*, GEO-SLOPE International Ltd., Calgary, Alberta, Canada.

Krahn J (2004b) *Stability Modelling with SLOPE/W: An Engineering Methodology*, GEO-SLOPE/W International Ltd., Calgary, Alberta, Canada.

Lee YS and Bolton MD (2006) Centrifugal modelling of the landslides triggering mechanism in layered fill slopes. In *Physical Modelling in Geotechnics, Two Volume Set: Proceedings of the Sixth International Conference on Physical Modelling in Geotechnics, 6th ICPMG'06, Hong Kong, 4–6 August 2006* (Ng CWW, Zhang LM and Wang YH (eds)). Taylor & Francis Group, London, UK, CRC Press, vol. 1, pp. 355–360.

Ling H and Ling HI (2012) Centrifuge model simulations of rainfall-induced slope instability. *Journal of Geotechnical and Geoenvironmental Engineering*, 138(9), 1151-1157.

Lucas DR, Fankhauser K and Springman SM (2017) Application of geotechnical and geophysical field measurements in an active alpine environment. *Engineering Geology*, 219, 32-51, <https://doi.org/10.1016/j.enggeo.2016.11.018>

Morgenstern NU, and Price VE (1965) The analysis of the stability of general slip surfaces. *Géotechnique*, 15(1), 79-93, <https://doi.org/10.1680/geot.1965.15.1.79>.

Ng CWW and Shi Q (1998). Influence of rainfall intensity and duration on slope stability in unsaturated soils. *Quarterly Journal of Engineering Geology and Hydrogeology*, 31(2), 105-113.

Oggier NC (2011) *Simulierung von Murgängen mit RAMMS am Beispiel des Meretschibachs*. Master Thesis, ETH Zürich und Forschungsanstalt für Wald Schnee und Landschaft (WSL), Zürich, Switzerland.

Park DS (2013) The effect of radial G-field on the centrifuge modelling. In *ICPMG2014–Physical Modelling in Geotechnics: Proceedings of the 8th International Conference on Physical Modelling in Geotechnics 2014* (ICPMG2014), Perth, Australia, 14-17 January 2014 (Gaudin C and White D (eds)). Taylor & Francis, London, UK, pp. 385–390.

Schofield AN (1978) Use of centrifugal model testing to assess slope stability. *Canadian Geotechnical Journal* 15(1): 14–31.

Schofield AN (1980) Cambridge geotechnical centrifuge operations. *Géotechnique* 30(3): 227–268, <https://doi.org/10.1680/geot.1980.30.3.227>.

Springman SM, Laue J, Boyle R, White J, and Zweidler A (2001) The ETH Zurich geotechnical drum centrifuge. *International Journal of Physical Modelling in Geotechnics*, 1(1), 59-70.

Springman SM, Jommi C and Teyssiere P (2003) Instabilities on moraine slopes induced by loss of suction: a case history. *Géotechnique* 53(1): 3–10.

Springman SM, Lucas DR, Oggier NC, Kos A, Fankhauser K and McArdell B (2015) Study of the seasonal response of a scree slope and debris flow catchment in the Swiss Alps. In *XVI European Conference on Soil Mechanics and Geotechnical Engineering (XVI ECSMGE 2015)*, Edinburgh, UK, 13.–17.9.2015 (Winter MG, Smith DM, Eldred PJL and Toll DG (eds)). ICE Publishing, Westminster, London UK. pp. 1897–1902.

Take WA (2014) Physical modelling of instability and flow in loose granular slopes. In *ICPMG2014 – Physical Modelling in Geotechnics: Proceedings of the 8th International Geotechnics*, Perth, Australia, 14–17 January 2014 (Gaudin C and White D (eds)). Taylor & Francis, CRC Press, Balkema, London, UK, pp. 113–124.

Take WA and Beddoe RA (2014) Base liquefaction: a mechanism for shear-induced failure of loose granular slopes. *Canadian Geotechnical Journal*, 51(5), 496-507.

Taylor RE (1995) *Geotechnical Centrifuge Technology*. CRC Press, London, UK. <https://doi.org/10.1201/9781482269321>.

Timpong S, Itoh K and Toyosawa Y (2007) Geotechnical centrifugemodelling of slope failure induced by ground water table change. In *Landslides and Climate Change* (McInnes R, Jackeways J, Fairbank H and Mathie E (eds)). Taylor & Francis Group, London, UK, pp. 107–112.

6.9 Appendix. Supplementary material

6.9.1 Field and instrumentation location

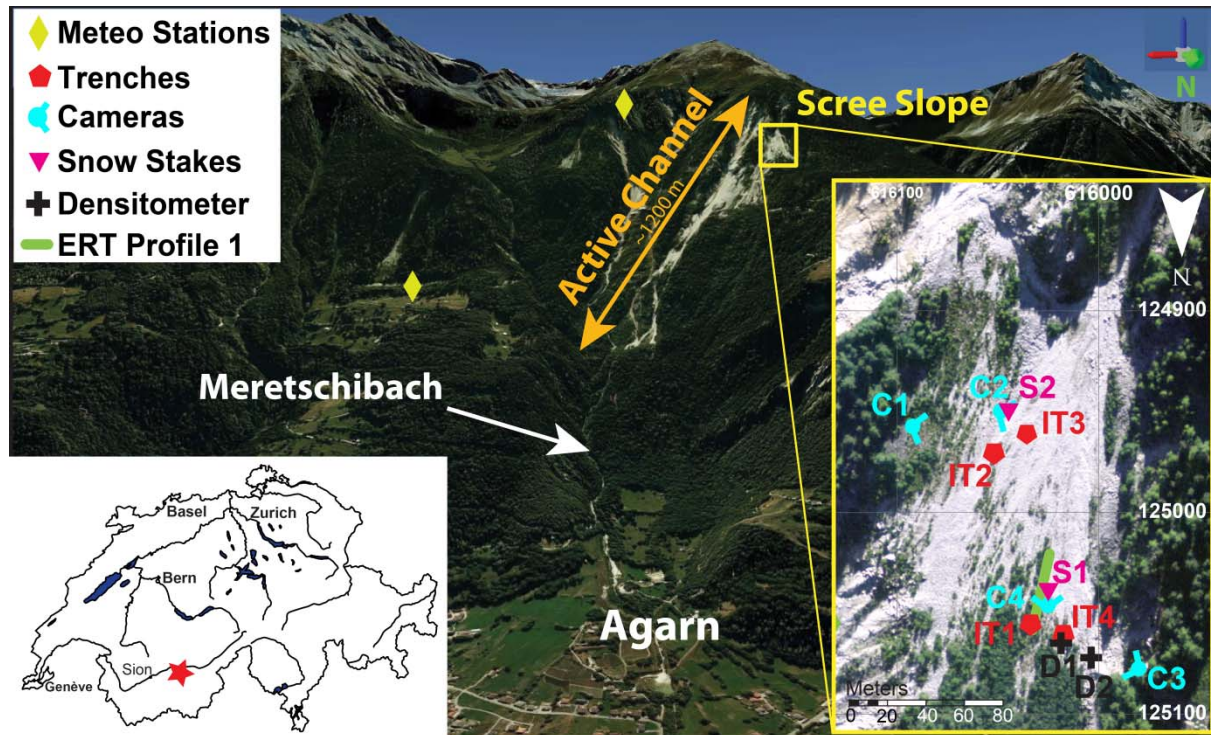


Figure S6.9.1. Overview of the field area, located in canton Valais, Switzerland (star on small map). The image looking south shows a view of Agarn, situated on the Rhone valley floor and the Meretschibach catchment on the mountain slopes behind. The most active area within the catchment can be divided into an active channel and a scree slope. The weather stations (yellow diamonds) are located at 1370 m.a.s.l. (IGT) and 2220 m.a.s.l. (WSL). The right image shows an enlargement of the scree slope (yellow rectangle) with the locations of the instrumented trenches (IT1-IT4), the ERT profile on which the monitoring was performed, snow stakes (S1-S2), densitometer measurements (D1-D4) and cameras (C1-C4). Lucas et al. (2017) <https://doi.org/10.1016/j.enggeo.2016.11.018>

$$N = \frac{w^2 * r}{g} (-)$$

$$w = 23.10 \Rightarrow rpm = w * \frac{60}{2 * \pi} = 220.58 \left(\frac{rad}{s}\right)$$

Calculation tilted in mm

$$Tilted (mm) = d * \cos \alpha$$

$$\text{with } d = \frac{400}{N}$$

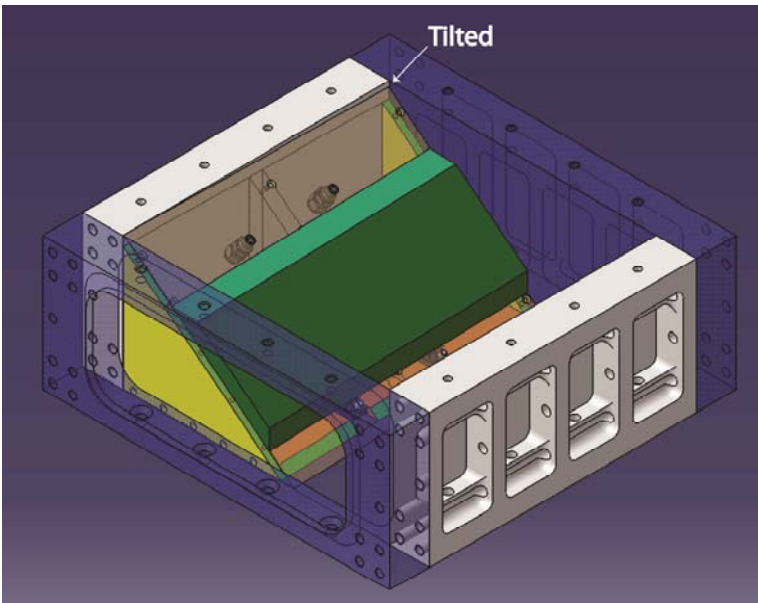


Figure S6.9.3. 3D sketch with bedrock step and tilting of bedrock plate (after H. Buschor 2018).

6.9.2.3 Bedrock steps and bedrock slope geometry

Bedrock step geometry

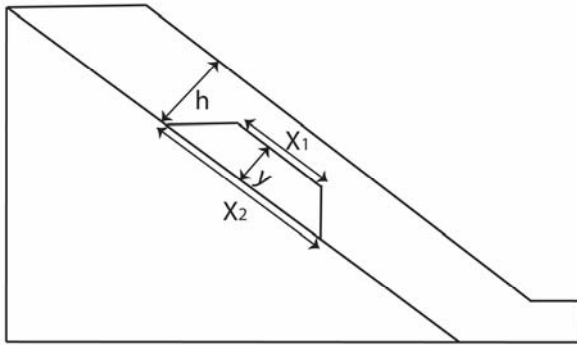
Tables S6.9.2, S6.9.3 and Figures S6.9.4-S6.9.5 show the 4 cases of bedrock step geometry (model scale). The tilted bedrock geometry is reflected in the wall side (opposite to the plexiglas). Therefore, the geometry is shown for both sides of the box (plexiglas and wall sides).

Table S6.9.2. Cases of bedrock step geometry side 1 (plexiglas).

cases	h (mm)	y (mm)	y/h (-)	X ₁ (mm)	X ₂ (mm)	X ₁ /X ₂ (-)
1	30.00	15.00	0.50	29.40	61.80	0.48
2				136.20	168.55	0.81
3	30.00	22.50	0.75	13.30	61.80	0.22
4				120.00	168.55	0.71

Where:

h: Soil thickness X₁: Length at the top of bedrock step
y: Height of bedrock step X₂: Length at the base of bedrock step

**Figure S6.9.4.** Sketch geometry model side 1 (plexiglas).**Table S6.9.3.** Cases of bedrock step geometry side 2 (wall).

cases	h (mm)	y (mm)	y/h (-)	X ₁ (mm)	X ₂ (mm)	X ₁ /X ₂ (-)
1	30.00	15.00	0.50	29.40	61.80	0.48
2				136.20	168.55	0.81
3	30.00	22.50	0.75	13.30	61.80	0.22
4				120.00	168.55	0.71

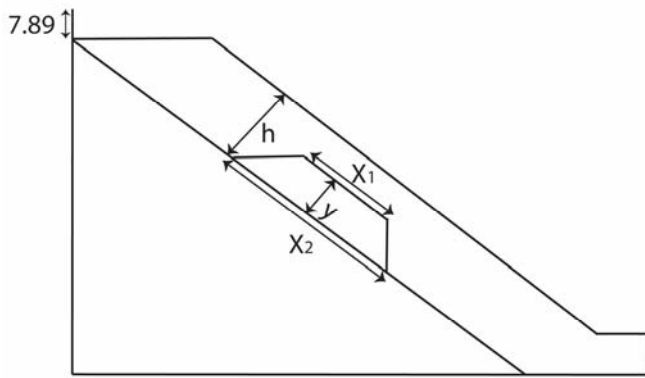


Figure S6.9.5. Sketch geometry model side 2 wall

6.9.2.4 Slope geometry

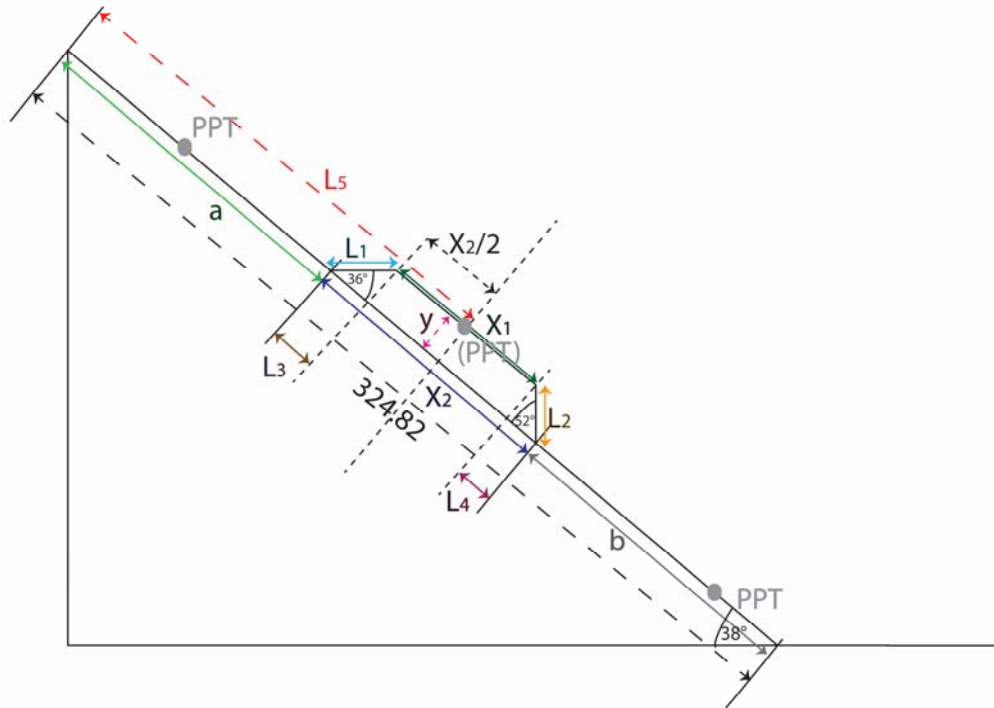
Tables S6.9.4, S6.9.5 and Figure S6.9.6 show the slope geometry (model scale).

Table S6.9.4. Geometry bedrock side 1 (plexiglas) with 4 cases of bedrock step.

geometry	h (mm)	y (mm)	y/h (-)	X ₁ (mm)	X ₂ (mm)	a (mm)	b (mm)	L ₁ (mm)	L ₂ (mm)	L ₃ (mm)	L ₄ (mm)	L ₅ (mm)	length slope bedrock (mm)
1	30.00	15.00	0.50	29.40	61.80	149.80	113.20	25.50	19.00	20.60	11.70	185.20	324.82
2				136.20	168.55	91.74	64.50					180.50	
3	30.00	22.50	0.75	13.30	61.80	148.00	115.00	38.20	28.50	30.90	17.50	185.60	324.82
4				120.00	168.55	91.74	64.50					182.60	

Table S6.9.5. Geometry bedrock step side 2. (Wall) with 4 cases of bedrock step.

geometry	h (mm)	y (mm)	y/h (-)	X ₁ (mm)	X ₂ (mm)	a (mm)	b (mm)	L ₁ (mm)	L ₂ (mm)	L ₃ (mm)	L ₄ (mm)	L ₅ (mm)	length slope bedrock (mm)
1	30.00	15.00	0.50	29.40	61.80	149.80	100.30	25.50	19.00	20.60	11.70	185.20	311.98
2				136.20	168.55	91.50	51.90					180.20	
3	30.00	22.50	0.75	13.30	61.80	148.00	102.20	38.20	28.50	30.90	17.50	185.60	311.98
4				120.00	168.55	91.50	51.90					182.50	



Figures S6.9.7-S6.9.8 show the PPTs location observed from the plexiglas and wall sides. Figure S6.9.9 show the PPTs location from a frontal view of the bedrock plate. All dimensions in model scale.

Sampling rates were 10 Hz for PPTs model a: 11325 (PPT1), 6437k (PPT2), 11322 (PPT2), 11321 (PPT4), model b: 11189 (PPT1), 11391(PPT2, 4), 6430k (PPT2), 11401 (PPT4), 9448(PPT6) and 1 Hz for the remaining six model a: 9373(PPT3), 9355 (PPT5), 9356 (PPT6), and model b: 9357(PPT2), 11193 (PPT3), 9359 (PPT5).

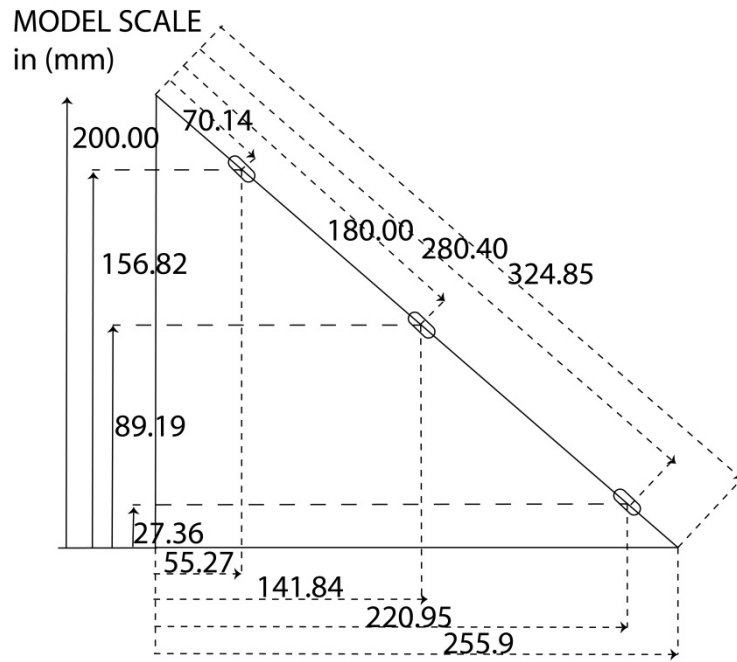


Figure S6.9.7. Sketch with geometry of PPT location in bedrock view side 1 (Plexiglas)

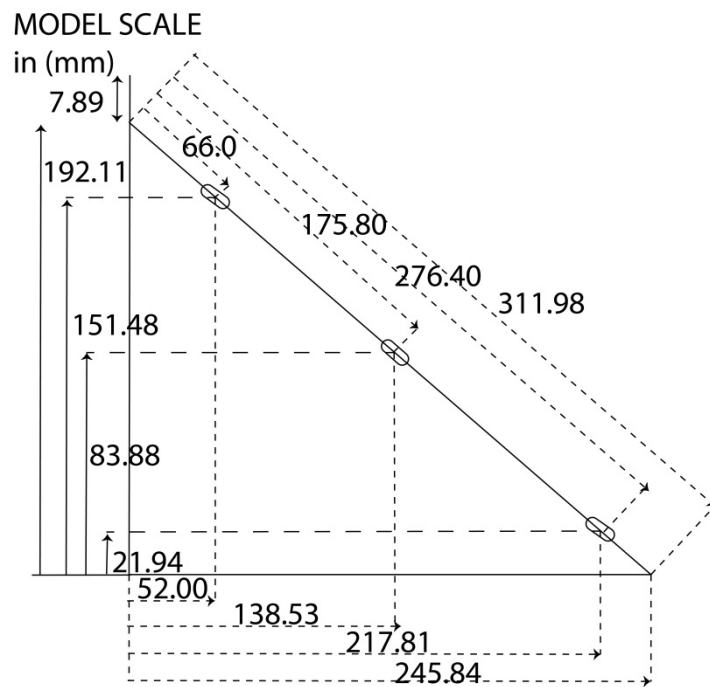


Figure S6.9.8. Sketch with geometry of PPT location in bedrock view side 2 (wall)

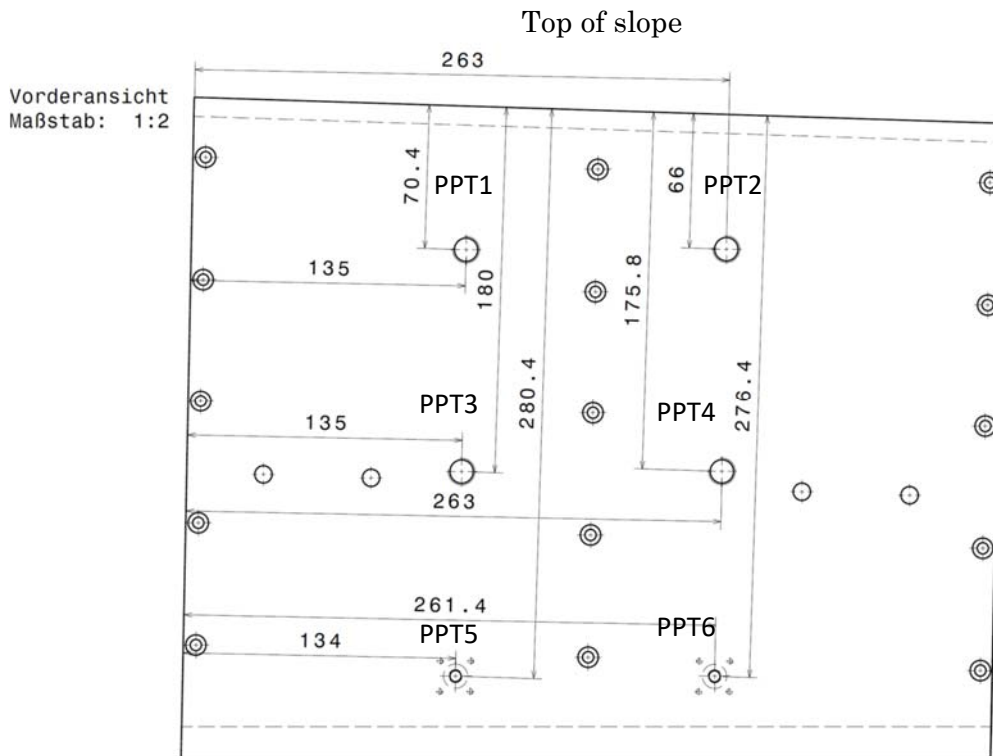


Figure S6.9.9. Sketch with geometry of PPT location in bedrock top view

6.9.2.6 Climate chamber

The climate chamber (Figure S6.9.10) is the top box container placed on top of model container, which contain the rain nozzles, Groundwater distribution system and the photography cameras.

Figure S6.9.10, show for models a, b the interior of the climate chamber: nozzles and cameras, and the exterior: cameras and inner and outer rain pipe channels. Figure S6.9.11 show the position of model container and climate chamber in the centrifuge.

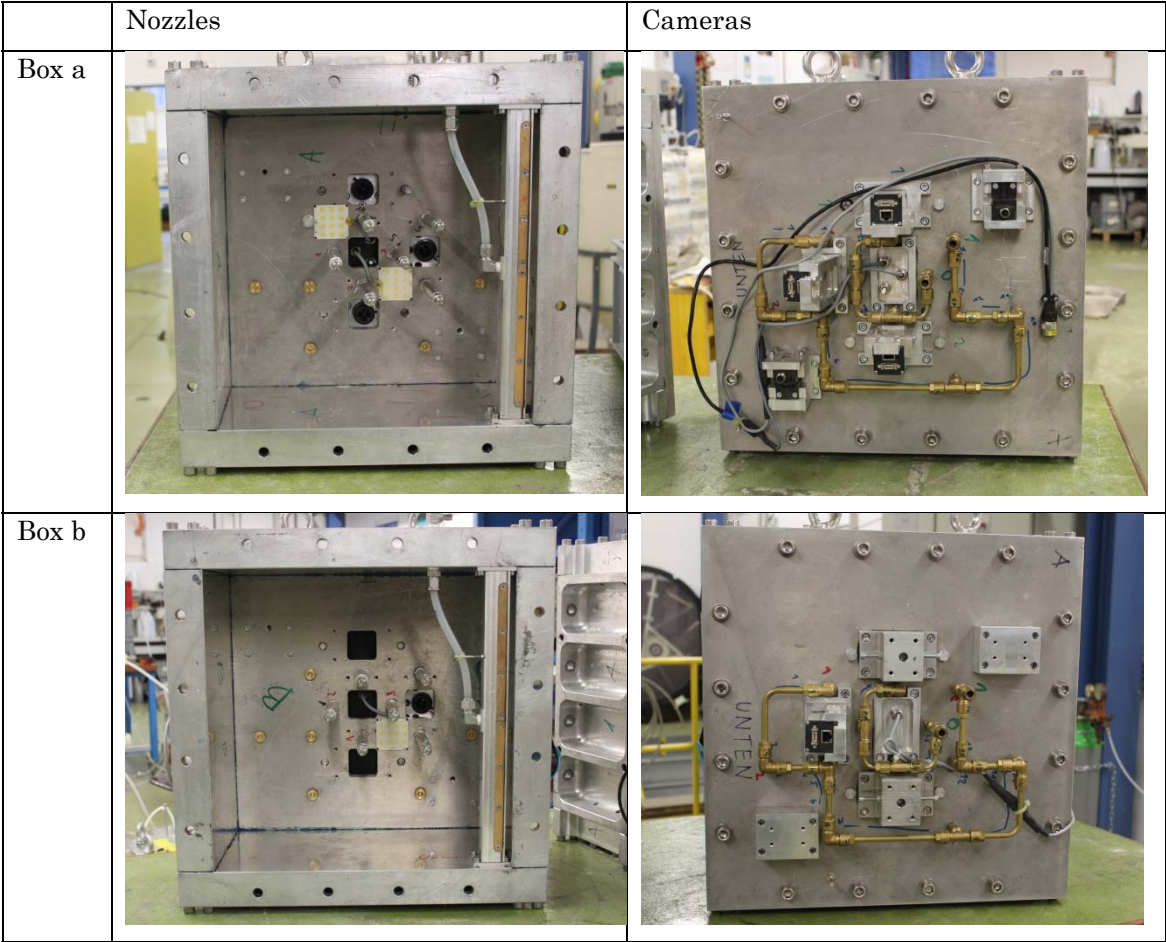


Figure S6.9.10. Climate chamber of models a and b. Frontal view of nozzles, cameras, inner and outer channels for rainfall.

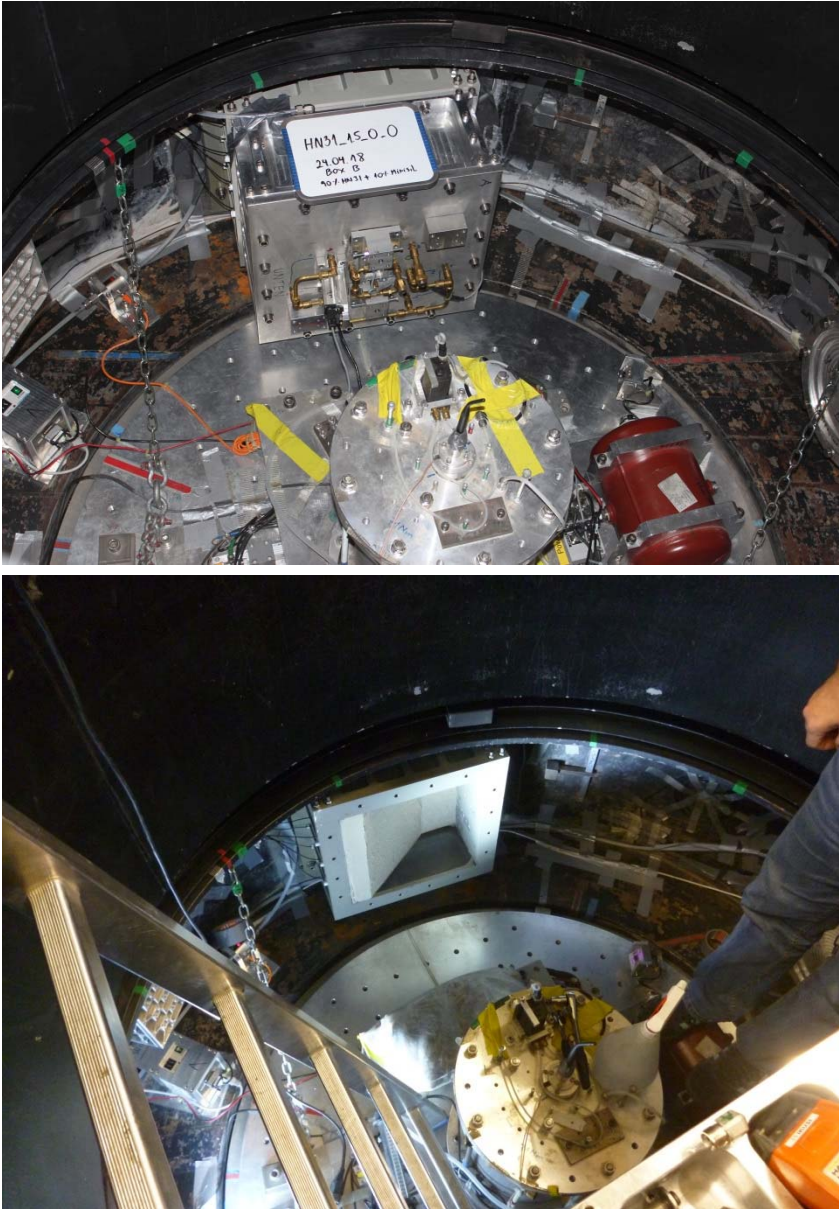


Figure S6.9.11. Climate chamber and model box in the drum centrifuge in testing position.

6.9.2.7 Rainfall nozzles

The rainfall is applied over the slope by means of non-uniformly distributed nozzles (Figure S6.9.12), which have been extended below the strong box roof to a certain height above the slope surface to reduce the Coriolis effect. The fine fraction of the soil can be washed out if the nozzles are too close to the soil surface. Therefore, the rainfall was sprayed into the chamber through aluminium extension tubes of 5 to 10 cm in length, so

that the rainwater emerged as a spray within a range of 18.9-26.7 cm and 13.9-21.7 cm respectively, above the ground surface.

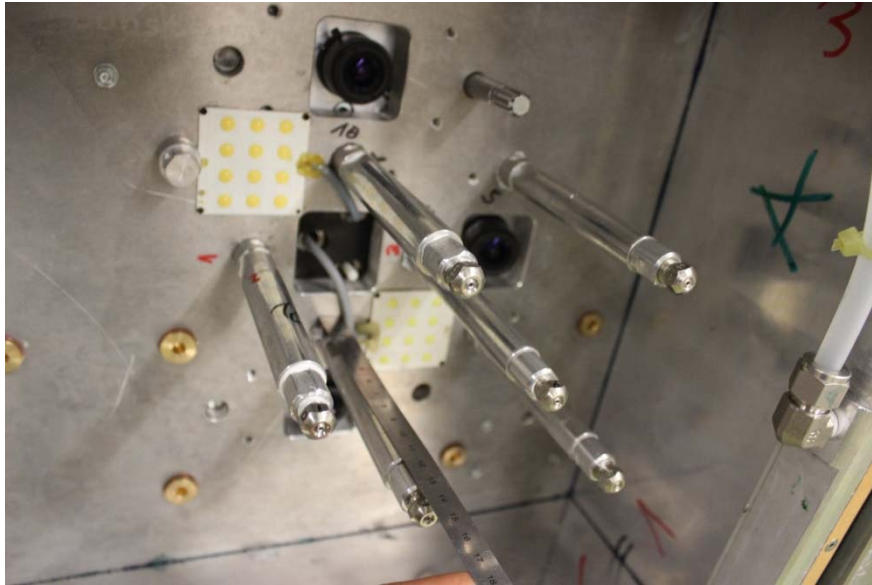


Figure S6.7.12. Rain nozzles six MW7 with 10 cm extension.

The rain intensity per nozzle was calculated measuring their respective flow (mL/min) Figure S6.9.13 and area (Table S6.9.6), depending on length extension. Assuming that each nozzle rain spray overlapped the soil surface, the total rainfall intensity in model scale (mm/h) (Table S6.9.7) is estimated as the addition all intensities. Applying scaling laws the rain intensity at prototype is estimated as N times smaller than the model scale (Askarinejad, 2013) (Table S6.9.8).

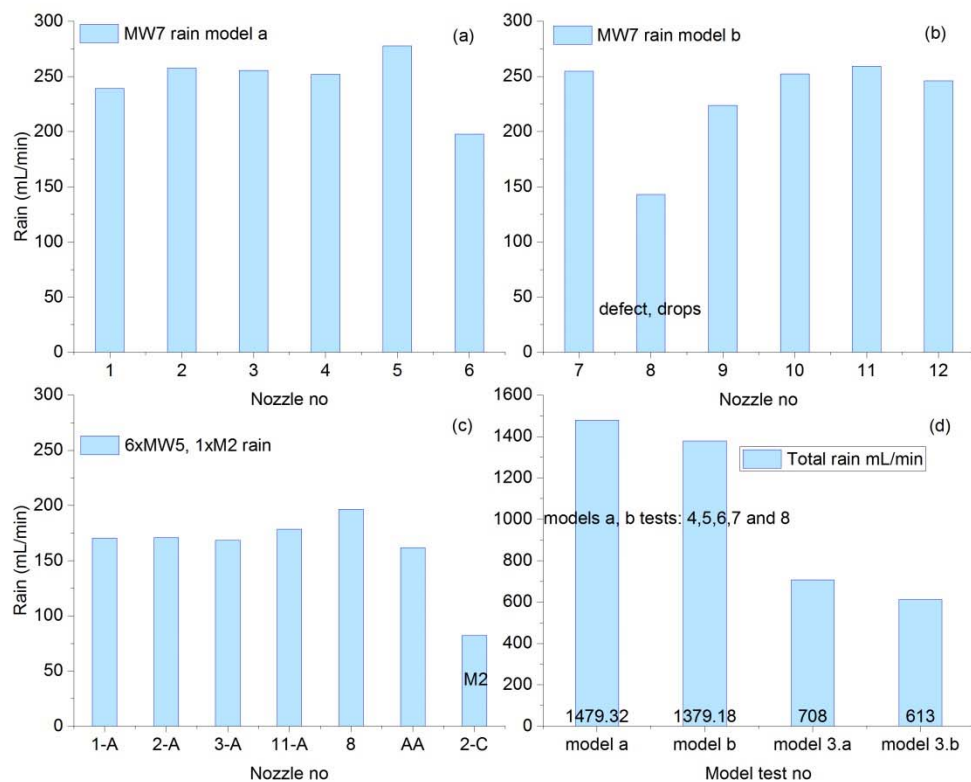


Figure S6.9.13. Rain: a) nozzle model a (tests:4-8), b) nozzle model b (tests 4-8), c) nozzle tests 3a,3b, d) total rain per model and test.

Table S6.9.6. Calculation rainfall area.

nozzle	distance nozzle to soil average (cm)	length nozzle extension (cm)	time (min)	average radius (cm)	area (cm ²)	average (cm ²)
M2	17.80	10.00	1.00	16.00	804.25	780.00
M2				15.50	754.77	
M2	22.80	5.00	1.00	18.00	1017.88	911.00
M2				16.00	804.25	
MW5	17.80	10.00	1.00	33.00	3421.19	3526.00
MW5				34.00	3631.68	
MW5	22.80	5.00	1.00	35.00	3848.45	3848.00
MW5				35.00	3848.45	
MW7	17.80	10.00	1.00	35.00	3848.45	3848.00
MW7				35.00	3848.45	

Table S6.9.7. Calculation of rainfall intensity per nozzle.

Nozzles	Average flow (mL/min)	Average flow (cm ³ /hr)	Tube extension (cm)	Average area infiltration (cm ²)	Rain intensity model scale (cm/h)	Rain intensity model scale (mm/h)	Rain intensity prototype scale (mm/h)
MW5	176.99	10619.51	5.00	3848.00	2.76	27.60	0.55
MW5	176.99	10619.51	10.00	3526.00	3.01	30.12	0.60
M2	82.28	4936.60	5.00	911.00	5.42	54.19	1.08
M2	82.28	4936.60	10.00	780.00	6.33	63.29	1.27
MW7 model a	246.55	14793.20	10.00	3848.00	3.84	38.44	0.77
MW7 model b	229.86	13791.80	10.00	3848.00	3.58	35.84	0.72

Table S6.9.8. Calculation of rainfall intensity per test.

Test	Nozzle	Tube extension (cm)	Rain intensity total model scale (mm/h)	Rain intensity total prototype scale (mm/h)
test 3a	2xMW5	5.00	55.19	1.10
	2xMW5	10.00	60.24	1.20
		total	115.43	2.31
test 3.b	1xM2	5.00	54.19	1.08
	1xMW5	5.00	27.60	0.55
	2xMW5	10.00	60.24	1.20
		total	142.02	2.84
Model a tests 4-8	6xMW7	10.00	230.66	4.61
Model b test 4-8	6xMW7	10.00	215.05	4.30

6.9.2.8 PPT zero offset measurements

Zero offset was measured for every PPTs at different dates (Figure S6.9.14) in the laboratory.

The differences in zero offset between dates for a same PPT, could be due to a variation in the atmospheric pressure changes, this is shown in Figure S6.9.15. Were atmospheric pressure QFE (hPa indicating the atmospheric pressure (Q) adjusted to mean sea level

and certain field elevation (FE). Data obtained from automatic weather station in Mythenquai (Zürich, Switzerland) located at 406 m.a.s.l. website <https://www.tecson-data.ch/zurich/mythenquai/>

Zero offset measurements were not measured between consecutive tests which were performed in a row in a limited period of time. During this time PPTs were kept carefully moist and the measurement from zero offset from a closer test for this PPT was adopted (Table S6.9.9).

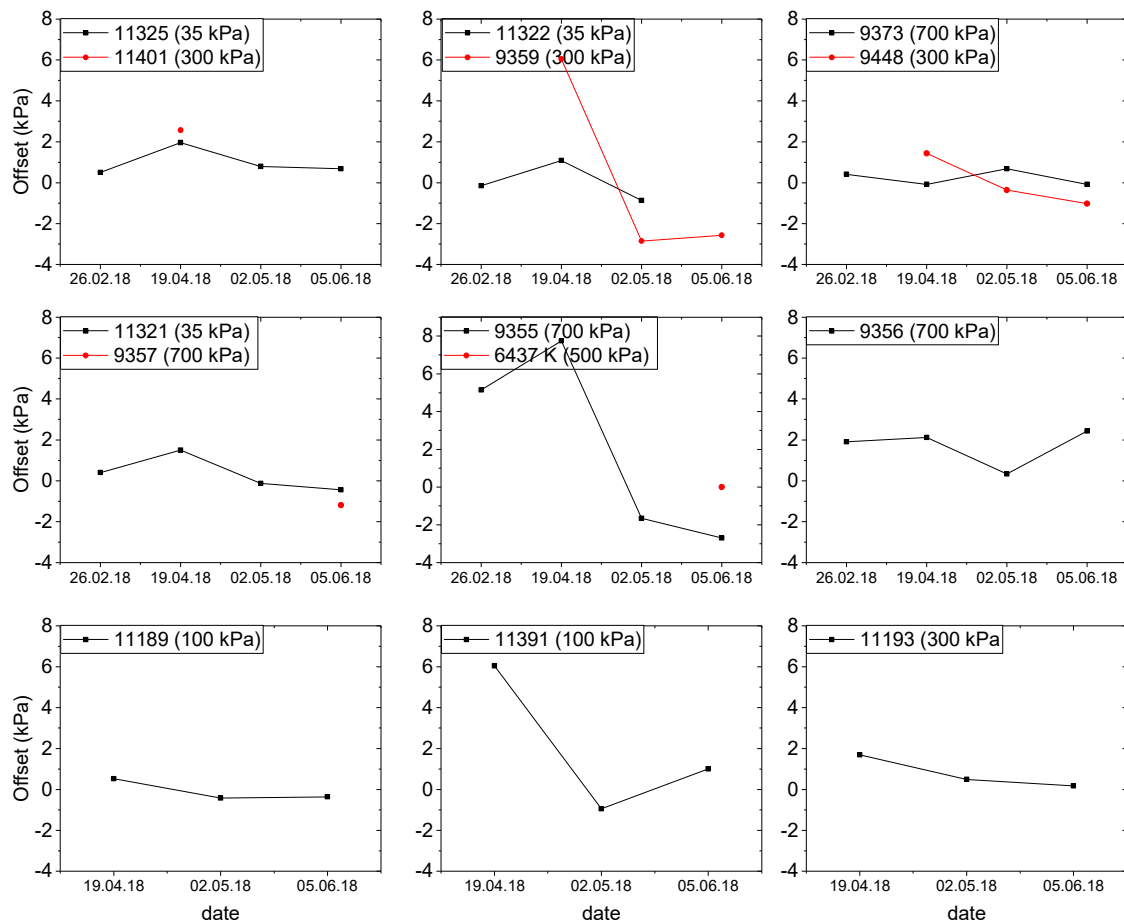


Figure S6.9.14. PPT's zero offset measurements by date in parenthesis the range of measurement in kPa.

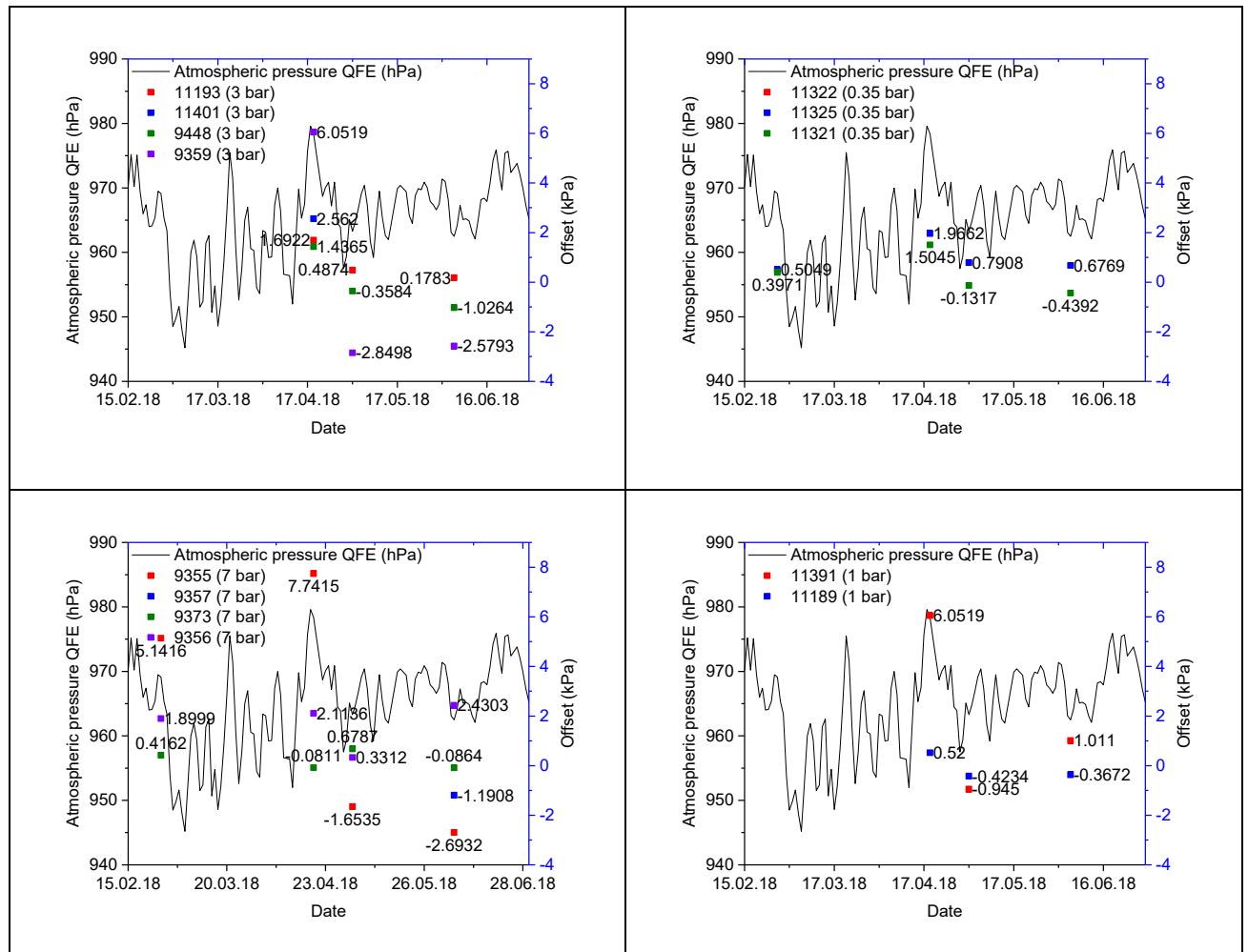


Figure S6.9.15. PPTs zero offset measurements by date in parenthesis the range of measurement in kPa and variation of atmospheric air pressure.

Table S6.9.9 zero offset applied to PPTs in test.

test	upslope PPT (#)	zero offset (kPa)	midslope PPT (#)	zero offset (kPa)	downslope PPT (#)	zero offset (kPa)	date offset test	zero offset adopted
proof	11325	0.5049	9373	0.4162	9355	5.1416	26.02.2018	26.02.2018
	11322	-0.1502	11321	0.3971	9356	1.8999		
1a	11325	1.9662	9373	-0.0811	9355	7.7415	19.04.2018	19.04.2018
	11322	1.0805	11321	1.5045	9356	2.1136		
1 b	11189	0.52	11193	1.6922	9359	6.0519		
	11391	6.0519	11401	2.562	9448	1.4365		
2a	11325	0.7908	9373	0.6787	9355	-1.6535	02.05.2018	02.05.2018
	11322	-0.8628	11321	-0.1317	9356	0.3312		
2b	11189	-0.4234	11193	0.4874	9359	-2.8498		
	6430K		11391	-0.945	9448	-0.3584		
3a	11325	0.7908	9373	0.6787	9355	-1.6535	(-)	02.05.2018
	11322	-0.8628	11321	-0.1317	9356	0.3312		
3b	11189	-0.4234	11193	0.4874	9359	-2.8498		9357 (05.06.2018)
	9357	-1.1908	11391	-0.945	9448	-0.3584		
4a	11325	0.7908	9373	0.6787	9355	-1.6535	(-)	02.05.2018
	11322	-0.8628	11321	-0.1317	9356	0.3312		
4b	11189	-0.4234	11193	0.4874	9359	-2.8498		9357 (05.06.2018)
	9357	-1.1908	11391	-0.945	9448	-0.3584		
5a	11325	0.6769	9373	-0.0864	9355	-2.6932	(-)	05.06.2018
	11322	-0.8628	11321	-0.4392	9356	2.4303		11322 (02.05.2018)
5b	11189	-0.3672	11193	0.1783	9359	-2.5793		
	9357	-1.1908	11391	1.011	9448	-1.0264		
6a	11325	0.6769	9373	-0.0864	9355	-2.6932	(-)	05.06.2018
	6437K	0.0041	11321	-0.4392	9356	2.4303		
6b	11189	-0.3672	11193	0.1783	9359	-2.5793		
	9357	-1.1908	11391	1.011	9448	-1.0264		
7a	11325	0.6769	9373	-0.0864	9355	-2.6932	05.06.2018	05.06.2018
	6437K	0.0041	11321	-0.4392	9356	2.4303		
7b	11189	-0.3672	11193	0.1783	9359	-2.5793		
	9357	-1.1908	11391	1.011	9448	-1.0264		
8a	11325	0.6769	9373	-0.0864	9355	-2.6932	(-)	05.06.2018
	6437K	0.0041	11321	-0.4392	9356	2.4303		
8b	11189	-0.3672	11193	0.1783	9359	-2.5793		
	9357	-1.1908	11391	1.011	9448	-1.0264		

6.9.2.9 Water distribution system for GW flow

Figure S6.9.16 shows the water distribution system located in the climate chamber and used in the centrifuge tests to apply the groundwater flow.

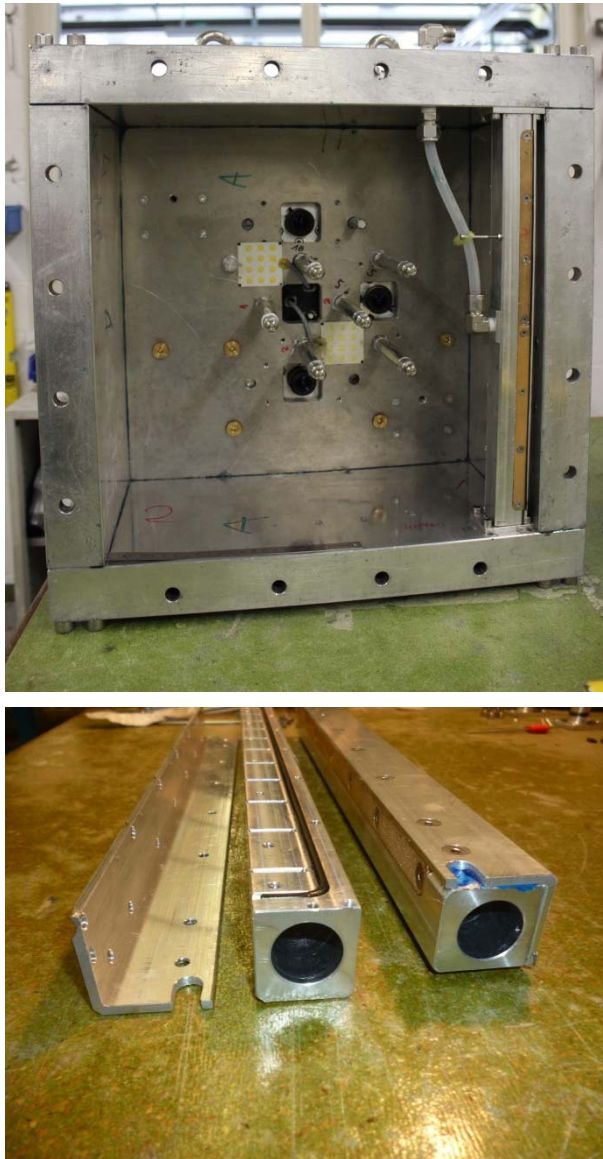


Figure S6.9.16. Top: water distribution system placed in climate chamber; bottom: channel, cover and porous stone.

Adjustments water distribution system to $1g$ and N_g component for more uniform flow across the slope.

Figure S6.9.17 show the top view geometry model in drum centrifuge all dimensions in mm.

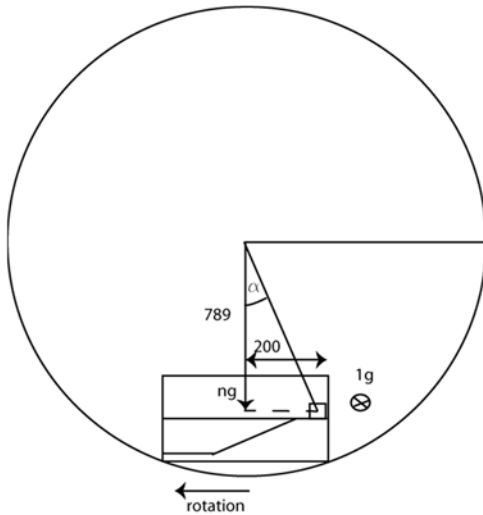


Figure S6.9.17. Sketch of top view of model in drum

The acceleration at radius 789 mm (centre of the tube water distribution system) is calculated to $N_g = 42.237g$

$$\text{angle } \alpha (^{\circ}) = \tan^{-1} \left(\frac{200}{789} \right) \sim 14$$

Then to calculate the deviation of the flow at the bottom of the tube due to the $1g$ vertical is 9.47 mm:

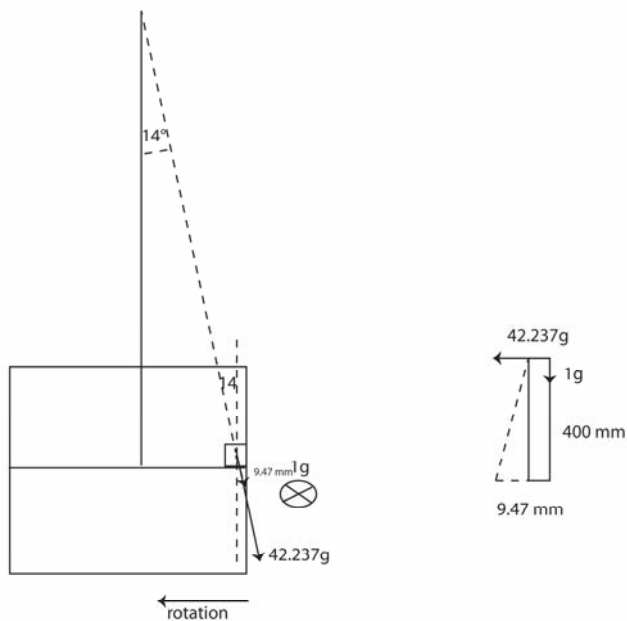


Figure S6.9.18. Top view from the model

Projecting this distance in the wall of the climate chamber is: $9.47 * \cos(14^\circ) = 9.18 \text{ mm}$

9.18 mm is the deviation we need to correct at the extreme bottom of the tube in order to fill the full tube of water more uniformly (Figure S6.9.18, S6.9.19).

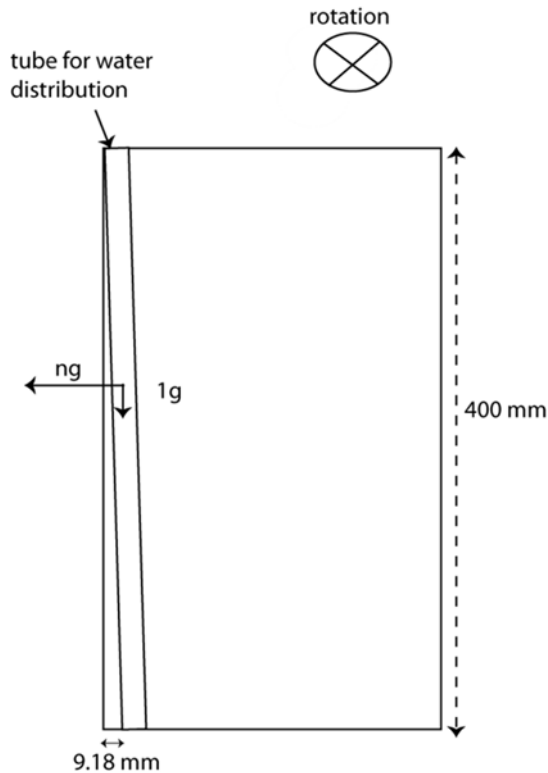


Figure S6.9.19. Displacement correction for water distribution system.

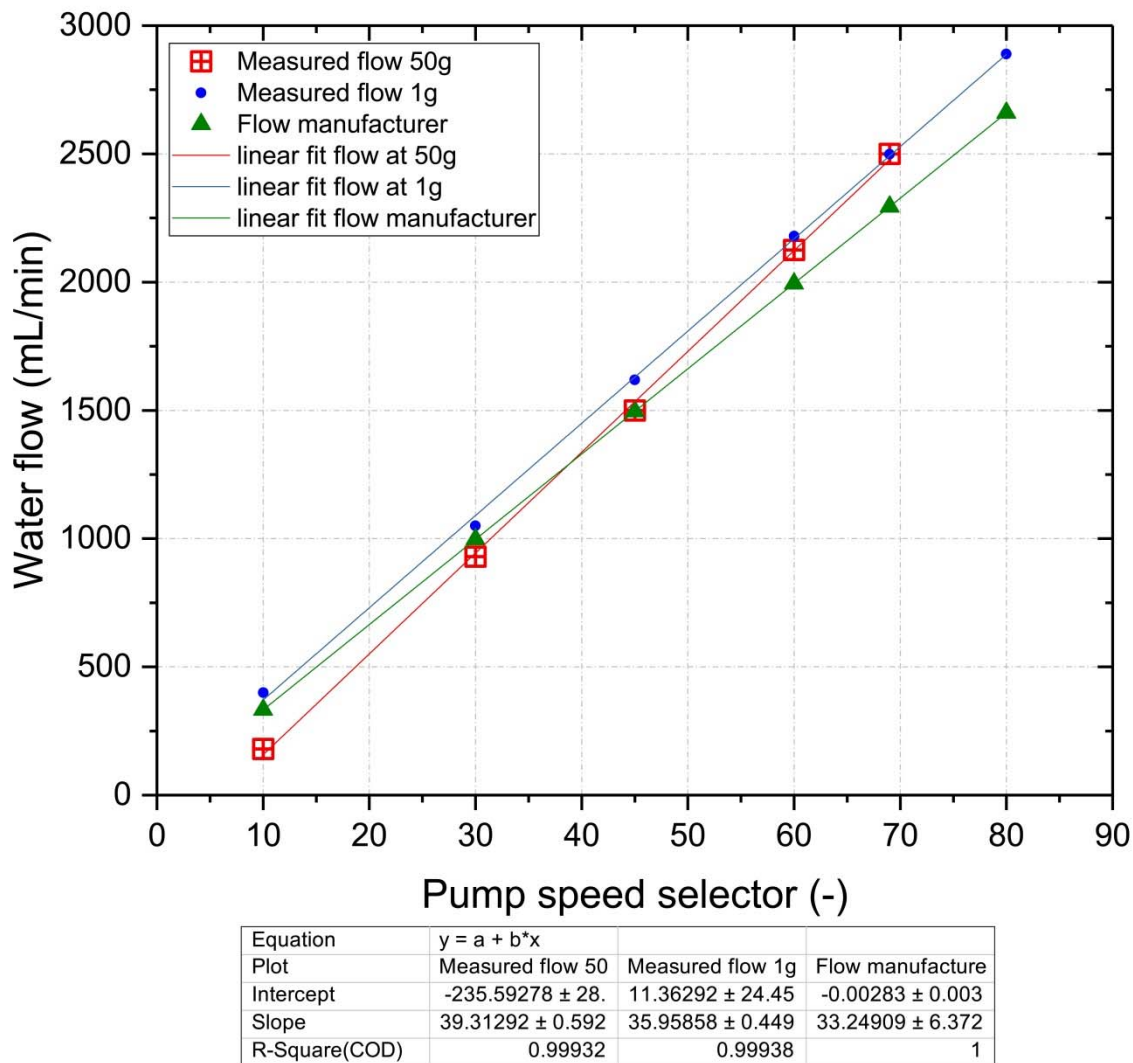
6.9.2.10 Pump calibration at 50g

The calibration of the pump (Reglo-Z, Analog Z-140, Ismatec) was performed at the laboratories of ETH Zürich.

Table S6.9.10, Figure S6.9.20 show the flow measured at 50g level during centrifuge tests, the flow measured at 1g level, and the nominal flow by the manufacturer for different pump speeds.

Table S6.9.10. Water flows measured in pump.

pump speed selector (-)	pump speed (rpm)	time (min)	measured Flow Lab 50g level (mL/min)	Measured Flow lab 1g level (mL/min)	Flow manufacturer (mL/min)	centrifuge @ 50g (rpm)	Ng level	radius (m)
80	4040	1.00		2890	2659.90			
69	3485	1.00	2500	2500	2294.20	211	50	1
60	3030	1.00	2125	2180	1994.90	211	50	1
45	2273	1.00	1500	1620	1496.20	211	50	1
30	1515	1.00	930	1050	997.47	211	50	1
10	505	1.00	180	400	332.49	211	50	1

**Figure S6.9.20.** Comparison of flow at different pump velocity at 1g (green), 50g and (red) and reference manufacturer (blue).

6.9.2.11 Programme physical modelling

The detailed programme of the centrifuge testing is given in Table S6.9.11.

Table S6.9.11. Programme centrifuge testing.

Test name number	Test name	GW of failure (mL/min)	rpm	g level	GW flow range mL/min	Nozzle rain	length nozzle (cm)	rain (mL/min)
1.0Proof (same as 1a)	HN31_1.5_0.75_8.5	Failure at 1500	221	50	500-2000	(-)	(-)	(-)
1a	HN31_1.5_0.75_8.5	Failure at 1500	221	50	500-2000	(-)	(-)	(-)
1b	HN31_1.5_0_0	No failure after max flow	225	52	500-2500	(-)	(-)	(-)
2a	HN31_1.5_0.5_8.5	No failure after max flow	225	52	500-2500	(-)	(-)	(-)
2b	HN31_1.5_0.75_3	Failure at 2500	225	52	500-2500	(-)	(-)	(-)
3a	HN31_1.5_0.5_8.5_R	No failure after max flow	225	52	500-2500	4xMW5	5 top, 10 bottom	708
3b	HN31_1.5_0.75_3_R	No failure after max flow	225	52	500-2500	3xMW5+1 M2	5 top (M2), 10 bottom	613
4a	HN31_1.0_0.75_8.5_R	erosion near plexiglas at 500	225	52	500-1000	6XMW7	10	1479.32
4b	HN31_1.5_0.75_3_R	remobilisation at 1500+rain	225	52	500-2500	6XMW7	10	1379.18
5a	HN31_1.5_0.75_8.5_R	Failure at 1000 +rain	225	52	500-1000	6XMW7	10	1479.32
5b	HN31_1.5_0.5_3_R	No failure after max flow and rain	225 & 230	52	500-2500	6XMW7	10	1379.18
6a	HN31_3.0_0.375_8.5_R	No failure after max flow and rain	225	52	500-2500	6XMW7	10	1479.32
6b	HN31_1.5_0_0_R	No failure after max flow and rain	225	52	500-2500	6XMW7	10	1379.18
7a	HN31_1.25_0.6_8.5	Failure near plexiglas at 2000	225	52	500-2000	(-)	(-)	(-)
7b	HN31_1.25_0.6_3_R	Failure with max flow and rain	225	52	500-2500	6XMW7	10	1379.18
8a	HN31_1.25_0.6_8.5_R	Failure at 1500 +rain	230	54	500-1000	6XMW7	10	1479.32
8b	HN31_1.25_0_0_R	No failure after max flow and rain	230	54	500-2500	6XMW7	10	1379.18

6.9.3 Results

Centrifuge test results

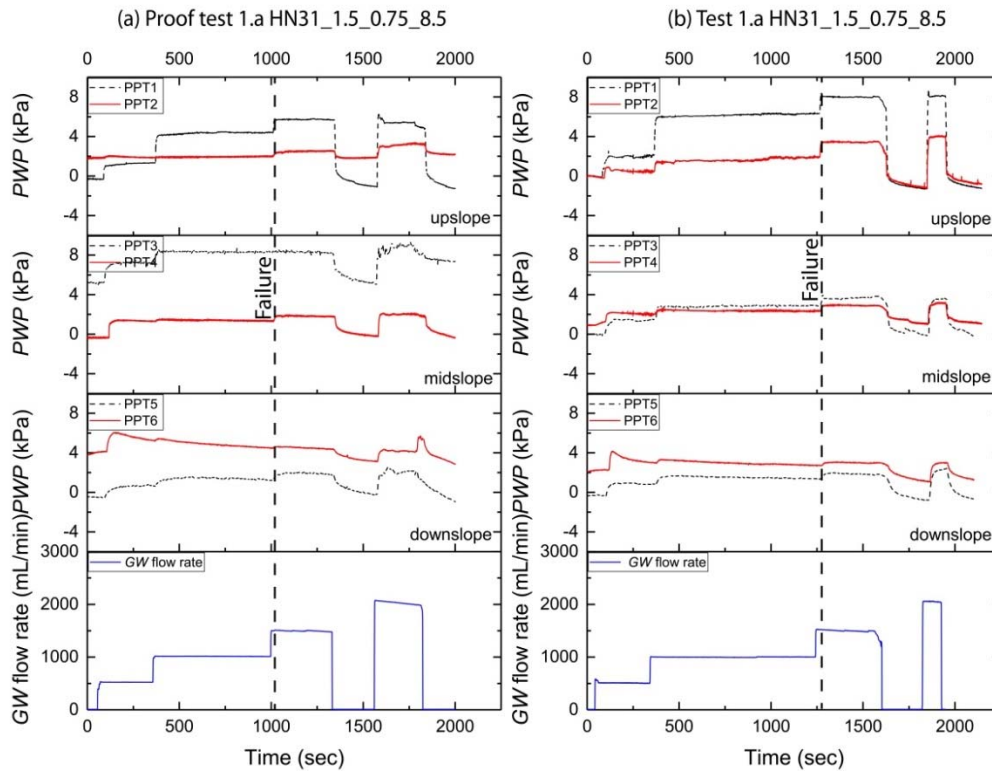


Figure S6.9.21. PWP and GW flow rate versus time for identical models with $h=1.5$ m, and bedrock step $y/h=0.75$ with bedrock step length $X_2= 8.5$ m (prototype). A black dashed line shows the time of failure. (a) Proof test 1.a and (b) test 1.a.

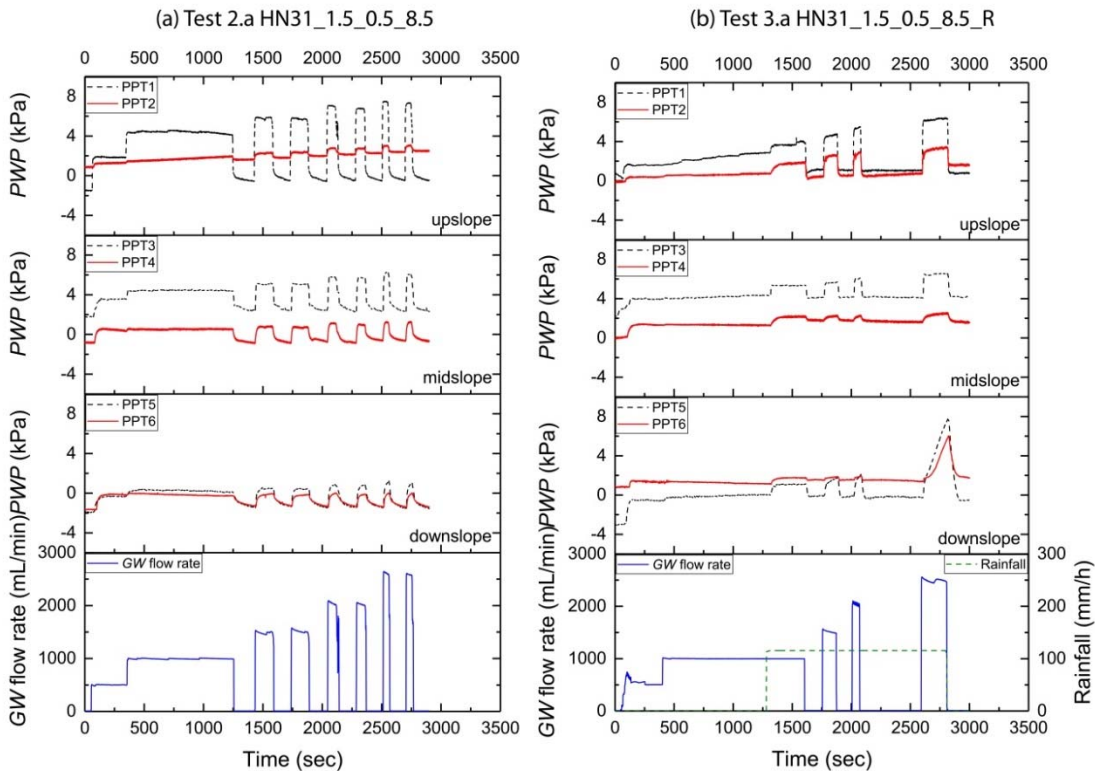


Figure S6.9.22. PWP and GW flow rate versus time for identical models with $h=1.5$ m, and bedrock step $y/h=0.5$ with bedrock step length $X_2= 8.5$ m (prototype). (a) test 2.a and (b) test 3.a.

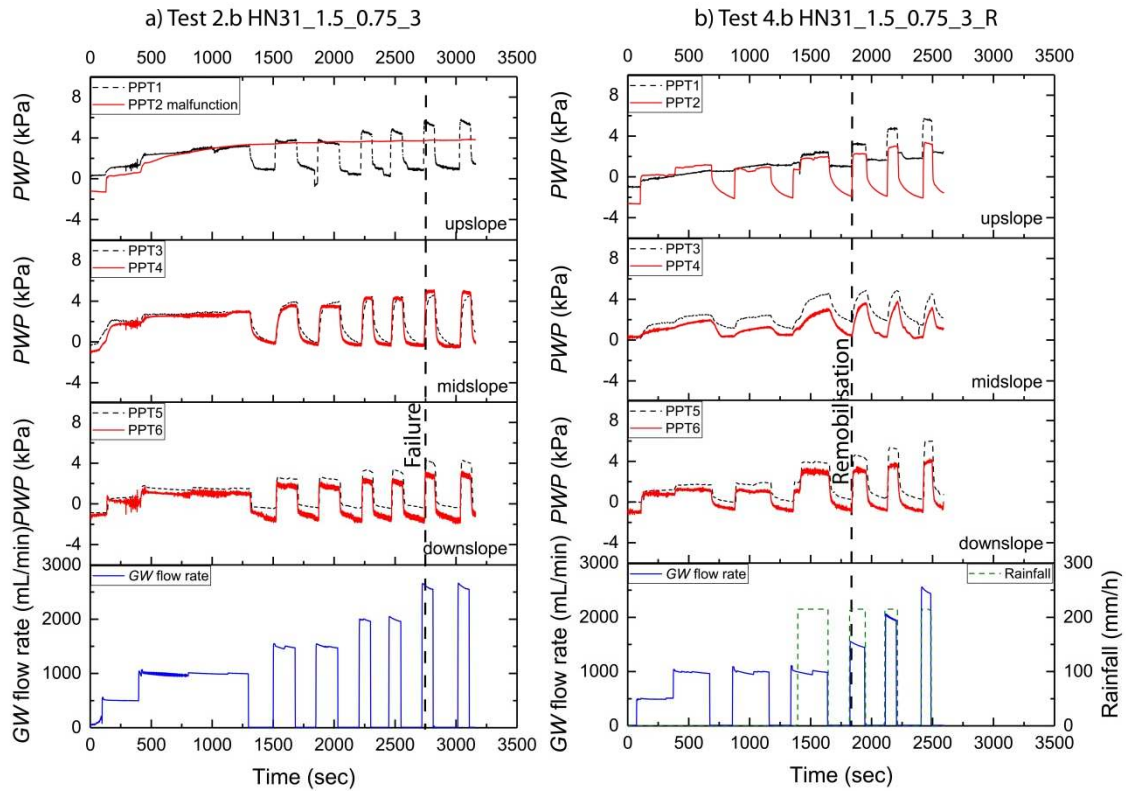


Figure S6.9.23. PWP and GW flow rate versus time for identical models with $h=1.5$ m, and bedrock step $y/h=0.75$ with bedrock step length $X_2= 3$ m (prototype). (a) test 2.b and (b) test 4.b.

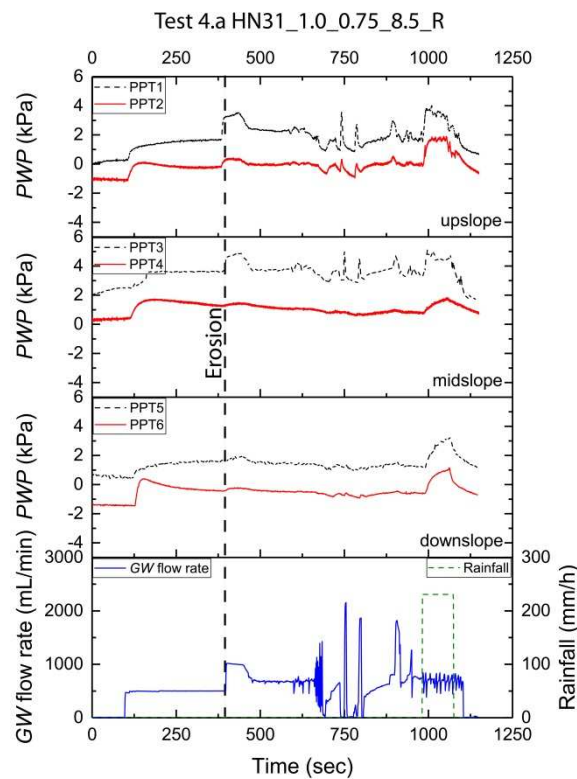


Figure S6.9.24. PWP and GW flow rate versus time model with $h=1.0$ m, and bedrock step $y/h=0.75$ with bedrock step length $X_2= 8.5$ m.

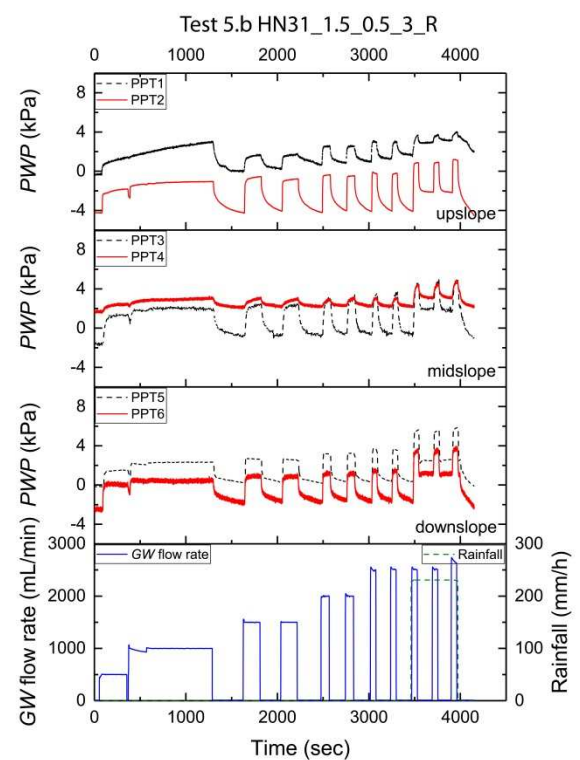


Figure S6.9.25. PWP and GW flow rate versus time model with $h=1.5$ m, and bedrock step $y/h=0.5$ with bedrock step length $X_2= 3$ m.

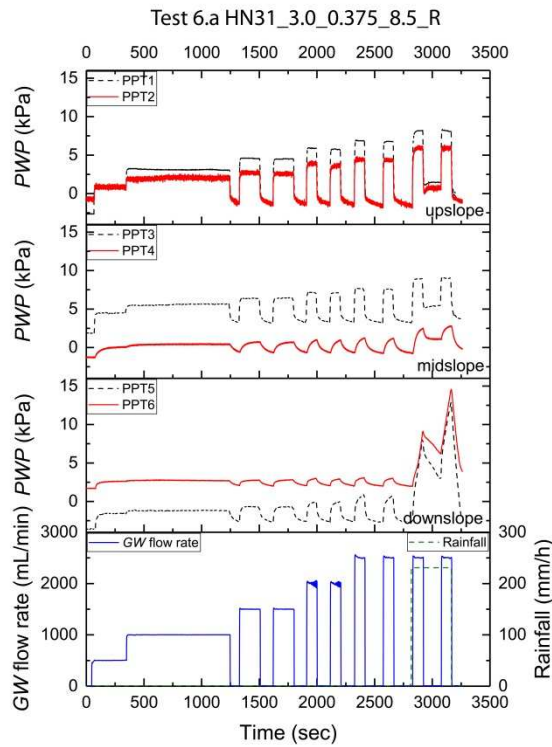


Figure S6.9.26. PWP and GW flow rate versus time model with $h=3.0$ m, and bedrock step $y/h=0.375$ with bedrock step length $X_2=8.5$ m.

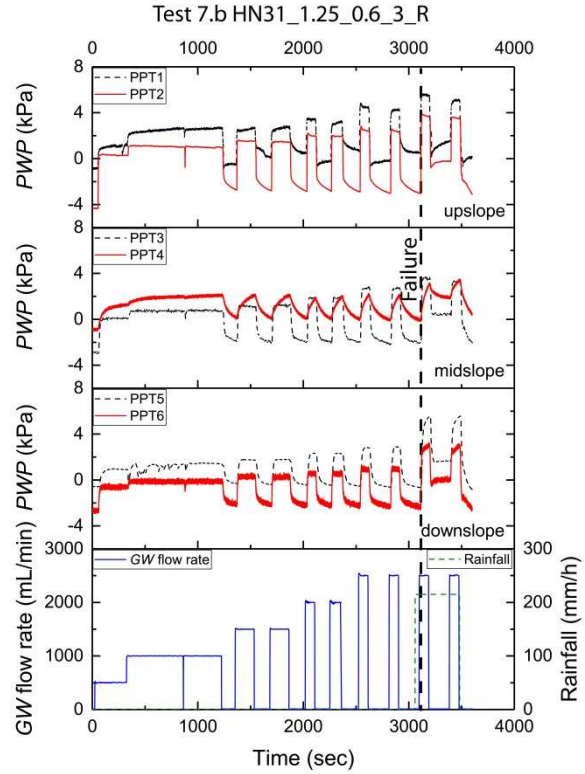


Figure S6.9.27. PWP and GW flow rate versus time model with $h=1.25$ m, and bedrock step $y/h=0.6$ with bedrock step length $X_2=3$ m.

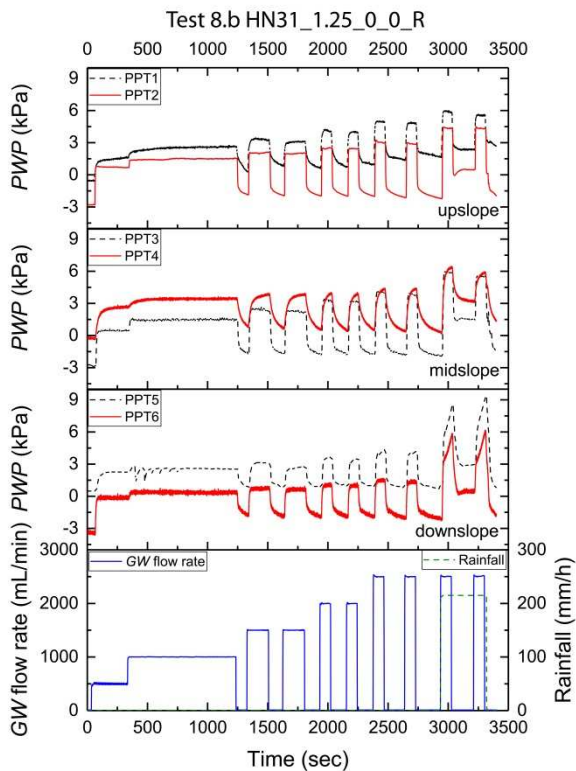


Figure S6.9.28. PWP and GW flow rate versus time model with $h=1.25$ m, and bedrock step $y/h=0$ with bedrock step length $X_2=0$ m.

7 Conclusions and outlook

The potential hazards for a gravelly scree slope in the Swiss Alps that has been subjected to daily and seasonal variations of weather at altitudes between 1500-2000 m.a.s.l. were explored, including the effect of a mixed hydraulic regime of groundwater flow, snow and rainfall. A ground model of the alpine gravelly scree slope was created based on characterisation through field and laboratory investigations, including strength parameters determined by triaxial stress-path testing to represent pore pressure increase in the slope.

Long-term field monitoring of volumetric water content (VWC) and temperature was carried out to explore the seasonal response. A worst-case hazard scenario for shallow mass movement was developed, with subsequent simulation of selected prototypes of a combination of bedrock features, soil thickness, groundwater flow and rain intensity in physical and numerical models.

Complementary geophysical and geotechnical techniques were applied to investigate the alpine landslide debris during the field monitoring and characterisation. The bedrock depth was defined across a specific area of the scree slope and results compared with data from the geotechnical test pits and field observations. Furthermore, the VWC estimated from ERT measurements were found to agree well with the VWC results obtained from sensors installed in the four instrumented trenches.

7.1 Field monitoring

A long-term geotechnical monitoring campaign led to a better understanding of the soil behaviour during seasonal weather conditions. The measurements were recorded in four trenches, instrumented with sensors to measure temperature and VWC, which were installed at different depths (up to 1 m). These were complemented by four cameras, two meteorostations and two snow stakes. The cameras revealed the hourly dynamic processes taking place on the scree slope, and helped in the interpretation of the data.

The VWC was measured in gravelly soil using TDR and capacitance sensors EC-5/10HS (Decagon devices). Data were processed and documented extensively over a period lasting up to 3 years. Some authors have documented sensor performance comparison between EC-5/10HS and TDR (Mittelbach et al., 2011, 2012; Bogaen et al., 2007) in silty loam, clayey loam, and loamy silt, respectively, however there has been a gap in the application to gravelly soils. This was a challenging environment, the VWC and

temperature recorded are distinctive because of the type of soil, altitude and hence weather conditions. These included temperatures ranging from above and below 0°C, and a hydrological regime of precipitation, either as rain or snow, and snow melting, all within one year.

One of the main findings from the field monitoring was that the VWC and temperatures present patterns that are strongly related to the seasonal weather changes. For instance, temperatures and VWC reach minimum values (near zero) during winter, whereas in spring and summer, the snow melting and rainfall cause the VWC to rise. Furthermore, the data obtained from these sensors revealed that the range of VWC in this poorly graded granular soil is rather low (<0.25), and that the soil could become saturated through intense rainfall, which could be enhanced by periods of snow melting.

The effect of temperature on the determination of VWC was of special interest because of the variation of temperatures at the field site. The influence of temperature on the dielectric constant of the soil has been mentioned by other authors (Pepin et al. 1995; Topp 1980; Bogaen et al. 2007; Mittelbach 2012). They present different evidence-based opinions on whether there are changes in the dielectric constant and whether these lead to an increase or decrease, although not much information about gravels was found in the literature. The site-specific calibration of sensors at the Meretschibach included variations in temperature, ranging from -6 to 23°C. The results show small variations that could be attributed to the heterogeneity of the soil, and so the relationship between the soil temperatures and the estimation of the VWC was assumed to be related primarily to the grading of the soil in situ, locally, around the sensors. Hence, it was found that a site-specific calibration is highly recommended when monitoring gravelly soil ($D_{\max} = 31.5$ mm), because the use of smaller sizes (e.g. $D_{\max} = 4$ mm of the same soil) could lead to an underestimation of the VWC.

Although the instrumentation of heterogeneous gravel presented challenges in the installation, monitoring and data analyses, the sensors performed well, and more or less continuously during the three years of monitoring. There were a few exceptions when the location was hit by a rockfall, or an avalanche happened, causing the data logger to stop recording until it was repaired.

7.2 Soil characterisation

The grain size distribution of the gravelly soil corresponding to excavations made in the four instrumented trenches varied, depending on the location within the scree slope. Larger particles were remobilised downslope by gravitational forces, while fines were transported by seepage as a result of rain or snow melting. Processes causing disturbances, like rainfall infiltration, groundwater flow and avalanches that can affect the sorting and dynamics in scree slopes, have been investigated by Statham (1973); Gerber and Scheidegger (1974), but no literature was found about stability of gravelly scree slopes.

Based on the work of Zhu and Anderson (1998), Anderson and Sitar (1995), Springman et al., (2003) and Casini et al., (2010, 2012), a triaxial testing programme was performed on soil elements by applying a stress path that replicates a rainfall-induced landslide. CSD (constant shear stress drained) stress paths were used during shearing to failure in medium (15 cm diameter) and large (25 cm diameter) reconstituted poorly graded gravelly specimens, in which the maximum particle size was limited to 16 and 31.5 mm respectively.

Considering that soil in steep slopes experiences a highly anisotropic stress state, the tests were carried out with a $K_c=1.83$ to 2.42 , which were conservatively lower than $K_c=3.3-4.3$, calculated by Anderson as one tenth of the slope angle ($33-43^\circ$). The CSD triaxial stress path reproduced the mechanism of failure due to rain infiltration, increasing the PWP and moving the stress path horizontally in $p'-q'$ space to intersect the failure envelope, causing the soil to fail.

The results provided strength parameters of the soil at critical state, $\phi' = 42^\circ$ and 41° (for the medium and large specimens respectively), and zero cohesion. These replicated, to a large extent, results obtained by Teyssie (2006) and Springman et al. (2003) on well-graded alpine moraines, which also mobilised $\phi' = 39^\circ$ in large (25 cm diameter) triaxial tests under the same stress path and $\phi' = 41^\circ$ in large scale (25 x 25 cm) in situ direct shear tests. These values can be thought of as conservative minimum values given that:

- a. firstly, larger grain sizes were removed from the field samples, and will be likely to reinforce the ground and increase the mobilised shear strength at failure (e.g. Bolton et al., 1991) in the field, and

- b. secondly, considerable dilatancy was observed under lower confining pressures. The lower the mean effective stress, the higher the dilatancy and hence maximum mobilised (strain-dependent) shear strength (Bolton, 1986). This would be attributable also to coarse, steep granular slopes in the field, as measured by Arnold et al., (2006) in reconstituted large-scale direct shear specimens. Dilatancy angles obtained in this research ranged from $\Psi = 1.12$ to 17.26° between p' ranging from 73.5 kPa to 12 kPa, which are still much greater stresses than those applied to surficial failures in the field at depths between 1-3 m.

Two geophysical methods, ERT and ground-based penetrating radar (GPR), were applied in this project (Fankhauser 2014) and met the purpose very well. They provided subsurface images, as well as an alternative estimation for the VWC from the former. The depth to bedrock was determined using (GPR) profiles that covered the whole scree slope. The bedrock was found to be shallow with a maximum depth of 3 m. ERT tomograms in the scree slope suggested ranges of bedrock depth that agreed well with GPR results. Furthermore, ERT measurements of soil resistivity, determined through Archie's law enabled preliminary estimations of VWC, which were comparable with the values of VWC measured by the sensors installed in the instrumented trenches.

Notwithstanding the challenges presented by the terrain, the measurements delivered with the soil properties and behaviour, accompanied by reliable map showing the bedrock contours, with satisfactory results and would be recommended for the future monitoring schemes.

7.3 Numerical and physical modelling

Numerical and centrifuge simulations were performed to investigate slope stability under simplified steady state hydrological conditions, combining a groundwater (GW) regime and rainfall necessary to cause surficial landslides in the models.

A numerical method was used as a simplified 2D analysis of the state at failure. This enabled a study to be made of the bedrock geometry effect using a steady state analysis of flow in less time than a physical model, providing a useful opportunity to explore the range of options available in designing the subsequent centrifuge model tests. But this analysis did not consider the hydraulic transient analysis and deformations, and tensile cracking of the soil. Therefore, centrifuge testing was used to validate and complement the results. Centrifuge modelling captured the failure initiation, cracking, timing, run

out, and measured the PWP processes in transient time in 3D, providing valuable additional information.

A critical steady state groundwater flow could be calculated for a factor of safety of 1 for slope instability under nominal two-dimensional plane strain conditions for each geometrical parameter variation for the slope. The greatest GW flow/rainfall was needed to induce failure when the bedrock was parallel to the slope surface, which happened with no step ($y/h=0$). Since the physical model was expected to need a berm to prevent local erosion at the toe from influencing the results (Take & Beddoe 2015), this was also investigated in the numerical modelling to aid design of the appropriated dimensions.

These numerical simulations have shown that a bedrock step increases the likelihood of a shallow landslide. The analysis in terms of factor of safety, exhibiting a decrease in F.S. as the bedrock step increases in height (y) and length (X_2). Furthermore, an increase in bedrock step length (X_2) had a greater impact than an increase in height, decreasing the GW flow necessary to cause failure.

Based on developments reported by Lee and Bolton, (2006), Take et al., (2004), Ling and Ling, (2012), Askarinejad, (2013), Park, (2014), Take and Beddoe, (2014), Take et al. (2014), a testing programme was designed using centrifuge modelling for triggering slope failure with groundwater flow and seepage was performed in a climate chamber in the geotechnical drum centrifuge at IGT. The model slope had a 38° inclination, with a range of bedrock geometries, including the prototype case with the bedrock parallel to the ground surface. Some relevant aspects of the testing are given below:

- a. Challenges in physical modelling at 50g with particle size approximations and in supplying a plane flow across the top of the slope, given that the radius at the top of the slope - bottom meant that the nominal gravity changed by 9.6g (Schofield, 1980). This necessitated a complicated design to represent bedrock that was nominally parallel in terms of flow conditions to the surface (Lucas et al. 2019).
- b. Without a bedrock step, the prototype case with bedrock nominally parallel to the surface led to greater volumes of debris being mobilised and, highest flow rates needed plus addition of intense rainfall to cause a slope failure.
- c. Bedrock steps of different sizes and soil thicknesses between 1-3 m (at prototype scale) were tested under critical combinations of groundwater seepage and rainfall infiltration. The results confirmed that the groundwater table and hence PWP will

rise upslope of a bedrock step, saturating the soil, inducing loss of suction and effective stress, eventually leading to a failure above the step at lower flow rates than without a step. Furthermore, if the bedrock step is close to, or outcrops at, the surface, the shallow landslide occurs upslope of the bedrock step mobilising smaller volumes of debris. The increase of PWP were recorded by PPTs during the test, and the failure captured by high-speed cameras. The failure was observed in the form of cracking, runout, or remobilisation of the soil downstream.

The centrifuge modelling tested the effect of the bedrock geometry on the slope stability under hydraulic regimes of groundwater and rain, with good results. Mixed scaled soil (SP-SM) was a combination of Hostun sand plus 10% fines Minisil, and the bedrock geometry was simplified with a berm at the bottom of the slope. Nine physical models were tested in the drum centrifuge at ETH under regimes of groundwater only, and combined with rainfall, and generally agreed with the findings from the numerical modelling. Similarities were observed in terms of PWP generation, magnitude of GW flow at failure, and failure location.

Both numerical and physical models supported the hypothesis that GW flow and rainfall infiltration increase the PWP, reduce suction and increase the potential for surficial landsliding. GW flow, combined with intense rainfall in centrifuge tests, led to both bottom-up and top-down saturation (Kienzler 2007), which decreased suction and increased the unsaturated hydraulic conductivity of the soil. This promotes faster rainfall infiltration (Ng & Shi, 1998), leading to a more sudden and greater increase of PWP, increasing the hazard considerably.

The centrifuge testing proved to be a crucial addition to the analysis, showing in a 3-dimensional scaled model, the development of PWP and the failure mechanisms for several model configurations. The results confirmed the role of the bedrock geometry on the slope stability under a combined regime of groundwater flow and rain, providing invaluable information regarding the failure triggering mechanism and the runout of the released mass.

7.4 Preliminary hazard assessment

The scree slope can experience different types of mass movement due to its process dynamics: toppling, rockfall and shallow landslides. Data collected during the monitoring campaign, which were supported by the field observations, indicated that a hazardous scenario for the scree slope is a shallow landslide triggered by rainfall that

mobilised considerable amount of the thickness of the soil. Eventually, this could reach the village downslope.

After analysis of the monitoring data, laboratory testing, characterisation, numerical and physical simulations, the main aspects described below shall be considered in the analysis of a shallow landslide:

- The VWC range variation (up to 1 m depth) is rather low (<0.25) for the instrumented trenches IT1-IT4.
- It is unknown whether the soil reaches saturation over larger areas and at depths greater than 1 m.
- Considering the bedrock maximum depth (3 m) and the plot showing bedrock depth in the scree slope (Figure 5.10), a landslide that would mobilise an average soil thickness of 1.5 m, with triangular area with a base of 100 m and a height of 200 m would have a volume of roughly 15000 m³.

Therefore, it is concluded that although rainfall infiltrates into the poorly graded gravel, it is unlikely for the soil to reach saturation (up to 1 m depth), due to the high permeability and effective drainage of the gravel and the high hydraulic gradient. The conditions that could favour the occurrence of a shallow landslide in the scree slope are: a combination of an outcrop bedrock step plus intense rainfall, enhanced by the snow melting during spring in a section of the slope steeper than 38°. A failure would then be triggered by the increase of PWP and loss of effective stress and the location would be determined mainly by the bedrock geometry, soil thickness and water flow intensity.

The implications of the combined experimental results for the hazard assessment require knowledge about the several disciplines involved, in order to interpret the data effectively, and to integrate this information into a realistic model. The triggering of shallow landslides requires an analysis of rainfall intensity and water seepage in the slope to determine whether conditions exist for initiation in the field. Centrifuge modelling results for similar ground models could be useful as a reference of the initiating rainfall intensities.

Subsequently, the strength parameters of the gravelly soil of $\phi' = 42^\circ$ and $c' = 0$ obtained from the triaxial testing, can be used for prediction of the factor of safety and testing of additional hazard condition scenarios. It should be taken into consideration that the

strength parameters are derived from testing on reconstituted specimens using an average GSD of the four instrumented trenches in the scree slope.

Once the failure is reached, the question arises as to how the mass will be released and the volume of this displaced mass. Centrifuge testing gave good indicators to exploring these aspects further: it was observed that when the bedrock was shallower, the PWP increased as the whole soil layer was saturated. If the water ponded and accumulated behind the bedrock step, an outflow (spring) can emerge at, and erode, the surface. Tension cracks may also develop, as was observed in several centrifuge model tests (with GW and GW plus rain), inducing greater macro-permeability, higher saturation, more displacement and, eventually, greater run out. The behaviour of the mass released after failure depends on the intensity of the GW/rain, saturation degree, geometry of the bedrock and soil thickness.

7.5 Outlook

The following recommendations are given to help to develop an understanding of the hazard assessment at Meretschibach further. The list below, grouped by section is meant to answer the open questions in this research, and provides a list of future tasks that, in the author's opinion, could help to extend the understanding of failure mechanisms in scree slopes:

Characterisation

1. The CSD triaxial testing in chapter 5 was performed for two specimen dimensions of 15 and 25 cm in diameter. A CSL line was drawn for each set of tests, and strength parameters were obtained. It is recommended for the mid-scale triaxial apparatus to run tests at a higher confining pressure, to obtain the critical state strength parameters and to improve determination of the CSL, and to observe the dependency of the soil behaviour and strength parameters on the confining pressure. This task will additionally allow the comparison of the CSL obtained from mid and large-scale specimens at a similar range of effective stresses, and check on the dilatancy of the adopted GSD. Finally, the K_c for mid-scale specimens was 1.83-1.94 before shearing, and the results showed a K_c at failure ranging between 4.6-5.1, therefore a higher initial stress ratio (using higher $\sigma'_{3,B}$) could be used, closer to the incipient state of failure.

Field monitoring

2. A methodology was provided in chapter 4 to obtain the VWC from ERT measurements using Archie's law (1942). These preliminary results were compared to the VWC obtained, pointwise, from instrumented trenches, with good agreement. The advantage of using ERT measurements in the determination of VWC is that data can be obtained along a profile, providing more redundancy in the measurements. This would be highly recommended due to problems of scale. Therefore, more measurements of VWC with ERT are advised, in parallel with TDR measurements, to enhance the application of geophysical and geotechnical techniques already applied successfully in this project. Archie's law (1942) determines the resistivity of the soil as function of the saturation, porosity, and the resistivity of the pore fluid. These parameters are combined with empirical parameters, such as the cementation factor m , coefficient of saturation n , tortuosity factor. In this research, values were inferred for preliminary measurements, therefore the factors m and n were obtained from matching values of VWC from past results, and the water resistivity from literature. In a further application it is recommended that the water resistivity is measured, and the constants m , n , a can be determined more directly.

The site-specific recalibration was used to determine VWC using TDR, EC-5/10HS with good results for the positive range of temperature. Despite the fact that this calibration worked relatively well to estimate VWC in the winter season (with temperatures near or below zero), there is a potential gap in the determination of VWC in the soil under freezing temperatures. This conclusion is based on results from some sensors, which showed inconsistencies in the VWC under winter conditions. The voids in frozen/unfrozen soil can be filled with unfrozen water, ice and air, so there is a temperature gradient in the soil (due to daily ambient temperature variations) and processes such frost heave (Miller, 1973; Taber, 1929; Taber, 1930) could take place, which would affect the VWC in this case. The question to answer is how the VWC estimated with the actual calibration differs from the VWC determined using a calibration based on calibration in frozen/unfrozen soil.

3. Although this research focused on the response of the slope to rainfall, the VWC behaviour in winter-time is of interest, especially in an alpine environment, due to the complex interaction between air, ice, an insulating snow layer, unfrozen water, and infiltrating water. Furthermore, a study of the freezing and thawing during

winter and their combined effects on the water infiltration, run off and erosion could lead to a deeper understanding of the hazard associated to snow melting and avalanches, as well as their influence in the occurrence of shallow landslides in the scree slope.

4. The field instrumentation recorded VWC and temperature in the soil using instrumented trenches up to 1 m depth in selected locations in the slope. 1 m depth was the maximum reachable in a test pit excavated by hand, without collapse of the vertical granular walls of the slope. It is recommended to measure the potential water table (if there is any) depth in order to analyse further the hazard. An instrumented well near IT4 (due to the relatively flat ground surface and the less coarse grain sizes, which facilitate the drilling) would meet the purpose.

Numerical and physical modelling

5. The preliminary numerical analysis was performed using steady state hydrological conditions in the model (SEEP/W). Although this allowed the slope stability analysis using SLOPE/W, an improvement can be made using a transient analysis instead of steady state, this is because the development of PWP and infiltration are time dependent processes. The development of PWP could be analysed from the centrifuge tests with time in this research.
6. The centrifuge programme was designed to investigate the slope stability for several bedrock models under hydraulic regimes of groundwater/rain and to quantify a factor of safety. The objective of understanding, in a simplified model, the mechanism of failure and PWP development was fulfilled. However, the scree slope at Meretschibach presents several features that provided more complex interactions and demands additional study, if the project would continue in order to give further advice to the community of Agarn. These factors include the soil heterogeneity, vegetation, effect of water runoff, group of bedrock step interaction, debris flow erosion, and slope inclination, among others. One of the parameters that has not yet been included in centrifuge testing, and it is suggested as being relevant due to the interaction with the shear strength of the soil, is the effect of roots. Askarinejad (2013) found, from investigating the effect of roots in silty sand, that the soil ductility increased, indicating larger deformations prior to failure. This could serve as a basis for further interesting research.

7.6 References

- Anderson, S. A., & Sitar, N. (1995). Analysis of rainfall-induced debris flows. *Journal of Geotechnical Engineering*, 121(7), 544-552.
- Archie, G. E. (1942). The electrical resistivity log as an aid in determining some reservoir characteristics. *Transactions of the AIME*, 146(01), 54-62.
- Arnold, A., Thielen, A., & Springman, S. M. (2005). On the stability of active layers in alpine permafrost. In *Landslides and Avalanches: Proceedings of the 11th International Conference and Field Trip on Landslides* (pp. 19-25). Taylor & Francis.
- Askarinejad A., (2013). Failure mechanisms in unsaturated silty sand slopes triggered by rainfall. ETH Dissertation, Nr. 21423, <https://doi.org/10.3929/ethz-a-010002526>.
- Bogena, H.R., Huisman, J.A., Oberdörster, C., & Vereecken H. (2007). Evaluation of a low-cost soil water content sensor for wireless network application. *Journal of Hydrology*, 344(1), 32-42.
- Bogoslovsky, V.A., & Ogilvy, A.A. (1977). Geophysical methods for the investigation of landslides. *Geophysics*, 42(3), 562-571.
- Bolton, M. D. (1986). Strength and dilatancy of sands. *Géotechnique*, 36(1), 65-78.
- Bolton, M. D., Fragaszy, R. J., & Lee, D. M. (1991). Broadening the specifications of granular fills. *Transportation Research Record*, 1309, 35-41.
- Casini, F., Jommi, C., & Springman, S. (2010). A laboratory investigation on an undisturbed silty sand from a slope prone to landsliding. *Granular Matter*, 12(3), 303-316.
- Casini, F., Serri, V., & Springman, S. M. (2012). Hydromechanical behaviour of a silty sand from a steep slope triggered by artificial rainfall: from unsaturated to saturated conditions. *Canadian Geotechnical Journal*, 50(1), 28-40.
- Fankhauser, K., (2014). Geophysical slope characterization using GPR and ERT in an active debris flow catchment. *Master Thesis*, EEG, ETH Zurich.
- Gerber, E., & Scheidegger, A. E. (1974). On the dynamics of scree slopes. *Rock Mechanics*, 6(1), 25-38.

Kienzler P., (2007). Experimental study of subsurface stormflow formation. ETH Dissertation, Nr. 17330, <https://doi.org/10.3929/ethz-a-005477823>.

Lucas, D., Herzog, R., Iten, M., Buschor, H., Kieper, A., Askarinejad, A., & Springman, S.M. (2019). Modelling of landslides in a scree slope induced by groundwater and rainfall. *International Journal of Physical Modelling in Geotechnics* on Physical modelling of Landslides. <https://doi.org/10.1680/jphmg.18.00106>

Lee, Y. S., & Bolton, M. D. (2006). Centrifugal modelling of the landslides triggering mechanism in layered fill slopes. In *Proceedings of the Sixth International Conference on Physical Modelling in Geotechnics, Hong Kong* (pp. 355-360).

Ling, H., & Ling, H. I. (2012). Centrifuge model simulations of rainfall-induced slope instability. *Journal of Geotechnical and Geoenvironmental Engineering*, 138(9), 1151-1157.

Miller, R. D. (1973). Soil freezing in relation to pore water pressure and temperature, paper presented at 2nd International Conference on Permafrost. *Natl. Acad. Sci., Yakutsk, Russia*.

Mittelbach, H., Casini, F., Lehner, I., Teuling, A. J., & Seneviratne, S. I. (2011). Soil moisture monitoring for climate research: Evaluation of a low-cost sensor in the framework of the Swiss Soil Moisture Experiment (SwissSMEX) campaign. *Journal of Geophysical Research: Atmospheres*, 116(D5).

Mittelbach, H., Lehner, I., & Seneviratne, S. I. (2012). Comparison of four soil moisture sensor types under field conditions in Switzerland. *Journal of Hydrology*, 430, 39-49.

Ng, C. W. W. & Shi, Q. (1998). Influence of rainfall intensity and duration on slope stability in unsaturated soils. *Quarterly Journal of Engineering Geology and Hydrogeology*, 31(2), 105-113.

Park, D. S. (2013). The effect of radial G-field on the centrifuge modelling. In ICPMG2014-Physical Modelling in Geotechnics: Proceedings of the 8th International Conference on Physical Modelling in Geotechnics 2014 (ICPMG2014), Perth, Australia, 14-17 January 2014 (p. 385). CRC Press.

Pepin, S., Livingston, N. J., & Hook, W. R. (1995). Temperature-dependent measurement errors in time domain reflectometry determinations of soil water. *Soil Science Society of America Journal*, 59(1), 38-43.

- Schofield, A.N. (1980). Cambridge geotechnical centrifuge operations: 20th Rankine lecture. *Géotechnique*, 30(2): 129-170.
- Springman, S. M., Askarinejad, A., Casini, F., Friedel, S., Kienzler, P., Teyssere, P., & Thielen, A. (2012). Lessons learnt from field tests in some potentially unstable slopes in Switzerland. *Acta Geotechnica Slovenica*, 1, 5-29.
- Springman, S. M., Jommi, C., & Teyssere, P. (2003). Instabilities on moraine slopes induced by loss of suction: a case history. *Géotechnique*, 53(1), 3-10.
- Statham, I. (1973). Scree Slope Development under Conditions of Surface Particle Movement. *Transactions of the Institute of British Geographers*, (59), 41-53. doi:10.2307/621711
- Taber, S. (1929). Frost heaving. *The Journal of Geology*, 37(5), 428-461.
- Taber, S. (1930). The mechanics of frost heaving. *The Journal of Geology*, 38(4), 303-317.
- Topp, G. C., Davis, J. L., & Annan, A. P. (1980). Electromagnetic determination of soil water content: Measurements in coaxial transmission lines. *Water Resources Research*, 16(3), 574-582.
- Take, W. A., Bolton, M. D., Wong, P. C. P., & Yeung, F. J. (2004). Evaluation of landslide triggering mechanisms in model fill slopes. *Landslides*, 1(3), 173-184.
- Take, W. A., & Beddoe, R. A. (2014). Base liquefaction: a mechanism for shear-induced failure of loose granular slopes. *Canadian Geotechnical Journal*, 51(5), 496-507.
- Take, W. A., Beddoe, R. A., Davoodi-Bilesavar, R., & Phillips, R. (2015). Effect of antecedent groundwater conditions on the triggering of static liquefaction landslides. *Landslides*, 12(3), 469-479.
- Zhu, J. H., & Anderson, S. A. (1998). Determination of shear strength of Hawaiian residual soil subjected to rainfall-induced landslides. *Géotechnique*, 48(1), 73-82.

[This page is intentionally left blank]

8 Appendix: Application of geotechnical and geophysical field measurements in an active alpine environment

Daisy Lucas

ETH Zürich, Institute for Geotechnical Engineering
Stefano-Franscini-Platz 5, 8093 Zürich, Switzerland
E-Mail address: daisy.lucas@igt.baug.ethz.ch

Kerstin Fankhauser¹

ETH Zürich, Institute for Geotechnical Engineering and Institute of Geophysics
Stefano-Franscini-Platz 5, 8093 Zürich, Switzerland
E-Mail address: kerstin.fankhauser@erdw.ethz.ch

Sarah M. Springman

ETH Zürich, Institute for Geotechnical Engineering
Stefano-Franscini-Platz 5, 8093 Zürich, Switzerland
E-Mail address: sarah.springman@igt.baug.ethz.ch

Submitted to IOP Conference Series: Earth and Environmental Science.

Status: Published

Lucas, D. R., Fankhauser, K., & Springman, S. M. (2015). Application of geotechnical and geophysical field measurements in an active alpine environment. In IOP Conference Series: Earth and Environmental Science (Vol. 26, No. 1, p. 012023). IOP Publishing.

¹ Current employer: focusTerra ETH-Bibliothek
Sonneggstrasse 5, 8092 Zürich, Switzerland

Abstract

Rainfall can trigger landslides, rockfalls and debris flow events. When rainfall infiltrates into the soil, the suction (if there is any) is reduced, until positive water pressure can be developed, decreasing the effective stresses and leading to a potential failure. A challenging site for the study of mass movement is the Meretschibach catchment, a location in the Swiss Alps in the vicinity of Agarn, Canton of Valais. To study the effect of rainfall on slope stabilities, the soil characterization provides valuable insight on soil properties, necessary to establish a realistic ground model. This model, together with an effective long term-field monitoring, deliver the essential information and boundary conditions for predicting and validating rainfall-induced slope instabilities using numerical and physical modelling. Geotechnical monitoring, including soil temperature and volumetric water content measurements, has been performed on the study site together with geophysical measurements (ERT) to study the effect of rainfall on the (potential) triggering of landslides on a scree slope composed of a surficial layer of gravelly soil. These techniques were combined to provide information on the soil characteristics and depth to the bedrock. Seasonal changes of precipitation and temperature were reflected in corresponding trends in all measurements. A comparison of volumetric water content records was obtained from decagons, time domain reflectometry (TDR) and electrical resistivity tomography (ERT) conducted throughout the spring and summer months of 2014, yielding a reasonable agreement.

List of notation

a	→	Tortuosity factor
Dec, Decagon	→	Dielectric permittivity sensor EC-5 Decagon devices
ERT	→	Electrical resistivity tomography
ETH, IGT	→	Institute of geotechnical engineering at ETH Zürich
IT	→	Instrumented Trench
K_a	→	Dielectric constant
m	→	Cementation factor
n	→	Coefficient of saturation
OTT Pluvio ²	→	Meteostation
S	→	Saturation
Temp. surface	→	Temperature in data logger
TDR	→	Time domain reflectometry sensor, Campbell Scientific
TP	→	Handmade test pit
VWC	→	Volumetric water content
WSL	→	Swiss Federal Institute for Forest, Snow and Landscape Research
ρ	→	Resistivity of the porous soil
ρ_w	→	Resistivity of the pore filling
ρ_{ERT}	→	Electrical resistivity measured by ERT
Φ	→	Soil Porosity

8.1 Introduction

The Meretschibach catchment (Figure 8.1), situated in the Swiss Alps, within the Canton of Valais, provides an environment in which different kinds of mass movements occur more or less frequently where the slope of inclination is steeper than the angle of repose. Furthermore, this complex field environment consists of a type of soil that is challenging for monitoring and characterisation. Shallow landslides can be triggered within this catchment by a decrease of suction due to rainfall, followed by an increase in pore water pressure with a consequent reduction in effective stress within the gravelly soil. Triggering of a mass movement event can generate debris flows, which have the potential to reach the village of Agarn and cause significant damage to infrastructure, as well as loss of life [1]. Some of these events have been documented [2], but little has been published in the case of slope instabilities triggered in gravelly soils. The project at Meretschibach involves the soil characterisation, including the determination of soil properties at different depths, thickness of soil (depth of bedrock) and the establishing of a realistic ground model. This characterisation forms the base of an effective field monitoring to observe and measure the response of the scree slope to rain infiltration and saturation processes. A long-term monitoring campaign, integrating geotechnical and geophysical methods together with laboratory analyses, allows a progressively more detailed calibration and validation of the ground model. Ultimately a collection of all acquired data is used for numerical and physical modelling to study the mechanism of failure due to rainfall [3], hence enabling a hazard assessment to be made and the implementation of suitable safety measures, along with early warning systems.

Instrumentation is placed at shallow depths within three geotechnical trenches (IT1-3 at elevations of 1868-1914 m.a.s.l., Figure 8.1) in one of the steep scree slopes in the catchment, to perform real-time monitoring of the volumetric water content (VWC), temperature and suction [4, 5]. Electrical resistivity tomography (ERT) measurements were conducted repeatedly throughout the summer months of 2014, on a profile located closely to IT1, to complement the geotechnical data [6], allowing the VWC recordings to be validated in specific locations. Furthermore, the precipitation in the area is measured at two weather stations located within 1 km, at an elevation of 2220 m.a.s.l., and of 1370 m.a.s.l., respectively.

The data acquired in two of the instrumented trenches (IT1 and IT3) are analysed separately and compared to the corresponding data in the other trench. Trends in temperature, as well as VWC in the scree slope's gravelly soil, correspond well to expected seasonal changes. Peaks in VWC can be related to intense rainfall events. Unanticipated variations and deviations can be explained by isolated rockfall events and freezing/thawing cycles. A good correlation between the peaks in various measurements is observed for the times when debris flows occurred in the Meretschibach in July 2014.

A comparison between the VWC measurements performed by time domain reflectometry (TDR) and decagon sensors within each trench is made, and the degree of saturation is calculated. Furthermore, the VWC obtained from the two geotechnical instruments is compared to the VWC estimates obtained from the ERT acquisitions using Archie's law [7, 8]. All trends and values agree well with each other, proving that the three different methods are consistent. The VWC and the suction measurements, provide valuable information to be able to assess changes in soil resistance, particularly in a partially saturated state.

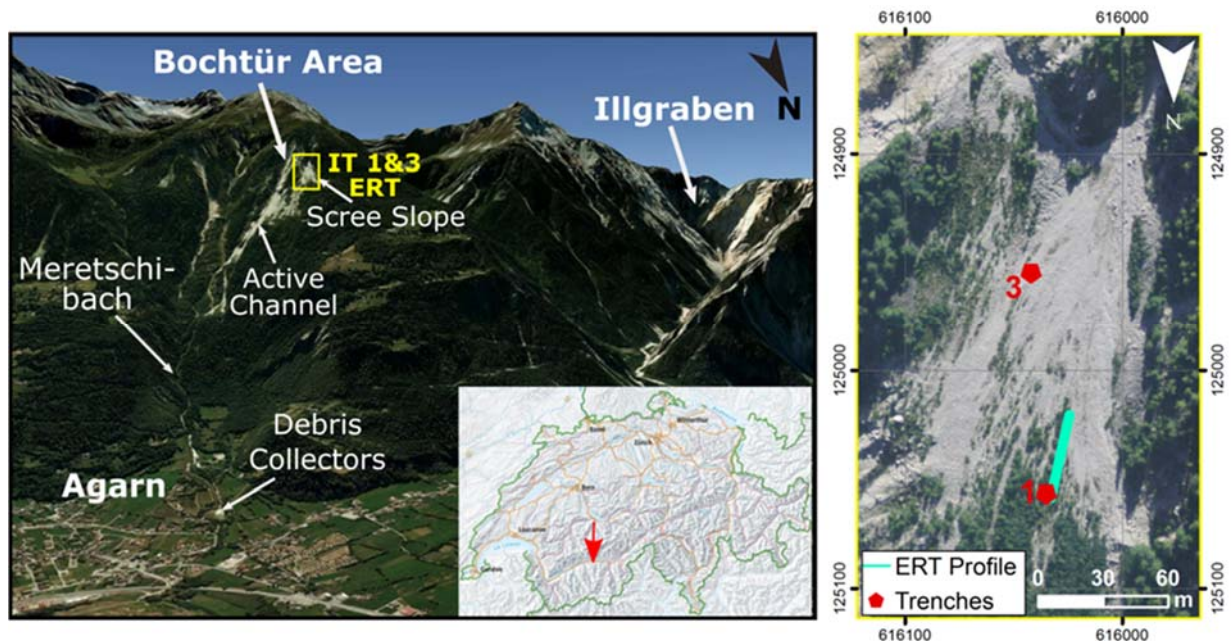


Figure 8.1. Overview of the field area, located in the canton of Valais, Switzerland (small map). The left image looking to the south shows a view of Agarn, situated on the Rhone valley floor and the Meretschibach catchment on the mountain slopes behind. The most active area within the catchment, the Bochtür area, can be divided into an active channel and a scree slope. The right image shows an enlargement of the scree slope (yellow rectangle) and the locations of the instrumented trenches (IT1 and IT3) are indicated along with the ERT profile on which the monitoring was performed.

8.2 Soil and ground characteristics

8.2.1 Soil classification

Figure 8.1 shows the location of the research site and specifically the location of instrumented trenches 1 and 3 (IT1 – IT3). Samples were taken from three test pits TP1-3, near IT1 to perform grain size analysis. The work was carried out during dry summer weather conditions. The following characteristics were noted: the ground surface was considered to be ‘depth zero’ for each test pit, at least 4 kg of soil were extracted for each disturbed sample, some cobbles larger than 70 mm and any boulders were left at the site, and roots were found in almost all of the samples.

The soil is classified (Figures 8.2, 8.3 and Table 8.1) according to USCS and Swiss standard classification SN 670 004-2NA, as gravel with silt and sand (GM). Figure 8.2, shows the soil profiles at the trenches to a depth of 38 cm. IT1 on the left, consists of a layer of approximately 30 cm thickness (A and B, above the orange dashed line) of gravel with more fines, overlying coarser gravel. This upper layer can further be divided into an upper (A) and a lower (B) part with more and less roots respectively. At IT3, the top layer consists of finer gravel (D) and a transition to slightly coarser gravel (E) can be inferred.



Figure 8.2. Soil at instrumented trenches IT1 (left) and IT3 (right). The following description is based on field observations. IT1: A (~0-12 cm), gravel with silt, sand and roots; B (~12-25 cm), gravel with silt and sand; C (below ~25-30 cm), coarser gravelly soil with less fines. IT3: D (~0-25 cm), gravelly soil with little content of sand and silt; E (below ~25 cm) change to a coarser gravel.

Table 8.1. Soil classification from test pits.

Test Pit	USCS Classification	Moisture content [%]	Percent of fines [%]	C_u [-]	C_c [-]	G_s [-]
TP1	GM	2.9-3.7	5.7-8.2	73.6-139.3	8.3-14.4	2.68
TP2	GM	3.0-5.4	5.5-10.8	33.3-105.1	7.9-11.2	
TP3	GM	3.7-4.3	6.7-16.4	72.8	9.1	

C_u : Coefficient of uniformity, C_c : Coefficient of curvature; G_s : Specific gravity

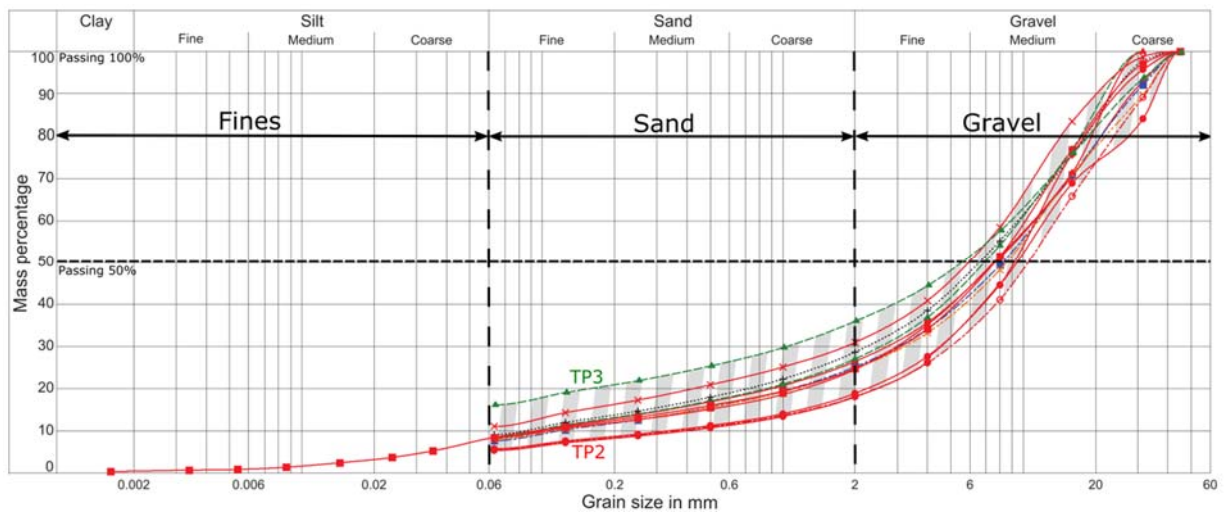


Figure 8.3. Grain size distribution: samples from Meretschibach scree slope test pits 1-3. A range is marked in grey to illustrate the characteristics and content of fines for the entire set of samples. A sample in green from test pit 3 (TP3) at a depth of 30-40 cm and a sample in red from test pit 2 (TP2) at a depth of 20-40 cm set the upper and lower limit respectively.

8.3 Monitoring methodology

8.3.1 Instrumented trench

Selected spots on the slope(s) (i.e. landslide source areas) are monitored *in situ* to measure water infiltration-suction characteristics in the ground, to provide time-series data about infiltration quantities and rates, and the effect on the inter-particle suction, which directly affects the *in situ* effective stress. Suction is measured with tensiometers, providing complementary data to calculate effective stress and hence to assess changing shear stress conditions.

Two vertical monitoring profiles were installed (IT1-IT3), consisting of sets of co-located tensiometers, time domain reflectometry (TDR) soil moisture, decagons and temperature sensors. Freezing/thawing conditions, particularly during the crucial spring snowmelt

period, can be identified through measurements of temperature, while the TDRs are calibrated to measure the volumetric water content. An SR50A Campbell weather station was installed and monitored within the study area (precipitation, ambient air temperature, humidity) by the Swiss Federal Institute for Forests, Snow and Landscape research, (WSL), and a Pluvio OTT² (solid and liquid precipitation) was installed by ETH to measure total precipitation.

8.3.1.1 Sensors & calibration

The sensors used in this monitoring set up include: tensiometers, decagons, time domain reflectometry (TDR) and temperature devices. These have been described and used in previous landslide monitoring programmes [3]; technical details are given in Table 8.2. TDR and decagon sensors measure the volumetric water content of the soil in the field and have been used in the past [3, 9], to measure the VWC in unsaturated silty sand, and alpine moraine with good results. The performance of both sensors will be evaluated and compared in the field for application in gravelly soils. The decagons and TDRs were calibrated using the gravelly soil from the field, over the range of volumetric water contents estimated for unsaturated conditions in gravel. However, when comparing measurements between these two types of sensors the cylinder of influence as well as sensitivity to temperature changes should be taken into account.

Table 8.2. Technical information about the sensors installed.

Sensor	Name	Brand	Length	Measuring range
Decagon	EC-5	Decagon devices	0.089 m	Apparent dielectric permittivity ξ_a 1-50.
TDR	TDR100	Campbell Scientific	0.15 m	Apparent dielectric constant $K_a^{0.5}$.
Tensiometers		Keller AG Company	0.15, 0.30, 0.45 m	80-85 centibar.
Temperature sensors	RTD PT100	Heraeus		-50 to 100 °C.

8.3.2 ERT

A 2D electrical resistivity survey was carried out on a fixed profile line next to the instrumented trench 1 (Figure 8.1) to complement the TDR and decagon point measurements, achieving a more widespread characterisation of the subsurface. The

basic principle of geoelectrical resistivity measurements involves the injection of current into the ground through a pair of electrodes and measuring the resulting potential in the form of a voltage difference at another pair of electrodes along the subsurface current flow. 48 electrodes were planted along the profile line and the Syscal Pro system (IRIS instruments) was used to conduct six ERT measurements (three of which are presented here) in a monitoring phase from May to July, 2014. A Wenner configuration was used for all acquisitions due to the highly resistive environment. The inversion was performed using the BERT (Boundless Electrical Resistivity Tomography) software package [6, 10, 11, 12, 13].

8.3.3 Archie's law

ERT measurements are highly susceptible to changes in the subsurface water content/saturation as the current injected during a geoelectrical survey flows mostly through the pore water. An empirical relationship between the resistivity of a porous medium to the amount of pores, their connectivity and saturation, as well as the resistivity of the pore filling fluids, was found by Archie [7]:

$$\rho = a\rho_w\Phi^{-m}S^{-n} \quad (8.1)$$

where ρ is the resistivity of the porous soil, ρ_w is the resistivity of the pore filling fluid, Φ is the soil's porosity and S its saturation which can also be expressed as the ratio between the water content θ and the porosity (Eq. 8.2). Furthermore, a is the tortuosity factor set to 1 for granular soils, m is the cementation factor and n is the coefficient of saturation. The latter two factors are taken from literature (e.g. [7, 14, 15]) and are assumed to be constant: $m = 1.3$ and $n = 2$.

$$S = \frac{\theta}{\Phi} \quad (8.2)$$

Archie's law is considered to be valid in this case, as the soil consists mainly of gravel and sand and contains almost no fine material, especially clay (Figures 8.2 and 8.3 and Table 8.1) and has enabled effective comparisons between geotechnical soil moisture measurements and ERT acquisitions (e.g. [16, 17, 18]). The temporal variation of soil resistivities along the repeatedly measured profile can therefore be related to the temporal variation of soil saturation or water content (under the assumption that the porosity and the pore water resistivity remains constant) as:

$$\frac{\rho_t^{-\frac{1}{n}} - \rho_{t_0}^{-\frac{1}{n}}}{\rho_{t_0}^{-\frac{1}{n}}} = \left[\frac{\rho_t}{\rho_{t_0}} \right]^{-\frac{1}{n}} - 1 = \frac{S_t - S_{t_0}}{S_{t_0}} = \frac{\Delta S}{S_{t_0}} = \frac{\Delta \theta}{\theta_{t_0}} \quad (8.3)$$

The profile measured on May 15, 2014 was chosen as the baseline model (at time t_0) and variations in saturation in later acquisitions are relative to this profile. The advantage of this approach is the fact, that none of the constants (except for n) nor the porosity or the resistivity of the pore water need to be estimated to see a seasonal variation in soil saturation. The resulting trend can relatively be compared to the readings obtained from TDR and decagon measurements.

To achieve a more detailed comparison however, the parameters in Archie's law have to be estimated from soil and water samples extracted from the field and analysed through lab and field experiments. The values of the key parameters (Φ and ρ_w) have been estimated at this stage of the project on the basis of preliminary tests and the literature. These can be refined to improve the calculated soil saturation (and VWC) for comparison with field measurements in the trenches.

8.4 Results and discussion

8.4.1 Instrumented trench IT1

The data recorded from the end of October 2013 to April 2015 are shown in Figure 8.4, representing variations from four seasons with data from two winter's. The change of volumetric water content at 25 cm depth shows a general agreement between the measurements from the TDRs and decagons for the first eight months. The decagon readings differ from the TDR recordings after the rockfall event (beginning of August), but it is not possible to affirm that the impact of the rockfall affected the results at this depth. Values decrease to a minimum VWC during winter time (end of December to end of March), probably due to the accumulation of snow, leading to a low or non-existent rate of rain infiltration. This situation changes from April 2014 (spring season) through snow melt and rainfall, and continues to fluctuate due to varying seasonal precipitation to the end of 2014. Changes in VWC occur following to rain peaks. There is a gap from October 12 to November 10, 2014, with no precipitation information available at this time. However, it is still possible to see the variations in VWC, most probably due to precipitation.

A comparison of the temperatures in the soil at 15 cm depth and in the data logger, which was considered to be the local exterior temperature on the soil's surface, was also plotted in Figure 8.4. Temperatures are around 0°C, with minimum variation, for both sensors during the winter season, and this trend continues until April 2014. The temperatures increase again in May (spring season), and stay mainly between 10 – 15°C until August 2014 (summer season). They decrease again during November 2014 (autumn) and remain near zero degrees, illustrating an annual temperature curve with a range from approximately -8 to +26 °C.

A rockfall happened at the beginning of August 2014 (Figure 8.4) during an extended period of rain, with a debris flow observed (dashed brown line) at the end of July. At least one large boulder hit the trench breaking the stake and exposing the soil temperature sensor, causing some instability in the readings. An offset between the decagon and TDR readings was also observed. The boulder was removed and the sensor placed in the trench again on August 28, 2014, after which the temperature sensors (but not the decagons and TDRs) were recording similarly again. The VWC increased during January 2015, as water melted in the voids, when temperatures changed from a period of negative temperatures to above 0 °C.

Figure 8.5 shows the variation of pore water pressure with precipitation (SR50A weather station), recorded by the tensiometers, which were installed in June 2014 at depths of 15, 30 and 45 cm approximately three meters uphill of IT1. The correlation between the loss in suction after rainfall events can clearly be observed, in particular after all tensiometers show a significant increase in pore water pressure during the period of higher frequency in precipitation (July 2014). In addition, it should be noted, that the shallower tensiometer reacts faster the deeper tensiometers after a rainfall event, according to the direction of infiltration with depth.

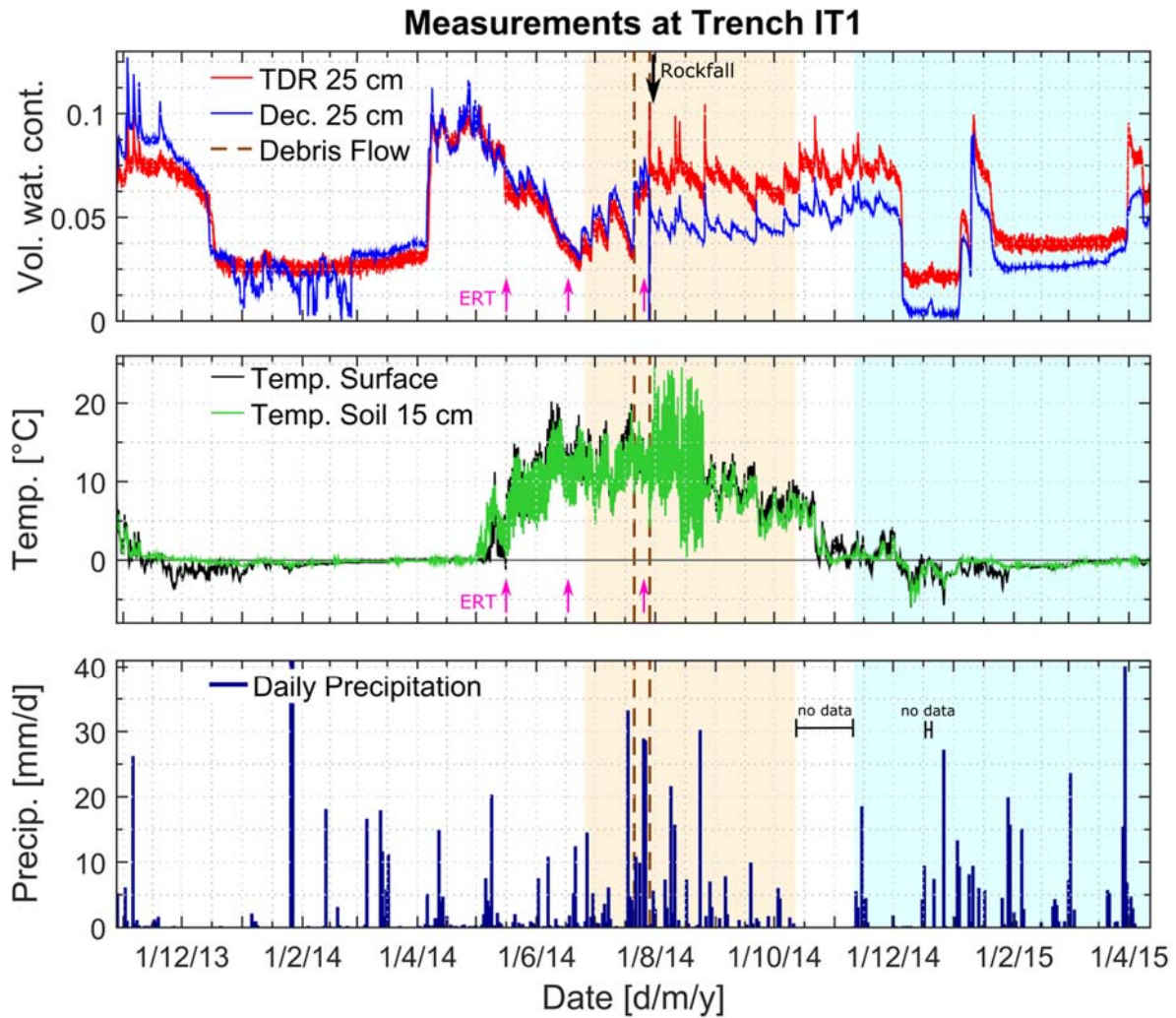


Figure 8.4. Measurements at IT1. From top to bottom: volumetric water content at 25 cm depth measured with TDR and decagons, temperature at 15 cm depth and in the data logger at the surface and daily total precipitation (28/10/2013–11/04/2015). Precipitation data were not recorded or not available during two periods, indicated in the bottom figure. A rockfall happened at the beginning of August (labelled black arrow), right after the second debris flow event (dashed brown lines indicate the two largest such events). Also indicated are the three ERT data acquisitions (magenta arrows), from which results are presented later (Figure 8.8). The colour change in the background reflects time windows during which tensiometer measurements (orange, Figure 8.5) or readings at instrumented trench IT3 (blue, Figure 8.6) are available. Precipitation data were supplied by WSL during the period of 2013 to October 2014.

8.4.2 Instrumented trench IT3

IT3 was installed at the end of October of 2014, and mainly reflects the seasonal changes in volumetric water content and temperature during the most recent autumn and winter seasons, with a short period corresponding to the beginning of the spring. Data from two sensors, a TDR and a decagon, located at depths of 15 and 20 cm respectively, are plotted in Figure 8.6 to show the change in VWC with temperature and precipitation. A comparison between the VWC values indicates similar trends in the readings, whether they originated from TDR or decagon, however some discrepancies are noticeable in

autumn and winter (December and January) and spring time (April). These changes could be due to a higher sensitivity of the decagons to a period of negative temperatures (from December to mid of January) and the differently sized cylinders of influence for the two types of sensors. TDRs have larger cylinders of influence and could therefore be considered as more representative measurement. Furthermore, a difference in readings might arise from the different installation depths of the two sensors.

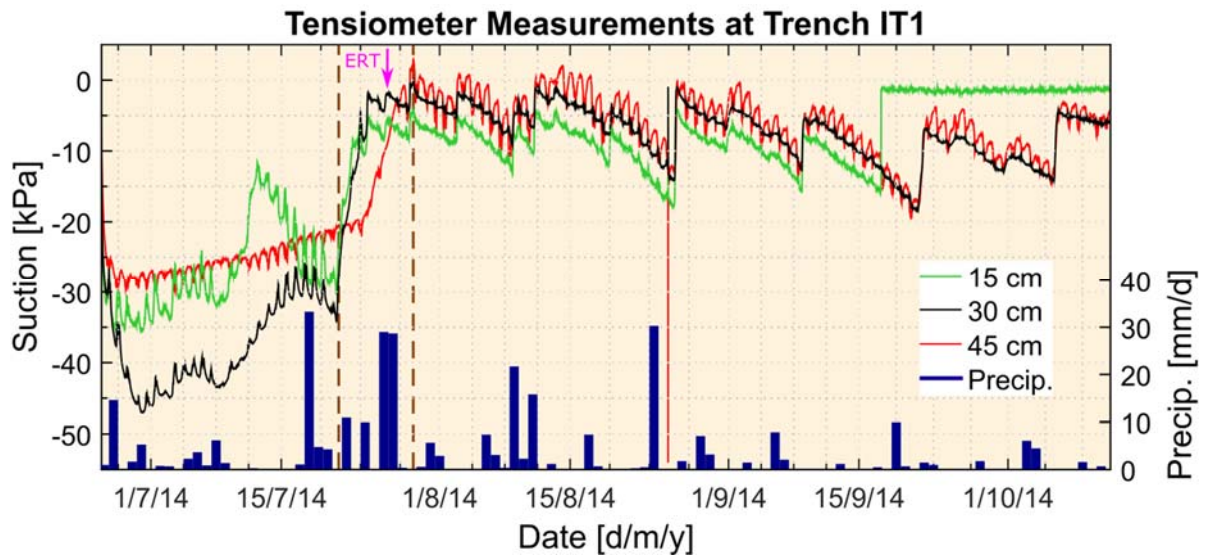


Figure 8.5. Tensiometer measurements at IT1 and precipitation data (25/6/2014-11/10/2014). Two debris flow events in the Meretschibach are indicated (brown dashed lines) and the ERT acquisition (Figure 8.8) on July 25, 2014 (magenta arrow). Precipitation data were supplied by WSL from the meteostation (SR50A) located at Meretschihorn 2220 m.a.s.l.

Temperatures remained near or below zero during the winter season (end of December to end of March), and the VWC reached minimum values due to minimal precipitation in form of rain (Figure 8.6). An increase in VWC is observed during the beginning to mid-January in the form of two peaks. The occurrence can be explained due to ice or snow melting after a transition from a negative temperature period to 0 °C, or slightly above freezing temperatures. The increase in temperature manifests itself in two corresponding peaks within the surface temperature and a continuous period of higher values in the soil temperature near 0 °C. The peaks in VWC during winter do not correlate with peaks in precipitation, as no such peaks are observable in the remaining winter period (February-March 2015) even though peaks in precipitation (mostly snowfall) can be noted. Peaks of VWC at IT3 show up in a very similar manner in IT1 (Figure 8.4 and 8.7, discussion in section 8.4.3).

Changes in VWC are also observed in April 2015 (Figure 8.6), when spring starts, but temperatures still remain close to 0 °C. A correlation to (a) rainfall event(s) is obvious; however thawing cycles could play a role in the increase of VWC in the soil, as the snow at the higher elevation start to melt.

In IT3, the decagon appears to be more sensitive to variation of precipitation and temperature, compared to the TDR. The relatively higher sensitivity of the decagon device is not as clearly detectable in IT1. During winter, at the end of 2014 (Figure 8.6), the decagon records more variation whereas the TDR device remains relatively steady at low VWC values over the entire season.

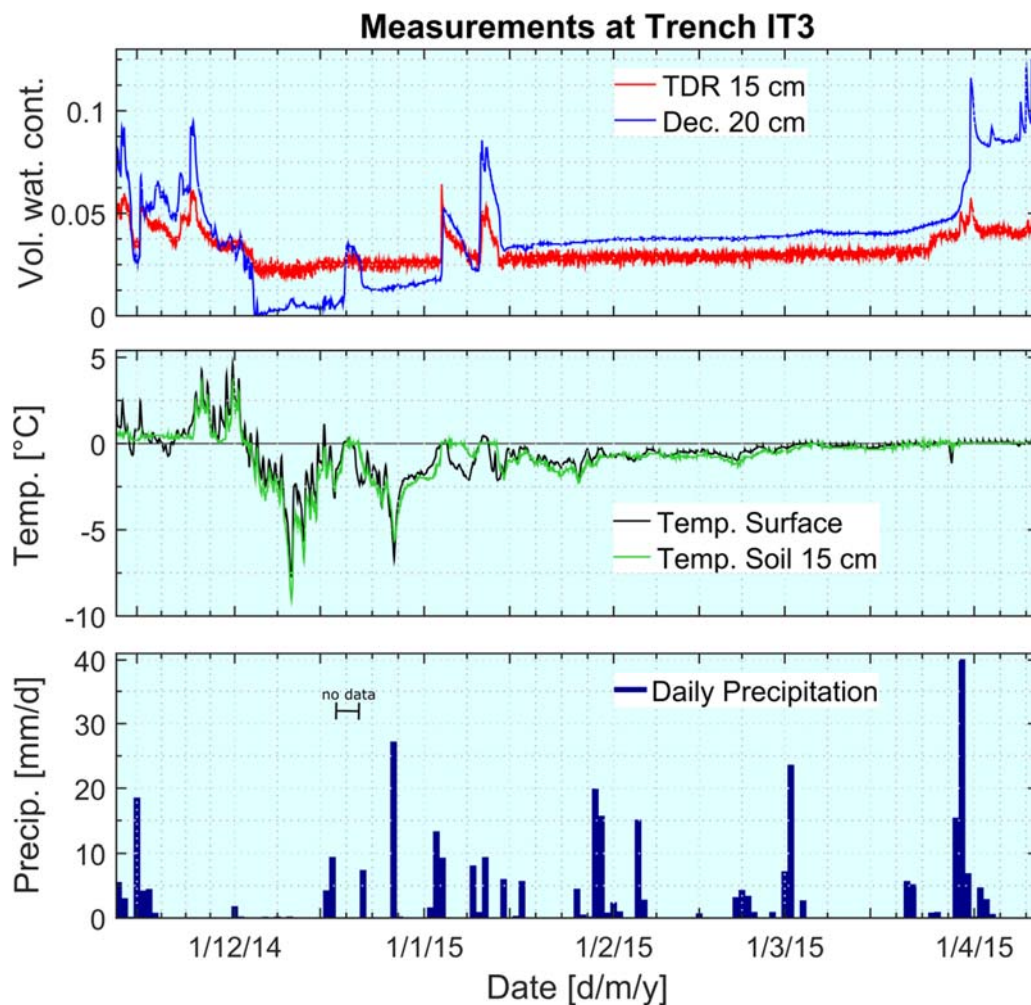


Figure 8.6. Measurements at IT3. From top to bottom: volumetric water content at 15 and 20 cm depth recorded with TDR and decagon sensors, temperature at 15 cm depth and in the data logger at the surface and daily total precipitation measured with Pluvio OTT² at 1370 m.a.s.l. (11/11/2014-11/04/2015). It should be noted, that the meteostation failed to record data during a period of four days (December 18-21, 2014) for unknown reasons.

8.4.3 Comparison between instrumented trenches

Figure 8.7 shows the comparison of the volumetric water content at IT1-IT3, located at elevations of 1868 m.a.s.l. and 1914 m.a.s.l. respectively. TDR and decagons were plotted separately, one from each trench over the same period, (as shown in Figure 8.4 and 8.7, marked with a blue background).

In addition, the precipitation and temperature are plotted in the same figure to facilitate a comparison in terms of correlation. The records of VWC agree within the seasonal changes: the changes in autumn (November- December 2014) are due to precipitation (rain/snow), and during winter when it reaches a minimum, the changes (e.g. the two peaks in beginning to mid-January 2015 marked in grey background) reflect rather temperature variations (thawing - freeze cycles) than actual increases in precipitation. Variations at the beginning of the spring season (April 2015) due to precipitation in the form of rainfall are again observed.

Most interestingly, the two large peaks in VWC data in January 2015 (Figure 8.7, grey background) were recorded in a very similar manner in both trenches. This not only means that both types of instruments expressed a comparable sensitivity most likely to a temperature variation, resulting in thawing (as discussed in section 8.4.2), but also that this specific event influenced the entire scree slope instead of isolated locations.

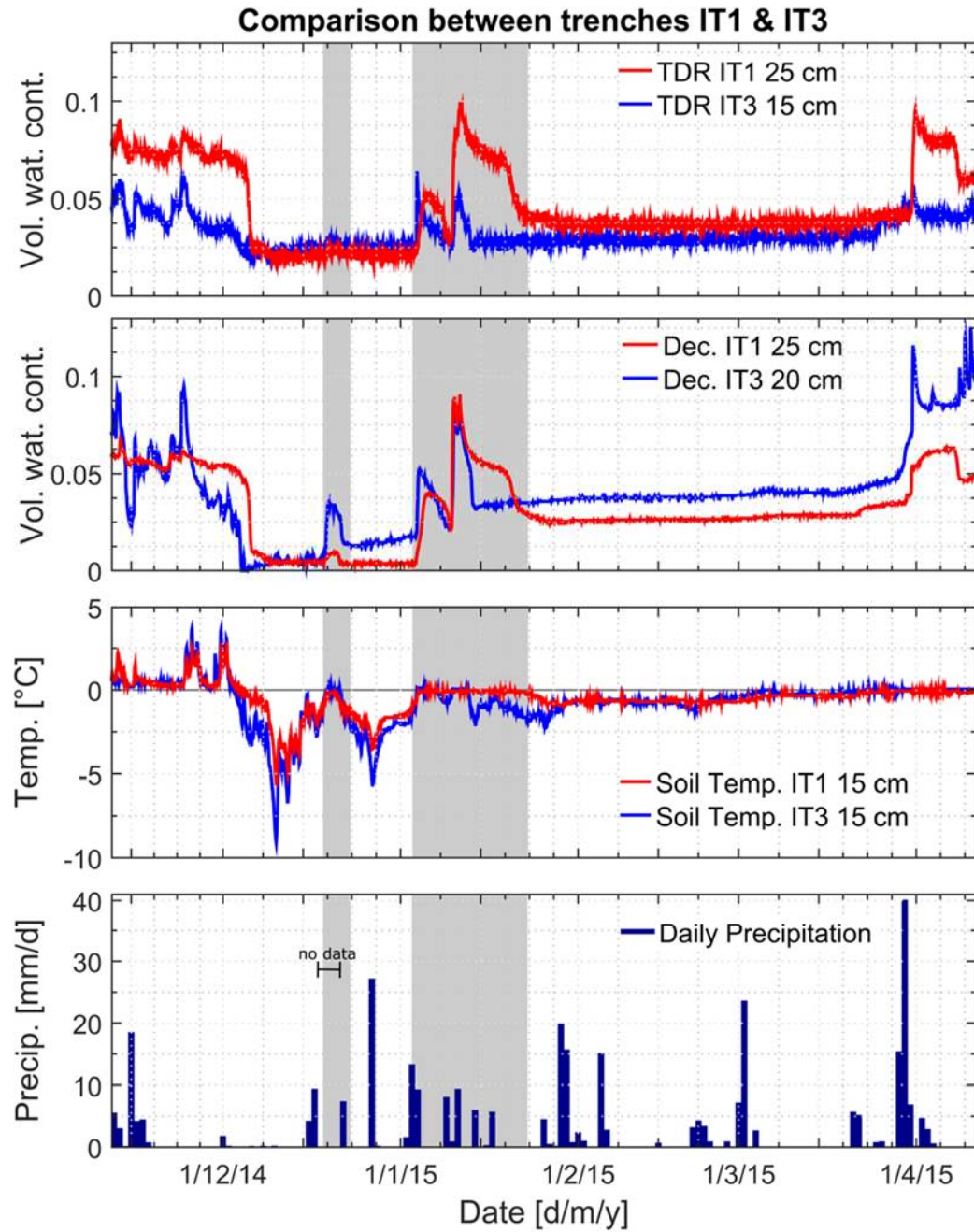


Figure 8.7. Comparison between TDR and decagon measurements at IT1 and IT3 during the period of 11/11/2014-11/04/2015 (same length of time as in Figure 8.6).

The possibility of isolated and sudden events such as avalanches on the scree slope is also considered for an explanation, although this scenario does not necessarily imply an increase of the VWC in the point of view of the authors. Instead, an explanation for this abrupt increase can be attributed to the difference in the dielectric constant of water and ice (approx., 80 and 3, respectively [6]). According to the Topp equation used for TDR calibration [3], the VWC increases with the dielectric constant. Since the total dielectric constant of a soil can be estimated from its components (solid, water and air),

freezing/thawing cycles have an impact on the magnitude of the calculated VWC. A better understanding of this widespread type of event will be possible when photographs from permanently installed cameras at the scree slope near IT3 are retrieved.

Furthermore, a third peak occurring at the end of December 2014 (grey background), was only detected by two decagons, but the peak remained smaller in IT1 compared to IT3. An increase in temperature was measured in both trenches at the same time. This again suggests a greater sensitivity of decagons (as an instrument type) to changes in temperature, in particular after longer periods of subzero conditions. Variations in VWC between trenches, as shown in Figure 8.7, can be due to a difference in the gravel characteristics as described in Figures 8.2 and 8.3.

8.4.4 Comparison between ERT and TDR

The resulting geoelectrical tomograms in Figure 8.8, show the subsurface resistivities obtained from inversion of the ERT data acquired on May 15, June 16 and July 25, 2014. All models depict a two-layered subsurface: an upper, relatively low resistive layer, which can be attributed to the gravelly soil and a highly resistive layer underneath, which is assumed to represent the quartzite bedrock.

The precipitation data before each of the acquisitions (magenta arrows in Figure 8.8) show that the conditions were dry and undergoing a drainage phase for the first two campaigns, whereas the data acquired in July was recorded within a period of heavy rainfalls. These seasonal changes are mostly reflected in resistivity changes within the soil layer, in particular as a significant reduction of resistivities in the July model. The saturation relative to the subsurface model obtained in May clearly reflects these conditions; there is a slight near-surface decrease in saturation in June, whereas an increase in saturation is observed within the soil layer in July. This trend in near-surface soil saturation corresponds very well to the volumetric water content measurements (which are directly proportional to saturation) from TDR and decagons installed at shallow depths within trench 1 (lowermost graph in Figure 8.8).

8.5 Conclusions

Combining geotechnical and geophysical techniques, has lead to greater insight about the characterisation of the ground forming the scree slope and its response to rainfall and snow in terms of saturation and desaturation. A monitoring campaign was designed to investigate this, using different methods consisting of two types of sensors installed in

instrumented trenches to determine the VWC. ERT was used to obtain resistivities which can be converted to VWC through Archie's law.

The monitoring of two instrumented trenches (IT1-IT3) gives valuable information regarding the response of the volumetric water content and temperature in the soil due to seasonal weather changes. In this aspect, the VWC increases in spring due to thawing cycles and precipitation in the form of rain, and reaches the lowest values during winter when temperatures, that stay near 0 °C or below, could lead to soil freezing under the protective insulation of a snow cover. The occurrence of isolated peaks in VWC during winter can be explained by thawing after relatively extended periods of subzero temperatures.

There is a good agreement in the data trend between decagons and TDR, but some differences can be observed, either due to rockfall events (IT1) or a greater sensitivity of one of the sensors, e.g. decagons to temperature changes during thawing periods (IT3). Additional sensor specific conditions, such as the cylinder of influence, can account for variations in the readings. The data collected from VWC in both trenches show that the response to seasonal changes are similar for the shallower layers at two different elevations on the scree slope.

The analyses of the volumetric water content time series obtained from instrumentation in the trenches not only showed very plausible seasonal trends and a clear correlation to increases in precipitation, but also compared reasonably well to saturation trends calculated from ERT measurements, conducted on different dates from May-July 2014. Thus, these results illustrate how well geotechnical and geophysical measurements can complement each other. Furthermore, models obtained from different ERT acquisitions consistently showed a subsurface separable into a highly resistive, underlying bedrock at shallow depths and a less resistive gravelly soil layer at the surface.

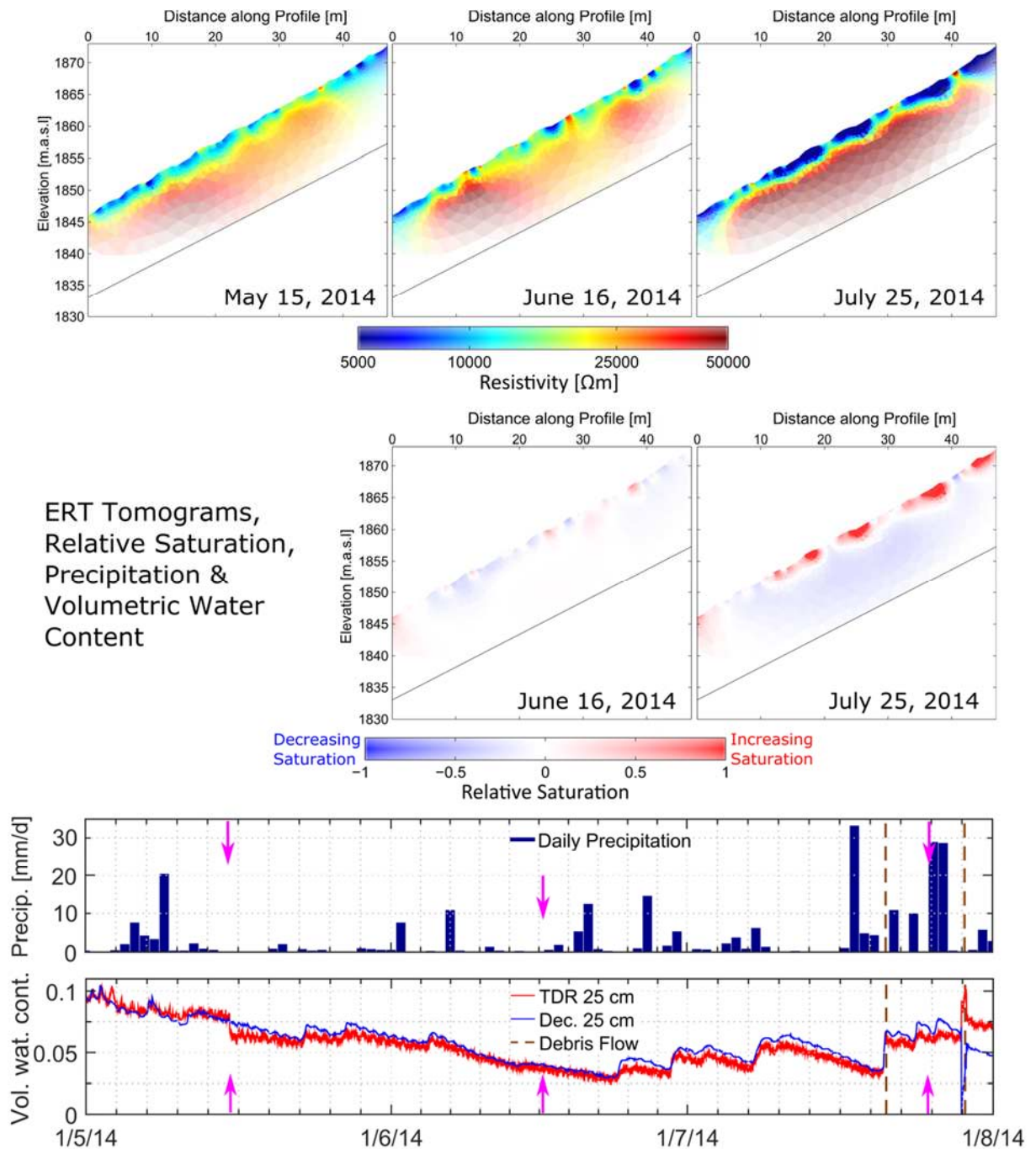


Figure 8.8. The uppermost row shows the resulting geoelectrical tomograms from May 15, June 16 and July 25, 2014. The resistivity scale beneath the tomograms is the same for every acquisition. The row below shows the increasing and decreasing saturation, relative to the subsurface model obtained on May 15. Finally, the three acquisition dates are indicated (purple arrows) within the precipitation and the volumetric water content measurements from TDR and decagon instrumentation in trench 1, shown in the lower most graphs from 01/05/2014-01/08/2014. Also indicated in both graphs are the debris flow events in July (see Figure 8.4 for description).

8.6 Acknowledgments

The authors are most grateful for funding from the SNF Project No. 200021_144326/1 and Canton Valais, together with the Councils of Agarn and Leuk. The project also contributes to the TRAMM2 programme of the Competence Centre of Environmental Sustainability.

In particular, we wish to acknowledge the support from Pascal Stoebener, WSL, as well as to Professor Dr. Hansruedi Maurer (Exploration and Environmental Geophysics, EGG), Dipl. Ing. Ralf Herzog, Ernst Bleiker and to Nicole Oggier, for giving access to part of the rainfall data used in the analysis.

8.7 References

- [1] Oggier N 2011 Simulierung von Murgängen mit RAMMS am Beispiel des Meretschibachs *Master Thesis* ETH Zürich & Forschungsanstalt für Wald Schnee und Landschaft (WSL).
- [2] Rickenmann D and Zimmermann M 1993 The 1987 debris flows in Switzerland documentation and analysis *Geomorphology* **8(2)** 175-89.
- [3] Askarinejad A 2013 Failure mechanisms in unsaturated silty sand slopes triggered by rainfall *ETH Dissertation* Nr. 21423.
- [4] Lucas D R, Askarinejad A A, Herzog R, Bleiker E and Springman S M 2015 Volumetric water content determination by TDR sensors and decagons in gravelly soils *submitted to the XVI European Conference on Soil Mechanics & Geotechnical Engineering (ECSMGE)* Edinburgh.
- [5] Springman S M, Lucas D R, Oggier N C, Kos A, Fankhauser K and McArdell B, 2015 Study of the seasonal response of a scree slope and debris flow catchment in the Swiss alps *submitted to the XVI European Conference on Soil Mechanics & Geotechnical Engineering (ECSMGE)* Edinburgh.
- [6] Fankhauser K 2014 Geophysical slope characterization using GPR and ERT in an active debris flow catchment *Master Thesis* EEG ETH Zurich.
- [7] Archie G E 1942 The electrical resistivity log as an aid in determining some reservoir characteristics *AIME* **146** 54-62.
- [8] Friedel S, Thielen A, Springman S M 2006 Investigation of a slope endangered by rainfall-induced landslides using 3D resistivity tomography and geotechnical testing *J. of Appl. Geophys.* **60** 100-14.
- [9] Teyssiere P 2005 Geotechnische Eigenschaften von Möranen *ETH Dissertation* Nr. 16322, ETH Zürich.
- [10] Günther T, Rücker C and Spitzer K 2006 Three-dimensional modelling and inversion of DC resistivity data incorporating topography - II. Inversion *Geophys. J. Int.* **166** 506-17.
- [11] Günther T and Rücker C 2013 Boundless electrical resistivity tomography - the

user tutorial available at: www.resistivity.net.

- [12] Rücker C, Günther T and Spitzer K 2006 Three-dimensional modelling of DC resistivity data incorporating topography - I. Modelling *Geophys. J. Int.* **166** 495-505.
- [13] Günther T 2011 Timelapse ERT inversion approaches and their applications *Int. Workshop on Geoelectric Monitoring Within the Frame of the FWF Project TEMPEL (TRP 175-n21) and the 7th FP European Project SafeLand: Berichte der geologischen Bundesanstalt Nr.93 (Vienna, 30 November - 2 December 2011)* pp 91-7.
- [14] Lowrie W 2007 *Fundamentals of Geophysics* (New York: Cambridge University Press).
- [15] Schön J 1983 *Petrophysik Physikalische Eigenschaften von Gesteinen und Mineralen* (Berlin: Akademie-Verlag).
- [16] Brunet P, Clément R and Bouvier C 2010 Monitoring soil water content and deficit using Electrical Resistivity Tomography (ERT)—a case study in the Cevennes area France *J. of Hydro.* **380(1)** 146-53.
- [17] Lehmann P, Gambazzi F, Suski B, Baron L, Askarinejad A, Springman S M and Or D 2013 Evolution of soil wetting patterns preceding a hydrologically induced landslide inferred from electrical resistivity survey and point measurements of volumetric water content and pore water pressure *Water Resources Research* **49(12)** 7992-8004.
- [18] Springman S M, Thielen A, Kienzler P and Friedel S 2013 A long-term field study for the investigation of rainfall-induced landslides *Geotechnique* **63(14)** 1177-93.